

**DOCTORAL THESIS**

# Development of Catalysts for Oxygen Electoreduction: A Doping Approach

Ehsan Zarmehri

TALLINN UNIVERSITY OF TECHNOLOGY  
DOCTORAL THESIS  
69/2025

# **Development of Catalysts for Oxygen Electoreduction: A Doping Approach**

EHSAN ZARMEHRI



TALLINN UNIVERSITY OF TECHNOLOGY  
School of Science  
Department of Chemistry and Biotechnology

NATIONAL INSTITUTE OF CHEMICAL PHYSICS AND BIOPHYSICS  
Energy Technologies Group

This dissertation was accepted for the defence of the degree of Doctor of Philosophy in Chemistry 04/09/2025

**Supervisor:** Dr. Ivar Kruusenberg  
National Institute of Chemical Physics and Biophysics  
Tallinn, Estonia

**Co-supervisor:** Dr. Ragle Raudsepp  
National Institute of Chemical Physics and Biophysics  
Tallinn, Estonia

**Opponents:** Dr. Dana Schonvogel  
Institute of Engineering Thermodynamics  
German Aerospace Center (DLR)  
Oldenburg, Germany

Prof. Nadežda Kongi  
Faculty of Science and Technology  
Institute of Chemistry  
University of Tartu  
Tartu, Estonia

**Defence of the thesis:** 30/09/2025, Tallinn

**Declaration:**

Hereby I declare that this doctoral thesis, my original investigation and achievement, submitted for the doctoral degree at Tallinn University of Technology has not been submitted for doctoral or equivalent academic degree.

Ehsan Zarmehri



European Union  
European Regional  
Development Fund



Investing  
in your future

-----  
signature

Copyright: Ehsan Zarmehri, 2025

ISSN 2585-6898 (publication)

ISBN 978-9916-80-379-0 (publication)

ISSN 2585-6901 (PDF)

ISBN 978-9916-80-380-6 (PDF)

DOI <https://doi.org/10.23658/taltech.69/2025>

Zarmehri, E. (2025). *Development of Catalysts for Oxygen Electroreduction: A Doping Approach* [TalTech Press]. <https://doi.org/10.23658/taltech.69/2025>

TALLINNA TEHNIKAÜLIKOO  
DOKTORITÖÖ  
69/2025

**Katalüsaatormaterjalide arendamine  
hapniku redutseerumise tarvis:  
dopeerimispõhine lähenemine**

EHSAN ZARMEHRI







## Contents

List of publications .....	7
Author's contribution to the publications .....	8
Abbreviations and symbols .....	9
Introduction .....	11
1 Literature overview .....	13
1.1 Fuel cells .....	13
1.1.1 Polymer electrolyte membrane fuel cells .....	13
1.2 Oxygen reduction reaction .....	16
1.2.1 Oxygen reduction on non-precious metal catalysts .....	18
1.2.2 ORR on heteroatom doped carbon nanomaterials .....	19
1.2.3 Oxygen reduction on metal-nitrogen-carbon (M-N-C) catalysts .....	23
1.2.4 Oxygen reduction on carbon-supported metal-phthalocyanines .....	26
2 Experimental .....	30
2.1 Synthesis of catalyst materials .....	30
2.1.1 Synthesis of Pb-N-doped carbon, and V-N-doped carbon .....	30
2.1.2 Synthesis of boron, fluorine and nitrogen-doped graphene/FWCNT .....	30
2.2 Modification of GC electrodes .....	30
2.3 Electrochemical measurements .....	31
2.4 Physical characterization instruments .....	33
3 Results and discussion .....	35
3.1 Oxygen electroreduction on Pb and N-doped carbon nanotubes .....	35
3.1.1. Physical characterisation of Pb and N-doped catalyst material. ....	35
3.1.2 Electrochemical characterization Pb and N-doped catalyst material .....	42
3.2 Oxygen electroreduction on V and N-doped carbon nanotubes .....	50
3.2.1. Physical characterization of V and N co-doped catalyst material. ....	50
3.2.2 Electrochemical characterization V and N-doped catalyst material .....	56
3.3 Oxygen reduction reaction on boron and fluorine co-doped carbon composite. ....	62
3.3.1. Physical characterisation of B and F co-doped carbon catalyst. ....	62
3.3.2 Electrochemical characterization B and F co-doped carbon catalyst .....	66
4 Conclusions .....	73

References .....	75
Acknowledgments.....	98
Abstract.....	99
Lühikokkuvõte.....	100
Appendix 1 .....	101
Appendix 2 .....	113
Appendix 3 .....	125
Curriculum vitae.....	139
Elulookirjeldus.....	141

## List of publications

- I. **Zarmehri, E.**, Raudsepp, R., Šmits, K., Käämbre, T., Šutka, A., Yörük, C. R., Zacs, D., & Kruusenberg, I. (2023). Lead and Nitrogen Co-Doped Multi-Walled Carbon Nanotube Electrocatalyst for Oxygen Reduction Reaction. *Journal of The Electrochemical Society*, 170(11), 114505. <https://doi.org/10.1149/1945-7111/AD0072>
- II. **Zarmehri, E.**, Raudsepp, R., Danilson, M., Šutka, A., & Kruusenberg, I. (2023). Vanadium and carbon composite electrocatalyst for oxygen reduction reaction. *Materials Chemistry and Physics*, 307, 128162. <https://doi.org/10.1016/J.MATCHEMPHYS.2023.128162>
- III. Raudsepp, R., Türk, K. K., **Zarmehri, E.**, Joost, U., Rauwel, P., Saar, R., Mäeorg, U., Dyck, A., Bron, M., Chen, Z., Noda, S., Kruusenberg, I., & Tammeveski, K. (2024). Boron and Fluorine Co-Doped Graphene/Few-Walled Carbon Nanotube Composite as Highly Active Electrocatalyst for Oxygen Reduction Reaction. *ChemNanoMat*, 10(6), e202300546. <https://doi.org/10.1002/CNMA.202300546>

## **Author's contribution to the publications**

Contribution to the papers in this thesis are:

- I. The author was responsible for carrying out the catalyst materials synthesis, performing all the electrochemical measurements, and analysing the data. The author interpreted the electrochemical testing data and spectroscopy and characterization analysis and participated in the writing of the manuscript.
- II. The author was responsible for carrying out the catalyst materials synthesis, performing all the electrochemical measurements, and analysing the data. The author interpreted the electrochemical testing data and spectroscopy and characterization analysis and participated in the writing of the manuscript.
- III. The author was responsible for electrochemical measurement and analysing the data. The author interpreted the electrochemical testing data and participated in the writing of the manuscript.

## Abbreviations and symbols

A	geometric surface area of an electrode
AEI	anion exchange ionomer
AEMFC	anion-exchange membrane fuel cell
BE	binding energy
BET	Brunauer-Emmett-Teller
BF	boron-fluorine
BFC	boron-fluorine-carbon
CNT	carbon nanotubes
CPV	cumulative pore volume
PbPc	lead (II)phthalocyanine
VPc	vanadyl phthalocyanine
CuPc	copper (II)phthalocyanine
C <sub>O2</sub> <sup>b</sup>	concentration of oxygen in the bulk solution
CV	cyclic voltammetry
D <sub>O2</sub>	diffusion coefficient of oxygen
d <sub>p</sub>	diameter of pores
DFT	density functional theory
DMFC	direct methanol fuel cell
E	electrode potential
e	electron charge
E <sup>0</sup>	standard potential
E <sub>1/2</sub>	half-wave potential
E <sub>onset</sub>	onset potential
EDX	energy dispersive X-ray spectroscopy
F	Faraday constant
FePc	iron (II)phthalocyanine
FC	fuel cell
FCEV	fuel cell electric vehicle
FWCNT	few walls carbon nanotube
GC	glassy carbon
GDL	gas diffusion layer
HER	hydrogen evolution reaction
HOR	hydrogen oxidation reaction
I	current
I <sub>d</sub>	diffusion-limited current
I <sub>k</sub>	kinetic current
ICP-MS	inductively coupled plasma mass spectrometry
j	current density
j <sub>d</sub>	diffusion-limited current density

$j_k$	kinetic current density
K-L	Koutecky-Levich
LSV	linear sweep voltammogram
MEA	membrane-electrode assembly
MFC	microbial fuel cell
M-N-C	metal-nitrogen-carbon
MOF	metal-organic framework
MWCNT	multi-walled carbon nanotube
$n$	number of electrons transferred per $O_2$ molecule
N-C	nitrogen-carbon
NNMC	non-noble metal catalyst
NPMC	non-precious metal catalyst
OER	oxygen evolution reaction
ORR	oxygen reduction reaction
PEMFC	proton-exchange membrane fuel cell
PGM	platinum group metal
Pt/C	carbon-supported Pt catalyst
RDE	rotating disk electrode
rGO	reduced graphene oxide
RHE	reversible hydrogen electrode
RRDE	rotating ring-disk electrode
SAC	single atom catalyst
SCE	saturated calomel electrode
SEM	scanning electron microscopy
SHE	standard hydrogen electrode
SSA	specific surface area
SWCNT	single-walled carbon nanotubes
TEM	transmission electron microscopy
$V_p$	total volume of pores
XAS	X-ray absorption spectroscopy
XPS	X-ray photoelectron spectroscopy
XRD	X-ray powder diffraction
$\nu$	kinematic viscosity of the solution
$\omega$	electrode rotation rate

## Introduction

The increasing global demand for energy is leading to higher levels of environmental pollution and the deterioration of living conditions. According to the International Energy Agency, the energy consumption in the world is increasing by 1% every year and transport has the big portion of it (Nazir et al., 2020; Staffell et al., 2019). Most of the world's energy supply currently comes from fossil fuels, which release pollutants such as CO<sub>2</sub> and NO<sub>x</sub> into the atmosphere. Fuel cells and batteries have long been considered- and continue to be- promising alternatives to fossil fuel-based energy systems in order to reduce pollution.

Low-temperature fuel cells generate electricity and heat through an electrochemical reaction between hydrogen and oxygen, with water and heat being the only byproducts. This clean energy conversion process makes them an attractive option for sustainable and environmentally friendly energy solutions (Vesborg & Jaramillo, 2012). Main problems towards the widespread usage of fuel cell are cost and durability (Zine et al., 2024). The oxygen reduction reaction (ORR) which takes place at the fuel cell cathode is a most important reaction in the fuel cell that unfortunately has a sluggish kinetics (Patowary et al., 2022). To accelerate this reaction a catalyst with high performance is needed. Until today platinum is considered the most effective catalyst for the oxygen reduction reaction (ORR) due to its optimal binding energy with ORR intermediates which arises from its favorable electronic structure (Nørskov et al., 2004). Nevertheless, Pt is expensive, with limited source and its mining produces huge amounts of CO<sub>2</sub> (Alonso et al., 2012). Remarkable effort has been made to reduce the Pt amount in PEM fuel cells, over the past 10 years Pt amount has been reduced around 50%, from 0.4-0.6 mg/cm<sup>2</sup> to approximately 0.1–0.2 mg/cm<sup>2</sup> (Müller-Hülstede et al., 2023; Shuxiu Yang et al., 2024). However, there is still a strong drive to develop non-platinum catalyst materials, which could address all the aforementioned issues associated with platinum, including its high cost, limited availability, and susceptibility to degradation. In 1964, Dr. Jasinski published the first study on a non-platinum fuel cell catalyst (Jasinski, 1964). Subsequently, research on non-platinum catalysts expanded significantly, leading to the publication of numerous studies and papers in this field. Discovery of new carbon nanomaterials such as carbon nanotube (CNT) (Iijima, 1991) and graphene (Novoselov et al., 2004), as a support material for both platinum-based and non-platinum based catalysts, has decreased the price and enhanced active site dispersion (Shui, Wang, et al., 2015). The study on catalyst for low temperature fuel cell is divided to two main topics: Platinum Group Metals (PGM) and PGM free. Transition metals, alkali metals, and p-block metals, in combination with carbon, nitrogen, and oxygen, have been identified as promising PGM free catalysts for PEM fuel cells (T. Tang et al., 2020).

The electrochemical reduction of oxygen remains a compelling field of study, with numerous experimental and theoretical techniques aimed at understanding catalytic mechanisms, improving reaction efficiency, and developing more effective and durable catalyst materials (Zhongwei Chen et al., 2011; Higgins & Chen, 2013; Jaouen et al., 2010; Rabis et al., 2012). ORR may occur by either a two-electron pathway, resulting in the production of hydrogen peroxide, or a direct four-electron pathway, which is an important reaction in fuel cells and leads to the formation of water as the final product. The efficiency of the fuel cell is directly influenced by the kinetics of the oxygen reduction reaction. (Song & Zhang, 2008).



The aim of this PhD thesis was to explore the electrocatalytic activity of nanocarbon supported non-precious metal catalysts (NPMCs), such as lead and nitrogen doped carbon [I], vanadium and nitrogen doped carbon [II], boron and fluorine doped carbon [III]. Co-doping was used in all studies as it has been shown to enhance the ORR due to the synergetic effect (R. Ma et al., 2019; Shakil et al., 2018). Various doping precursor-to-carbon nanomaterial ratios, as well as different synthesis temperatures, were employed to identify the optimal synthesis conditions for preparing efficient ORR electrocatalysts. Electrochemical experiments were carried out using rotating disc electrode and rotating ring disc electrode. The surface structure, composition and morphology of carbon nanomaterials and nanocarbon supported catalysts has been examined by transmission electron microscopy, high-resolution scanning electron microscopy, X-ray photoelectron spectroscopy, Raman spectroscopy and X-ray powder diffraction analysis. The goal was to design new and improved carbon supported catalysts and to establish clear structure–property relationships that can drive further advancements in the field of fuel cell electrocatalysis. The aim was to identify low-cost, environmentally friendly alternatives to Pt/C catalysts in order to reduce the overall cost of low-temperature fuel cells while maintaining or enhancing their performance and durability.

# 1 Literature overview

## 1.1 Fuel cells

A fuel cell is a device that converts a fuel, such as hydrogen, and an oxidant, often oxygen in air, into electricity, heat, and a byproduct in the form of water. There are five types of fuel cells used in various applications: the polymer electrolyte membrane fuel cell, the alkaline fuel cell, the solid oxide fuel cell, the molten carbonate fuel cell, and the phosphoric acid fuel cell. In the fuel cell the fuel, which is hydrogen carrier or pure hydrogen, undergoes oxidation at the anode. Simultaneously, oxygen is reduced at the cathode, resulting in the formation of water by the utilization of protons produced from the oxidized hydrogen (Delavar & Wang, 2022; Ramasamy et al., 2024).

### 1.1.1 Polymer electrolyte membrane fuel cells

In polymer electrolyte membrane fuel cell, the transportation of protons or anions to the cathode or anode respectively is facilitated by an ion conductive polymeric membrane. Given that the membrane has electrical insulating properties, the movement of electrons occurs through an external circuit, so enabling their use for practical purposes, as seen in Figure 1. Low temperature polymer exchange fuel cells are divided into the anion exchange membrane fuel cells (AEMFC) and proton exchange membrane fuel cells (PEMFC). In PEMFC protons are produced during the oxidation of hydrogen fuel at the anode and transported through the membrane to the cathode, where it reacts with reduced oxygen to form a water. During the oxidation process also, the electrons are released to the external circuit, and thus electric current is produced (Qasem & Abdulrahman, 2024). In an AEMFC, the anode is supplied with fuel in the form of either hydrogen or methanol, while the cathode receives water and oxygen. At the cathode, the process of oxygen reduction results in the generation of hydroxide ions ( $\text{OH}^-$ ), which subsequently move across the electrolyte towards the anode. At the anode, the hydroxide ions undergo a chemical reaction with the fuel, resulting in the formation of water molecules and the release of electrons (Das et al., 2022).

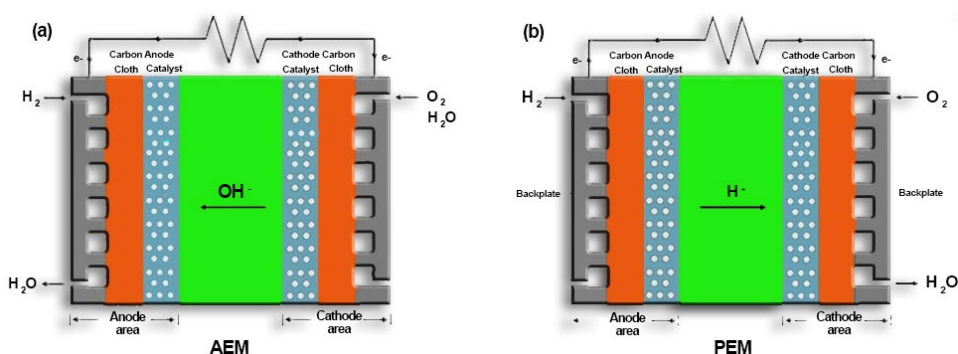


Figure 1. (a) Anion exchange membrane fuel cell and (b) proton exchange membrane fuel cell (adapted from Zhang et al. (H. W. Zhang et al., 2015)).

In addition to polymer electrolyte membrane fuel cells, the microbial fuel cell (MFC) is working in neutral medium. In MFC, electroactive microorganisms oxidize organic substrates at the anode under anaerobic conditions, releasing protons and electrons.

The electrons are transferred to the external circuit, generating an electric current, while the protons migrate through a membrane or electrolyte to the cathode. At the cathode, under aerobic conditions, oxygen is reduced and combines with the protons to form water. This bioelectrochemical process occurs efficiently in neutral media, making MFCs suitable for applications such as wastewater treatment with simultaneous electricity generation (Kruusenberg, 2013; Santoro et al., 2017).

Using a single-cell membrane electrode assembly (MEA) as an illustrative case, the fuel cell generally contains catalysts that are either deposited onto or incorporated into a carbon material, constituting the anode and cathode components. The electrodes are then applied onto the polymeric membrane and positioned between gas diffusion layers (GDLs). GDL is often composed of carbon paper or carbon cloth and serve the function of facilitating the effective transportation of gases to and water from the electrodes. The membrane electrode assembly (MEA) is situated between flow field of bipolar plates, which function as additional conduits for the transportation of gas and water vapor (Figure 2). These plates are often composed of graphite or metal that has been coated with layers resistant to corrosion, because of the acidic environment inside a PEMFC (Stein & Ein-Eli, 2020). Additionally, they provide support to the MEA and contribute to the structural integrity of the fuel cell stack (Zarmehri et al., 2013).

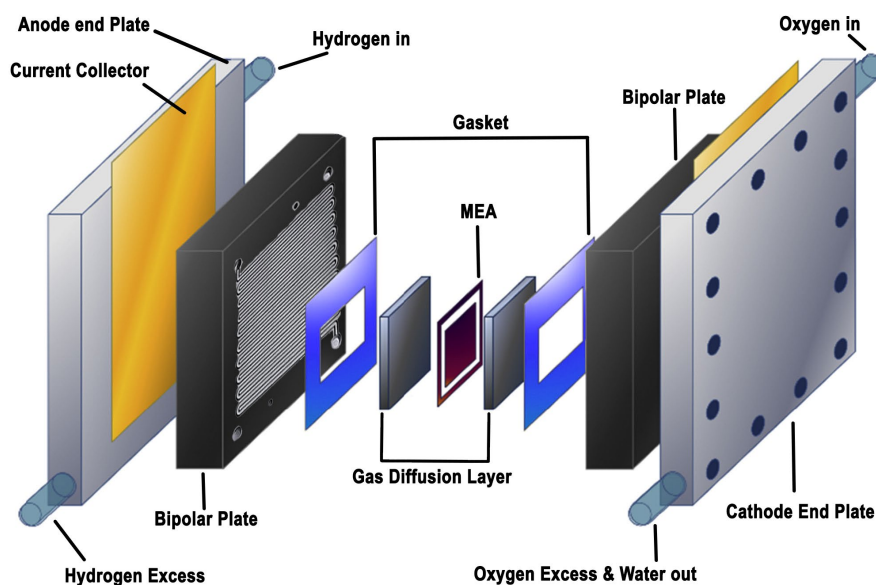


Figure 2. Low temperature fuel cell structure (adapted from Cruz-Martínez et al (Cruz-Martínez et al., 2019)).

The main issues in fuel cell industry that must be addressed are durability and affordability. The cost breakdown analysis of PEMFC stack reveals that the catalyst component makes a substantial contribution (59%) to the overall cost of stack (Figure 3). The order costs are associated with the bipolar plate, membrane, gas diffusion layer, electrodes and gaskets (Anderson et al., 2023; Madheswaran et al., 2023; Pollet et al., 2019).

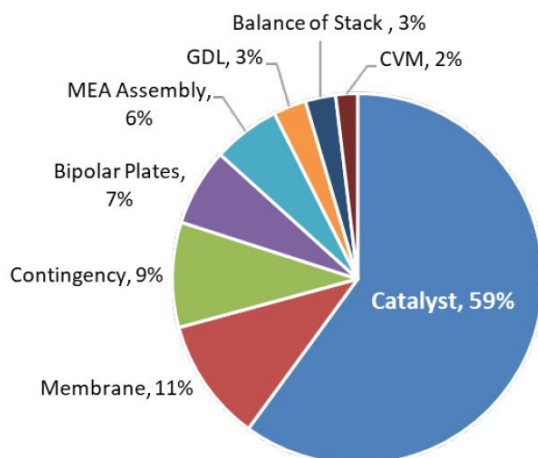


Figure 3. The cost breakdown for stack at 50000 systems per year (Gregory Kleen et al., 2022).

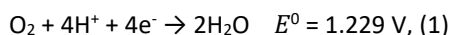
The increased cost of specialized Pt catalysts compared to untreated Pt metal may be ascribed to factors such as material processing expenses and manufacturer markup. The prices of PEMFCs have been decreased at a similar rate to those of lithium-ion batteries via the process of manufacturing scale-up (Porstmann et al., 2019; Schmidt et al., 2017). Nevertheless, the cost of the catalyst mostly consists of material expenses and does not decrease in proportion to the annual production volume of systems. Therefore, it is crucial to reduce the quantity of Pt-based catalyst used while yet preserving its durability. The decrease of catalyst loading may be achieved by the discovery of an enhanced catalyst possessing a greater level of activity in ORR. This can be further facilitated by augmenting the surface area of the catalyst and reducing the losses associated with mass transport, particularly under conditions of high current density. Nevertheless, there has been a resurgence of interest in cathode catalysts that do not include PGM. Notably, their effectiveness has been greatly enhanced, although only in the presence of oxygen (Charalampopoulos et al., 2023). Due to the limited intrinsic activity of catalysts devoid of PGM for ORR, a higher quantity of catalyst is required to achieve comparable performance, particularly in the presence of air. Increased loadings of catalysts that are devoid of PGM lead to a much thicker catalyst layer, which may be up to 100 times thicker than catalysts containing PGM. This is accompanied by greater resistance within the catalyst layer and losses in mass transfer.

The development of PEMFCs is often given to Willard Thomas Grubb and Leonard Niedrach, both of whom were associated with General Electric (GE) in the early 1960s. The research conducted on PEMFCs had a primary focus on enhancing the efficiency and functionality of the Gemini missions (Nail et al., 2008). The challenge of the significant demand for Pt in the manufacturing process of GE fuel cells has been acknowledged as a primary barrier to their widespread adoption from its beginnings (Nail et al., 2008). In contemporary times, PEMFCs have attained significant achievements. Prominent automobile manufacturers such as Toyota, Hyundai, Honda, Ford, Chevrolet, and Mercedes-Benz have unveiled their respective car models equipped with PEM fuel cell technology (Debe, 2012). Furthermore, Plug Power, a corporation specialized in the manufacturing of hydrogen-powered forklifts, disclosed a revenue of \$230 million in the fiscal year 2020 (*Plug Power Inc. Financials - Annual Reports*, 2021). Over the last decade,

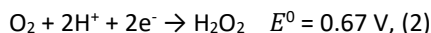
there has been a notable increase in both the specific activity and bulk activity of catalysts based on Pt (F. Guo et al., 2023; Hussain et al., 2020; Pollet et al., 2019; Xiaqing Wang et al., 2025). However, the successful implementation of these catalyst-level advancements into large-scale fuel cell stacks has proven to be a significant challenge (Ly et al., 2020). Based on the most optimistic forecasts, it is projected that the maximum platinum loading for PEMFC technology is 0.1 g kW<sup>-1</sup> (Pollet et al., 2019). This suggests that around 14% of the global platinum reserves would be required for the implementation of PEMFC technology, disregarding any possible losses resulting from recycling and catalyst production. The long-term feasibility of using platinum-based catalysts in PEMFCs for fuel cell electric vehicles (FCEVs) is questionable (Y. Wang et al., 2021). The inclusion of NPMC materials in the roadmaps of the US Department of Energy for PEMFC provides support for this approach (Thompson & Papageorgopoulos, 2019).

## 1.2 Oxygen reduction reaction

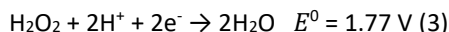
One of the key electrochemical processes is the electroreduction of oxygen. Not only does it provide power via fuel cells, but it is also essential for biological respiration, which sustains life. In acidic aqueous solutions ORR (Figure 4 right) can follow either a 4-electron pathway (eq. 1-4) (Anastasijević et al., 1987):



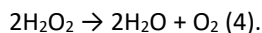
or 2-electron pathway:



followed by further reduction of hydrogen peroxide



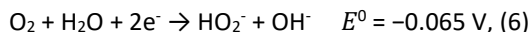
or disproportionation



In alkaline conditions (Figure 4 left) the ORR can also proceed via two pathways. The 4-electron pathway (eq. 5-8):



or 2-electron pathway:



followed by further reduction



or disproportionation



with all the standard potential ( $E^0$ ) values given versus the standard hydrogen electrode (SHE) at 25 °C.

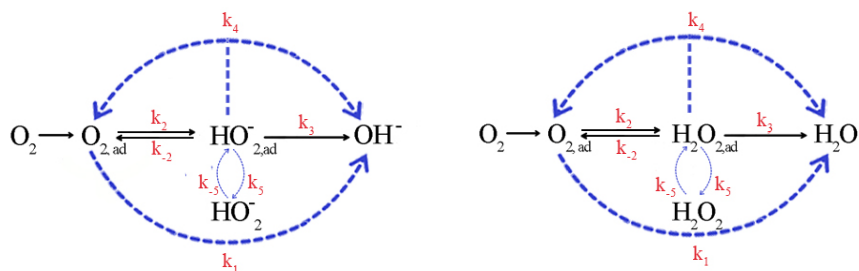


Figure 4. Simplified mechanism of oxygen reduction reaction in cathode of fuel cell in alkaline (left) and in the acidic media (right) (adapted from Kruusenberg (Kruusenberg, 2013)).

In fuel cells, the 4-electron pathway is consistently preferred. The 2-electron pathway leads to the formation of hydrogen peroxide too, and if not further reduced, can have corrosive effects on fuel cell components. Moreover, the formation of  $\text{H}_2\text{O}_2$  (or  $\text{HO}_2^-$ ) leads to a reduction in fuel cell efficiency (A. Yu et al., 2024). On noble metal surfaces, such as platinum, ORR proceeds along a direct 4-electron pathway. In the presence of acidic environment, platinum is well recognized as the electrocatalyst with the highest level of activity towards ORR. It exhibits selectivity in reducing oxygen via the 4-electron pathway (D. Zhang et al., 2023). Nevertheless, in alkaline media, the oxygen reduction reaction (ORR) can proceed via both inner-sphere and outer-sphere electron transfer mechanisms. The outer-sphere pathway involves the one-electron reduction of molecular oxygen without the necessity for specific adsorption onto the catalyst surface, typically forming a solvated superoxide anion, which is subsequently protonated to hydroperoxide ( $\text{HO}_2^-$ ). This reaction route is surface-independent and thus permits the effective use of a broader range of NPMs, as it bypasses the strong chemisorption requirement that is essential in acidic media where inner-sphere mechanisms dominate. Although the outer-sphere mechanism primarily yields peroxide species rather than water, its prevalence in alkaline conditions significantly broadens the scope for catalyst design beyond platinum-group metals (Figure 5) (Ramaswamy & Mukerjee, 2011, 2012). However, it has been shown that some catalytic sites, such as the  $\text{MN}_4$  coordination center, which are NPMs, may still facilitate the direct reduction of oxygen by a  $4e^-$  process in both acidic and alkaline environments (Asset & Atanassov, 2020; Byeon et al., 2023; Mineva et al., 2019).

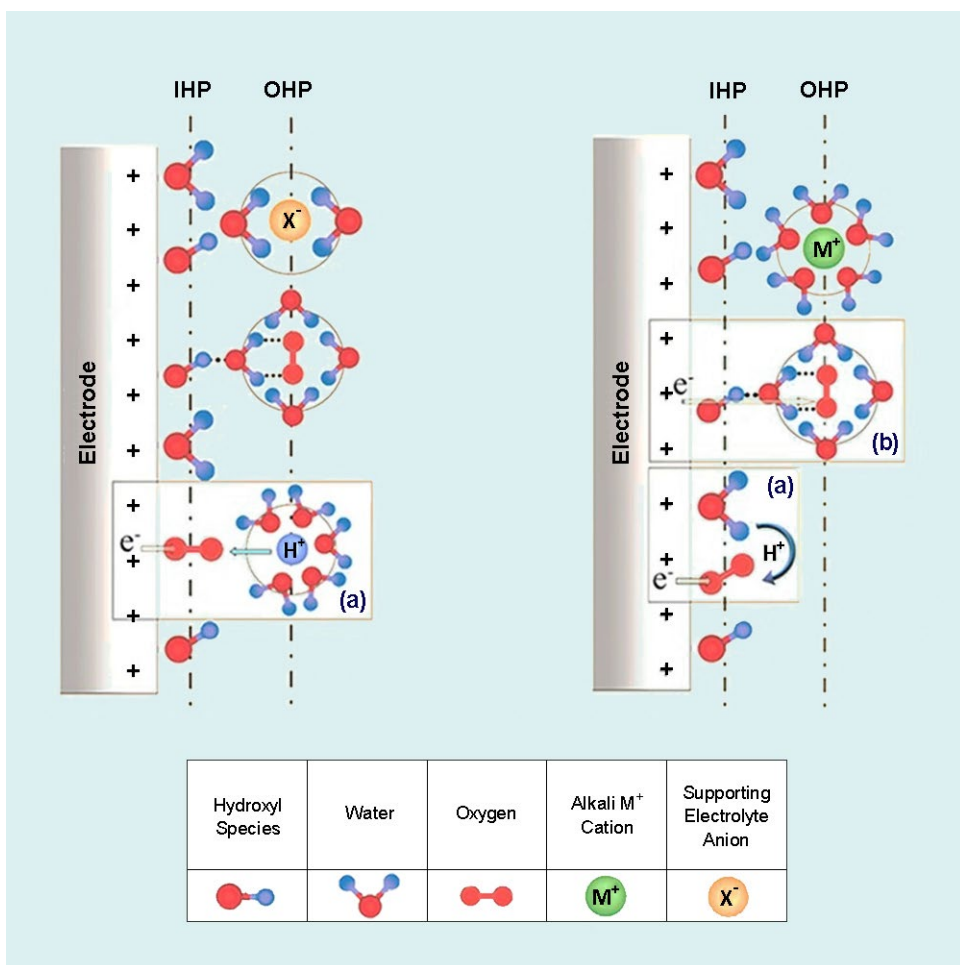


Figure 5. Schematic illustration of the double-layer structure during the ORR in acidic (left) and alkaline (right) conditions. Insets (a) and (b) illustrate the inner- and outer-sphere electron transfer processes. (adapted from Ramaswamy et al. (Ramaswamy & Mukerjee, 2011)).

### 1.2.1 Oxygen reduction on non-precious metal catalysts

The search for alternative materials to substitute platinum in the realm of oxygen reduction has a long historical lineage that predates the development of PEMFCs. Non-precious metal catalysts (NPMCs) have garnered significant attention as cost-effective alternatives to platinum-based catalysts for the oxygen reduction reaction (ORR) in fuel cells. Among these, iron-nitrogen-carbon (Fe-N-C) catalysts have demonstrated remarkable ORR activity, attributed to the presence of atomically dispersed Fe-N<sub>4</sub> sites within a carbon matrix. Recent studies have shown that increasing the concentration of these active sites enhances catalytic performance, achieving half-wave potentials up to 0.886 V versus the reversible hydrogen electrode (RHE) in alkaline media (Yuan Zhao et al., 2024). In addition to Fe-N-C catalysts, heteroatom-doped carbon materials, such as those doped with nitrogen, sulfur, boron, phosphorus, and fluorine, have been explored for ORR applications. These dopants modify the electronic structure of carbon, enhancing its catalytic activity. A recent review

highlighted the progress in combining transition metals with heteroatom doping, underscoring the synergistic effects that result in improved catalytic performance (Jannath & Saputra, 2024). Metal phthalocyanines have been extensively studied as molecular precursors for M-N-C catalysts due to their well-defined metal-N<sub>4</sub> coordination, providing insights into the active sites responsible for enhanced ORR performance. High-temperature treatment enhances the interaction between the MN<sub>4</sub> macrocycles and the substrate, leading to improved contact and integration (Jahnke et al., 1976). It must be noted that such thermal treatments can also lead to modifications of the active sites' structure and composition, an important issue that remains under active investigation. Nevertheless, it is crucial to acknowledge that this particular intervention also induced modifications to the attributes of the active site, a topic that will be further expounded upon in later discourse. In the year 1989, Gupta and colleagues achieved a notable breakthrough by replacing the expensive MN<sub>4</sub> macrocycles with a combination of a readily available nitrogen source, namely polyacrylonitrile (PAN), and basic metal salts like cobalt or iron acetate. The mixtures were subjected to pyrolysis at increased temperatures ranging from 300 to 950 °C, leading to the formation of highly regarded NPMCs at that time (Gupta et al., 1989). However, unlike the physically adsorbed macrocycle-based catalysts, which had a well-defined structure, these new heat-treated materials proposed the important question about the exact nature of the active sites for ORR after pyrolysis, which has only begun to be answered in the recent years (S. Liu et al., 2022; Mineva et al., 2019; Rukmani Krishnan et al., 2024).

Carbon contains in the large majority of the materials (atomic percentage) and provides the substance with chemical stability, electrical conductivity, porous structure, and mechanical strength (Jiang Li et al., 2023). Carbon materials with a significant surface area, such as Vulcan XC72 and Black Pearls BP2000, have been extensively used as support materials for heterogeneous catalysts, particularly as carriers for Pt nanoparticles (Shao et al., 2016; Yeager, 1984). Nevertheless, carbon alone has little electrocatalytic activity towards ORR, especially towards 4-electron reaction (Wei et al., 2023). The most effective technique so far in the creation of active sites for ORR without the use of platinum involves doping the carbon material with transition metals and heteroatoms. This approach promotes the formation of metal-nitrogen moieties and other defects that serve as catalytically active centers (Barkholtz & Liu, 2017; X. Li et al., 2022; Shao et al., 2016; Dan Wang et al., 2021).

### **1.2.2 ORR on heteroatom doped carbon nanomaterials**

Heteroatom doping of nanocarbons has emerged as an easy and effective way to enhance the kinetics of ORR, alongside many alternative non-platinum catalysts (Chattopadhyay et al., 2022; Gutru et al., 2023; Vikkisk et al., 2015; Woo et al., 2021). In fact, doped carbon materials are attractive due to their low cost, good tolerance to fuel impurities, long-term stability and good electrocatalytic activity towards the ORR (F. Kong et al., 2022; Woo et al., 2021). Since the seminal work by Gong et al. (K. Gong et al., 2009), which unveiled the electrocatalytic capabilities of N-doped carbon nanotube arrays for ORR in alkaline environments, a substantial body of research has emerged on metal-free carbon-based electrocatalysts (X. Kong et al., 2020). Various heteroatoms, including nitrogen (L. Sun et al., 2012; D. Yu et al., 2010; N. Zhou et al., 2018), boron (Bo & Guo, 2013; Jang et al., 2018; Sheng et al., 2011), phosphorus (J. Wu et al., 2013; Zhu et al., 2015), and sulfur (Klingele et al., 2017; Seredych et al., 2015; Z. Yang et al., 2012), have been used for the purpose of doping. However, it is worth noting that N-doped



carbon nanomaterials continue to be extensively researched and used as catalysts for ORR (Jeon et al., 2020; J. Wang et al., 2020). The N-doping technique has earned significant attention due to the comparable atomic radii of nitrogen and carbon, measuring at 74 picometers (pm) and 77 pm, respectively. This interest stems from the ease of the N-doping procedure and the enhanced stability it offers in comparison to other heteroatoms (Nagappan et al., 2022). The heteroatoms discussed above exhibit distinct electronegativity values and atomic sizes relative to carbon. Consequently, the introduction of dopants will cause changes in carbon charge distribution and electrical properties (Kaur et al., 2019). The proximity of nitrogen to carbon in the periodic table facilitates its integration into the carbon framework with little deformation, owing to similarities in atomic sizes and number of valence electrons (Jeon et al., 2020). The introduction of N-functionalities will result in the creation of supplementary electrocatalytically active sites (Qian et al., 2020; X.-L. Zhou et al., 2021). Although nitrogen can generate chemically stable species within the carbon structure, potentially improving certain aspects of electrochemical performance, the overall durability is often higher in more graphitized, defect-free carbons due to their superior resistance to oxidative degradation (Quílez-Bermejo et al., 2020). The electronegativity of nitrogen with a value of 3.04 is greater than that of carbon with a value of 2.55 (Jeon et al., 2020; Kaur et al., 2019). Consequently, the introduction of nitrogen into the carbon structure leads to the formation of defects, as the nitrogen atoms undergo a change in their configuration (Kaur et al., 2019; Sekhon & Park, 2021). Defects within carbon materials have been seen to have a significant impact on many properties, including electrical conductivity, wettability, and surface polarity. Consequently, these defects have been found to enhance the electrocatalytic activity towards ORR (X.-L. Zhou et al., 2021). Indeed, it is worth noting that various defects, such as unsaturated carbon atoms, vacancies, or extra structural defects, have a significant role in electrocatalytic activity (Quílez-Bermejo et al., 2020). The beneficial impact of defects is contingent upon the maintenance of a sufficiently high level of conductivity in the catalysts, hence facilitating efficient electron transportation to the active sites (Quílez-Bermejo et al., 2020). The presence of nitrogen atoms results in the induction of a net positive charge in adjacent carbon atoms. This phenomenon of charge delocalization enhances the adsorption of  $O_2$  and further reduction (Kaur et al., 2019; Sekhon & Park, 2021). There is much debate on the significance of the nitrogen content in the bulk material with respect to its electrochemical activity. However, some studies have shown a correlation between the catalytic activity and the content of nitrogen, as evidenced by previous research (Kaur et al., 2019). In contrast, further research has shown that the correlation between doping sites and catalytic activity has more significance compared to the quantity of nitrogen (Kaur et al., 2019; Quílez-Bermejo et al., 2020; X.-L. Zhou et al., 2021). The functional group known as pyridinic-N has been primarily attributed to the significant activity seen in ORR (Quílez-Bermejo et al., 2020). Its significance arises from the presence of a localized lone pair of electrons on the nitrogen atom, which is available for interaction with adsorbed oxygen molecules. This lone pair increases the electron-donating character of adjacent carbon atoms, thereby promoting the reductive adsorption and activation of  $O_2$  during the oxygen reduction process (Kaur et al., 2019). The active sites responsible for the reduction of  $O_2$  are not specifically nitrogen atoms, but rather the adjacent carbon atoms.  $O_2$  is first attracted to these sites, chemisorbed, and ultimately reduced (Quílez-Bermejo et al., 2020).

There are four common types of bonding nitrogen functionalities on the surface of N-doped catalysts: pyrrolic N, pyridinic N, graphitic N and oxidized N. (Figure 6). In pyrrolic N, nitrogen atom is in the ring of five carbons atoms, whereas pyridinic nitrogen is in the ring of six carbon atoms. If nitrogen atom is located in the plane of graphene substituting the carbon atom, it is called graphitic. Bonding between oxygen and nitrogen is oxidized N (Kasera et al., 2022). These species can be detected using XPS – pyridinic, pyrrolic, graphitic and N-oxide appear in 398.1 ( $\pm$  0.1) eV, 400.3 ( $\pm$  0.2) eV, 401.1 ( $\pm$  0.1) eV and 402.2 ( $\pm$  0.2) eV respectively (NIST, Gaithersburg, 20899, 2000; Ratso, Kruusenberg, Joost, et al., 2016). Pyridinic N is considered as the most efficient one for ORR among the forementioned nitrogen species (Ayyubov et al., 2023; Fukushima et al., 2015; D. Guo et al., 2016; Sakaushi et al., 2017).

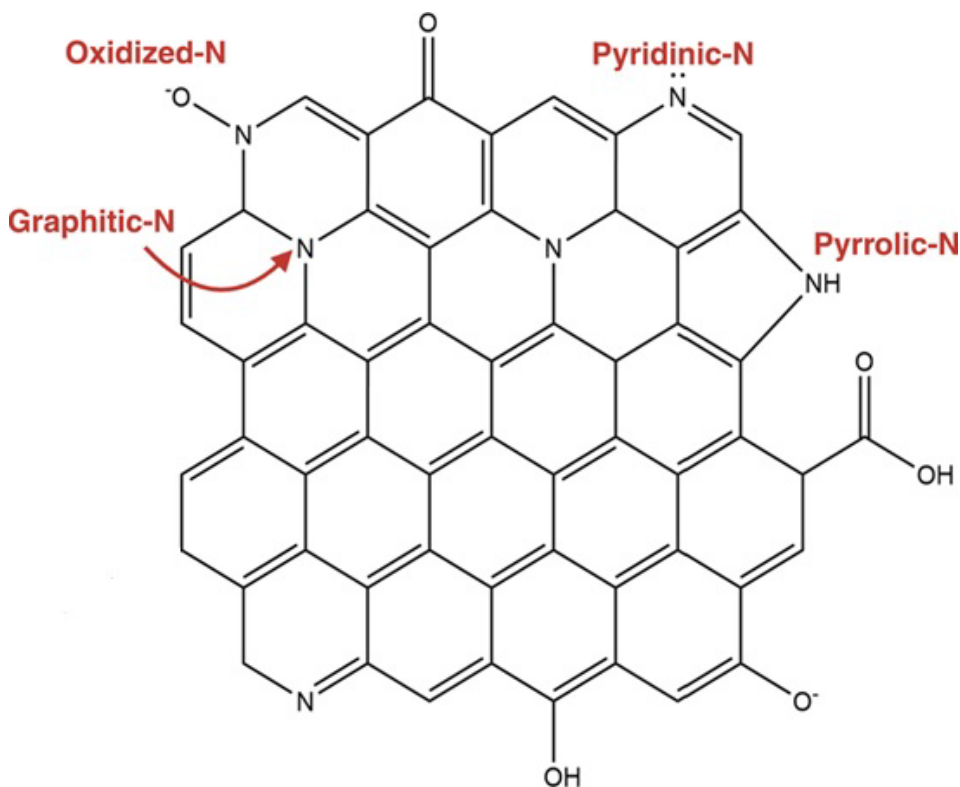


Figure 6. Hypothetical structure of N-doped biochar (Kasera et al., 2022).

Recently, there has been high interest in carbon materials doped with fluorine, mostly due to the element's strong electronegativity (J. Guo et al., 2018; Panomsuwan et al., 2015; Sim et al., 2022; Zeng et al., 2022). The use of fluorine as a co-dopant, in conjunction with nitrogen, boron, and sulfur, has been employed (Akula & Sahu, 2020; X. Bai et al., 2017).

The incorporation of atoms with differing electronegativities into the carbon framework disturbs the local charge distribution, creating polarized regions and positively charged carbon sites adjacent to the heteroatoms (Gutru et al., 2023; Yu Zhao et al., 2013). These positively charged carbon sites are favorable for the adsorption of O<sub>2</sub> molecules, which exhibit a partial negative charge due to electron withdrawal from antibonding orbitals as

they approach the catalyst surface. This charge interaction promotes the initial adsorption and activation of oxygen, a critical step in ORR (Peera et al., 2024; Xia et al., 2020; Zeng et al., 2022). Although the doping of carbon materials with nitrogen has been extensively investigated, the doping of materials with boron and fluorine remains relatively less studied.

There exist three primary approaches for incorporating boron atoms into the carbon framework: (1) using chemical vapor deposition with carbon and boron sources alongside a catalyst, (2) subjecting carbon material to thermal annealing (single-step) in the presence of a boron precursor, and (3) utilizing a two-step thermal treatment procedure (Bo et al., 2013; Y. Cheng et al., 2014; Kondo et al., 2014). In a manner similar to the incorporation of boron atoms, fluorine may be integrated into the carbon framework. In addition to the techniques indicated above, plasma treatment and direct chemical synthesis have also been used for the purpose of fluorine doping (Panomsuwan et al., 2015; Yeom et al., 2015; Zeng et al., 2022).

According to existing literature, it has been proposed that the process of pyrolysis at high temperatures leads to the removal of oxygen-containing groups from the surface of carbon nanomaterials. Consequently, defects are formed within the framework, which serve as active sites for the introduction of boron or fluorine doping (Bo et al., 2013; Yeom et al., 2015; J. Zhang et al., 2021). For instance, it has been shown that carboxylic groups exhibit decomposition tendencies throughout the temperature range of 350–750 °C, whereas quinone and phenolic groups have similar decomposition patterns within the temperature range of 500–950 °C (Bansal & Goyal, 2005; Bernal et al., 2018). In their study, Schniepp et al. investigated the impact of heat-treatment on the C/O ratio in graphene oxide (GO). Their findings revealed that when subjected to temperatures below 500 °C, the C/O ratio was measured at 7. Conversely, temperatures over 750 °C resulted in a higher C/O ratio exceeding 13 (Schniepp et al., 2006).

When boron is introduced into the carbon network, it induces a partial positive charge on the boron atoms due to its electronegativity of 2.04. Consequently, these partly positively charged boron atoms function as active sites for ORR (B. Wang et al., 2021). The study conducted by Lazar et al. shows that the incorporation of boron into the carbon network may occur either by replacement or addition, depending on the chemical properties of the doping agent (Lazar et al., 2014). According to previous research (Bo et al., 2013), the process of substitutional doping involves the bonding of boron to carbon within the  $sp^2$  network by replacing carbon atoms present in the network. Upon further boron doping,  $sp^3$  carbon atoms will be incorporated into the  $sp^2$  carbon lattice, accompanied by the introduction of  $BH_2$  species on the surface and edges of the carbon material (Lazar et al., 2014). The predominant bonding patterns of boron integrated into a carbon network are  $BCO_2$ ,  $BC_2O$ ,  $BC_3$ , and  $B_4C$  (Wenjun Cheng et al., 2018; Sadhanala & Nanda, 2016; Sreekanth et al., 2015). The significance of B-C bonding in the mechanism of ORR has been highlighted in previous research conducted by Jo and Shanmugam. The researchers provided evidence that catalysts with larger concentrations of  $B_3C$ ,  $B_4C$ , and  $BC_3$  species exhibited greater activity in ORR (Jo & Shanmugam, 2012). This finding suggests that a greater B/C ratio may have a positive impact on improving the kinetics of ORR, a conclusion that was further supported by Cheng et al. (Y. Cheng et al., 2014).

Previous research has shown that the presence of positively charged boron leads to the chemisorption of oxygen molecules. Indeed, the transfer of electrons to  $O_2$  results in the destabilization of the O-O bond, so initiating the process of ORR. The electrons are derived from neighboring carbon atoms, with boron serving as a mediator (L. Yang et al.,

2011). The preference for associative ORR over dissociative ORR on B-doped carbon materials was revealed by Fazio et al. (Fazio et al., 2014). This implies that after the adsorption of O<sub>2</sub> in an end-on orientation, dioxygen species are generated, which undergo directly reduction to hydroperoxo species, bypassing the formation of energetically expensive side-on intermediates seen in the dissociative process (Fazio et al., 2014).

The investigation of F-doping remains rather limited. This suggests that the mechanism of ORR on doped materials and the precise function of fluorine in these materials remain uncertain. Thus far, fluorine has mostly been linked to the increase of electrical conductivity in the catalyst material (Ni et al., 2020). Due to its high electronegativity and an abundance of valence electrons compared to nitrogen and boron, the introduction of fluorine into carbon materials is expected to consistently result in semiconducting behavior at low levels of F-doping, whereas higher concentrations are likely to induce a conductive behavior (C. Tang et al., 2005; Xue et al., 2013). According to previous studies, it has been shown that fluorine has the ability to efficiently eliminate and substitute oxygen functional groups of graphene oxide (GO), while simultaneously introducing fluorine atoms into both the basal plane and edges of graphene. Hence, the incorporation of F-doping may also be regarded as a simultaneous approach for the reduction of graphene oxide (X. Cheng et al., 2017; D. Y. Kim et al., 2011; Sim et al., 2022; Sysoev et al., 2020) .

The investigation conducted by Chokradjaroen et al. (Chokradjaroen et al., 2020) focused on the synthesis of carbon nanomaterials doped with boron and fluorine using a single-step solution plasma technique. The researchers discovered that the catalyst treated with both boron and fluorine exhibited the most significant ORR activity in comparison to carbon materials that were either non-doped or only doped with boron. Nevertheless, the catalyst material that underwent dual-doping also facilitated ORR via a 2-electron pathway.

### **1.2.3 Oxygen reduction on metal-nitrogen-carbon (M-N-C) catalysts**

Metal-nitrogen-carbon (M-N-C) catalysts consist of a combination of a transition metal, nitrogen, and carbon. Doping carbon with transition metals and nitrogen is a more cost-effective method for creating active sites for ORR compared to using platinum (Barkholtz & Liu, 2017; He & Wu, 2022; Jaouen et al., 2009; Marshall-Roth et al., 2020; Shao et al., 2016; Yeager, 1984). For understanding the precise characteristics of the active site, it is vital to acquire comprehension regarding the manufacturing process of these components. The prevalent techniques used in the synthesis of M-N-C catalysts include (Ratso, 2020):

1. The doping process involves the pyrolysis of a synthesis mixture including a carbon carrier, a nitrogen dopant, either a polymer or a smaller molecule with a high concentration of nitrogen atoms, and a metal source, often an inexpensive salt, to introduce dopants into the carbon material. The nitrogen and metal sources may be effectively coupled, such as by the use of a macrocycle that includes the necessary metal. The precursors are frequently combined through either liquid-phase method such as sonication or stirring in a solvent, or solid-phase methods such as grinding, mixing, or milling. Subsequently, the resulting mixture is subjected to high-temperature pyrolysis, leading to the fusion of the precursors. This process alters the chemical properties of both the dopants and the substrate, resulting in the formation of active sites for ORR (Bashyam & Zelenay, 2006; Ferrandon et al., 2012; Lefèvre et al., 2009; Vikkisk et al., 2013; G. Wu et al., 2011).

One notable benefit of using this particular approach is in the use of a pre-existing carbon material, which serves to determine the characteristics of the resulting catalyst, including its structure, porosity, and level of graphitization.

2. The in-situ doping method, resembling method 1, involves the formation of a doped carbon network through pyrolysis using carbon, nitrogen, and metal sources. These sources can either be the same, such as Fe-doped ZIF-8, or different, such as a carbon-based polymer, a nitrogen-containing molecule, and an iron salt. The use of this approach often enables a greater concentration of nitrogen and metals in comparison to method 1. However, it presents challenges in terms of regulating the structure and porosity of the resultant catalyst. This issue is often mitigated by using a precursor (or precursors) that has a well-defined structure, such as metal-organic frameworks (MOFs) (Proietti et al., 2011; Ramaswamy & Mukerjee, 2011; Shui, Chen, et al., 2015; Strickland et al., 2015; H. Zhang et al., 2017; Zitolo et al., 2015), metal macrocycles (Kramm et al., 2016; José H. Zagal et al., 2006), macrocyclic aerogels (Zion et al., 2020), or polymers (Jiang et al., 2018; Xiaojuan Wang et al., 2016).

3. The hard-template method, also known as the sacrificial support method (SSM), employs a similar approach as described in method 1. However, it involves the use of a hard template, often composed of silica, to contain the precursors throughout the pyrolysis process. The use of a stable template throughout the pyrolysis process enables the determination of the ultimate configuration of the catalyst (Gokhale et al., 2017; Monteverde Videla et al., 2016; Serov et al., 2015). Hence, this approach amalgamates two advantageous aspects from methods 1 and 2. However, it is accompanied by the drawback of necessitating the removal of the template subsequent to pyrolysis. This process may also induce modifications in the resulting catalyst by etching certain metal components. It is worth noting that such modifications can potentially enhance the stability of the final catalyst (Serov et al., 2015).

In a number of cases, a combination of approaches is used, whereby the catalyst generated using the hard-template method is subsequently doped by the addition of more compounds containing nitrogen and subsequent pyrolysis of the mixture (Jiazhan Li et al., 2018), or through pyrolysis in the presence of ammonia (Strickland et al., 2015; Zitolo et al., 2015). The use of acid washing is a prevalent practice in all techniques aimed at eliminating inactive metal species that may cause fuel cell contamination during operation. However, it is worth noting that this method necessitates an additional heat treatment to deprotonate the N-groups on the surface. This deprotonation process is crucial as it prevents the binding of anions, which could potentially reduce the catalyst's activity (Herranz et al., 2011). Mostly, metal is coordinated with X (e.g. 4) nitrogen atoms, named M-N<sub>x</sub> (Zitolo et al., 2015). Determining the precise characteristics of the M-N<sub>x</sub> sites that exhibit the highest activity towards ORR poses significant challenges, mostly due to the multitude of active sites of this specific kind inside a catalyst. The presence of different kinds of active sites has been seen in all catalysts synthesized using the high-temperature pyrolysis process, which is known for its imprecise nature. The identification of active species in a catalyst is often accomplished by the use of XPS, Mössbauer spectroscopy, or XAS. Nevertheless, it should be noted that the signals obtained from M-N<sub>x</sub> sites, and in the case of XPS, other nitrogen moieties, tend to overlap. Consequently, a significant aspect of the identification process involves the deconvolution and fitting of peaks (Asset & Atanassov, 2020). In the case of graphene, a material known for its exceptional properties, atomic-level imaging has been successfully accomplished (Chung et al., 2017). However, when it comes to catalysts, most of them exhibit an amorphous structure

unlike graphene. Consequently, the precise determination of the number and type of atoms that are linked to the metal center remains speculative due to the limitations of existing imaging techniques.

Synthesizing a catalyst with a single type of active site is difficult, so determination of exact mechanism of reaction is hard. Figure 7 shows a comprehensive illustration of ORR occurring on a catalyst composed of M-N-C (in this case, Fe-N-C) in acidic environment (Asset & Atanassov, 2020).

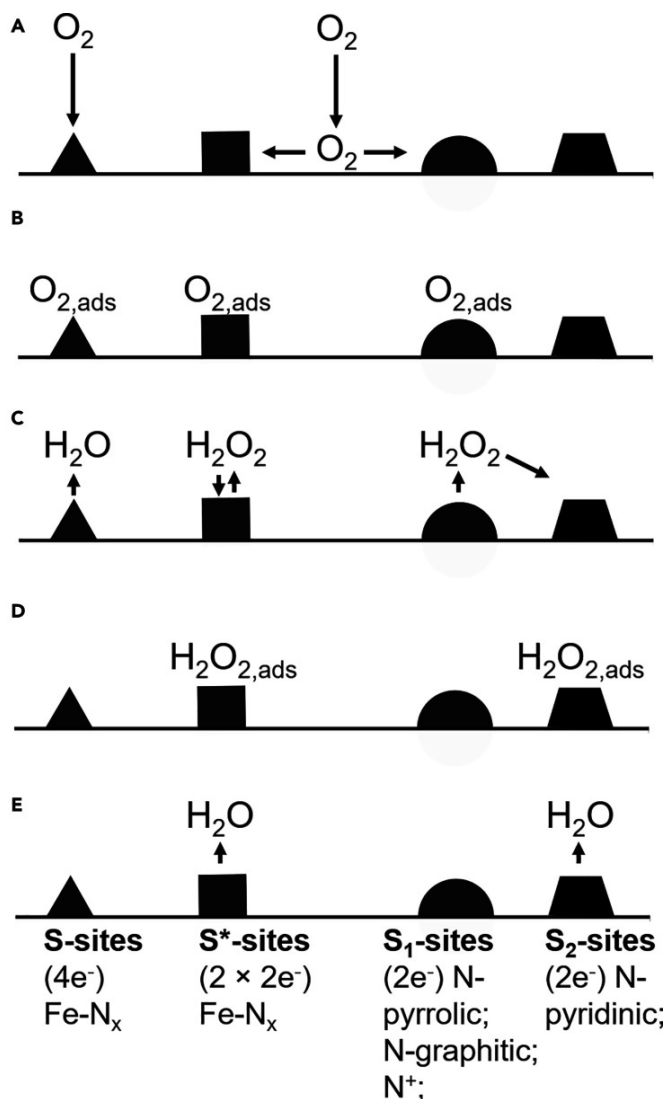


Figure 7. ORR on a M-N-C catalyst with different active sites: S, S\*, S1 and S2 (Asset & Atanassov, 2020).

As shown in Figure 7,  $Fe-N_x$  sites catalyse a direct 4-electron reduction of oxygen to water or the  $2 \times 2e^-$  reduction, where both of the steps take place on either the same active site or another  $S^*$  site. On nitrogen moieties without any coordinated iron, the ORR undertakes the  $2+2e^-$  reduction with the first steps of oxygen adsorption and

reduction to  $\text{H}_2\text{O}_2$  taking place on pyrrolic or graphitic nitrogen and the second step on pyridinic nitrogen, (Ramaswamy & Mukerjee, 2011, 2012). However, it must be noted that the surrounding carbon also has an influence on the active sites and can thus change the selectivity (Kruusenberg, 2013; Ratso, 2020).

The processes depicted in Figure 7 are:

- (A)  $\text{O}_2$  in solution or surface diffusion to the active sites.
- (B)  $\text{O}_2$  adsorption on the different active sites.
- (C)  $\text{O}_2$  reduction in  $\text{H}_2\text{O}$  (on S sites) or  $\text{H}_2\text{O}_2$  (on  $\text{S}^*$  or  $\text{S}_1$  sites) followed by diffusion in solution.
- (D) Re-adsorption on  $\text{S}^*$  or  $\text{S}_2$  sites.
- (E)  $\text{H}_2\text{O}_2$  reduction in  $\text{H}_2\text{O}$ , followed by diffusion in solution (Asset & Atanassov, 2020).

#### 1.2.4 Oxygen reduction on carbon-supported metal-phthalocyanines

Metal macrocyclic complexes such as metal phthalocyanines (Figure 8) and porphyrins are highly adaptable compounds that serve as catalysts for a diverse range of electrochemical reaction (Abarca et al., 2019; Lu & Kobayashi, 2016; Sorokin, 2013; José H. Zagal et al., 2010). Phthalocyanine (Pc) is composed of four isoindole subunits, which are connected through N atoms located at the meso-position. By altering the central ion, the structure of Pcs enables a wide range of functionalities. Ligands can be attached to the metal center at the axial positions, while substituents can be attached at the  $\alpha$ - or  $\beta$ -positions (peripheral or non-peripheral) (Shaoxuan Yang et al., 2021). The majority of elements from various groups in the periodic table have the ability to interact with the N atoms in the Pc macrocycle. consequently, there are over 70 different types of metal or metalloid macrocycle complexes. The physical characteristics of the Pc are significantly influenced by the central metal cation (Wenjing Cheng et al., 2022; Patowary et al., 2022; L. Sun et al., 2012). If the oxidation state of the central metal cation is +1, two nitrogen atoms bind to the ions. A common example of this is dilithium phthalocyanine ( $\text{Li}_2\text{Pc}$ ) (D. Yu et al., 2010; N. Zhou et al., 2018). Additionally, there are metal-oxide phthalocyanines, such as vanadyl Pc and titanyl Pc. As previously stated, subjecting MPc to heat treatment enhances their electrocatalytic activity and stability (Shaoxuan Yang et al., 2021). The precise mechanisms behind the catalytic activity of  $\text{MN}_4$  macrocycles in ORR remain unclear. Some scientists believe that the split of the O-O bond occurs as a result of the creation of a peroxo dimer on the two active metal sites (dual-site mechanism) (José H. Zagal et al., 2006). According to some authors, it has been suggested that the catalysis of ORR by  $\text{MN}_4$  macrocycles occurs via a dual-site mechanism. In this process, oxygen molecules align both to the metal active center and to a nitrogen atom on the macrocyclic ligand (Tanaka et al., 1987). There is an agreement in the literature that the nitrogen ligands present in  $\text{MN}_4$  macrocycle catalysts, in addition to the transition metal, significantly contribute to the stability and activity of these catalysts. However, the exact composition of the final active sites remains unknown, as shown by previous studies (Ding et al., 2012; Nabae et al., 2010). It is significant to emphasize that support material has the potential to function as an axial ligand, hence potentially leading to distinct features of the complexes in the adsorbed form (José H. Zagal et al., 2006). Various investigations in the area of oxygen reduction electrocatalysis have used catalysts such as carbon nanotubes, carbon nanofibers, graphene, Ketjen Black, and Vulcan carbon to include FePc and CuPc complexes (Mamuru & Ozoemena, 2010; Mocchil & Trasatti, 2003; Okunola et al., 2009; Pan et al., 2012; Yamazaki et al., 2005; José H. Zagal et al., 2009; S. Zhang et al., 2011). The enhancement of electrocatalytic capabilities of phthalocyanine

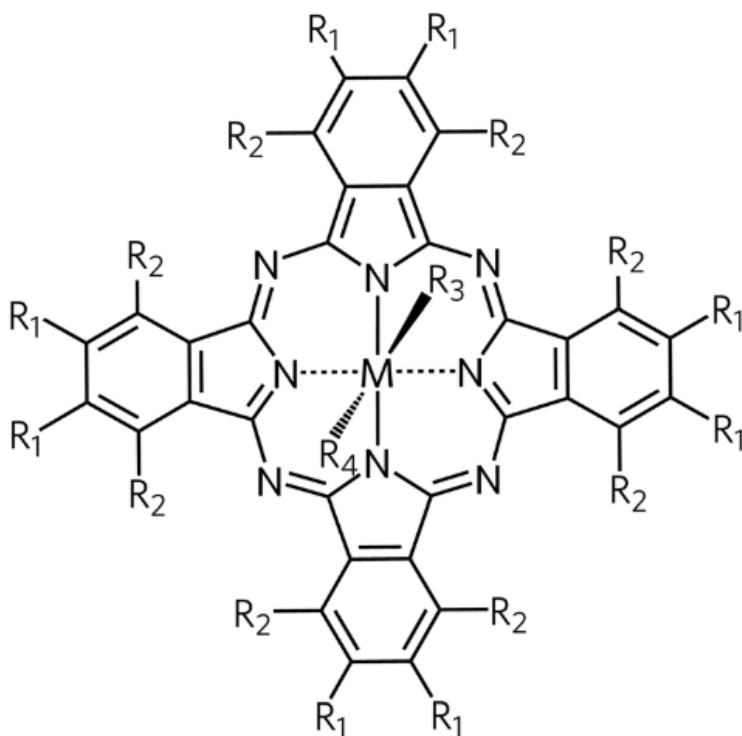
complexes by the functionalization of CNTs has been shown in previous studies (Dong et al., 2012; Z. Xu et al., 2011). Phthalocyanines exhibit a robust adsorption on CNTs via noncovalent  $\pi$ - $\pi$  interactions, resulting in the formation of “molecular phthalocyanine electrodes” (José H. Zagal et al., 2009).

In addition to these electronic and molecular-level interactions, the spatial distribution and surface accessibility of the  $MN_4$  catalytic sites on the support play a critical role in determining overall electrocatalytic activity. The quantity of  $MN_4$  catalysts present on the support material's surface is an additional factor that impacts the electrocatalytic activity of the catalyst material. Some research has shown a clear correlation between the thickness of the catalyst layer on the support material and oxygen reduction currents. According to the findings of Fierro et al., it has been shown that only 30% of the catalyst present on the porous support material exhibits activity for ORR (Fierro et al., 1990). Additionally, research has shown that just the outermost layer of the catalyst is accessible to oxygen molecules, making it the only active site for oxygen reduction. The presence of an excessively thick coating of the catalyst has been seen to have a detrimental effect on the electrical conductivity, resulting in a drop in the current associated with the reduction of oxygen (Pavez et al., 2005). Research has shown that subjecting catalyst materials to pyrolysis in an inert environment leads to an enhancement in both their catalytic activity and stability (Bouwkamp-Wijnoltz et al., 1998; Lalande et al., 1997). Since the seminal investigation conducted by Jahnke et al. (Jahnke et al., 1976), which documented the impact of heat-treatment, a number of studies have been undertaken to discover and enhance the parameters of pyrolysis, as well as to elucidate the precise configuration of the catalytic site responsible for the electrocatalytic activity pertaining to ORR (Li Zhu et al., 2010; Meng et al., 2010). The selection of the heat-treatment temperature is contingent upon the particular  $MN_4$ -macrocycle under consideration. The temperatures used for the pyrolysis of  $MN_4$ -macrocycles in an inert environment range from 500 to 1000 °C. However, research has shown that macrocycles generally exhibit optimal activity within the temperature range of 500 to 600 °C. At high temperatures, the catalytic activity of the material may exhibit a decline, while concurrently experiencing an increase in stability. There are three primary mechanisms involved in the pyrolysis process of the  $MN_4$ - macrocycles (José H. Zagal et al., 2006). According to Van Veen (van Veen et al., 1981; van Veen & Colijn, 1981), optimal catalytic activity may be attained within the temperature range of 500 to 600 °C, without causing full degradation of the macrocycles but ligand modification instead. Stability is attained by the binding of ligands to the carbon support, therefore mitigating oxidative attacks on the catalyst material. Yeager (Yeager, 1984) expressed disagreement with the findings obtained by van Veen and arrived at the conclusion that the degradation of the macrocycles began at a temperature as low as 400 °C. At a temperature of 800 °C, the macrocycles undergo decomposition, resulting in the loss of coordination between the metal and the nitrogen ligand atoms. Instead of that, metallic ions coordinate or adsorb onto the carbon surface and interact with nitrogen to generate the resulting composition as well. Yeager postulated that the resultant structure serves as the catalytic site for ORR. Regarding heat treatment parameters, the focus has mostly been on temperature, since it has a substantial impact on the structure of Pcs. Higher temperatures may lead to the degradation of the Pc and result in the aggregation of metals (Adeleye et al., 2021; Ladouceur et al., 1993). The optimal synthesis temperature is dependent upon both the Pc and the central metal. Although there are conflicting findings in the literature, it is evident that subjecting the material to temperatures over



700 °C resulted in the creation of a metal-N<sub>x</sub>-C structure (Shaoxuan Yang et al., 2021). In the context of non-pyrolysed transition metal phthalocyanines, the reactivity of metals exhibits a decrease in the following sequence: Fe > Co > Ni > Cu > Mn (Jose H. Zagal & Bedioui, 2016). However, it is important to note that the majority of catalysts used in contemporary applications undergo pyrolysis. Consequently, the characteristics of the active site significantly deviate from those of a pristine metal phthalocyanine (Tammeveski & Zagal, 2018; José H. Zagal & Koper, 2016), resulting in distinct variations in activity trends.

As per Wiesener's findings (Wiesener, 1986), the presence of metal ions inside the MN<sub>4</sub>-macrocycles facilitates the breakdown of the chelate at elevated temperatures, therefore leading to the generation of nitrogen-doped carbon. In this particular instance, the presence of metal residues resulting from the decomposition of MN<sub>4</sub>-macrocycles does not have any significant influence on ORR. Conversely, the introduction of nitrogen into carbon structures generates an active group that facilitates the process of oxygen reduction. In the latter scenario, it was seen that the transition metal in the precursor compound forms a nitrogen bond with a carbon matrix resembling graphite. This carbon matrix is generated by the process of pyrolysis. The remaining of the inner core structure of the MN<sub>4</sub> macrocycle during pyrolysis has been suggested, and it is believed to serve as a catalytic center for ORR (Fiechter et al., 2004). The precise identification of catalytic active sites remains unclear, leading to ongoing debates among scientists (D. Guo et al., 2016; Hu et al., 2022; Jia et al., 2019; L. Liu & Corma, 2021). One perspective suggests that MN<sub>4</sub>-centers are attributed to the catalytic active sites, whereas another perspective favors nitrogen heteroatoms as preferred catalytic sites (Herranz et al., 2007; Matter et al., 2007; Wiesener, 1986). Lalande et al. (Lalande et al., 1997) have shown the significance of nitrogen in the MN<sub>4</sub> catalyst material. Wiesener (Wiesener, 1986) proposes that Metal-N<sub>4</sub>, or metal-N<sub>2+2</sub>, might potentially serve as active sites. Several research groups have also proposed that the presence of quinone groups on the surface of carbon materials may contribute to the creation of active sites. Elbaz and colleagues provided empirical support on the development of stabilized MN<sub>4</sub> macrocycle-quinone complexes on carbon-based surfaces, with the aim of designing catalysts for ORR that do not rely on noble metals (Elbaz et al., 2010).



M = central metal or metalloid

R<sub>1</sub> = peripheral (or  $\beta$ ) position

R<sub>2</sub> = non-peripheral (or  $\alpha$ ) position

R<sub>3</sub>, R<sub>4</sub> = axial position

Figure 8. Structure of metal phthalocyanine. Adapted from Yang et al. (Shaoxuan Yang et al., 2021).

## 2 Experimental

### 2.1 Synthesis of catalyst materials

#### 2.1.1 Synthesis of Pb-N-doped carbon, and V-N-doped carbon

Lead (II) phthalocyanine (PbPc) (Sigma-Aldrich) or vanadyl phthalocyanine (VPc) (Sigma-Aldrich) was mixed with MWCNTs in different MPc-to-MWCNT (M: Pb, V) mass ratios (1:7, 1:3, 1:1, 3:1, 7:1) and suspended in 5 ml of ethanol followed by magnetic stirring and sonication for 2 h to achieve the adsorption of MPc on the surface of MWCNT's. The catalyst suspension was poured into a quartz boat followed by drying at 70 °C for 20 min and heat-treatment at 600, 800, and 1000 °C for 2 hours in a flowing nitrogen 99.999% (argon 99.999% for VPc) atmosphere. Also, dihydrogen phthalocyanine (HPc) (Sigma-Aldrich) was mixed with MWCNT (1:1) and pyrolysed at 800 °C for comparison with PbPc/MWCNT. The prepared catalysts are designated as MPc/MWCNT (X:Y), where X and Y represent the relative masses of metal phthalocyanine (MPc, either PbPc or VPc) and multi-walled carbon nanotubes (MWCNTs), respectively, used during the synthesis.

#### 2.1.2 Synthesis of boron, fluorine and nitrogen-doped graphene/FWCNT

Few-walled carbon nanotubes (FWCNT) were synthesized by fluidized-bed chemical vapor deposition purchased from Noda Lab (Japan) (Zhongming Chen et al., 2014; D. Y. Kim et al., 2011) and reduced graphene oxide (rGO) was synthesized from graphite powder (Graphite Trading Company) by a modified Hummers method (Hummers & Offeman, 1958), (L. Sun et al., 2012). Boron trifluoride diethyl etherate (BTDE) (Sigma Aldrich) was used as boron and fluorine source in the doping process. Firstly, the FWCNTs were oxidized at room temperature in a mixture of 1:1 H<sub>2</sub>SO<sub>4</sub> and HNO<sub>3</sub> solution in order to introduce oxygen-containing groups on the carbon nanotube surface, which in turn introduces reactive sites for further modification of FWCNTs.

B and F co-doped carbon nanomaterials were synthesized by a single-step pyrolysis method. FWCNTs and rGO with a ratio of 1:1 were mixed with a BTDE. Four different mass ratios were used (FWCNT and rGO/BTDE = 1:2.5, 1:5, 1:10 and 1:20) and the prepared catalysts are designated as 1BFC, 2BFC, 3BFC and 4BFC, respectively. All the mixtures were sonicated for 1 h and then dried in a vacuum oven. The materials were pyrolyzed in nitrogen atmosphere at 800 °C for 2 h and then cooled down to room temperature. For comparison purposes also pyrolysis at temperatures of 600 °C and 1000 °C was carried out.

In addition, Pt/C 20% commercial (Alfa-Aesar) was used as a benchmark. NaCl, Na<sub>2</sub>HPO<sub>4</sub>, KCl and KH<sub>2</sub>PO<sub>4</sub> (Sigma-Aldrich) were used to prepare 0.1 M phosphate buffer solution (PBS) pH 7.5 at room temperature (23 ± 1 °C). All the solutions were made using MilliQ-water.

### 2.2 Modification of GC electrodes

A glassy carbon (GC) disk (GC-20SS, Tokai Carbon) was used as the substrate material for the rotating disk electrode (RDE) tests, with a geometric surface area (A) of 0.2 cm<sup>2</sup>. GC disks were embedded in a Teflon holder, and the GC electrodes were meticulously polished with 1.0 and 0.3 µm alumina powder (Buehler) to a mirror-like finish. The GC disk electrodes were sonicated in isopropanol for 5 minutes and then in water for

5 minutes after the polishing process. The electrodes were modified with MPC/MWCNT (M: Pb, V) electrocatalysts utilizing aqueous suspensions ( $4 \text{ mg ml}^{-1}$ ) containing ionomer to prepare a uniform catalyst layer on the GC surface. Ionomer was 0.25% Nafion perfluorinated resin solution (Aldrich, USA) for acid and neutral media, and 0.15% FAA-3  $\text{OH}^-$  ionomer (FumaTech Germany) for alkaline media. The catalyst suspensions were sonicated for 1 h in the ultrasonication bath, keeping the temperature at  $<30^\circ\text{C}$ , and on a vortex mixer for two minutes. Then,  $5 \mu\text{l}$  aliquot of the well-dispersed ink was loaded onto the polished, clean GC electrode, completely covering the GC. It was repeated four times to reach  $20 \mu\text{l}$ . The ink droplet was dried in the ambient atmosphere. Thus, for electrochemical testing, the electrocatalyst loading was  $0.4 \text{ mg cm}^{-2}$ . Also, HPC/MWCNT and 20% Pt/C catalysts were tested in alkaline, neutral and acidic media for comparative purposes, with the same catalyst ink preparation procedure as used for the MPC/MWCNT. For the industrial 20 wt.% Pt/C used for the comparison purposes, catalyst with a loading of  $0.4 \text{ mg cm}^{-2}$  was applied, resulting in a Pt loading of  $80 \mu\text{g cm}^{-2}$ . The carbon material doped with BF was dispersed in isopropanol at a concentration of  $4 \text{ mg ml}^{-1}$ , with the addition of 0.25% Tokuyama ionomer AS-4 (Tokuyama Corporation, Japan) for the alkaline medium and 0.5% Nafion solution (Sigma-Aldrich) for the acid medium. A volume of  $20 \mu\text{L}$  of the catalyst suspension that had been made was applied onto the surface of the GC, followed by a drying process at a temperature of  $70^\circ\text{C}$  for a duration of 30 minutes.

## 2.3 Electrochemical measurements

To test the metal-phthalocyanine modified MWCNT catalyst materials, the RDE setup of an OrigaTrod rotator with speed control device (OrigaLys, France) was used for electrochemical measurements, with the electrode rotation rate ( $\omega$ ) varied between 400 and 4400 rpm. The potential was applied with a Gamry potentiostat/galvanostat 1010E (Gamry Instruments, USA) at a scan rate of  $10 \text{ mV s}^{-1}$  and step size  $10 \text{ mV}$ . A graphite rod served as the counter electrode, whereas a saturated calomel electrode Hg/HgCl (SCE), 4.2 M KCl reference electrode (SI-Analytix B 3410+, Germany) served as the reference electrode. Three electrolytes 0.5 M  $\text{H}_2\text{SO}_4$  (pH 0.3), 0.1 M phosphate buffer solution (pH 7.5) and 0.1 M KOH (pH 13) were used in the electrochemical experiments. The electrolyte solution was saturated with  $\text{O}_2$  (99.999%, AGA) for ORR current density and  $\text{N}_2$  (99.999%) for background measurements. During the electrochemical testing, a steady flow of these gases was maintained over the solution.

For BFC catalyst the counter electrode used in the experiment was composed of platinum foil, while a SCE was utilized as the reference electrode. To prevent the migration of Pt nanoparticles into the electrolyte solution, the Pt foil was positioned inside a separate quartz cuvette equipped with a filter. The validity of this counter electrode has been established and its performance has been compared to that of a graphite rod electrode. The experimental setup used a modified glassy carbon disk. The working electrode employed in the study had a geometric area of  $0.2 \text{ cm}^2$ .

All experiments were carried out at room temperature ( $23 \pm 1^\circ\text{C}$ ). For all RDE measurements the adhesion of the composite electrocatalysts to the GC disk was excellent and no loss of the catalyst occurred during the measurements as evidenced by an unchanged and stable cyclic voltammogram before and after the ORR testing.

The cyclic voltammetry (CV) was used for stabilization before the linear sweep voltammetry test. It was run between 0 V and 1 V vs RHE in different pH media. The scan rate was  $100 \text{ mV s}^{-1}$ . No rotation rate was applied. Linear sweep voltammetry (LSV) in

different rotation rates between 4400 to 400 rpm was employed to study the kinetics of electrode reactions. the voltage range was between 0 V to 1 V vs RHE. The scan rate was 10 mV s<sup>-1</sup>.

Methanol tolerance was used to evaluate catalyst tolerance against methanol poisoning at alkaline, buffer and acidic environment. Tests were carried out at specific potential and at 1900 rpm, 3 M MeOH was added at 300 s, then test continued for 900 s. In this study, chronoamperometry was run for all catalysts and Pt/C® in all environments. Also, the electrode rotated at 200 rpm during the test to avoid bubble accommodation under electrode. The chronoamperometry test was carried out for 20 h at 0.6 V.

The stability of the prepared catalysts was evaluated by carrying out 5000 potential cycles at a scan rate of 100 mV s<sup>-1</sup> while the rotation rate was set to 1000 rpm. After every 100 cycles the LSVs were recorded at 10 mV s<sup>-1</sup>.

Experiments were conducted to evaluate the durability of the highly active catalyst produced at a temperature of 800 °C. These experiments were carried out in alkaline, buffer and acidic environments, and the findings were compared to those obtained with a commercial 20% Pt/C catalyst. The duration of test was 72000 seconds across all mediums for PbPc, VPc catalysts and 60000 seconds for BFC.

Electrochemical impedance spectroscopy (EIS) was used for calculation of iR compensation for all experiments, the ohmic resistance was measured for each test. We used a special sequence in Gamry framework software to measure it.

In this thesis,  $E_{\text{onset}}$  is defined as the potential value when the current density reaches 0.1 mA cm<sup>-2</sup>.

The Koutecky-Levich (K-L) equation (9) was used to calculate the number of electrons transferred per O<sub>2</sub> molecule (n) [66]:

$$\frac{1}{j} = \frac{1}{j_k} + \frac{1}{j_d} = -\frac{1}{nFkc_{O_2}^b} - \frac{1}{0.62nFD_{O_2}^{\frac{2}{3}}\nu^{-\frac{1}{6}}c_{O_2}^b\omega^{\frac{1}{2}}} \quad (9)$$

where  $j$  is the measured current density,  $j_d$  and  $j_k$  are the diffusion-limited currents density and kinetic current density, respectively,  $k$  is the electrochemical rate constant for O<sub>2</sub> reduction,  $\omega$  is the rotation rate (rad s<sup>-1</sup>),  $F$  is the Faraday constant (96,485 C mol<sup>-1</sup>),  $D_{O_2}$  is the diffusion coefficient of oxygen (1.9×10<sup>-5</sup> cm<sup>2</sup> s<sup>-1</sup> for alkaline and neutral media and 1.8×10<sup>-5</sup> cm<sup>2</sup> s<sup>-1</sup> for acid media,  $C_{O_2}^b$  is the concentration of oxygen in the bulk (1.2 ×10<sup>-6</sup> mol cm<sup>-3</sup> for alkaline and neutral media and 1.132 × 10<sup>-6</sup> mol cm<sup>-3</sup> for acid media and  $\nu$  is the kinematic viscosity of the solution (0.01 cm<sup>2</sup> s<sup>-1</sup>) (Gottesfeld et al., 1987; K.K. Türk et al., 2018). If the intercepts of the extrapolated K-L lines were close to zero, this illustrates that the mechanism of oxygen reduction is almost completely controlled by diffusion(K.K. Türk et al., 2018), but the non-zero intercepts of the extrapolated K-L lines indicating that the process of ORR is controlled by the mixed kinetic-diffusion.

To make the research data obtained more easily comparable with the literature and with different materials that are presented in this work, the electrode potentials that were recorded vs. SCE were calculated to the reversible hydrogen electrode (RHE) scale by employing Nernst equation (10):

$$E_{RHE} = E_{SCE} + 0.059pH + E_{SCE}^0 \quad (10)$$

where  $E_{SCE}$  is the potential value recorded vs. SCE, and  $E_{SCE}^0 = 0.242$  V at 25 °C. All the potential values are stated against RHE, unless noted otherwise. All the potentials in this

paper are expressed in terms of the reversible hydrogen electrode (RHE) except of stability curves.

Through RRDE test, the concentration of  $H_2O_2$  is measured to calculate the number of electron transfer ( $n$ ), which indicates the average number of electrons transferred per oxygen molecule during reduction, and which pathway dominates under specific experimental conditions. The percentage yield of peroxide formation at the disk electrode was determined using Eq. (11).

$$\%H_2O_2 = 2 \frac{\frac{I_r}{N}}{I_d + \frac{I_r}{N}} \times 100\% \quad (11)$$

Here,  $I_d$  represents the disk current,  $I_r$  denotes the ring current, and  $N$  is the collection efficiency of the Pt ring electrode (with  $N = 0.25$ , as determined by the hexacyanoferrate (III) reduction reaction). The value of  $n$  was calculated from the RRDE results using Eq. (12).

$$n = 4 \frac{I_d}{I_d + \frac{I_r}{N}} \quad (12)$$

## 2.4 Physical characterization instruments

Scanning electron microscopy (SEM) LYRA3, Tescan, Schottky field emission gun (FEG), 1.2 nm at 30 kV, was used to study the surface morphology of the MPC/MWCNT (M: Pb, V) catalysts and high-resolution scanning electron microscope (HR-SEM) NanoLab 600 (FEI), 1.1 nm at 30 kV, was deployed for BFC catalyst.

Transmission electron microscopy (TEM) images of the catalysts were obtained by using Helios 5UX (ThermoFisher, USA) for MPC/MWCNT (M: Pb, V) dual beam system 0.6 nm @ 30 kV, and TEM JEOL 2200 FS (Japan) Schottky-type Field Emission Gun (FEG), 0.19 nm (200 kV) for BFC instrumentation.

X-ray diffraction (XRD) analysis was used to characterize the crystalline structure and phase composition of catalysts. The measurements were performed using a PANalytical apparatus, operating with Cu K $\alpha$  radiation ( $\lambda = 0.154$  nm), 45 kV beam voltage and 40 mA beam current. Patterns were obtained in the range from 10° to 90° with 0.02° increments and the exposure time of 100 s, for the analysis High Score Plus software was used.

NovaTouch 4LX Analyzer (Quantachrome) was used to evaluate porosity of the catalyst materials and for that record the  $N_2$  adsorption/desorption isotherms of the catalyst samples at nitrogen's boiling temperature (77 K). Before the measurement, the samples were degassed for 20 hours under vacuum at 200 °C and then backfilled with  $N_2$ . Up to a nitrogen relative pressure of  $P/P_0 = 0.2$ , the specific surface area ( $SSA$ ) was determined using either the Brunauer-Emmett-Teller (BET) theory (as  $S_{BET}$ ) or the density functional theory (DFT). Near saturation pressure of  $N_2$  ( $P/P_0 = 0.98$ ), the total volume of pores ( $V_{tot}$ ) was measured. Using the t-plot technique and deBoer statistical thickness, the microporosity ( $V$ ) was determined.  $dp = 2V_{tot}/S_{BET}$  was used to calculate the average diameter of pores ( $dp$ ) for a slit-type pore shape.

The surface composition was studied with employing X-ray photoelectron spectroscopy (XPS). The XPS sample was prepared dissolving the MPC/MWCNT catalyst in ethanol (4 mg  $ml^{-1}$ ) and applying it to a glassy carbon substrate (1.1 × 1.1 cm), after which the solvent was allowed to evaporated in the air. A Scienta Gammadata SES-100 hemispherical energy analyser (operated at 200 eV pass energy, with a ~0.9 eV overall spectral resolution) combined with a non-monochromated Mg K $\alpha$  X-ray source (h $\nu$  1253.6 eV, operated at 300 W source power) were used for the XPS measurements.

To estimate the at.% composition, the spectrometer transmission was checked against multiple spectral line intensities of sputter cleaned Au, Ag and Cu metals, and the photoionization cross sections. Most of the XPS data analysis was performed using the CasaXPS software, apart from the C 1s spectral fit, where the proper sp<sup>2</sup> carbon Doniach-Sunjic asymmetric peak was fitted using the SPANCF macro package for IgorPro software.

The XPS Axis Ultra DLD (Kratos Analytical) was used to analyze the surface chemistry of the pyrolysed VPC/MWCNT samples. Monochromatic Al K $\alpha$  X-ray source was used with source power of 105 W for survey scan and 225 W for characteristic energies to excite the photoelectrons. Pass energy of 160 eV was used for survey scan and pass energy of 20 eV for narrow core-level regions scans. The binding energy scale was corrected using C1 peak (284.6 eV) as a reference.

Raman spectroscopy is used to analyze the structural properties, defects, and carbon bonding in catalysts. The Raman spectra were recorded using a Renishaw via Raman spectrometer using a green laser (max 20 mW) beam; objective x100, 514 nm, 100% laser power, 1 accumulation (extended), 150–4000 cm<sup>-1</sup>, exposure time 10s. The substrates were cleaned Si wafer plates. The I<sub>D</sub>/I<sub>G</sub> ratios were extracted by fitting the spectra with two Lorentzian peaks.

### 3 Results and discussion

#### 3.1 Oxygen electroreduction on Pb and N-doped carbon nanotubes

##### 3.1.1. Physical characterisation of Pb and N-doped catalyst material.

This part is written based on the first journal paper (I) (Zarmehri, Raudsepp, Šmits, et al., 2023). The morphology and microstructure of sample PbPc/MWCNT (3:1) were assessed using scanning electrode microscopy (SEM) and transmission electron microscopy (TEM). SEM pictures shown in Figure 9a-c reveal that, while some agglomerates are present, the catalyst exhibits a generally uniform dispersion on the SEM substrate. This favorable distribution facilitates effective diffusion of both oxygen and solution throughout the deposited catalyst layer. The presence of Pb particles, which are characterized by their light appearance, and MWCNTs, identifiable by their gray coloration, is observable. During the process of pyrolysis, the carbon structure was effectively maintained in a favorable state as carbon nanotubes. The dispersion of Pb nanoparticles on the catalyst subjected to pyrolysis at 1000 °C exhibits superior characteristics compared to those seen on materials pyrolyzed at 800 °C and 600 °C. In Figure 9b, a higher degree of agglomeration of Pb particles inside certain regions of CNT clusters is evident in the material subjected to heat treatment at 800 °C. Conversely, Figure 9a displays fewer agglomerated particles in the sample that underwent annealing at 600 °C.

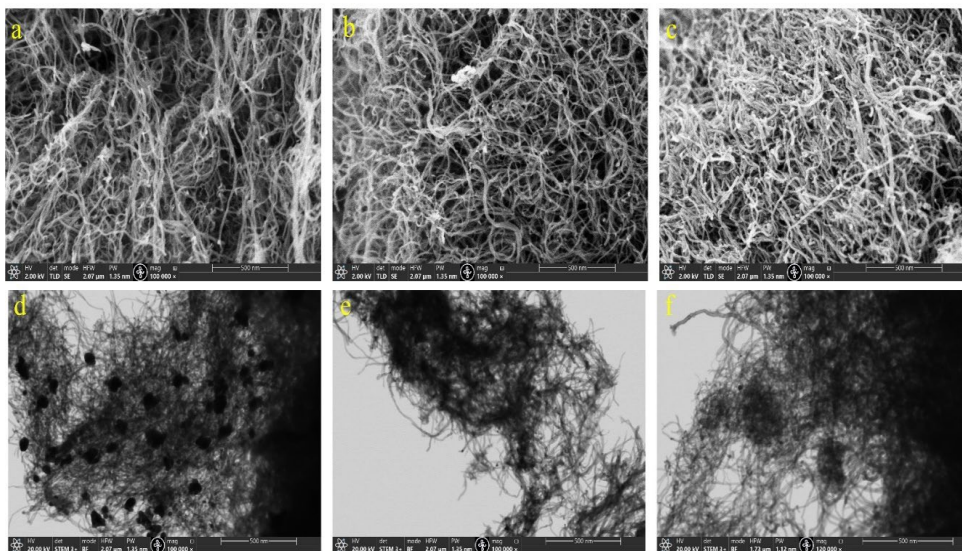


Figure 9. SEM images of PbPc/MWCNT (3:1) catalyst materials heat treated at 600 °C (a), 800 °C (b) and 1000 °C (c). TEM images of catalyst materials heat treated at 600 °C (d), 800 °C (e) and 1000 °C (f).

Figure 9d-f display TEM pictures of the PbPc/MWCNT (3:1) sample. The surface modification of the PbPc/MWCNT catalyst material was successfully carried out, as seen by the TEM picture, without the introduction of significant defects. It is crucial to guarantee that the carbon catalysts doped with Pb-N maintain their expected properties. Furthermore, TEM examinations shown in Figures 9d-f do not reveal the presence of larger amorphous carbon particles or any other contaminants. The presence of a



clustering effect can be seen in Figure 9; nevertheless, the formation of large-scale agglomeration of MWCNT has been successfully prevented. The catalyst that was synthesized at a temperature of 600 °C exhibits evidence of particle aggregation of Pb, as seen in Figure 9d. EDX pictures seen in Figure 10 demonstrate a uniform distribution of both nitrogen and Pb over the surface of the carbon nanotubes, also particles are clearly seen.

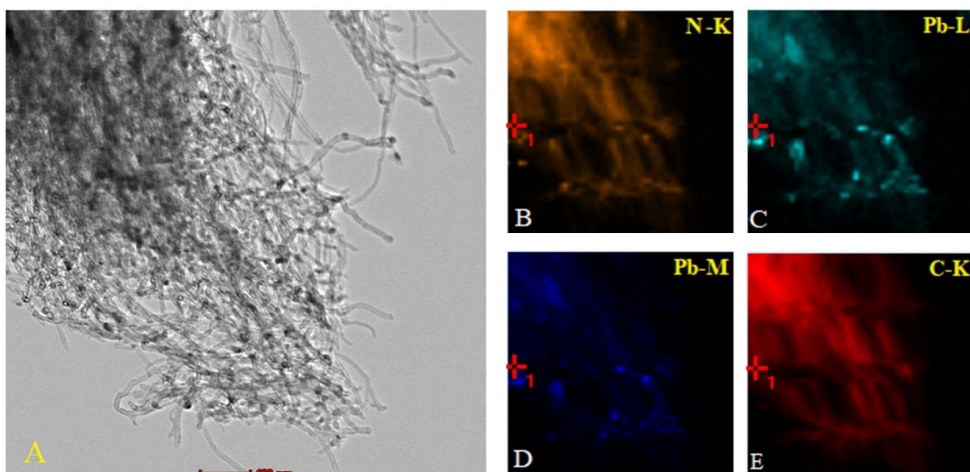


Figure 10. Distribution mapping via EDX of PbPc/MWCNT (3:1) 800 °C pyrolysed, TEM of the same cluster place (A), Nitrogen (B), Lead (C, D) and Carbon (D).

Raman spectroscopy is a commonly used technique for characterizing the structure and level of disorder in materials composed of carbon (Celiešiuė et al., 2014; Ferrari & Robertson, 2000; Trusovas et al., 2016). The Raman spectra of the PbPc/MWCNT (3:1) are shown in Figure 11. The D-band, which corresponds to disordered carbon structures, has a peak at around  $1350\text{ cm}^{-1}$ . On the other hand, the G-band, associated with graphitic carbon, appears as peaks within the range of  $1560\text{--}1600\text{ cm}^{-1}$ . These two bands are widely recognized as the most conspicuous features in the Raman spectrum of carbon materials. Significant attention has been devoted to the examination of surface imperfections, since they have a crucial significance in determining the performance of carbon catalysts. Tao et al. and Liu et al. demonstrated, by the use of DFT calculations and physical characterization techniques, that carbon atoms located near the edge defect exhibited a greater electron cloud density in comparison to regular carbon atoms (Behler et al., 2006; Contreras-Navarrete et al., 2015). The D-band is a feature that arises from double resonance and is generated by disorder. The G-peak at  $1580\text{ cm}^{-1}$  in graphite is attributed to the tangential vibrations of carbon atoms, but the peak at  $1345\text{ cm}^{-1}$  is indicative of the presence of disordered amorphous carbon. The 2D-peak seen at  $2680\text{ cm}^{-1}$  in the spectra is closely connected with graphene and exhibits sensitivity to the number of graphene layers. The analysis revealed that the  $I_D/I_G$  ratio of the PbPc/MWCNT (3:1) @ 800 °C sample was determined to be 1.26. This ratio suggests that the proportion of disordered carbon material is greater than that of ordered graphite inside the material. The  $I_D/I_G$  ratio was determined to be 1.14 for PbPc/MWCNT treated at 1000 °C and 1.23 for PbPc/MWCNT treated at 600 °C.

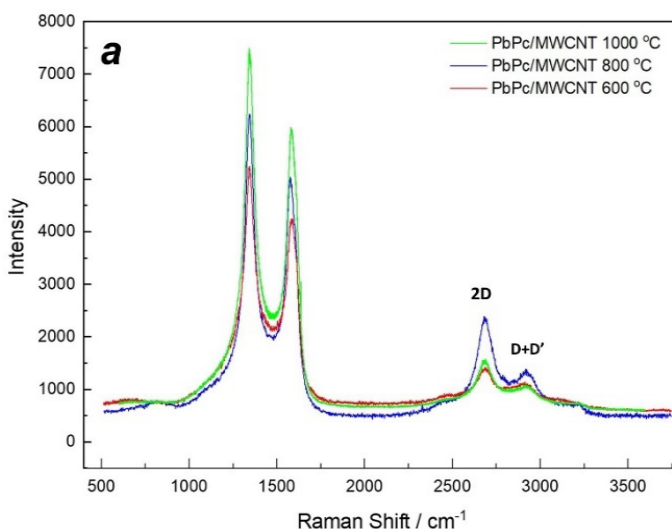


Figure 11. Raman spectra of PbPc/MWCNT (3:1) catalyst.

XRD investigation indicated the presence of metallic phases in the PbPc/MWCNT samples. The diffraction patterns exhibited multiple types of peaks, which may be ascribed to the presence of graphitic carbon and Pb (Figure 12). The distinctive reflections of Pb were seen at  $19.9^\circ$ ,  $24.7^\circ$ ,  $27.1^\circ$ ,  $40.4^\circ$ ,  $53.9^\circ$ ,  $62.5^\circ$ , and  $77.5^\circ$   $2\theta$ . The Miller indices were allocated to the peak positions of the lead phase (PDF card 98-005-4312 from the ICDD PDF-2 database) that showed the closest match. Distinctive reflections associated with graphitic carbon were seen at degrees of  $25.8^\circ$ ,  $29.6^\circ$ ,  $43.9^\circ$ ,  $44.3^\circ$ ,  $52.6^\circ$ , and  $53.9^\circ$   $2\theta$ . The Miller indices were allocated to the peak positions of the graphite phase (PDF card 98-018-5973 from the ICDD PDF-2 database) that exhibited the closest match.

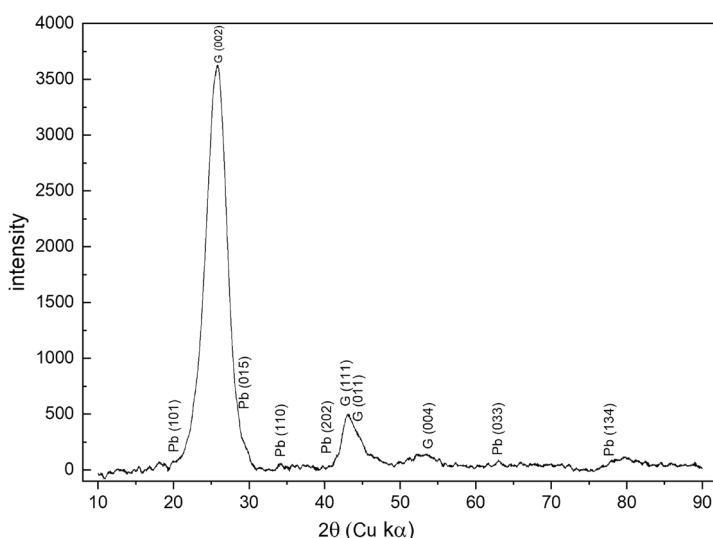


Figure 12. XRD (Cu  $K\alpha$ ) spectrum for PbPc/MWCNT (3:1) catalyst.

N<sub>2</sub> physisorption measurement is a technique used to determine the specific surface area of materials, particularly porous solids such as catalysts, adsorbents, and powders. Table 1 presents the calculated BET specific surface areas, pore volumes, micropore volumes, and average pore sizes. The catalyst with the greatest surface area, lowest average pore size, and biggest pore volume among all the catalysts is PbPc/MWCNT (3:1) synthesized at 1000 °C. In contrast, PbPc/MWCNT (3:1) synthesized at 600 °C has less surface area and pore volume compared to the other two catalysts. The alteration in catalyst layer structure and pore characteristics occurs as a consequence of subjecting materials to pyrolysis at varying temperatures. The catalyst's BET surface area is found to be twice as large when it is subjected to pyrolysis at 800 °C compared to when it is produced at 600 °C. Similarly, the catalyst's surface area is seen to be three times greater when it undergoes pyrolysis at 1000 °C in comparison to the catalyst created at 600 °C.

*Table 1. Volume and surface properties of catalysts in various pyrolysis temperatures.*

<b>Catalyst pyrolysis Temperature</b>	<b>Multipoint BET (m<sup>2</sup>/g)</b>	<b>DFT method cumulative surface area (m<sup>2</sup>/g)</b>	<b>DFT method cumulative pore volume (cm<sup>3</sup>/g)</b>	<b>Total Pore Volume (cm<sup>3</sup>/g)</b>	<b>DFT method pore radius (nm)</b>	<b>Average Pore Size (nm)</b>
600 °C	88.7	91.6	0.55	0.88	11.38	19.91
800 °C	169.7	146.4	0.81	1.18	11.38	13.94
1000 °C	246.1	206.5	1.08	1.52	11.38	12.34

The pore size was measured in the nitrogen adsorption test. The pore width for the catalyst PbPc/MWCNT (3:1) @ 600 °C is 15 nm to 33 nm. The cumulative pore volume (CPV) for pores with width less than 20 nm is about 0.05 cm<sup>3</sup> g<sup>-1</sup>, while it is 0.50 cm<sup>3</sup> g<sup>-1</sup> for pores with width greater than 20 nm (Figure 13). There are no pores smaller than 15 nm at this temperature. In contrast, pyrolysis at 800 °C and 1000° C results in the formation of smaller pores. PbPc/MWCNT (3:1) @ 800 °C has pores 4 nm to 10 nm wide, the CPV is about 0.03 cm<sup>3</sup> g<sup>-1</sup> for these small pores. The CPV for pores larger than 10 nm is 0.81 cm<sup>3</sup> g<sup>-1</sup> for this catalyst. The CPV for PbPc/MWCNT (3:1) @ 1000 °C is 0.047 cm<sup>3</sup> g<sup>-1</sup> for pores smaller than 10 nm and 1.08 cm<sup>3</sup> g<sup>-1</sup> for larger pores. It is concluded that the higher pyrolysis temperature not only leads to the formation of micropore less than 10 nm in width, but also creates more pore volume for pores larger than 10 nm in width.

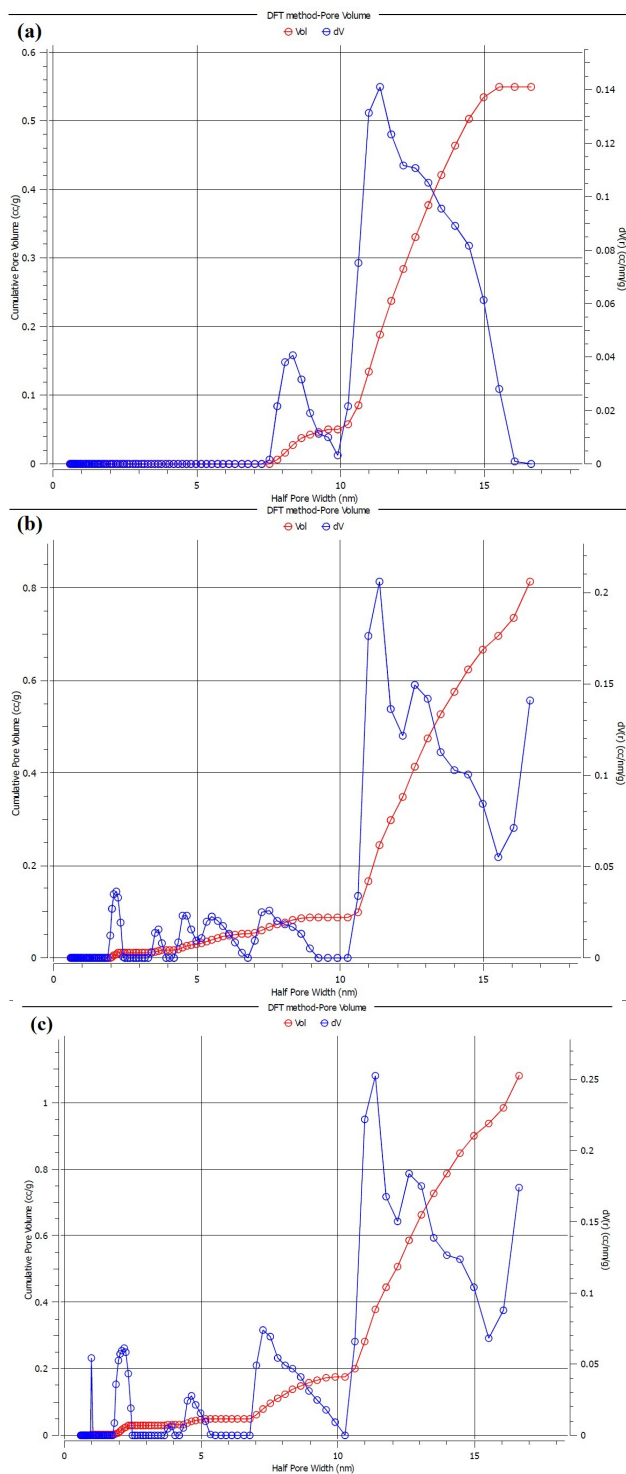


Figure 13. Pore width and pore volume distribution for catalysts (a) PbPc/MWCNT (3:1) @ 600 °C, (b) PbPc/MWCNT (3:1) @ 800 °C and (c) PbPc/MWCNT (3:1) @ 1000 °C based on DFT method.

XPS was used to analyze the surface composition of the catalyst material PbPc/MWCNT (3:1) after pyrolysis at a temperature of 800 °C. XPS survey spectra shown in Figure 14a indicate the detection of oxygen, nitrogen, carbon and lead components. The atomic percentage (at. %) of nitrogen elements and their corresponding relative concentrations (%) were determined using XPS peak intensities. These results are shown in Table 2 and visually depicted in the insets of Figure 14. The peaks seen in the high-resolution N1s spectrum shown in Figure 14b may be attributed to several nitrogen species, including oxidized N (403.8 eV), graphitic N (401.1 eV), pyrrolic N (400.4 eV), metal-N (399.5 eV), and pyridinic N (398.1 eV) (Artyushkova, 2020). In the graphene basal plane, the hexagonal ring structure is modified by the substitution of N atoms for C atoms, leading to links to three carbon atoms. This substitution process leads to the release of a single p-electron, which becomes part of the aromatic  $\pi$ -system. During the process of moderate pyrolysis, several nitrogen functionalities such as pyridones, protonated pyridinic N, and pyridinic N oxides undergo conversion to pyridinic N. Additionally, pyrrolic N is converted into pyridinic N while carbon structural development takes place (Xiao et al., 2005). The process of pyrolysis conducted at high temperatures leads to the formation of pyridinic N at the edges of graphene layers, or graphitic N inside the interiors of the graphene layers. The thermal stability of nitrogen functional groups may be arranged in the following order: C (graphitic N) > C (pyridinic N) > C (pyrrolic N) > C (oxidized N) (Xiao et al., 2005).

It is worth noting that the likelihood of metal-N<sub>x</sub> species being present is high, as shown by the component binding energy falling between the distinct peaks associated with pyridinic and pyrrolic N species. In the context of macrocycle-metal N-doped carbon materials, the nitrogen species known as graphitic N and pyridinic N are often acknowledged as the nitrogen species that exhibit activity in ORR (Ratso, Kruusenberg, Joost, et al., 2016; Dongliang Wang et al., 2023; G. Xing et al., 2023).

Previous studies have shown that elevated pyrolysis temperatures have a significant impact on the removal of oxygen surface groups from carbon (Aliev et al., 2012; Chandra et al., 2010). Despite the presence of residual oxygen in our catalyst products, the determination of the specific characteristics and distribution of these oxygen functions is challenging due to the closely matched binding energies of the several surface groups containing oxygen (Figure 14e). Despite the fact that a significant portion of oxygen groups on the surface of a carbon nanomaterial are eliminated at high pyrolysis temperatures, a clear O1s peak may still be seen (Aliev et al., 2012; Chandra et al., 2010). The peak seen at 529.8 eV in the O1s spectrum may be attributed to the binding energy associated with the interaction between oxygen and a lead atom (Gomez-Bolivar et al., 2019). The peak seen at 531.5 eV in the O1s spectrum is attributed to the presence of doubly bonded oxygen in the carbonyl group. On the other hand, the peak at 533.0 eV is indicative of a carbon-oxygen single bond and is also associated with the presence of adsorbed moisture and oxygen, as reported in previous studies (Bakry et al., 2020; Kundu et al., 2008; Mannan et al., 2019). The peak seen at the greatest binding energy (535.1 eV) in the O1s spectrum is ascribed to the presence of hydroxyl groups (Bakry et al., 2020; Mannan et al., 2019).

XPS spectra of the C1s orbital exhibits a mostly undisturbed sp<sup>2</sup> hybridized bonding configuration. This observation is consistent with previous studies, where the C1s peak centered at 284.7 ± 0.2 eV has been attributed to the presence of carbon-carbon (C = C) bonds (Ermolieff et al., 2001). The peak seen at 286 eV in the C1s spectrum is attributed to several carbon-oxygen functional groups, such as carboxyl and quinone groups. These groups have been identified on the surface of carbon nanotubes in many experimental studies (Langley et al., 2006; Masheter et al., 2007; Karl Kalev Türk et al., 2015).

Table 2. Elemental composition of PbPc/MWCNT (3:1) @ 800 °C catalysts determined by XPS.

Catalyst	C at.%	N at.%	O at.%	Pb at.%	
PbPc/MWCNT (3:1)	90.6	3.6	5.2	0.5	
Relative concentration (%) of N moieties in the catalysts	Pyridinic	Pyrrolic	Graphitic	N-metal	N-Oxide
PbPc/MWCNT (3:1)	30.9	30.2	12.3	15.5	10.9

The Pb 4f spectrum is fitted with a single spin-orbit doublet with appropriate 4:3 intensity ratio corresponding to the electron count in the 4f<sub>7/2</sub> and 4f<sub>5/2</sub> levels (Figure 14c), and the relatively narrow linewidth of 1.7 eV FWHM suggests the lead is included in the sample quite homogeneously (Pederson, 1982). The binding energy of the Pb 4f<sub>7/2</sub> peak at 138.9 eV is at least 2 eV too high for either PbO or PbO<sub>2</sub> (NIST, 2021). However, some of the previous studies have shown the presence of Pb-N bond at binding energy at 139 eV (Ai et al., 2020; NIST, 2021). XPS studies were also carried out with a catalyst material PbPc/MWCNT (3:1) synthesised at 600 °C and 1000 °C. Raising the pyrolysis temperature decreases the relative percentage of metal-nitrogen species. In addition, ICP-MS analysis was performed on catalysts synthesized at different temperatures, revealing that the level of impurities was negligible. Based on XPS result we conclude that the metal in metal-nitrogen species is Pb.

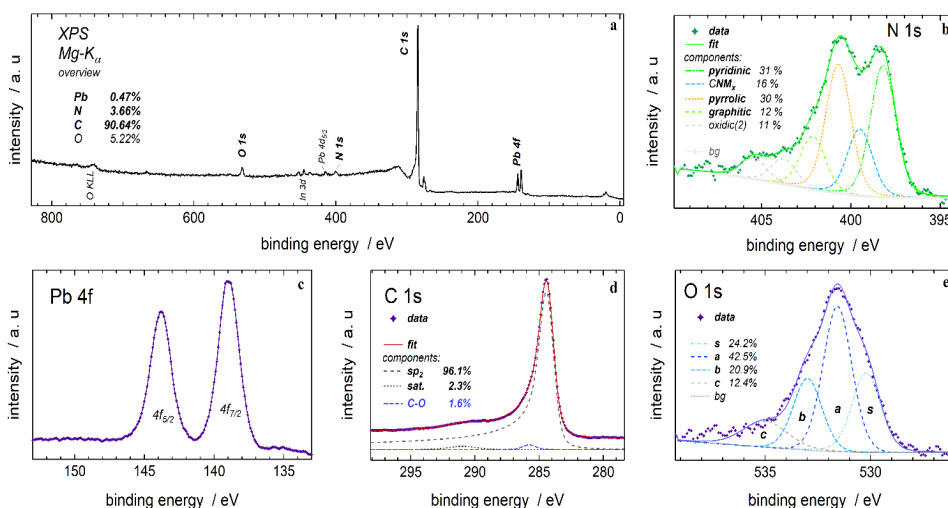


Figure 14. XPS spectra of PbPc/MWCNT (3:1) catalyst materials and high-resolution N1s (b), Pb4f (c), C1s (d) and O1s (e) spectra.

### 3.1.2 Electrochemical characterization Pb and N-doped catalyst material

The investigation focused on the electrochemical reduction of oxygen utilizing RDE technique, using the PbPc/MWCNT catalyst. Initially, the impact of varying ratios of three distinct PbPc to MWCNTs on the performance of ORR was investigated. The findings of LSV experiment conducted in O<sub>2</sub>-saturated solutions of 0.1 M KOH, 0.1 M phosphate buffer, and 0.5 M H<sub>2</sub>SO<sub>4</sub>, at a rotating speed of 1600 rpm, are shown in Figure 15. The observed significant reduction current in all the electrocatalysts may be ascribed to the co-doping of Pb and N in MWCNT, as well as the consequent development of electrocatalytically active sites. The data shown in Figure 15a-c demonstrates that the catalyst material prepared by using 75% PbPc to 25% MWCNTs ratio (PbPc/MWCNT (3:1)) exhibits the greatest diffusion limited current density values ( $j_d$ ) throughout alkaline, neutral, and acidic conditions. The catalyst exhibited the greatest onset potential in acidic conditions, whereas in neutral and alkaline conditions, the onset potential was found to be unaffected by the proportion of PbPc to MWCNT. The phenomenon described may be attributed to the process of metal atom agglomeration, as shown by the observation of larger particles via the use of TEM and SEM techniques, conducted during high-temperature pyrolysis. This implies that augmenting the metal (PbPc) concentration in the initial catalyst precursor mixture will not result in a correspondingly elevated level of active sites. The ORR performance of agglomerated metal- and nitrogen-doped carbon catalysts is shown to be inferior when compared to that of well distributed M-N-C material (H. Zhang et al., 2017; Zion et al., 2020).

The investigation also included an examination of the impact of varying pyrolysis temperatures on the electrocatalytic activity of the lead and nitrogen co-doped material. The PbPc/MWCNT (3:1) catalyst subjected to heat treatment at 800 °C, exhibited the most pronounced ORR activity. Additionally, pyrolysis processes were conducted at temperatures of 600 °C and 1000 °C, using the same ratio of lead phthalocyanine to carbon support. Figure 15d-f demonstrates that the catalyst material, synthesized by pyrolysis at a temperature of 800 °C, showcases superior electrocatalytic performance for the reduction of O<sub>2</sub> in alkaline, neutral, and acidic environments. Furthermore, investigations have also been conducted on non-pyrolyzed catalysts. As seen in Figure 15d-f, these catalysts exhibit the least activity in terms of ORR. This observation strongly suggests the need of heat-treatment. Other research groups have also reported similar findings. For instance, Gupta et al. conducted a study that showed the limited effect of MN<sub>4</sub> macrocycles on the activity of ORR in acidic environments, even without the use of annealing (Gupta et al., 1989). The data shown in Table 3 demonstrates that pyrolysis conducted at a temperature of 800 °C results in the most positive values for  $E_{onset}$ ,  $E_{1/2}$ , and  $J_d$ .

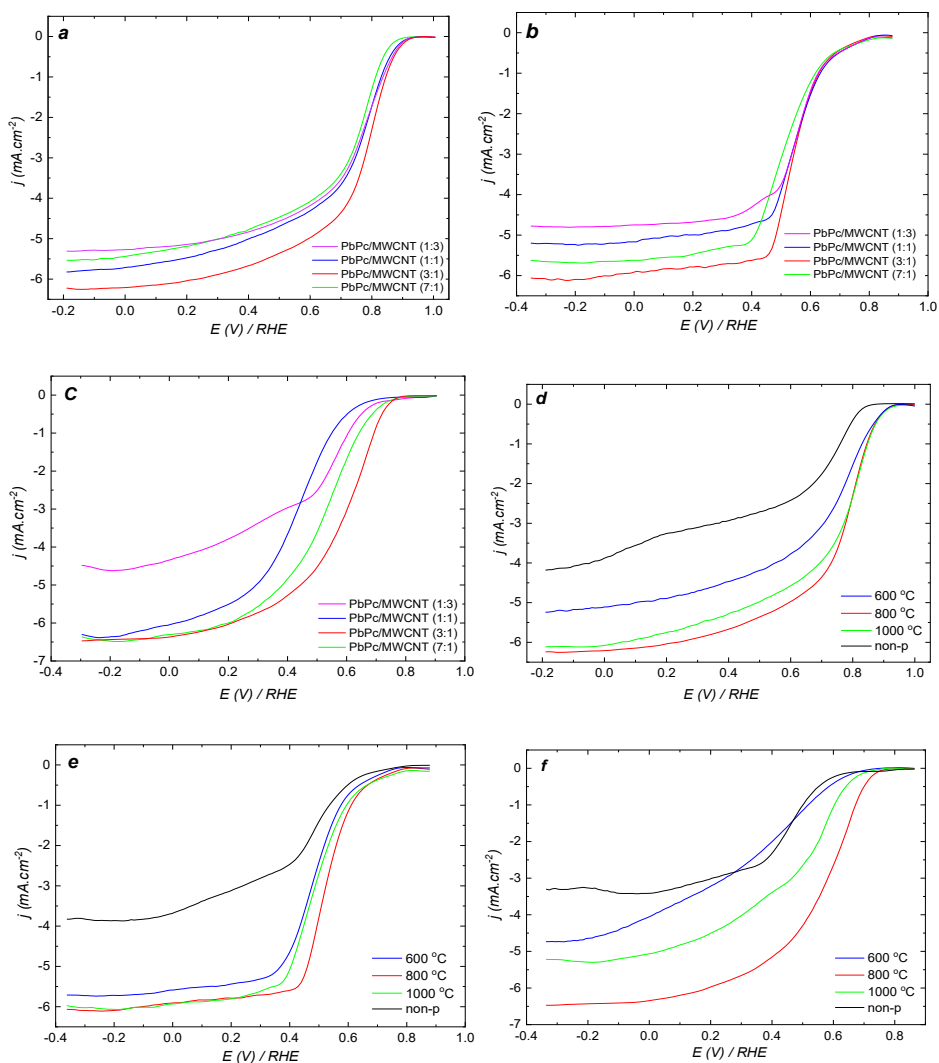


Figure 15. LSV curves for oxygen reduction on GC electrodes coated with (a, b, c) PbPc/MWCNT catalysts prepared using various ratios of precursors and heat treated at 800 °C, (d, e, f) PbPc/MWCNT (3:1) catalysts pyrolysed at various temperatures and not pyrolysed catalyst;  $O_2$ -saturated (a, d) 0.1 M KOH, (b, e) 0.1 M phosphate buffer and (c, f) 0.5 M  $H_2SO_4$ ,  $\nu = 10 \text{ mV s}^{-1}$ ,  $\omega = 1600 \text{ rpm}$ .



Table 3. ORR results obtained for catalysts of PbPc/MWCNT (3:1) prepared at various pyrolysis temperatures, in various electrolytes (1600 rpm).

Electrolyte	Pyrolysis Temperature	$E_{\text{onset}}$ (V)	$E_{1/2}$ (V)	$j_d$ (mA cm <sup>-2</sup> )	$n$
<b>Alkaline</b> KOH 0.1 M	600 °C	0.93	0.75	-5.2	3.6
	800 °C	0.93	0.78	-6.2	3.9
	1000 °C	0.94	0.77	-6.1	3.7
<b>Neutral</b> Phosphate buffer 0.1 M	600 °C	0.76	0.50	-5.7	3.0
	800 °C	0.80	0.55	-6.0	3.1
	1000 °C	0.79	0.50	-5.9	3.0
<b>Acid</b> H <sub>2</sub> SO <sub>4</sub> 0.5 M	600 °C	0.70	0.36	-4.8	2.8
	800 °C	0.77	0.58	-6.4	3.0
	1000 °C	0.73	0.52	-5.3	2.8

Previous studies have provided evidence that increasing the pyrolysis temperature results in an increase of electrocatalytically active surface species; consequently, the material synthesized at 800 °C exhibits higher activity compared to that synthesized at 600 °C (Jo & Shanmugam, 2012; Y. Liu et al., 2019; Ott et al., 2022). The potential explanation for the lower concentration of active sites on the catalyst synthesized at a temperature of 600 °C might be attributed to the incomplete decomposition of the macrocyclic molecule at lower pyrolysis temperatures (Hiraike et al., 2015; Jingkun Li et al., 2020). The temperature as high as 1000 °C may break the Pb-N bonds and decompose the structure rich of active surface groups and defect sites (Jingkun Li et al., 2020; Y. Ma et al., 2020).

Figure 16 shows a series of polarization curves for ORR obtained under different electrolyte conditions (alkaline, neutral, and acidic) and at varying electrode rotation speeds ( $\omega$ ). The PbPc/MWCNT (3:1) catalyst modified glassy carbon electrodes exhibit the highest level of activity among the tested catalysts. The onset potentials for ORR in alkaline, neutral, and acidic fluids are around 0.93 V, 0.80 V, and 0.76 V vs RHE, respectively. In the case of PbPc/MWCNT (3:1) in a neutral environment, as seen in Figure 16b, it can be observed that with more negative potentials (about 0.0 V) and increased rotation speeds, a second reduction wave starts. The wave under consideration is associated with the 2e<sup>-</sup> pathway that leads to the formation of the H<sub>2</sub>O<sub>2</sub> intermediate. This intermediate has two possible fates: it may either diffuse away or be grabbed by another active site. In the latter case, the H<sub>2</sub>O<sub>2</sub> is subsequently reduced to H<sub>2</sub>O in a subsequent 2e<sup>-</sup> step. The observed behavior is often seen in carbon materials that have been co-doped with metal and heteroatoms, particularly in neutral environments. This finding is consistent with other studies (K.K. Türk et al., 2018; W. Wang et al., 2019). The occurrence of the two-step reduction current plateau has been seen in carbon materials as well (Kruusenberg et al., 2009). The Pb/N/C catalyst surfaces may support

multiple ORR pathways as a result of the presence of various active sites characterized by distinct structural patterns. However, the absence of a pre-wave is found at lower rotation rates. The observed electrocatalytic behavior may be attributed to the appearing of novel active sites arising from the co-doping of Pb and N. Ge et al. conducted a study whereby they observed that the introduction of nitrogen into the carbon structure leads to a rise in positive charge on the surrounding carbon atoms via charge delocalization. This, in turn, enhances the activity of p-electrons and facilitates the adsorption of O<sub>2</sub> molecules (Ge et al., 2015). As previously stated, among the four nitrogen moieties, pyridinic and graphitic N exhibit the most pronounced catalytic activity in relation to ORR. Based on XPS findings, it has been shown that the PbPc/MWCNT (3:1) catalyst comprises nitrogen at a concentration of 3.66 atomic percent. Further analysis reveals that 30.9% of the nitrogen content corresponds to pyridinic N, while 12.4% corresponds to graphitic N. A significant proportion, namely 30.3%, of the nitrogen species present exhibits pyrrolic characteristics. It is worth noting that pyrrolic nitrogen is comparatively less stable when compared to pyridinic and graphitic nitrogen. Moreover, during the process of ORR, pyrrolic nitrogen has a higher susceptibility to oxidation (Xing et al., 2014). Furthermore, it has been shown that a significant proportion of nitrogen (15.5%), forms a bond with the metal element Pb. This interaction is recognized as an active site for ORR (Gewirth et al., 2018). Pb atoms have the ability to function as axial ligands. When incorporated into carbon structures as Pb-N dopants, they exhibit catalytic activity in ORR via a dual-site mechanism. In this process, oxygen molecules coordinate with both the metal atom and the nitrogen atom inside the Pb-N active center (José H. Zagal et al., 2006). Given the absence of any existing literature on the topic of Pb and N co-doped carbon material for the purpose of ORR, we might propose the potential impact of Pb on improving ORR performance, drawing on the findings of a study conducted by Luo et al. (Luo et al., 2020). The researchers conducted a study on carbon nanomaterials co-doped with Sn and N to investigate their potential as electrocatalysts for ORR. Through DFT calculations, it was shown that the presence of Sn centers greatly enhances the adsorption of O<sub>2</sub>, to the extent that it may even induce spontaneous splitting of the molecule. According to the RDE results we can conclude that the modification of carbon support with Pb and N atoms can lead to the improvement of electrocatalytic ORR activity in terms of onset potential, half-potential and limiting current values.

Based on Koutecky-Levich equation and LSV curves in various rotation speed, the number of electron transfer was calculated at different potentials for PbPc/MWCNT (3:1) catalyst in different electrolytes, and plotted in Figure 16d-f. The direct 4-electron pathway is often preferred for fuel cells, leading to the mainly usage of platinum group metals due to their well-known ability to catalyze the 4-electron pathway (Erikson et al., 2019). The N and Pb co-doped catalysts exhibited a *n* value approximating 4 for the whole of the potential range investigated in alkaline conditions. This observation suggests that the PbPc/MWCNT catalysts exhibit a high performance and possess significant promise as cathode catalysts in the context of AEMFC. In both neutral and acidic environments, the observed value of *n* was about three, indicating the presence of a mixed ORR pathway including both 2e<sup>-</sup> + 2e<sup>-</sup> and 4e<sup>-</sup> processes. This observation aligns with prior research findings, which indicate that the ORR on phthalocyanine modified MWCNT mostly proceeds by a combination of 2e<sup>-</sup> and 4e<sup>-</sup> pathways. Specifically, at lower overpotentials, the formation of HO<sub>2</sub><sup>-</sup> occurs, which is then reduced at more negative potentials (Kruusenberg et al., 2009, 2016; Praats et al., 2021; Ratso, Kruusenberg, Sarapuu, et al., 2016).

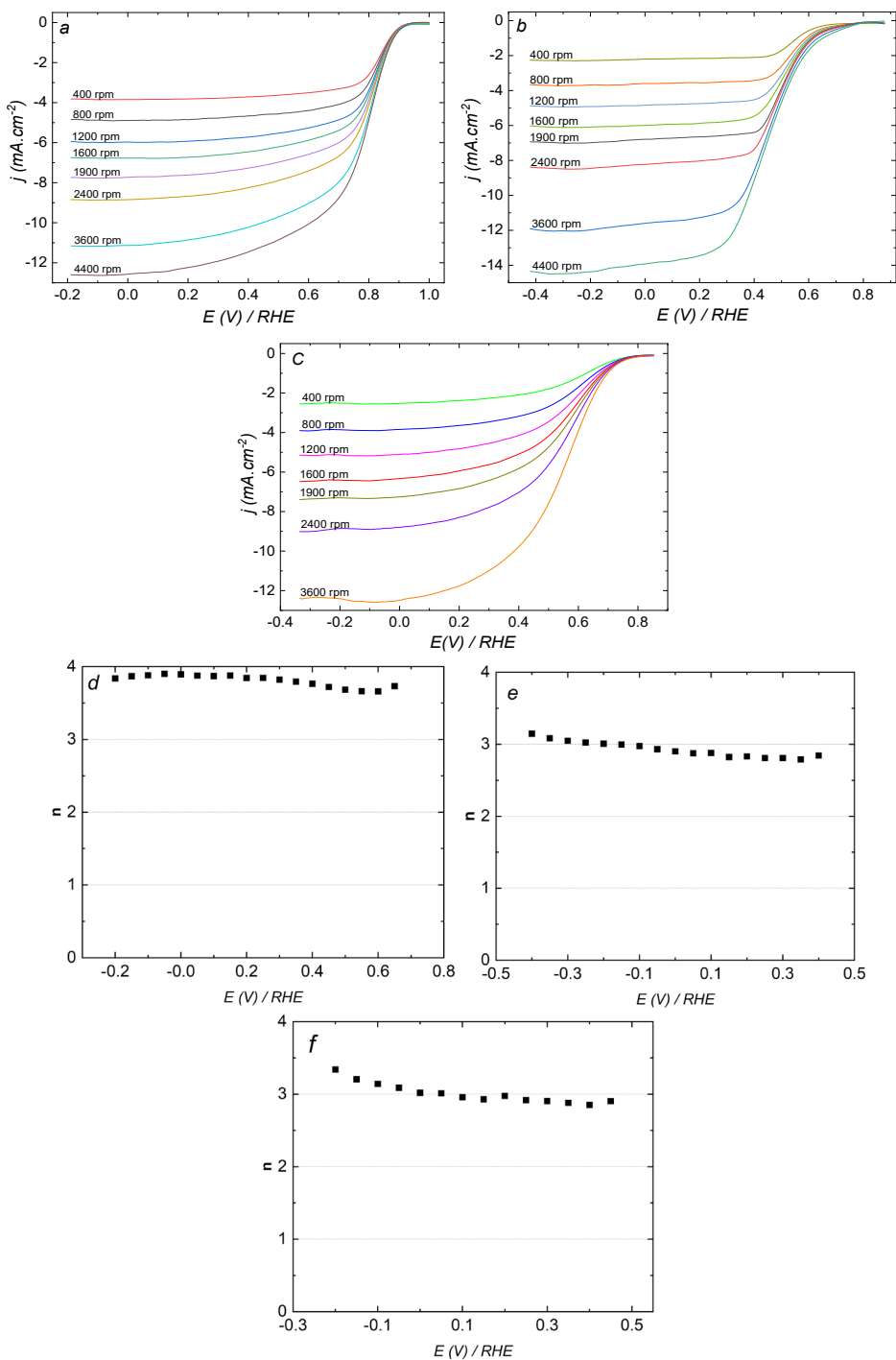


Figure 16. (a, b, c) LSV curves in various rotation speed for oxygen reduction on PbPc/MWCNT (3:1) catalyst in O<sub>2</sub>-saturated (a) 0.1 M KOH, (b) 0.1 M phosphate buffer and (c) 0.5 M H<sub>2</sub>SO<sub>4</sub>,  $\nu = 10 \text{ mV s}^{-1}$ ,  $\omega = 400\text{--}4400 \text{ rpm}$ ; (d, e, f) number of electron transfer based on Koutecky-Levich equation for ORR on PbPc/MWCNT (3:1) at various potentials per O<sub>2</sub> molecule in (d) 0.1 M KOH, (e) 0.1 M phosphate buffer and (f) 0.5 M H<sub>2</sub>SO<sub>4</sub>.

Regarding the fact that the mechanism of the ORR process and oxygen adsorption on N-doped carbon materials is still under investigation, it is thought that oxygen molecules are chemisorbed onto the carbon atoms in the N-doped carbon material primarily due to the various nitrogen functionalities and their electronic properties (Kiani et al., 2021). The carbon atoms with nitrogen dopants must have a very high positive charge density to counteract the strong electronic affinity of the nitrogen atom. At the Fermi level, the conjugation effect of nitrogen lone-pair electrons in nitrogen and carbon-system increases bulk electrical conductivity and density of states (W. Wang et al., 2019). The above-mentioned charge delocalization is also thought to modify the adsorption behaviour of carbon material towards  $O_2$  molecules, effectively weakening the O-O bond and facilitating oxygen electroreduction (Matter et al., 2006; B. Wu et al., 2022). The formation of metal bonds plays a critical role in catalyst activity, influencing whether the reaction follows a 2-electron or 4-electron pathway (H. Xu et al., 2024; X. Zhang et al., 2023). The nature and quantity of nitrogen on the catalyst content, and thus the formation of catalytically active centers, have been found to be influenced by the metal center chosen (Mazzucato et al., 2023; Oh & Kim, 2012). In addition to the metal based catalytic centers, M-N-C catalysts also contain  $N_x-C_y$  active sites.  $Pb-N_x$  sites are considered to reduce oxygen via a 4-electron pathway, while on  $N_x-C_y$  sites the ORR seems to proceed via the 2+2-electron pathway, with the underlying metal stabilising the intermediates (Strickland et al., 2015; Ye et al., 2024; Zitolo et al., 2015).  $Pb-N_x$  doping introduces an unpaired electron, which causes the localized distribution of the molecule orbitals and significantly improves the chemical reactivity of the MWCNT (L. Zhang & Xia, 2011). It is uncertain what kind of atoms and how many atoms are bound to the metal center and it is rather speculative with current imaging capabilities.

Figure 17a-c provide a comparative analysis of the polarization curves for ORR across different catalyst materials. The LSV curve of catalysts co-doped with N and Pb is being compared to that of a commercially available carbon-supported Pt catalyst with a platinum loading of 20 wt.%. The Pt/C catalyst has an onset potential that is about 0.1 V more positive in alkaline medium, 0.05 V more positive in neutral medium, and 0.15 V more positive in acidic medium, when compared to the PbPc/MWCNT (3:1) catalyst. The LSV curves of MWCNT and a material prepared by pyrolysis of HPC and MWCNT in a 3:1 ratio has been included for the purpose of comparison.

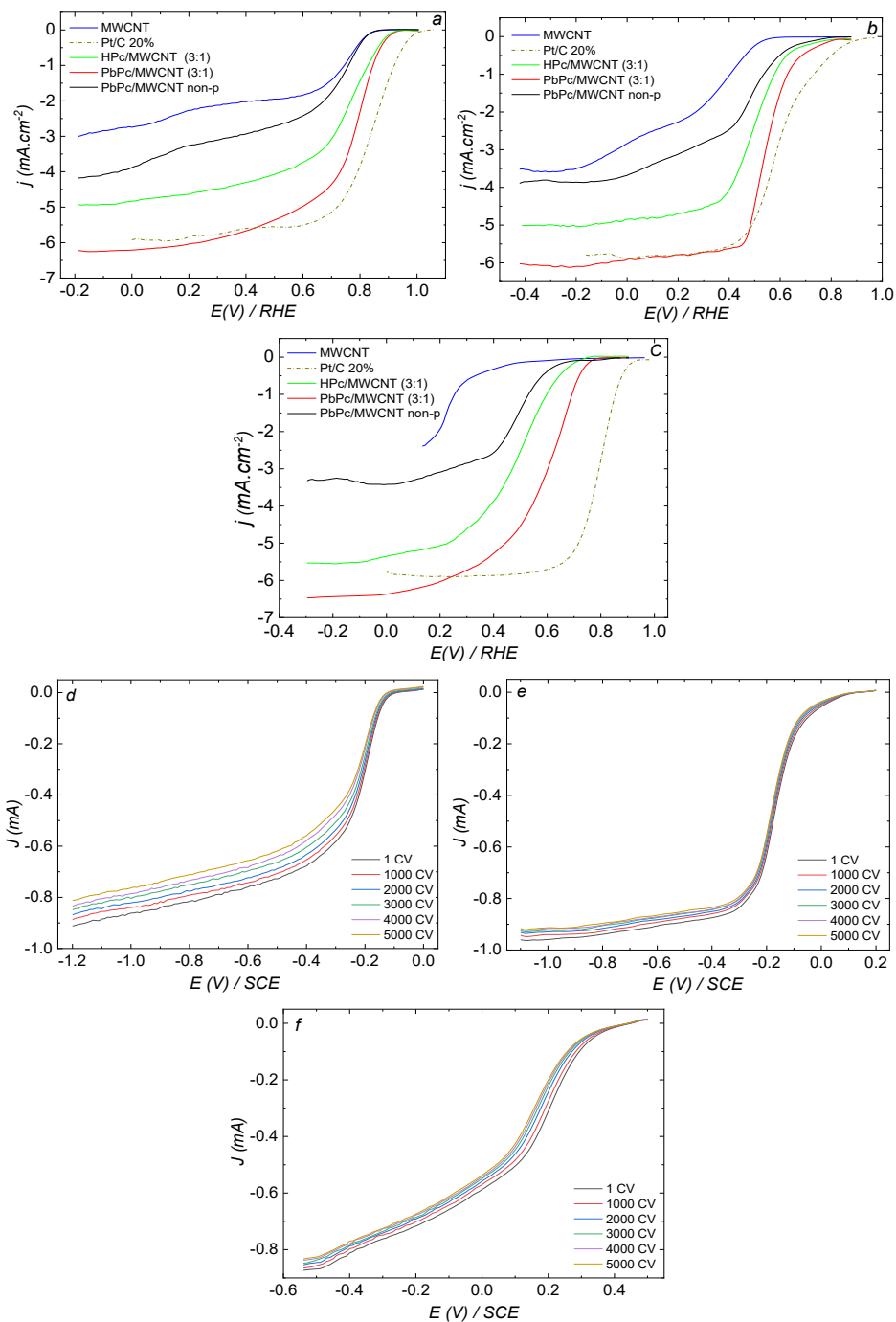


Figure 17. (a, b, c) Comparison of RDE results of oxygen reduction on MWCNT, not pyrolysed material, HPc/MWCNT (3:1), PbPc/MWCNT (3:1) and Pt/C modified GC electrodes in  $O_2$ -saturated (a) 0.1 M KOH, (b) 0.1 M phosphate buffer and (c) 0.5 M  $H_2SO_4$ .  $v = 10 \text{ mV s}^{-1}$ ,  $\omega = 1600 \text{ rpm}$ ; (d, e, f) Stability of PbPc/MWCNT (3:1) coated GC electrodes in  $O_2$ -saturated (d) 0.1 M KOH, (e) 0.1 M phosphate buffer and (f) 0.5 M  $H_2SO_4$ ,  $v = 10 \text{ mV s}^{-1}$ ,  $\omega = 1600 \text{ rpm}$ .

The  $E_{\text{onset}}$  and  $E_{1/2}$  values for the HPc/MWCNT material are comparatively more negative than those of the PbPc/MWCNT (3:1) material, suggesting that the presence of Pb atoms enhances the performance of the catalyst. Tables 4, 5 and 6 provide a comprehensive analysis of the RDE outcomes achieved for PbPc/MWCNT catalysts at varied PbPc to carbon ratios (pyrolyzed at 800 °C), as well as HPc/MWCNT and Pt/C catalysts in different media.

*Table 4. Comparison of the ORR results obtained for PbPc/MWCNT catalysts pyrolysed at 800 °C, non-pyrolysis material, HPc/MWCNT and Pt/C in 0.1 M KOH (1600 rpm).*

Catalyst	$E_{\text{onset}}$ (V)	$E_{1/2}$ (V)	$j_d$ (mA cm <sup>-2</sup> )	$n$
MWCNT	0.84	0.69	-3.0	2.5
Non-pyrolysis	0.84	0.73	-4.1	2.7
HPc/MWCNT 3:1	0.91	0.75	-4.9	3.0
PbPc/MWCNT 1:3	0.92	0.77	-5.3	3.7
PbPc/MWCNT 1:1	0.92	0.77	-5.8	3.7
PbPc/MWCNT 3:1	0.93	0.78	-6.2	3.9
PbPc/MWCNT 7:1	0.88	0.75	-5.5	3.6
Pt/C 20 %	0.98	0.84	-5.9	3.9

*Table 5. Comparison of the ORR results obtained for PbPc/MWCNT catalysts pyrolysed at 800 °C, non-pyrolysis material, HPc/MWCNT and Pt/C in 0.1 M phosphate buffer (1600 rpm).*

Catalyst	$E_{\text{onset}}$ (V)	$E_{1/2}$ (V)	$j_d$ (mA cm <sup>-2</sup> )	$n$
MWCNT	0.52	0.31	-3.5	3.0
Non-pyrolysis	0.62	0.47	-3.9	3.0
HPc/MWCNT 3:1	0.65	0.50	-5.0	2.9
PbPc/MWCNT 1:3	0.80	0.57	-4.7	3.0
PbPc/MWCNT 1:1	0.80	0.58	-5.1	3.0
PbPc/MWCNT 3:1	0.80	0.55	-6.0	3.1
PbPc/MWCNT 7:1	0.80	0.53	-5.5	3.0
Pt/C 20%	0.90	0.60	-5.9	3.7

Table 6. Comparison of the ORR results obtained for PbPc/MWCNT catalysts pyrolysed at 800 °C, non-pyrolysis material, HPc/MWCNT and Pt/C in 0.5 M H<sub>2</sub>SO<sub>4</sub> (1600 rpm).

Catalyst	$E_{\text{onset}}$ (V)	$E_{1/2}$ (V)	$j_d$ (mA cm <sup>-2</sup> )	$n$
MWCNT	0.40	0.24	-2.5	3.0
Non-pyrolysis	0.60	0.44	-3.4	3.0
HPc/MWCNT 3:1	0.71	0.48	-5.5	2.7
PbPc/MWCNT 1:3	0.64	0.49	-4.5	2.5
PbPc/MWCNT 1:1	0.60	0.41	-6.3	3.2
PbPc/MWCNT 3:1	0.77	0.58	-6.4	3.0
PbPc/MWCNT 7:1	0.69	0.48	-6.4	2.4
Pt/C 20%	0.93	0.80	-5.9	3.8

Part of the electrochemical activity may be attributed to the successful doping of nitrogen atoms during the pyrolysis process and decomposing of the phthalocyanine compound (Z. Xu et al., 2012; Shaoxuan Yang et al., 2021). The most active lead and nitrogen co-doped catalyst material was subjected to a stability assessment, whereby LSV curves were repeatedly cycled for a total of 5000 cycles. The outcomes of this experiment are shown in Figure 17d-f. The observed ORR stability was found to be satisfactory for the doped catalyst material which was prepared by mixing of PbPc and MWCNT at a ratio of 3:1 and heat treated at a temperature of 800 °C. Only minor variations in the  $E_{1/2}$  values and no change in the onset potential seen in both neutral and acidic environments. The stability in alkaline media was lower, as seen by the decline in  $E_{1/2}$  values and diffusion-limited current when  $E < -0.5$  V. The findings presented in this study effectively illustrate the exceptional stability of lead containing catalyst in sulfuric acid, indicating the potential of lead as a non-noble metal dopant for the fabrication and application of fuel cell electrocatalysts. Lead-based catalyst demonstrates good result for using in the cathode of fuel cell. This is an entry work into in-depth study of Pb-based catalyst in the moving from old battery to new battery generation. Recycled lead from lead-acid-battery can be used as the base materials for Pb-based catalysts.

## 3.2 Oxygen electroreduction on V and N-doped carbon nanotubes

### 3.2.1. Physical characterization of V and N co-doped catalyst material

This part is written based on the second journal paper (II) (Zarmehri, Raudsepp, Danilson, et al., 2023). SEM image (Figure 18a) reveals a uniform distribution of the catalyst material across the substrate surface, with no visible signs of significant agglomeration. Furthermore, SEM results provide empirical support for the preservation of the structural integrity of carbon nanotubes following the pyrolysis process. The placement of vanadium within the structure of carbon nanotubes is demonstrated through high-resolution transmission electron microscopy (HR-TEM) analysis, as depicted in Figure 18b-c. The bright regions observed in the dark-field HR-TEM image (Figure 18c) are attributed to the presence of a metallic element. In this particular case, vanadium is

identified as the sole metal, as confirmed by the absence of any other metals detected through XPS and XRD measurements, which will be discussed in subsequent sections of this manuscript.

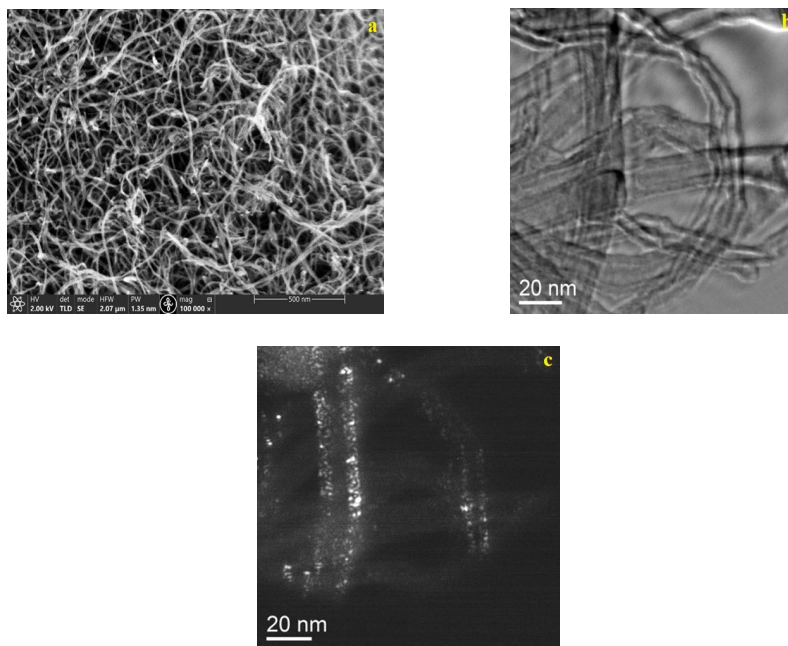


Figure 18. SEM (a) and HR-TEM (b, c) images of VPc/MWCNT (1:3) catalyst materials heat treated at 800 °C.

The Raman spectra of V and N co-doped MWCNTs are depicted in Figure 19. The Raman spectrum of carbon-based materials exhibits significant peaks at approximately  $1350\text{ cm}^{-1}$  (referred to as the D-band) and within the range of  $1560\text{--}1600\text{ cm}^{-1}$  (known as the G-band). The 2D-peak detected at a wavenumber of  $2680\text{ cm}^{-1}$  is indicative of a carbon structure resembling graphene. The intensity of this peak is directly associated with the average number of carbon layers present in MWCNT (Lehman et al., 2011). The catalytic performance of carbon materials has been linked to surface defects by numerous scientists. Liu et al. and Tao et al. conducted a study where they employed physical characterization techniques and DFT method to demonstrate that the electron cloud density of carbon atoms located at the edges of defects is higher compared to that of  $\text{sp}^2$ -hybridized carbon atoms (D. Liu et al., 2018; Tao et al., 2019). The ratio of  $I_D/I_G$  was determined to be 1.14 for the VPc/MWCNT (1:3) sample pyrolyzed at a temperature of 800 °C. This finding suggests that this particular catalyst has the highest amount of disordered carbon compared to the other catalysts. Four additional peaks were observed in the VPc/MWCNT sample at 600 °C, specifically at wavenumbers of  $1105\text{ cm}^{-1}$ ,  $1210\text{ cm}^{-1}$ ,  $1430\text{ cm}^{-1}$ , and  $1455\text{ cm}^{-1}$ . These peaks can be attributed to the H-C bend and isoindole stretch, which are known to be associated with VPc, as reported in reference (Jennings et al., 1996). The evidence presented indicates that the VPc structure remains partially intact and a portion of the VPc compound remains unaltered following the process of pyrolysis.



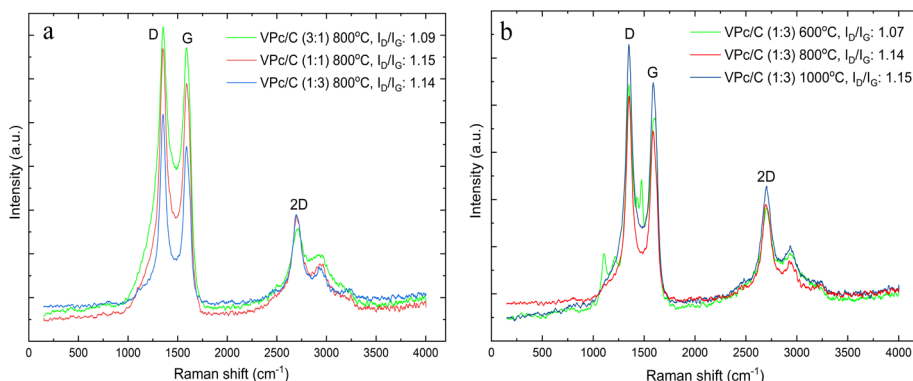


Figure 19. Raman spectra of VPC/MWCNT @ 800 °C catalyst with different VPC to CNT ratio (a) and VPC/MWCNT (1:3) synthesized using different pyrolysis temperature (b).

XRD analysis is shown in Figure 20. The observed peaks at angles of 26.5° and 44.5° can be related to the presence of graphitic carbon, (ICDD 96-901-1578). The presence of vanadium species, specifically  $V_2O_3$  and  $V_2O_5$ , was identified through XRD analysis. The reference pattern of  $V_2O_3$  shows distinct peaks at angles of 24.7°, 26.2°, 35.8°, 36.1°, 41.0°, 42.3°, 54.0°, and 62.7°, as documented in the JCPDS 41-1426 and ICDD 98-000-6286 databases (Y. Bai et al., 2013; Mjejri et al., 2018; Zaki et al., 2020; L. Zhao et al., 2014). The peak with the highest intensity in  $V_2O_3$  occurs at an angle of 26.2° and exhibits an overlap with a graphite carbon peak. The peak observed at an angle of 42.3° exhibits overlapping characteristics with peaks corresponding to graphitic carbon, carbon-nitrogen bonds, and metallic vanadium. The peak observed at an angle of 36.0° corresponds to two reference peaks of  $V_2O_3$  at angles of 35.8° and 36.1°. The diffraction peaks observed for  $V_2O_5$  are located at angles of 20.4°, 26.3°, 32.5°, 34.4°, 41.5°, 42.3°, and 51.5°, (ICDD 98-009-4904). In a similar manner to  $V_2O_3$ , it can be observed that the most prominent peaks of  $V_2O_5$  at 26.3° exhibit overlap with the peak corresponding to graphitic carbon. The identification of  $V_2O_3$  and  $V_2O_5$  species was also verified using XPS, which will be discussed in the subsequent section. Furthermore, based on the XRD and XPS analyses, the identified elements are carbon, nitrogen vanadium and oxygen. Notably, the absence of distinctive peaks at approximately 36° and 54° for carbon and nitrogen respectively provides additional evidence supporting the attribution of these peaks to a vanadium compound. XRD spectra shows three peaks for metallic vanadium at 42.6°, 61.8° and 78.0° (ICDD 96-151-2550) and (ICSD 426983) for materials with 50 and 75% of VPC in the catalyst mixture. Conversely, the catalyst with 25% of VPC displays two peaks at 42.6° and 78.0°. The  $C_3N_4$  compound exhibits three distinct peaks at angles of 27.4°, 44.0°, and 46.2°, as reported in the PDF 98-24-8326 and JCPDS 87-1526 references. However, the identification of these peaks is challenging due to the presence of intense graphitic peaks that overlap with them. Based on XRD findings, it is a challenging task to definitively ascertain or disprove the existence of vanadium and nitrogen within the sample. To confirm the existence of vanadium and nitrogen subsequent to the doping process, XPS analyses were conducted. These findings will be elaborated upon in the subsequent section.

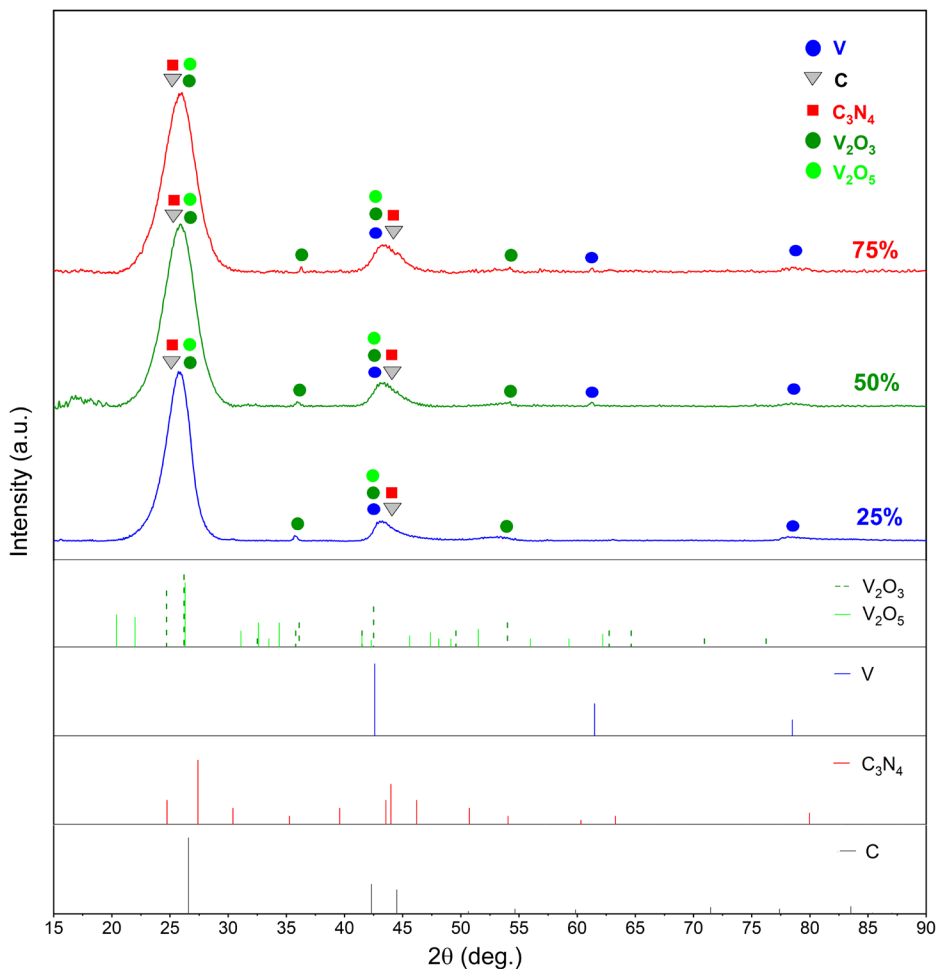


Figure 20. XRD spectra of VPC/MWCNT @ 800 °C for different VPC to MWCNT ratios with corresponding reference patterns.

Figure 21 displays XPS study of the VPC/MWCNT (1:3) sample, which was synthesized at a temperature of 800 °C. The survey spectrum exhibits four separate peaks, which can be attributed to the C1s, O1s, N1s, and V2p. These results indicate that nitrogen and vanadium doping occurred during the pyrolysis process of VPC with MWCNT. Based on the XPS spectrum presented in Figure 21, it is evident that the surface of the carbon nanomaterial shows distinct nitrogen species, totaling four in number. The detected peaks are subjected to deconvolution, resulting in the identification of pyrrolic-N (400.0 eV), N-oxide (401.9 eV), pyridinic-N (398.6 eV), and graphitic-N (401.1 eV). Table 8 presents the distribution of elemental components, together with the relative quantities of different nitrogen species. The presence of pyridinic-N and graphitic-N has been identified as significant active sites for ORR in carbon materials doped with MN<sub>4</sub> (Ratso, Kruusenberg, Joost, et al., 2016).

At a moderate pyrolysis temperature of 800 °C, it has been observed that N functional groups, specifically pyridinic-N oxides, pyridones, and protonated pyridinic-N, undergo

conversion to pyridinic-N (Xiao et al., 2005). At high temperatures, the formation of graphitic-N and pyridinic-N occurs within the internal layers and at the edges of graphene, respectively.

The determination of the specific kind of oxygen groups present on the surface is difficult due to the very similar binding energies seen across various groups. According to the existing literature, the O1s peaks are seen at 530.3 and 531.7 eV, which are associated with V-O and C = O, respectively (Bondarenka et al., 2003; L. Li et al., 2019; H. Wu et al., 2020). The observed peaks at 533.3 eV (O1s) and 286.0 eV (C1s) may be attributed to distinct C-O functional groups present on the surface of MWCNT. These functional groups, namely quinine and carboxyl groups, have been previously identified in several investigations focused on the characterization of carbon nanotube surfaces (Tian et al., 2019; Karl Kalev Türk et al., 2015; Vijayakumar et al., 2018). The V2p peaks seen at 517.2 and 524.4 eV are indicative of the presence of the V<sup>5+</sup> component inside the V-O bond (J. Liu et al., 2022; Simas et al., 2017). The absence of visible peaks corresponding to V-C and V-N bonding suggests that the existence of V is exclusively in its oxidized state. Liang et al. (Liang et al., 2011) have proposed that the bonding between transition metal oxides and carbon networks may occur via oxygen ligands.

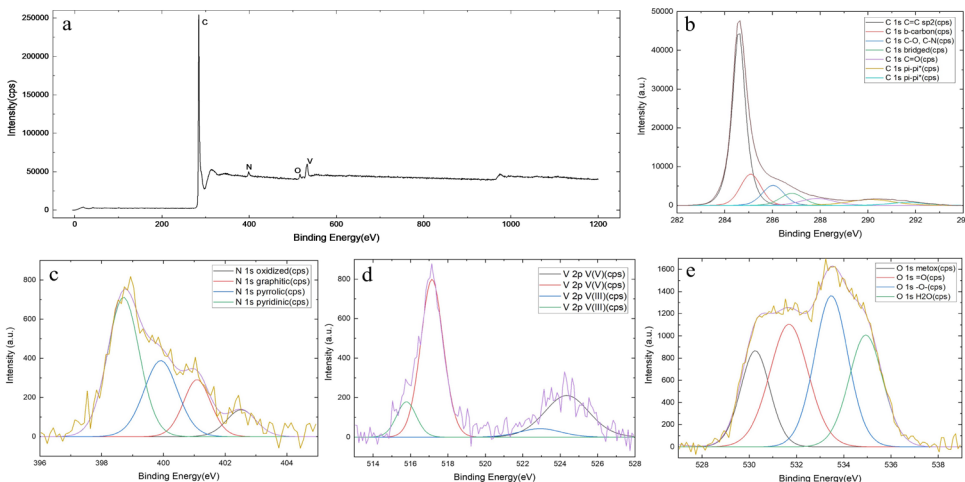


Figure 21. XPS survey spectra of VPC/MWCNT (1:3) catalyst material (a) and high-resolution C1s (b) N1s (c), V2p (d), and O1s (e) spectra.

Table 7 presents the specific surface area measurement, micropore volumes, pore volumes, and average pore diameters for materials that were produced at various temperatures. The investigation showed that the VPC/MWCNT catalyst, when subjected to a heat treatment at 1000 °C, exhibited the smallest average pore size, the largest surface area, and the highest pore volume. Conversely, the VPC/MWCNT catalyst heat treated at 600 °C exhibited the lowest pore volume and surface area. Different catalyst structures and pore structures are obtained as a result of the pyrolysis of materials at different temperatures (Behler et al., 2006; Contreras-Navarrete et al., 2015; Hansson et al., 2020). According to the obtained data, the specific surface area of the sample exhibits a declining trend in the following sequence: VPC/MWCNT at 1000 °C > 800 °C > 600 °C.

Table 7. Volume and surface properties of catalysts in various pyrolysis temperatures.

Catalyst pyrolysis temperature	Multipoint BET (m <sup>2</sup> /g)	DFT method cumulative surface area (m <sup>2</sup> /g)	DFT method cumulative pore volume (cm <sup>3</sup> /g)	DFT method pore radius (nm)	Average pore size (nm)
600 °C	136.8	112.9	0.21	2.04	6.92
800 °C	153.8	143.0	0.23	2.03	5.81
1000 °C	180.4	194.4	0.28	2.03	5.34

The relationship between the vanadium concentration and various pyrolysis temperatures can be explained by referring to Table 8. The sample subjected to pyrolysis at a temperature of 600 °C exhibits the greatest atomic percentage of vanadium, while the sample that had heat treatment at 1000 °C has the lowest vanadium content. Previous studies have demonstrated that the presence of transition metals promotes the process of graphitization (Goldie et al., 2021; Sevilla et al., 2007). This, in turn, leads to a reduction in surface area by decreasing the number of defects. Consequently, the material with the highest vanadium (V) content, specifically VPc/MWCNT (1:3) synthesized at 600 °C, exhibits the lowest surface area. Conversely, the sample with the lowest V content, VPc/MWCNT (1:3) synthesized at 1000 °C, demonstrates the highest surface area.

Table 8. Elemental composition of VPc/MWCNT catalysts determined by XPS.

Catalyst	C at. %	N at. %	O at. %	V at. %
VPc/MWCNT (1:3) 600 °C	94.1	2.2	1.7	2.0
VPc/MWCNT (1:3) 800 °C	95.9	1.6	1.4	1.0
VPc/MWCNT (1:1) 800 °C	93.5	1.9	3.0	1.6
VPc/MWCNT (3:1) 800 °C	92.6	1.8	2.6	2.9
VPc/MWCNT (1:3) 1000 °C	94.0	1.5	3.7	0.9
Relative concentration (%) of N moieties in the catalysts	Pyridinic at. %	Pyrrolic at. %	Graphitic at. %	N-Oxide at. %
VPc/MWCNT (1:3) 600 °C	57.4	21.3	12.1	9.2
VPc/MWCNT (1:3) 800 °C	45.4	38.8	9.7	6.1
VPc/MWCNT (1:1) 800 °C	47.6	27.5	16.4	8.4
VPc/MWCNT (3:1) 800 °C	44.2	8.8	42.6	4.4
VPc/MWCNT (1:3) 1000 °C	18.5	20.4	42.8	18.3

### 3.2.2 Electrochemical characterization V and N-doped catalyst material

Electrochemical reduction of oxygen on VPc/MWCNT was studied with the RDE technique using the same procedure as for PbPc/MWCNT catalysts. In all three media, the catalysts produced at the pyrolysis temperature of 800 °C had the highest activity, according to the results shown in Figure 22. The non-pyrolyzed catalyst had the lowest activity at all three pH-s, demonstrating the need of VPc heat treatment.

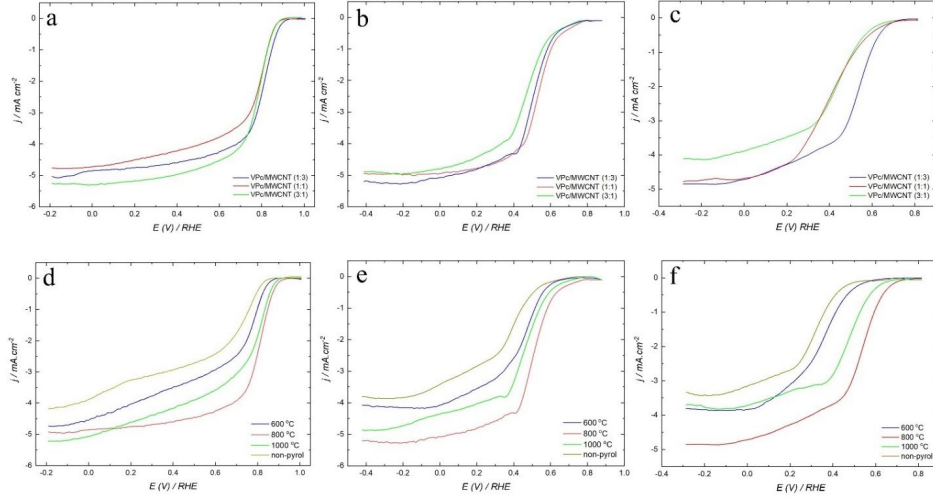


Figure 22. LSV curves for oxygen reduction reaction. Various ratios of VPc/MWCNT catalyst and heat treated at 800 °C (a, b, c), VPc/MWCNT (1:3) catalyst pyrolyzed at various temperatures and non-pyrolysis (d, e, f); O<sub>2</sub>-saturated 0.1 M KOH (a, d), 0.1 M PBS (b, e) and 0.5 M H<sub>2</sub>SO<sub>4</sub> (c, f),  $\nu = 10 \text{ mV s}^{-1}$ ,  $\omega = 1600 \text{ rpm}$ .

According to Table 9, the pyrolysis temperature of 800 °C is associated with the highest  $E_{\text{onset}}$  and  $E_{1/2}$  values as well as the highest limiting current density.

Table 9. ORR results obtained for catalysts of VPc/MWCNT (1:3) prepared at various pyrolysis temperatures in various electrolytes (1600 rpm).

Electrolyte	Pyrolysis Temperature	$E_{\text{onset}}$ (V)	$E_{1/2}$ (V)	$j_d$ (mA cm <sup>-2</sup> )	$n$
Alkaline KOH 0.1 M	600 °C	0.89	0.72	-4.8	3.6
	800 °C	0.93	0.80	-5.0	3.9
	1000 °C	0.91	0.76	-5.2	3.7
Neutral PBS 0.1 M	600 °C	0.61	0.45	-4.1	2.7
	800 °C	0.76	0.50	-5.2	2.9
	1000 °C	0.71	0.46	-4.9	2.8
Acid H <sub>2</sub> SO <sub>4</sub> 0.5 M	600 °C	0.56	0.35	-3.8	2.9
	800 °C	0.70	0.52	-4.9	3.0
	1000 °C	0.64	0.46	-3.9	3.0

A higher doping temperature has been shown to enhance the formation of electrocatalytically active species throughout the surface in prior investigations, and as a result, a catalyst made at 800 °C has a higher activity than one created at 600 °C (Jo & Shanmugam, 2012; Y. Liu et al., 2019). Due to the fact that the macrocyclic compound cannot fully decompose at low temperatures (such as 600 °C), active sites are not created on the catalyst surface. The pyrolysis conditions should be kept below a specified temperature since higher temperature might eliminate active sites, which lowers the onset potential and current densities. When cobalt phthalocyanine was pyrolyzed at 1000 °C as opposed to 800 °C, Zhi et al. demonstrated that the N/C ratio was approximately two times lower (Zhi et al., 2005).

For alkaline, neutral, and acidic media at various electrode rotation speeds ( $\omega$ ), ORR polarization curves are shown in Figure 23a–c using the catalyst material with the greatest activity, VPC/MWCNT (1:3) @ 800 °C. The onset potentials for alkaline, neutral, and acidic media are 0.93 V, 0.80 V, and 0.76 V vs RHE, respectively. At lower rotation rates and more negative potentials in neutral and acidic media, a second reduction wave is visible, indicating that  $O_2$  is reduced to an intermediate of  $H_2O_2$  through the  $2e^-$  pathway, followed by decomposition or further reduction to  $H_2O$  by a subsequent  $2e^-$  pathway. This is the process that is expected to occur for heteroatom and metal co-doped carbon materials in a neutral medium, according to previous similar studies (K.K. Türk et al., 2018; W. Wang et al., 2019).

It has been noted that the value of  $n$  obtained in an alkaline environment remains about four over the whole range of potentials investigated. This finding highlights the significant capabilities of VPC/MWCNTs as cathode catalysts, particularly in the context of AEMFC. In both acidic and neutral conditions, the value of  $n$  is determined to be around 3, indicating the presence of simultaneous 4-electron and 2-electron pathways (Gottesfeld et al., 1987; Kruusenberg et al., 2009).

The occurrence of multiple ORR pathways on the surface of a vanadium/nitrogen/carbon (V/N/C) catalyst may be attributed to the simultaneous presence of diverse active sites characterized by varying structures.

Nitrogen doping in carbon materials increases positive charge on nearby carbon atoms and enhances conductivity through lone-pair electron conjugation. This promotes charge delocalization, weakens the O–O bond, and facilitates oxygen reduction by enabling electron transfer to oxygen. The metal center also influences nitrogen content, affecting active site formation (Ge et al., 2015; W. Wang et al., 2019). XPS analysis conducted in this study has provided evidence indicating that the vanadium species present in the sample are mostly in an oxidation state of +5.  $V_2O_5$  has interstitial spaces within its structure, which facilitate the adsorption of oxygen on its surface (Sajid et al., 2020; Surnev et al., 2003). The exposed  $O_2$  molecule in  $V_2O_5$  facilitates the conductivity of catalyst, leading to enhanced ORR (Ji et al., 2016; Noori et al., 2017). The findings of the RDE study suggest that the observed increase in catalytic activity, mainly in terms of half-wave potential and onset potential, as well as increase in diffusion-limited current density, may be attributed primarily to the existence of vanadium oxide and nitrogen surface groups, which are known to be active in ORR.

To the best of our knowledge, there is no existing literature pertaining to carbon materials co-doped with V and N for the purpose of ORR. The idea on the potential ORR mechanism on this catalyst material is derived from previous studies on co-doped carbon materials including transition metals and nitrogen, as well as catalyst materials modified with vanadium oxide.

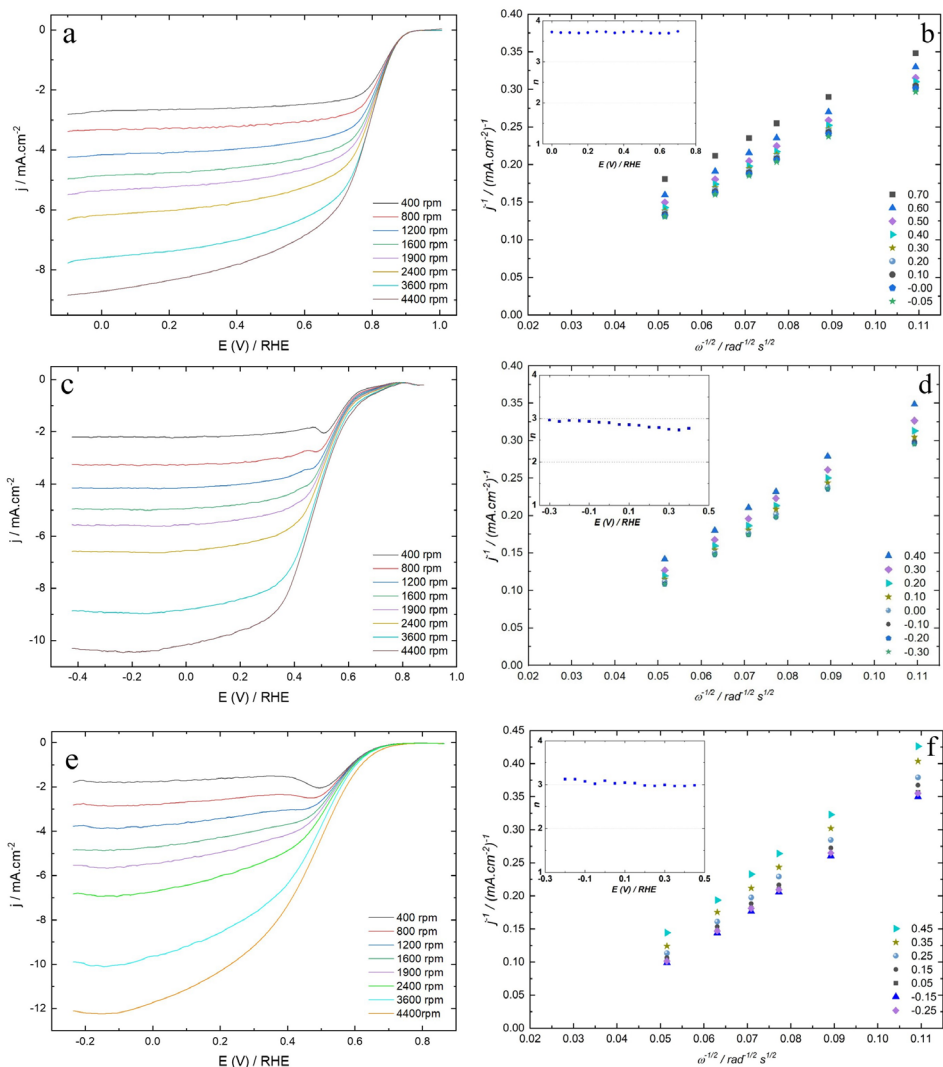


Figure 23. RDE polarization curves for the ORR on VPC/MWCNT (1:3) @ 800 °C catalyst in  $O_2$ -saturated 0.1 M KOH (a), 0.1 M PBS (c) and 0.5 M  $H_2SO_4$  (e),  $v = 10 \text{ mV.s}^{-1}$ ,  $\omega = 400\text{--}4400 \text{ rpm}$ ; Koutecky-Levich plots for ORR on VPC/MWCNT (1:3) modified GC electrodes in  $O_2$  molecule in 0.1 M KOH (b), 0.1 M PBS (d) and 0.5 M  $H_2SO_4$  (f). Inset shows the potential dependence of  $n$ .

Figure 24a-c show the comparative linear sweep voltammetry (LSV) curves of five different catalysts: commercial Pt/C, pure MWCNT, nitrogen-doped MWCNTs (HPc/MWCNT), and nitrogen/vanadium co-doped MWCNTs (VPc/MWCNT) with and without pyrolysis. The novel catalyst, VPc/MWCNT (1:3), exhibits more negative onset potential ( $E_{\text{onset}}$ ) in alkaline, neutral, and acidic conditions compared to the commercially available Pt/C catalyst. The observed differences in  $E_{\text{onset}}$  values are 0.04 V, 0.07 V, and 0.20 V, respectively. The observed decrease in  $E_{\text{onset}}$  between Pt/C and N/V co-doped catalysts in alkaline medium, relative to the other two media, suggests that the V-doped catalyst exhibits superior performance in an alkaline environment. The validity of this finding was further confirmed by the examination of  $n$  values. In comparison to

VPc/MWCNT (1:3),  $E_{\text{onset}}$  of HPc/MWCNT is more negative by 20 mV in alkaline medium, 50 mV in neutral media, and 20 mV in acidic media. Furthermore, it can be shown that the  $E_{1/2}$  values exhibit a decrease of 60 mV, 40 mV, and 30 mV in alkaline, neutral, and acidic environments, respectively, when using HPc/MWCNT. This finding provides insight into the influence of V atoms on the enhancement of catalytic performance. It is important to note that the electrocatalytic activity of the material doped with both vanadium and nitrogen is higher compared to the catalyst doped only with nitrogen. This observation provides evidence that vanadium oxide is mixed with carbon nanotubes, hence enhancing the electrocatalytic activity. Tables 10, 11 and 12 provide a comprehensive analysis of the data obtained from RDE experiments conducted on VPc/MWCNT catalysts with varying ratios of VPc to carbon, which were subjected to pyrolysis at a temperature of 800 °C. Additionally, the RDE experiments were performed on HPc/MWCNT and Pt/C catalysts in different media.

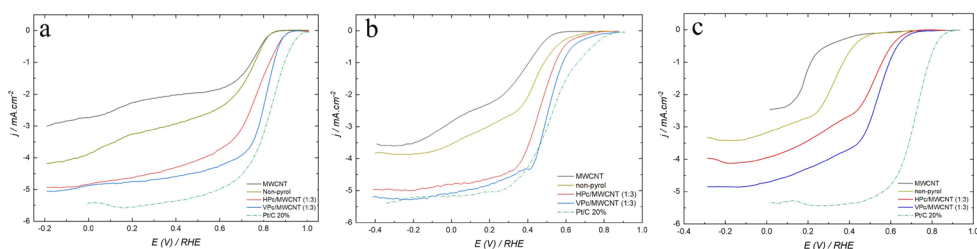


Figure 24. Comparison of RDE results of oxygen reduction on MWCNT, non-pyrolysis material, HPc/MWCNT (1:3), VPc/MWCNT (1:3) and Pt/C modified GC electrodes in  $O_2$ -saturated 0.1M KOH (a), 0.1M PBS (b) and 0.5M  $H_2SO_4$  (c),  $\nu = 10 \text{ mV.s}^{-1}$ ,  $\omega = 1600 \text{ rpm}$ .

Table 10. Comparison of the ORR results obtained for VPc/MWCNT catalysts pyrolyzed at 800 °C, non-pyrolysis material, HPc/MWCNT and Pt/C in 0.1 M KOH.

Catalyst	$E_{\text{onset}}$ (V)	$E_{1/2}$ (V)	$j_d$ ( $\text{mA cm}^{-2}$ )	$n$
MWCNT	0.84	0.69	-3.0	2.5
Non-pyrolysis	0.84	0.67	-4.1	2.7
HPc/MWCNT 3:1	0.91	0.74	-4.9	3.0
VPc/MWCNT 1:3	0.93	0.80	-5.0	3.9
VPc/MWCNT 1:1	0.88	0.78	-4.8	3.7
VPc/MWCNT 3:1	0.89	0.78	-5.3	3.9
Pt/C 20 %	0.97	0.82	-5.5	3.7



Table 11. Comparison of the ORR results obtained for VPc/MWCNT catalysts pyrolyzed at 800 °C, non-pyrolysis material, HPc/MWCNT and Pt/C in 0.1 M phosphate buffer.

Catalyst	$E_{\text{onset}}$ (V)	$E_{1/2}$ (V)	$j_d$ (mA cm <sup>-2</sup> )	$n$
MWCNT	0.54	0.31	-3.6	2.5
Non-pyrolysis	0.67	0.42	-3.8	2.7
HPc/MWCNT 3:1	0.71	0.46	-5.0	2.9
VPc/MWCNT 1:3	0.76	0.50	-5.2	2.9
VPc/MWCNT 1:1	0.78	0.53	-5.0	3.2
VPc/MWCNT 3:1	0.76	0.47	-4.9	3.0
Pt/C 20%	0.83	0.52	-5.0	3.6

Table 12. Comparison of the ORR results obtained for VPc/MWCNT catalysts pyrolyzed at 800 °C, non-pyrolysis material, HPc/MWCNT and Pt/C in 0.5 M H<sub>2</sub>SO<sub>4</sub>.

Catalyst	$E_{\text{onset}}$ (V)	$E_{1/2}$ (V)	$j_d$ (mA cm <sup>-2</sup> )	$n$
MWCNT	0.40	0.24	-2.5	2.4
Non-pyrolysis	0.50	0.31	-3.5	2.4
HPc/MWCNT 3:1	0.68	0.49	-4.0	2.9
VPc/MWCNT 1:3	0.70	0.52	-4.9	3.0
VPc/MWCNT 1:1	0.63	0.40	-4.8	3.2
VPc/MWCNT 3:1	0.62	0.43	-4.1	3.0
Pt/C 20%	0.90	0.72	-5.4	3.7

To evaluate the stability of the produced catalysts, VPc/MWCNT (1:3) was subjected to 1000 cycles in alkaline, neutral, and acidic environments. The LSV curves shown in Figure 25 provide evidence that the VPc/MWCNT (1:3) catalyst exhibits enhanced stability, with very little variation in  $E_{1/2}$  values seen in the acidic environment. Additionally, a slight decrease in both  $E_{1/2}$  and limiting current density values is observed in the alkaline environment. The observation that ORR polarization curves exhibit minimal reductions in current density values, without any change in the onset potential, provides evidence for the exceptional stability of these materials in both neutral and acidic conditions.

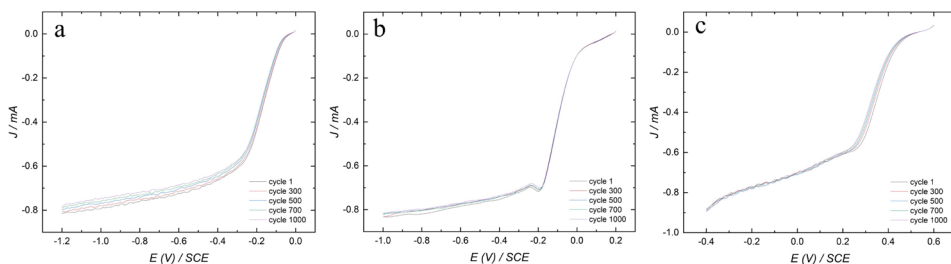


Figure 25. Stability of VpC/MWCNT (1:3) in  $O_2$ -saturated in 0.1 M KOH (a), 0.1 M PBS (b), and 0.5 M  $H_2SO_4$  (c),  $\nu = 10 \text{ mV s}^{-1}$ ,  $\omega = 1600 \text{ rpm}$ .

In light of the significant importance placed on the durability of catalyst materials in fuel cell technology, a series of chronoamperometric studies were conducted using the VpC/MWCNT (1:3) catalyst. The experiment was conducted under controlled conditions, maintaining a constant potential of 0.4 V vs RHE. The electrolyte used was a 0.1 M KOH solution that was saturated with oxygen. Figure 26 demonstrates that the VpC/MWCNT (1:3) catalyst maintains a significantly higher relative current of 87% even after a 20-hour testing period. The chronoamperometric studies were also conducted in 0.1 M PBS and 0.5 M  $H_2SO_4$  solutions. The relative current in these media is seen to drop to 92% from the starting current value. Similarly, the relative current on the Pt/C catalyst reduces to 77% at a constant potential of 0.4 V vs RHE in the 0.5 M  $H_2SO_4$  solutions. Furthermore, the relative current reaches 82% in the alkaline medium and 79% in the neutral medium. The findings of this study suggest that the VpC/MWCNT catalyst has much better electrochemical stability than the Pt/C catalyst.

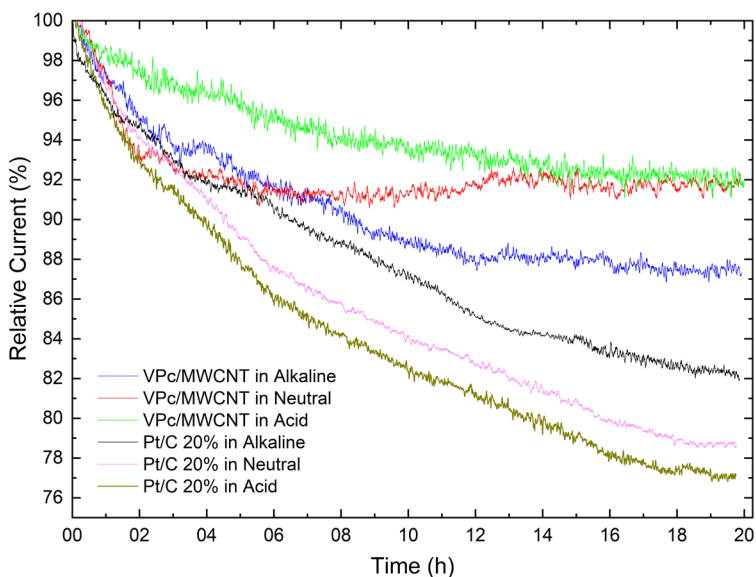


Figure 26. Chronoamperometric responses for the ORR on VpC/MWCNT(1:3) and Pt/C catalysts in  $O_2$  saturated 0.1 M KOH, 0.1 M PBS and 0.5 M  $H_2SO_4$  solution for 20 hours at 0.4 V vs RHE. Rotation speed: 200 rpm.

### 3.3 Oxygen reduction reaction on boron and fluorine co-doped carbon composite

#### 3.3.1. Physical characterisation of B and F co-doped carbon catalyst

This part is written based on the third journal paper (III) (Raudsepp et al., 2024). The surface of the GC electrode was analyzed using SEM after modification with boron and fluorine co-doped carbon nanomaterial. The provided illustration, denoted as Figure 27, showcases a SEM image of a catalytic material composed of rGO and FWCNT doped with boron and fluorine (BF). The BF-doped rGO/FWCNT composite material exhibits uniform distribution over the electrode surface, as seen in the Figure 27.

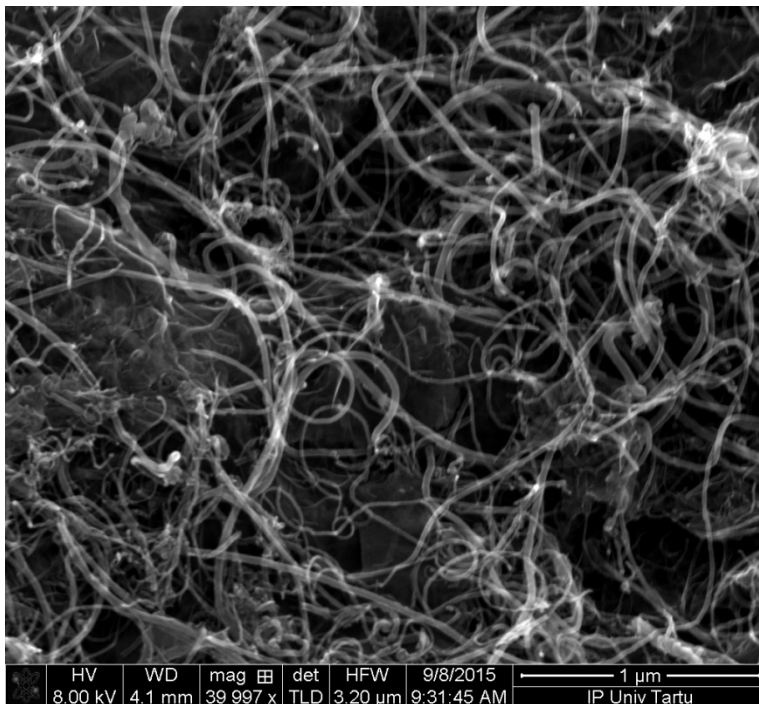
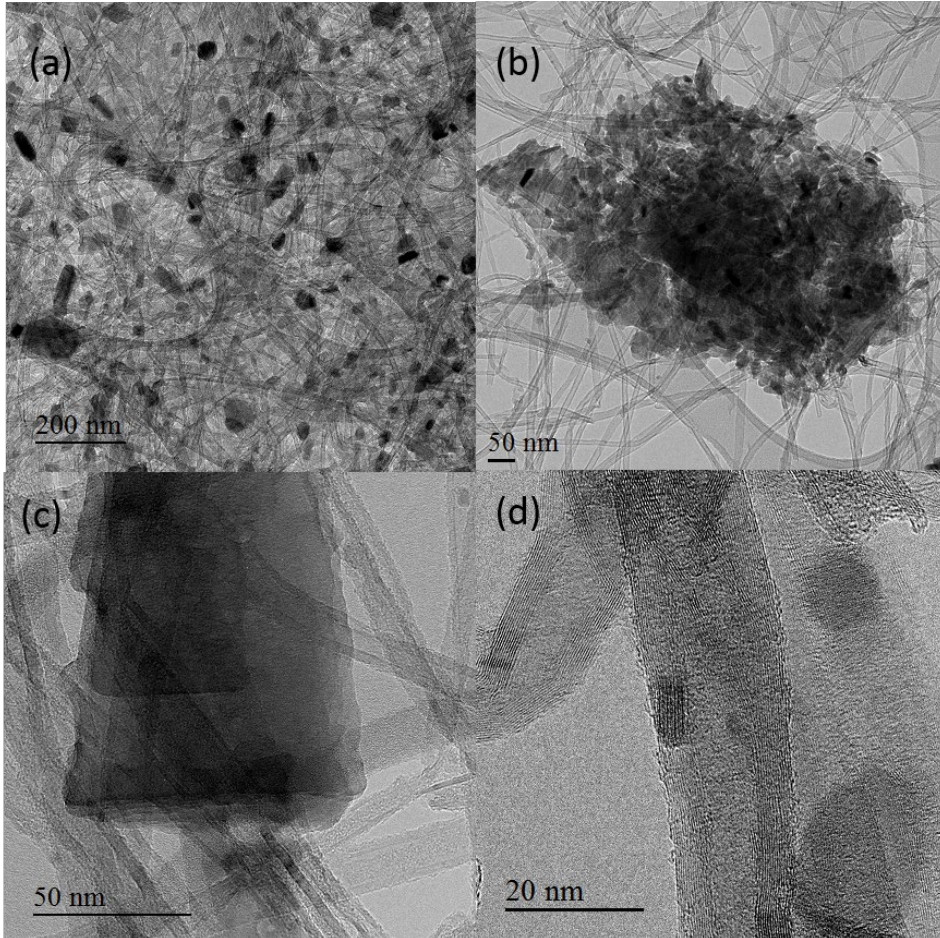


Figure 27. SEM image of boron and fluorine co-doped rGO/FWCNT composite material.

TEM analyses were conducted on the catalyst doped with both B and F elements, providing valuable insights into the material's morphology. The reduced graphene oxide co-doped material seen in Figure 28a exhibits a morphology characterized by nano-platelets with diameters ranging from 50 to 200 nm. The nano-platelets show a uniform distribution over the framework of FWCNT. The TEM picture shown in Figure 28b provides a comprehensive depiction of the catalyst material. It also serves to illustrate that not all of the nanotubes establish interactions with the graphene platelets, resulting in the presence of graphene-free nanotubes. In the shown picture, we see the presence of graphene platelets of bigger dimensions. Figure 28c displays an example of a bigger platelet. The platelet consists of many layers of graphene and is surrounded by numerous nanotubes that serve as spacers, thus inhibiting potential agglomeration of the layers (Karl Kalev Türk et al., 2015). Figure 28d displays a high magnification view of FWCNT used in the investigation. In this observation, it is evident that FWCNTs have a

distinct structural characteristic, consisting of 5–10 well-defined walls that are devoid of any amorphous carbon. Graphene platelets of diminutive dimensions, measuring as minute as 10 nm, may be seen. The presence of significant surface defects in graphene platelets has been observed, maybe attributed to the process of doping.



*Figure 28. TEM image of boron and fluorine co-doped rGO/FWCNT composite material. (a) and (b) overview of the catalyst. (c) larger flakes of rGO. (d) FWCNT used in the study.*

The investigation of the degree of graphitization and defect sites in the catalyst material was conducted using Raman spectroscopy. Figure 29 shows the presence of a prominent D peak at  $1310\text{ cm}^{-1}$  and a G peak at  $1584\text{ cm}^{-1}$  in the composite material prior to the co-doping of B and F. Upon the introduction of boron and fluorine doping, distinct peaks corresponding to the D and G bands manifest at wavenumbers of  $1303\text{ cm}^{-1}$  and  $1586\text{ cm}^{-1}$ , respectively. The G band is attributed to the scattering of  $E_{2g}$  phonons by  $sp^2$  hybridized carbon atoms, whereas the D band is associated with resonance Raman spectra resulting from distortions in the  $sp^2$  carbon system (Pawbake et al., 2018). The presence of a pronounced D band in the carbon network after acid treatment and doping suggests a significant increase in the number of defects inside the material.

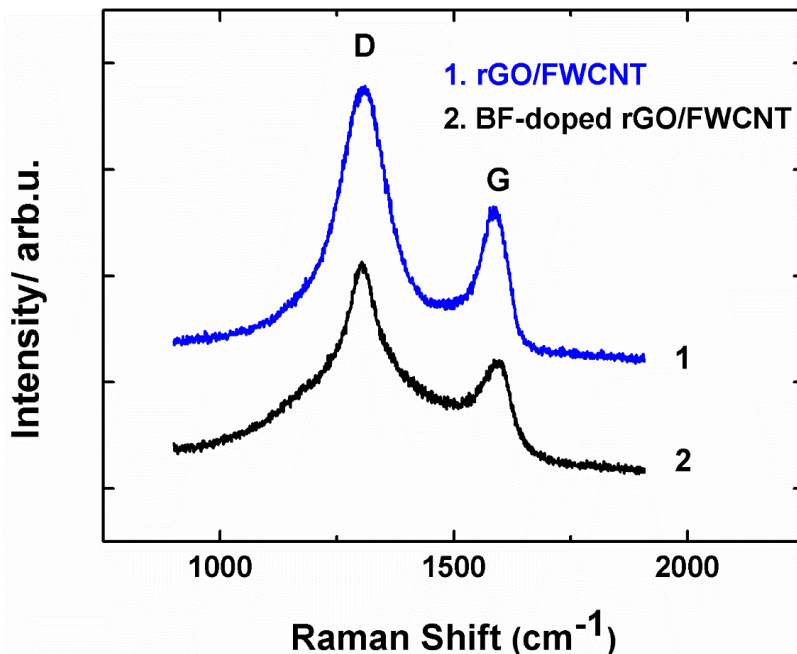


Figure 29. Raman spectra of rGO/FWCNT and BF co-doped rGO/FWCNT.

The determination of the D/G ratio enables the obtaining of insights on the magnitude of defects present in the material under investigation. The intensity ratio ( $I_D/I_G$ ) between the D and G bands is 1.69 for carbon material that is not doped, and 1.76 for carbon material that is doped with BF. The presence of a larger ratio implies a greater quantity of surface defects, therefore suggesting that the introduction of boron and fluorine doping results in an increase of surface flaws. This observation is supported by the research conducted by Kakaei and Balavandi, who discovered a significant increase in the  $I_D/I_G$  ratio after the introduction of fluorine into the graphene framework. This finding implies that fluorine doping is a major contributor to the generation of a disordered and defective carbon surface (Kakaei & Balavandi, 2017). The co-doping of carbon with nitrogen and fluorine has been shown to have a similar outcome, as it leads to the creation of defect sites and the disruption of the carbon skeleton in graphene, resulting in a higher level of distortion (H. Wang et al., 2021). A noticeable alteration seen in the Raman spectra is the progressive broadening of the D peak, suggesting a disruption of  $sp^2$  hybridization subsequent to B and F doping. The Raman spectroscopy findings presented in this study exhibit a high level of agreement with the findings published by Gong et al. (P. Gong et al., 2014).

XPS technique was used to investigate the surface chemical composition of the composite material doped with both B and F. XPS analysis reveals the detection of boron, carbon, oxygen, and fluorine elements, with atomic percentages of 1.7%, 92%, 6%, and 0.6%, respectively. According to the data shown in Figure 30a, distinct peaks were seen at certain binding energies for various elements. Specifically, a discernible peak corresponding to the B1s orbital was observed at a binding energy of 192.5 eV, the C1s orbital exhibited a peak at 284 eV, the O1s orbital displayed a peak at 534.5 eV, and the F1s orbital demonstrated a peak at 685.5 eV. In Figure 30b, the C1s peak was subjected

to deconvolution, resulting in the identification of five separate peaks. These peaks correspond to the C = C peak at 284 eV, the B-C peak at 285 eV, the C-C peak at 285.5 eV, the C-O peak at 286.5 eV, and the O-C = O peak at 288.2 eV. XPS peak corresponding to the carbon-fluorine (C-F<sub>3</sub>) bond is expected to manifest at around 291.8 electron volts (eV). However, due to the limited fluorine content present in the sample, which is in close proximity to the instrument's detection threshold, distinguishing the current peak from the C1s peak poses considerable challenges. According to Gong et al. (P. Gong et al., 2014), it has been shown that the degree of fluorine doping exhibits a significant sensitivity to elevated temperature processing. The proportion of carbon-incorporated fluorine exhibits a gradual rise throughout the process of heat-treatment until reaching a temperature of 700 °C. Subsequently, it begins to decline, with a significant decrease seen at 800 °C (P. Gong et al., 2014). This phenomenon may arise due to the thermal degradation of species containing fluorine at higher temperatures (P. Gong et al., 2014; J. Kim et al., 2018).

XPS spectrum in Figure 30c has a high level of detail, allowing for the identification of three distinct peaks corresponding to various boron species: B<sub>2</sub>O<sub>3</sub>, BCO<sub>2</sub>, and BC<sub>2</sub>O. These peaks are seen at binding energies of 193, 192.2, and 190.8 eV, respectively. The distribution of various boron species is characterized by a composition consisting of 60% B<sub>2</sub>O<sub>3</sub>, 22% BCO<sub>2</sub>, and 18% BC<sub>2</sub>O. The binding energy of the present B1s XPS peak, measured at 192.5 eV, exhibits a positive shift when compared to the binding energy of pure boron, which is recorded at 187.0 eV (NIST, 2021; Sankaran & Viswanathan, 2007). This observation suggests that a portion of the boron was integrated into the carbon material via the substitution of carbon atoms within the sp<sup>2</sup> carbon network. Upon analyzing the high resolution F1s XPS peak (Figure 30d), it is evident that the F1s peak may be separated into three distinct peaks. However, determining the precise characteristics and distribution of the various fluorine bonding forms proves to be challenging. It is anticipated that the introduction of BF co-doping may result in a diminished peak of covalent C-F bonding at higher binding energy levels, while simultaneously enhancing the intensity of semi-ionic and ionic C-F bonds. These bonds are primarily responsible for enhancing the charge transfer capabilities of the catalyst material (J. Kim et al., 2018; Panomsuwan et al., 2015; Parthiban et al., 2019). It is evident that fluorine is well doped into the carbon structure, since prior scientific studies have shown that the fluorine present in the ionic and semi-ionic CF bonds exhibits distinct characteristics compared to free fluorine ions in solution (J. Kim et al., 2018). Fu et al. have proposed that the increased proportion of ionic C-F bonds may also play a role in enhancing ORR activity of heteroatom-doped carbon catalysts (Fu et al., 2017). It has been observed that fluorine forms strong ionic and semi-ionic bonds with carbon, resulting in increased resistance to corrosion for the catalyst (Fu et al., 2017). Parthiban et al. have shown that the creation of semi-ionic C-F bonds plays a crucial role in achieving outstanding ORR activity (Parthiban et al., 2019).



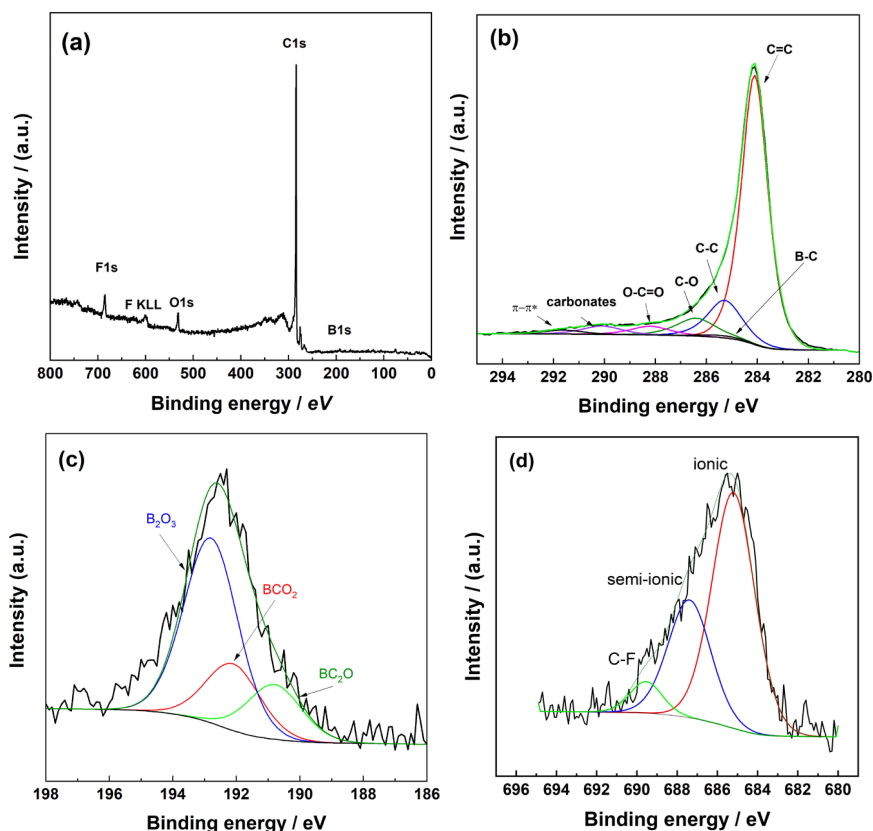


Figure 30. (a) XPS wide-scan spectrum of BF-doped carbon material. Core-level XPS spectra in (b) C1s, (c) B1s and (d) F1s regions.

### 3.3.2 Electrochemical characterization B and F co-doped carbon catalyst

The electrocatalytic activity of BF-doped rGO and FWCNT composite material towards ORR was investigated using RDE technique. The working electrode used in this study consisted of GC electrodes that were modified with BF co-doped carbon composite catalysts. The measurements were conducted in electrolyte solutions of O<sub>2</sub>-saturated 0.1 M KOH and 0.5 M H<sub>2</sub>SO<sub>4</sub>. The first phase of the study was an examination of ORR activity in relation to the mass ratio between the carbon composite and the BF source. The RDE findings in alkaline and acid media for all four distinct mass ratios of BF source to rGO/FWCNT pyrolyzed at 800 °C are shown in Figure 31a-b, respectively. The ORR polarization curves of these were compared to those of unmodified rGO/FWCNT material and the bare glassy carbon electrode.

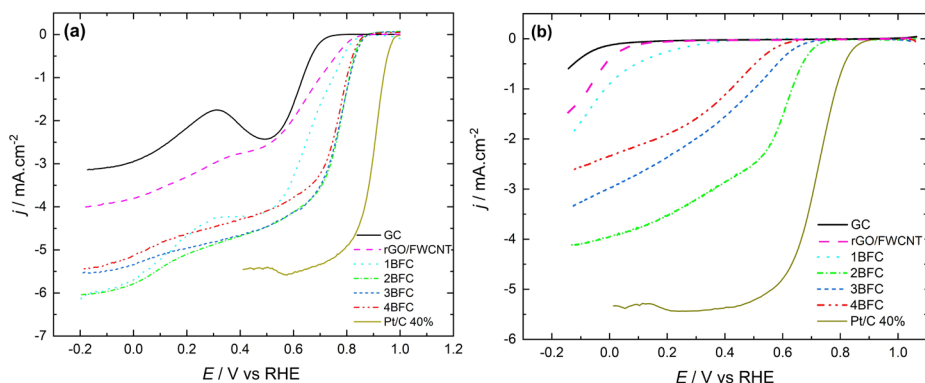


Figure 31. RDE voltammetry curves for oxygen reduction on GC electrodes modified with undoped rGO/FWCNT and BF-doped carbon composite materials in O<sub>2</sub>-saturated (a) 0.1 M KOH and in (b) 0.5 M H<sub>2</sub>SO<sub>4</sub>,  $\nu = 10 \text{ mV s}^{-1}$ ,  $\omega = 1900 \text{ rpm}$ . Curve GC corresponds to unmodified glassy carbon.

The observation in Figure 31a reveals that 2BFC, and 3BFC exhibit similar onset potentials for ORR in alkaline conditions, approximately 0.87 V vs. RHE. This value is slightly more positive than that of 4BFC, suggesting that further increasing the levels of boron and fluorine doping will eventually lead to a decrease in the electrocatalytic activity towards the ORR. Figure 31b shows analogous behavior in acidic environments, but with a more noticeable impact of dopant concentration. The clear superiority of the 2BFC catalyst over the other catalysts is obvious. While certain prior studies have indicated a positive correlation between the electrocatalytic activity of the catalyst material for ORR and the concentration of boron, it is important to note that there is a lack of existing literature on the utilization of boron trifluoride diethyl etherate (BTDE) as a source of boron or fluorine for the purpose of heteroatom doping in carbon nanomaterials (Bo et al., 2013; Y. Cheng et al., 2014). Previous studies have shown that there exists a certain threshold beyond which augmenting the boron content in the carbon network becomes more challenging only via the incremental addition of the boron source (Y. Cheng et al., 2014). Furthermore, the presence of defects and oxygen-containing functional groups on the surface of carbon materials significantly influences their electrocatalytic activity. A further factor contributing to the enhanced ORR kinetics on BF co-doped carbon is the concurrent increase in oxygen content resulting from the introduction of boron into the material. This is due to the ability of boron atoms to promote the adsorption of oxygen (Y. Cheng et al., 2014). There has been a proposal suggesting that the presence of positively charged boron atoms on the carbon surface might enhance the process of oxygen chemisorption. This chemisorption, in turn, serves as a bridge for the transfer of electrons from adjacent carbon atoms to oxygen, resulting in the weakening of the O-O bond (L. Yang et al., 2011). In contrast, the introduction of fluorine into rGO and FWCNTs results in the creation of a highly efficient p-type semiconductor with low fluorine concentration. At greater levels of fluorine coverage in the carbon composite material, these doped materials exhibit conductive properties (P. Gong et al., 2014; Ho et al., 2014). The addition of fluorine, a strongly electronegative element with an excess of valence electrons relative to boron or other heteroatoms, is expected to enhance the electrical conductivity of the catalyst material (P. Gong et al., 2014; Ho et al., 2014). One possible explanation for the enhanced ORR activity seen in BF-doped rGO/FWCNT composites is the introduction of fluorine



atoms into the carbon framework, which may lead to the creation of distinct structural defects that might serve as electrocatalytically active sites (Rosas-Medellin et al., 2022). This concept is also consistent with the findings from the Raman spectroscopy analysis discussed earlier.

Several research investigations have shown that the co-doping of graphene sheets with several heteroatoms is a more efficient approach for altering the chemical surface composition of graphene and facilitating the interaction between these diverse atoms (A. Liu et al., 2015; Y. Liu et al., 2013). Therefore, it is anticipated that the electrocatalytic activity will be enhanced when graphene oxide and FWCNTs are doped with fluorine and boron. The electronic hybrid structure of the carbon material may be manipulated by co-doping, which involves the formation of covalent bonds with the local  $\pi$ -orbital system of graphitic carbon. This process also leads to the production of novel bond interactions (P. Gong et al., 2013).

Furthermore, it is evident that the onset potential of ORR polarization curves for the heat-treated combination of rGO and acid-treated FWCNT exhibits an approximate shift of 100 mV in positive direction compared to the unmodified glassy carbon electrode in alkaline environments. The introduction of boron and fluorine co-doping results in a further change of the onset potential for ORR in the positive direction. The half-wave potential value exhibits an approximate positive shift of 200 mV in comparison to the unmodified glassy carbon electrode. Additionally, the reduction current values show a significant increase. The electrocatalytic effect is more pronounced in acidic environments, as shown by the 2BFC electrocatalyst exhibiting a positive shift in onset potential of 600 mV compared to heat-treated rGO/FWCNTs and about 700 mV compared to bare GC (refer to Figure 31b). Based on the obtained findings from RDE, it is evident that the introduction of boron and fluorine atoms into the carbon structure of rGO and FWCNT significantly alters the electrocatalytic characteristics of the catalyst material.

The investigation also included an examination of the impact of pyrolysis temperature on the electrocatalytic activity of the material doped with both boron and fluorine. At a temperature of 800 °C, 2BFC exhibited the most significant ORR activity. The pyrolysis processes conducted at temperatures of 600 °C and 1000 °C used an identical ratio of boron and fluorine precursor to carbon material. Figures 32a-b illustrate that the catalyst material, synthesized by pyrolysis at 800 °C, has superior electrocatalytic performance for O<sub>2</sub> reduction in both alkaline and acid environments. This is evident from its more positive onset potential and higher reduction current values compared to other catalyst materials. Previous studies have shown that raising the temperature during the doping process leads to an increase in the quantity of electrocatalytically active surface species. Consequently, the material synthesized at 800 °C exhibits higher activity compared to the material synthesized at 600 °C (Jo & Shanmugam, 2012; X. Xu et al., 2014). Several earlier studies have shown that increasing the pyrolysis temperature above 800 °C leads to more efficient heteroatom doping (X. Sun, Song, et al., 2013; Venkateswara Rao & Ishikawa, 2012). However, in the present study, the increase in temperature from 800 to 1000 °C during BF co-doping using BTDE did not result in an improvement in the electrocatalytic performance of the material for ORR. Hence, the use of BTDE for B and F co-doping may be regarded as a more economically viable option compared to using boron sources that exhibit similar electrocatalytic ORR activity after doping at higher temperatures (L. Yang et al., 2011).

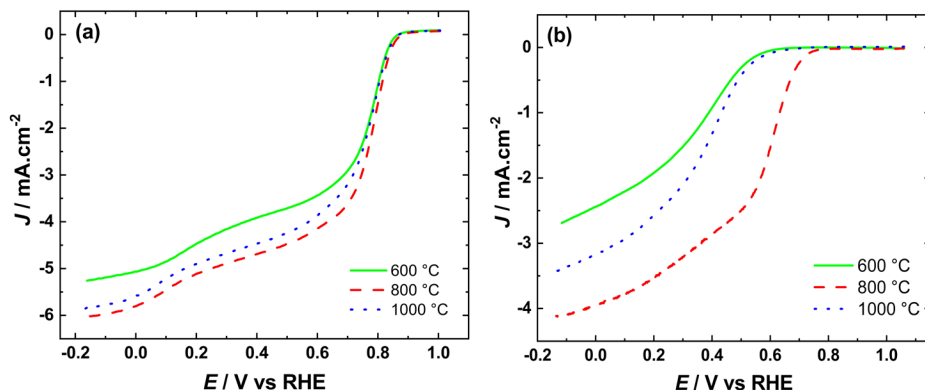


Figure 32. RDE voltammetry curves for oxygen reduction on a 2BFC/GC electrode in  $O_2$ -saturated (a) 0.1 M KOH and (b) 0.5 M  $H_2SO_4$ .  $\nu = 10 \text{ mV s}^{-1}$ ,  $\omega = 1900 \text{ rpm}$ . 2BFC material was prepared by pyrolysis at temperatures of 600, 800 and 1000 °C.

Figure 33a-b show a series of polarization curves for ORR obtained at various electrode rotation rates. These measurements were conducted using a highly active 2BFC catalyst-modified GC electrode, in both alkaline and acid environments, as indicated. The onset potential for ORR is estimated to be about 0.85 V vs RHE. At lower rotation speeds, the reduction current plateaus are seen, suggesting that the ORR process is mostly governed by diffusion control.

However, it is worth noting that this particular electrocatalytic activity may also be attributed to the emergence of novel active sites as a consequence of boron and fluorine co-doping. Specifically, fluorine has a tendency to induce defects in the surface, whilst boron aids in the attraction of oxygen species (Panomsuwan et al., 2015; L. Yang et al., 2011). Numerous prior investigations have consistently demonstrated that the introduction of fluorine into carbon frameworks leads to an augmentation of positive charge on adjacent carbon atoms. This, in turn, enhances the activity of p-electrons, thereby promoting stronger interactions between the catalyst sites and  $O_2$  molecules. Consequently, the electrocatalytic activity for ORR is increased (Parthiban et al., 2019; X. Sun, Song, et al., 2013; X. Sun, Zhang, et al., 2013). Based on the findings of the RDE analysis, it can be inferred that the simultaneous incorporation of boron and fluorine atoms into the graphitic frameworks of graphene and FWCNTs has the potential to enhance the electrocatalytic activity of ORR, as shown by improvements in both the onset potential and limiting current values.

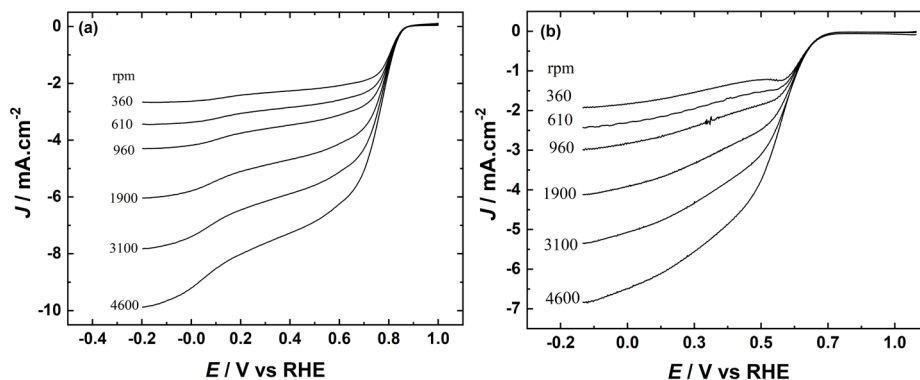


Figure 33. RDE voltammetry curves for oxygen reduction on a 2BFC/GC electrode in  $O_2$ -saturated (a) 0.1 M KOH and in (b) 0.5 M  $H_2SO_4$  at different rotation rates.  $\nu = 10 \text{ mV s}^{-1}$ .

The insets of Figure 34a-b present a comparison of the electron transfer number ( $n$ ) values derived from the Koutecky-Levich (K-L) equation at various applied potentials. In alkaline media,  $n$  value, as calculated from the K-L equation, approaches four. However, rotating ring-disk electrode (RRDE) measurements indicated  $n$  value closer to three. Additionally, the production of peroxide species increased from 40% to 60% as the potentials shifted towards more negative values (refer to Figure 35a). These RRDE results suggest that contrary to the K-L analysis, the oxygen reduction reaction (ORR) on the 2BFC nanocarbon catalyst proceeds via  $2e^-$  and two-step  $2e^- + 2e^-$  pathway, meaning that some of the peroxide is further reduced. This aligns with previous findings by Chokradjaroen et al., who reported a predominance of the two-electron pathway on boron and fluorine co-doped materials in alkaline media (Chokradjaroen et al., 2020). The variation in the fluorine species present in the catalyst may explain this behavior. In this study, fluorine predominantly exists in its ionic form, whereas in the work by Chokradjaroen et al., semi-ionic fluorine was more prevalent (Chokradjaroen et al., 2020). While both ionic and semi-ionic forms of fluorine enhance ORR activity, ionic fluorine is associated with higher electrical conductivity, exerting a greater influence on the carbon network's electronic structure (T. Gong et al., 2019).

In acidic media, at lower overpotentials ( $E > 0.36 \text{ V}$ ),  $n$  value is approximately two, indicating that  $O_2$  reduction primarily leads to the formation of peroxide as the final product. As the potential becomes more negative,  $n$  value gradually increases up to three, suggesting that some of the peroxide undergoes further reduction within this potential range. RRDE measurements in acidic media showed  $n$  value of 3.2 across all potential ranges, with 40% peroxide production (refer to Figure 35b). It should be noted that the Koutecky-Levich analysis of the undoped rGO/FWCNT material revealed  $n$  value in the range of 2 to 2.5 in both alkaline and acidic media. This indicates that while both the doped and undoped catalysts generate peroxide as an intermediate during the oxygen reduction reaction (ORR), the boron and fluorine co-doped material serves as a more effective catalyst for the further reduction of peroxide. This suggests enhanced catalytic performance for the doped material in driving the ORR towards a more complete reduction process.

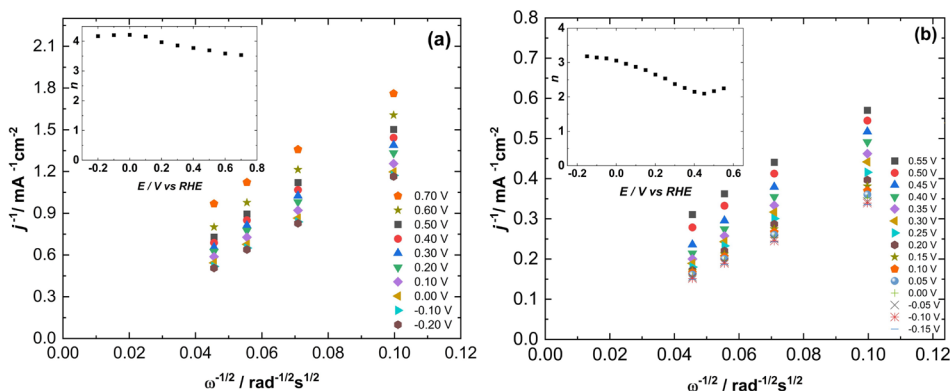


Figure 34. Koutecky-Levich plots for oxygen reduction on a 2BFC/GC electrode in (a) 0.1 M KOH and (b) 0.5 M H<sub>2</sub>SO<sub>4</sub>. Inset shows the potential dependence of the number of electrons transferred per O<sub>2</sub> molecule (*n*). Data derived from Figure 33.

The RRDE experimental data was utilized to calculate both the peroxide yield and the *n* values.

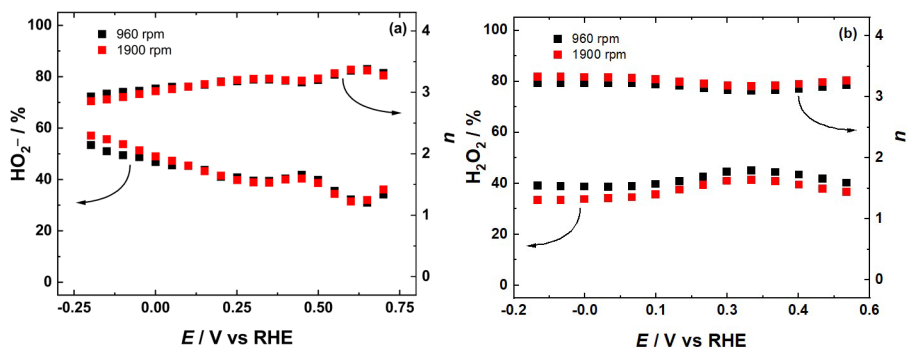


Figure 35. Percentage of HO<sub>2</sub><sup>-</sup> and H<sub>2</sub>O<sub>2</sub> and number of electrons transferred per O<sub>2</sub> molecule calculated based on RRDE measurements in alkaline (a) and acid media (b).

Durability and methanol tolerance tests were conducted on the most active catalyst (2BFC), synthesized at 800 °C, in both alkaline and acidic environments. These results were compared to those of the commercial 40% Pt/C catalyst. In the durability tests (Figure 36), the 2BFC material showed a 30% reduction in its initial current value after 60,000 seconds in both media, stabilizing at that point. In contrast, the 40% Pt/C catalyst exhibited a 35% drop in initial current over the same period, with a continued downward trend. When comparing methanol 3 M tolerance (Figure 37), the 2BFC catalyst demonstrated significantly better performance than the commercial Pt/C in both media. In alkaline conditions, 2BFC lost only 12% of its initial current, while the 40% Pt/C catalyst saw a 27% reduction. Similarly, in acidic media, 2BFC experienced a 15% decrease in current after 900 seconds following methanol injection (at 300 seconds), whereas the commercial catalyst lost nearly 40% of its initial current.

The importance of boron- and fluorine-doped catalysts has been recognized previously. However, the results obtained in this study provide further insights into their electrochemical properties. Based on the physical characterization results presented

above, it is evident that boron and fluorine play crucial roles in enhancing the electrocatalytic activity of these catalysts. The ORR electrocatalytic behavior improved between the doped B and F atoms. Electrochemical measurements clearly demonstrate that B and F co-doping effectively enhances ORR activity in both alkaline and acidic media. Therefore, such catalysts hold great potential for application in proton exchange membrane or anion exchange membrane fuel cells, as well as in metal-air batteries.

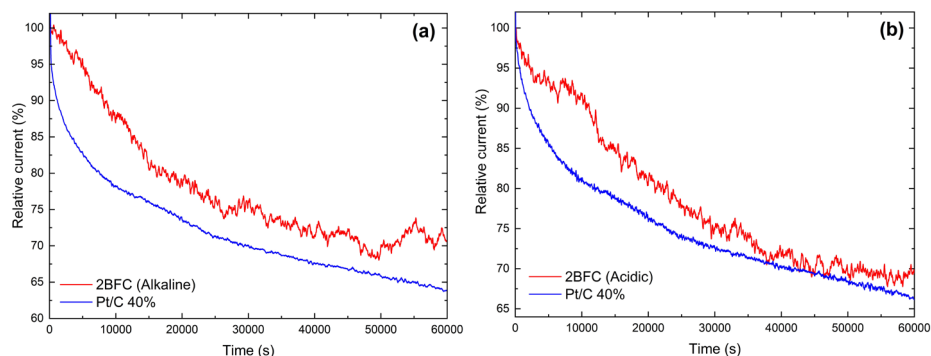


Figure 36. The durability of 2BFC compared with commercial 40% Pt/C in alkaline solution at 0.5 V vs. RHE (a), and acidic medium at 0.2 V vs. RHE (b).

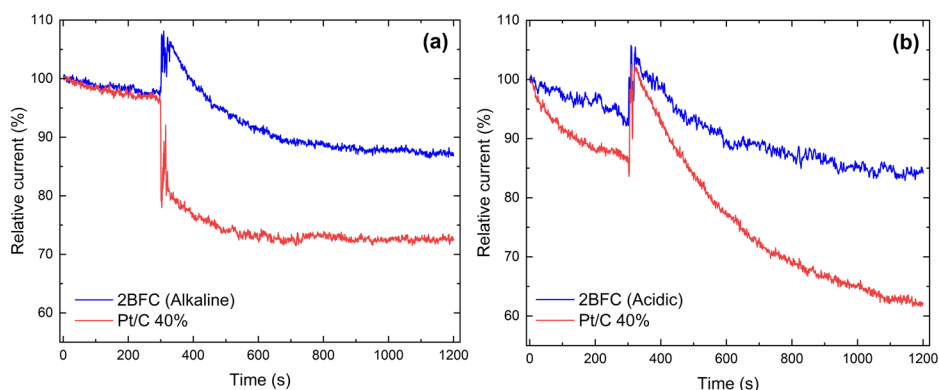


Figure 37. Methanol tolerance of 2BFC compared with commercial 40% Pt/C in alkaline at 0.5 V vs. RHE (a), and acidic medium at 0.2 V vs. RHE (b). 3 M methanol was added after 300 seconds.

## 4 Conclusions

In this work, three different approaches were studied to dope carbon support with non-noble metals and/or heteroatoms. Catalysts derived from metal phthalocyanines (MPc) and multi-walled carbon nanotubes (MWCNTs) were synthesized and evaluated for the oxygen reduction reaction (ORR). The study varied the ratios of MPc to MWCNTs and identified the optimal ratios for achieving the highest electrocatalytic activity. The best ratios were determined in alkaline media as PbPc/MWCNT 3:1 (onset potential 0.93 V vs RHE), VPc/MWCNT 1:3 (onset potential 0.93 V vs RHE), and GO/FWCNT/boron and fluorine source 1:5 (onset potential 0.86 V vs RHE). Across all materials, an 800 °C heat treatment consistently yielded the best results, with catalysts synthesized at this temperature demonstrating excellent ORR performance. In addition to electrochemical characterization, the successful modification of the carbon materials was confirmed through various physical characterization techniques, including SEM, TEM, XRD, N<sub>2</sub> adsorption, Raman spectroscopy, and XPS.

In the first part of the thesis (I), Pb and nitrogen co-doped carbon materials, synthesized using PbPc and MWCNTs, exhibited promising ORR activity, and diffusion-limited current density comparable to commercial Pt/C 20% catalysts, particularly in alkaline environment. Although the onset potential was more positive for Pt/C in all media, the inclusion of Pb played a crucial role in enhancing the electrocatalytic activity. This was clearly demonstrated by the significantly lower performance of catalysts synthesized without Pb. Notably, the Pb and N co-doped catalyst exhibited electrocatalytic activity comparable to that of commercial Pt/C, highlighting its potential as a promising alternative for ORR applications. Koutecky-Levich analysis revealed that in alkaline media, the catalyst favored a 4-electron reduction pathway ( $n \approx 4$ ), while in neutral and acidic media, the pathway was mixed  $2e^- + 2e^-$  and  $4e^-$ , with  $n \approx 3$ . The PbPc/MWCNT catalyst materials also demonstrated outstanding stability during linear sweep voltammetry (LSV) cycling in neutral and acidic media, though the stability was lower in alkaline conditions. These results suggest that PbPc/MWCNT materials have great potential as cathode catalysts in fuel cells, with the added advantage of using recycled lead from batteries as a raw material (I).

In the second part of the thesis (II), vanadium and nitrogen co-doped carbon nanomaterials were also prepared using a facile and cost-effective one-step synthesis method, with VPc as the vanadium and nitrogen precursor and MWCNTs as the carbon support. The catalyst synthesized with a VPc to MWCNT ratio of 1:3 had the most positive  $E_{\text{onset}}$  in alkaline (20 mV more negative than Pt/C) and acidic (50 mV more negative than Pt/C) media and the highest diffusion-limited current values in neutral and acidic electrolytes. Heat treatment at 800°C yielded the best ORR performance, with V–N co-doped catalysts showing higher diffusion-limited current values and more positive onset potential in neutral and acidic media compared to only N-doped MWCNTs. Furthermore, the V–N co-doped catalyst material exhibited superior stability, maintaining 92% of its initial current value after 20 hours in acidic electrolyte, compared to 77% for commercial Pt/C 20%. These results clearly indicate that vanadium doping significantly enhances the performance of ORR catalysts, making V–N co-doped materials promising candidates for fuel cell cathode applications (II).

In the third part of the thesis (III), boron and fluorine co-doped nanocarbon catalysts were successfully synthesized and tested for ORR. The doping was achieved using a mixture of few-walled carbon nanotubes (FWCNTs) and reduced graphene oxide (rGO) as the carbon support, with boron trifluoride diethyl etherate (BTDE) as the boron and

fluorine source. Morphological analysis revealed the presence of graphene nanoplatelets as small as 10 nm. The incorporation of boron and fluorine led to the formation of electrocatalytically active sites, as confirmed by XPS, and RDE measurements. The most active co-doped catalyst, prepared by heat-treating rGO/FWCNT and BTDE at 800 °C, demonstrated a 50 mV increase in onset potential in alkaline media and a remarkable 600 mV increase in acidic media compared to the undoped catalyst. The half-wave potential was also 100 mV more positive in alkaline media and 700 mV more positive in acidic media. These results reveal that these boron and fluorine co-doped materials possess significant electrocatalytic activity toward O<sub>2</sub> reduction and have great potential for use in polymer electrolyte membrane fuel cells and metal-air batteries (III).

In conclusion, the Pb/N, V/N, and BF co-doped carbon materials synthesized in this work exhibit promising electrocatalytic activity, stability, and economic feasibility, making them considerable candidates for future use as cathode catalysts in fuel cells and other electrochemical energy devices.

## References

- Abarca, G., Viera, M., Aliaga, C., Marco, J. F., Orellana, W., Zagal, J. H., & Tasca, F. (2019). In search of the most active MN4 catalyst for the oxygen reduction reaction. The case of perfluorinated Fe phthalocyanine. *Journal of Materials Chemistry A*, 7(43), 24776–24783. <https://doi.org/10.1039/C9TA09125D>
- Adeleye, A. T., Akande, A. A., Odoh, C. K., Philip, M., Fidelis, T. T., Amos, P. I., & Banjoko, O. O. (2021). Efficient synthesis of bio-based activated carbon (AC) for catalytic systems: A green and sustainable approach. *Journal of Industrial and Engineering Chemistry*, 96, 59–75. <https://doi.org/10.1016/J.JIEC.2021.01.044>
- Ai, S., Huang, Y., Xie, T., Zhang, X., & Huang, C. (2020). Fabrication of composites with ultra-low chitosan loadings and the adsorption mechanism for lead ions. *Environmental Science and Pollution Research*, 27(30), 37927–37937. <https://doi.org/10.1007/s11356-020-09906-7>
- Akula, S., & Sahu, A. K. (2020). Structurally Modulated Graphitic Carbon Nanofiber and Heteroatom (N,F) Engineering toward Metal-Free ORR Electrocatalysts for Polymer Electrolyte Membrane Fuel Cells. *ACS Applied Materials & Interfaces*, 12(10), 11438–11449. <https://doi.org/10.1021/acsami.9b18790>
- Aliev, S., Badmaeva, I. A., & Pokrovsky, L. D. (2012). Lead phthalocyanine films deposited by ECR plasma-induced sublimation. *Journal of Physics D: Applied Physics*, 45(30), 305202. <https://doi.org/10.1088/0022-3727/45/30/305202>
- Alonso, E., Field, F. R., & Kirchain, R. E. (2012). Platinum Availability for Future Automotive Technologies. *Environmental Science & Technology*, 46(23), 12986–12993. <https://doi.org/10.1021/es301110e>
- Anastasijević, N. A., Vesović, V., & Adžić, R. R. (1987). Determination of the kinetic parameters of the oxygen reduction reaction using the rotating ring-disk electrode. *Journal of Electroanalytical Chemistry and Interfacial Electrochemistry*, 229(1–2), 305–316. [https://doi.org/10.1016/0022-0728\(87\)85148-3](https://doi.org/10.1016/0022-0728(87)85148-3)
- Anderson, G. C., Pivovar, B. S., Alia, S. M., Liu, D.-J., Swider-Lyons, K., Patel, S., & Rainford, C. (2023). Projected Fuel Cell Stack Costs Using Non-PGM Cathode Electrocatalysts. *ECS Transactions*, 112(4), 225. <https://doi.org/10.1149/11204.0225ECST>
- Artyushkova, K. (2020). Misconceptions in interpretation of nitrogen chemistry from x-ray photoelectron spectra. *Journal of Vacuum Science & Technology A*, 38(3), 031002. <https://doi.org/10.1116/1.5135923>
- Asset, T., & Atanassov, P. (2020). Iron-Nitrogen-Carbon Catalysts for Proton Exchange Membrane Fuel Cells. *Joule*, 4(1), 33–44. <https://doi.org/10.1016/j.joule.2019.12.002>
- Ayyubov, I., Tálas, E., Berghian-Grosan, C., Románszki, L., Borbáth, I., Pászti, Z., Szegedi, Á., Mihály, J., Vulcu, A., & Tompos, A. (2023). Nitrogen doped carbonaceous materials as platinum free cathode electrocatalysts for oxygen reduction reaction (ORR). *Reaction Kinetics, Mechanisms and Catalysis*, 136(1), 125–147. <https://doi.org/10.1007/s11144-022-02331-6>
- Bai, X., Wang, Q., Xu, G., Ning, Y., Huang, K., He, F., Wu, Z., & Zhang, J. (2017). Phosphorus and Fluorine Co-Doping Induced Enhancement of Oxygen Evolution Reaction in Bimetallic Nitride Nanorods Arrays: Ionic Liquid-Driven and Mechanism Clarification. *Chemistry – A European Journal*, 23(66), 16862–16870. <https://doi.org/10.1002/chem.201703712>



- Bai, Y., Jin, P., Ji, S., Luo, H., & Gao, Y. (2013). Preparation and characterization of V<sub>2</sub>O<sub>3</sub> micro-crystals via a one-step hydrothermal process. *Ceramics International*, 39(7), 7803–7808. <https://doi.org/10.1016/J.CERAMINT.2013.03.040>
- Bakry, A. M., Awad, F. S., Bobb, J. A., & El-Shall, M. S. (2020). Multifunctional Binding Sites on Nitrogen-Doped Carboxylated Porous Carbon for Highly Efficient Adsorption of Pb(II), Hg(II), and Cr(VI) Ions. *ACS Omega*, 5(51), 33090–33100. <https://doi.org/10.1021/acsomega.0c04695>
- Bansal, R. C., & Goyal, M. (2005). *Activated Carbon Adsorption*. CRC Press. <https://doi.org/10.1201/9781420028812>
- Barkholtz, H. M., & Liu, D. J. (2017). Advancements in rationally designed PGM-free fuel cell catalysts derived from metal–organic frameworks. *Materials Horizons*, 4(1), 20–37. <https://doi.org/10.1039/C6MH00344C>
- Bashyam, R., & Zelenay, P. (2006). A class of non-precious metal composite catalysts for fuel cells. *Nature* 2006 443:7107, 443(7107), 63–66. <https://doi.org/10.1038/nature05118>
- Behler, K., Osswald, S., Ye, H., Dimovski, S., & Gogotsi, Y. (2006). Effect of Thermal Treatment on the Structure of Multi-walled Carbon Nanotubes. *Journal of Nanoparticle Research*, 8(5), 615–625. <https://doi.org/10.1007/s11051-006-9113-6>
- Bernal, V., Giraldo, L., & Moreno-Piraján, J. C. (2018). Physicochemical Properties of Activated Carbon: Their Effect on the Adsorption of Pharmaceutical Compounds and Adsorbate–Adsorbent Interactions. *C*, 4(4), 62. <https://doi.org/10.3390/c4040062>
- Bo, X., & Guo, L. (2013). Ordered mesoporous boron-doped carbons as metal-free electrocatalysts for the oxygen reduction reaction in alkaline solution. *Physical Chemistry Chemical Physics*, 15(7), 2459–2465. <https://doi.org/10.1039/C2CP43541A>
- Bo, X., Li, M., Han, C., & Guo, L. (2013). The influence of boron dopant on the electrochemical properties of graphene as an electrode material and a support for Pt catalysts. *Electrochimica Acta*, 114, 582–589. <https://doi.org/10.1016/j.electacta.2013.10.088>
- Bondarenka, V., Martunas, Z., Kaciulis, S., & Pandolfi, L. (2003). Sol–gel synthesis and XPS characterization of sodium–vanadium oxide bronze thin films. *Journal of Electron Spectroscopy and Related Phenomena*, 131–132, 99–103. [https://doi.org/10.1016/S0368-2048\(03\)00110-5](https://doi.org/10.1016/S0368-2048(03)00110-5)
- Bouwkamp-Wijnoltz, A. L., Visscher, W., & Van Veen, J. A. R. (1998). The selectivity of oxygen reduction by pyrolysed iron porphyrin supported on carbon. *Electrochimica Acta*, 43(21–22), 3141–3152. [https://doi.org/10.1016/S0013-4686\(98\)00076-0](https://doi.org/10.1016/S0013-4686(98)00076-0)
- Byeon, A., Yun, W. C., Kim, J. M., & Lee, J. W. (2023). Non-precious Metal Catalysts for Two-Electron Oxygen Reduction Reaction. *ChemElectroChem*, 10(17), e202300234. <https://doi.org/10.1002/CELC.202300234>
- Celiešiute, R., Trusovas, R., Niaura, G., Švedas, V., Račiukaitis, G., Ružele, Ž., & Pauliukaite, R. (2014). Influence of the laser irradiation on the electrochemical and spectroscopic peculiarities of graphene-chitosan composite film. *Electrochimica Acta*, 132, 265–276. <https://doi.org/10.1016/J.ELECTACTA.2014.03.137>
- Chandra, S., Sahu, S., & Pramanik, P. (2010). A novel synthesis of graphene by dichromate oxidation. *Materials Science and Engineering: B*, 167(3), 133–136. <https://doi.org/10.1016/j.mseb.2010.01.029>

- Charalampopoulos, G., Maniatis, I., & Daletou, M. (2023). Non-PGM Cathode Electrocatalysts for PEM Fuel Cells. *ECS Transactions*, 112(4), 335. <https://doi.org/10.1149/11204.0335ECST>
- Chattopadhyay, J., Pathak, T. S., & Pak, D. (2022). Heteroatom-Doped Metal-Free Carbon Nanomaterials as Potential Electrocatalysts. *Molecules*, 27(3), 670. <https://doi.org/10.3390/molecules27030670>
- Chen, Zhongming, Kim, D. Y., Hasegawa, K., Osawa, T., & Noda, S. (2014). Over 99.6 wt%-pure, sub-millimeter-long carbon nanotubes realized by fluidized-bed with careful control of the catalyst and carbon feeds. *Carbon*, 80, 339–350. <https://doi.org/10.1016/J.CARBON.2014.08.072>
- Chen, Zhongwei, Higgins, D., Yu, A., Zhang, L., & Zhang, J. (2011). A review on non-precious metal electrocatalysts for PEM fuel cells. *Energy & Environmental Science*, 4(9), 3167–3192. <https://doi.org/10.1039/C0EE00558D>
- Cheng, Wenjing, Sun, L., He, X., & Tian, L. (2022). Recent advances in fuel cell reaction electrocatalysis based on porous noble metal nanocatalysts. *Dalton Transactions*, 51(20), 7763–7774. <https://doi.org/10.1039/D2DT00841F>
- Cheng, Wenjun, Liu, X., Li, N., Han, J., Li, S., & Yu, S. (2018). Boron-doped graphene as a metal-free catalyst for gas-phase oxidation of benzyl alcohol to benzaldehyde. *RSC Advances*, 8(20), 11222–11229. <https://doi.org/10.1039/C8RA00290H>
- Cheng, X., Long, J., Wu, R., Huang, L., Tan, L., Chen, L., & Chen, Y. (2017). Fluorinated Reduced Graphene Oxide as an Efficient Hole-Transport Layer for Efficient and Stable Polymer Solar Cells. *ACS Omega*, 2(5), 2010–2016. <https://doi.org/10.1021/acsomega.7b00408>
- Cheng, Y., Tian, Y., Fan, X., Liu, J., & Yan, C. (2014). Boron Doped Multi-walled Carbon Nanotubes as Catalysts for Oxygen Reduction Reaction and Oxygen Evolution Reaction in Alkaline Media. *Electrochimica Acta*, 143, 291–296. <https://doi.org/10.1016/J.ELECTACTA.2014.08.001>
- Chokradjaroen, C., Kato, S., Fujiwara, K., Watanabe, H., Ishii, T., & Ishizaki, T. (2020). A comparative study of undoped, boron-doped, and boron/fluorine dual-doped carbon nanoparticles obtained via solution plasma as catalysts for the oxygen reduction reaction. *Sustainable Energy & Fuels*, 4(9), 4570–4580. <https://doi.org/10.1039/D0SE00708K>
- Chung, H. T., Cullen, D. A., Higgins, D., Sneed, B. T., Holby, E. F., More, K. L., & Zelenay, P. (2017). Direct atomic-level insight into the active sites of a high-performance PGM-free ORR catalyst. *Science*, 357(6350), 479–484. <https://doi.org/10.1126/science.aan2255>
- Contreras-Navarrete, J. J., Granados-Martínez, F. G., Domratheva-Lvova, L., Flores-Ramírez, N., Cisneros-Magaña, M. R., García-González, L., Zamora-Peredo, L., & Mondragón-Sánchez, M. L. (2015). MWCNTs oxidation by thermal treatment with air conditions. *Superficies y Vacío*, 28(4), 111–114.
- Cruz-Martínez, H., Tellez-Cruz, M. M., Guerrero-Gutiérrez, O. X., Ramírez-Herrera, C. A., Salinas-Juárez, M. G., Velázquez-Osorio, A., & Solorza-Feria, O. (2019). Mexican contributions for the improvement of electrocatalytic properties for the oxygen reduction reaction in PEM fuel cells. *International Journal of Hydrogen Energy*, 44(24), 12477–12491. <https://doi.org/10.1016/J.IJHYDENE.2018.05.168>
- Das, G., Choi, J.-H., Nguyen, P. K. T., Kim, D.-J., & Yoon, Y. S. (2022). Anion Exchange Membranes for Fuel Cell Application: A Review. *Polymers*, 14(6), 1197. <https://doi.org/10.3390/polym14061197>

- Debe, M. K. (2012). Electrocatalyst approaches and challenges for automotive fuel cells. *Nature* 2012 486:7401, 486(7401), 43–51. <https://doi.org/10.1038/nature11115>
- Delavar, M. A., & Wang, J. (2022). Charge and mass transport and modeling principles in proton-exchange membrane (PEM) fuel cells. I: *PEM Fuel Cells* (s. 173–197). Elsevier. <https://doi.org/10.1016/B978-0-12-823708-3.00010-9>
- Ding, L., Dai, X., Lin, R., Wang, H., & Qiao, J. (2012). Electrochemical Performance of Carbon-Supported Co-Phthalocyanine Modified with Co-Added Metals (M = Fe, Co, Ni, V) for Oxygen Reduction Reaction. *Journal of The Electrochemical Society*, 159(9), F577–F584. <https://doi.org/10.1149/2.058209JES/XML>
- Dong, G., Huang, M., & Guan, L. (2012). Iron phthalocyanine coated on single-walled carbon nanotubes composite for the oxygen reduction reaction in alkaline media. *Physical Chemistry Chemical Physics*, 14(8), 2557–2559. <https://doi.org/10.1039/C2CP23718K>
- Elbaz, L., Korin, E., Soifer, L., & Bettelheim, A. (2010). Evidence for the Formation of Cobalt Porphyrin–Quinone Complexes Stabilized at Carbon-Based Surfaces Toward the Design of Efficient Non-Noble-Metal Oxygen Reduction Catalysts. *The Journal of Physical Chemistry Letters*, 1(1), 398–401. <https://doi.org/10.1021/jz900310c>
- Erikson, H., Sarapuu, A., & Tammeveski, K. (2019). Oxygen Reduction Reaction on Silver Catalysts in Alkaline Media: a Minireview. *ChemElectroChem*, 6(1), 73–86. <https://doi.org/10.1002/celec.201800913>
- Ermoloeff, A., Chabli, A., Pierre, F., Rolland, G., Rouchon, D., Vannuffel, C., Vergnaud, C., Baylet, J., & Séméria, M. N. (2001). XPS, Raman spectroscopy, X-ray diffraction, specular X-ray reflectivity, transmission electron microscopy and elastic recoil detection analysis of emissive carbon film characterization. *Surface and Interface Analysis*, 31(3), 185–190. <https://doi.org/10.1002/SIA.955>
- Fazio, G., Ferrighi, L., & Di Valentin, C. (2014). Boron-doped graphene as active electrocatalyst for oxygen reduction reaction at a fuel-cell cathode. *Journal of Catalysis*, 318, 203–210. <https://doi.org/10.1016/j.jcat.2014.07.024>
- Ferrandon, M., Kropf, A. J., Myers, D. J., Artyushkova, K., Kramm, U., Bogdanoff, P., Wu, G., Johnston, C. M., & Zelenay, P. (2012). Multitechnique Characterization of a Polyaniline–Iron–Carbon Oxygen Reduction Catalyst. *The Journal of Physical Chemistry C*, 116(30), 16001–16013. <https://doi.org/10.1021/jp302396g>
- Ferrari, A., & Robertson, J. (2000). Interpretation of Raman spectra of disordered and amorphous carbon. *Physical Review B*, 61(20), 14095. <https://doi.org/10.1103/PhysRevB.61.14095>
- Fiechter, S., Berlin, H.-Z., Bogdanoff, P., Herrmann, I., Hilgendorff, M., Dorbandt, I., Fiechter, S., & Tributsch, H. (2004). Probing Structural Effects of Pyrolysed CoTMPP-based Electrocatalysts for Oxygen Reduction via New Preparation Strategies. *Journal of New Materials for Electrochemical Systems*, 7, 85–92. <https://www.researchgate.net/publication/40828629>
- Fierro, C. A., Mohan, M., & Scherson, D. A. (1990). in situ Moessbauer spectroscopy of a species irreversibly adsorbed on an electrode surface. *Langmuir*, 6(8), 1338–1342. <https://doi.org/10.1021/la00098a002>
- Fu, S., Zhu, C., Song, J., Engelhard, M. H., Xiao, B., Du, D., & Lin, Y. (2017). Nitrogen and Fluorine-Codoped Carbon Nanowire Aerogels as Metal-Free Electrocatalysts for Oxygen Reduction Reaction. *Chemistry – A European Journal*, 23(43), 10460–10464. <https://doi.org/10.1002/CHEM.201701969>

- Fukushima, T., Drisdell, W., Yano, J., & Surendranath, Y. (2015). Graphite-Conjugated Pyrazines as Molecularly Tunable Heterogeneous Electrocatalysts. *Journal of the American Chemical Society*, 137(34), 10926–10929. <https://doi.org/10.1021/jacs.5b06737>
- Ge, X., Sumboja, A., Wu, D., An, T., Li, B., Goh, F. W. T., Hor, T. S. A., Zong, Y., & Liu, Z. (2015). Oxygen Reduction in Alkaline Media: From Mechanisms to Recent Advances of Catalysts. *ACS Catalysis*, 5(8), 4643–4667. <https://doi.org/10.1021/acscatal.5b00524>
- Gewirth, A. A., Varnell, J. A., & DiAscro, A. M. (2018). Nonprecious Metal Catalysts for Oxygen Reduction in Heterogeneous Aqueous Systems. *Chemical Reviews*, 118(5), 2313–2339. <https://doi.org/10.1021/acs.chemrev.7b00335>
- Gokhale, R., Chen, Y., Serov, A., Artyushkova, K., & Atanassov, P. (2017). Novel dual templating approach for preparation of highly active Fe-N-C electrocatalyst for oxygen reduction. *Electrochimica Acta*, 224, 49–55. <https://doi.org/10.1016/j.electacta.2016.12.052>
- Goldie, S. J., Jiang, S., & Coleman, K. S. (2021). Cobalt nanoparticle catalysed graphitization and the effect of metal precursor decomposition temperature. *Materials Advances*, 2(10), 3353–3361. <https://doi.org/10.1039/D1MA00125F>
- Gomez-Bolivar, J., Mikheenko, I. P., Orozco, R. L., Sharma, S., Banerjee, D., Walker, M., Hand, R. A., Merroun, M. L., & Macaskie, L. E. (2019). Synthesis of Pd/Ru Bimetallic Nanoparticles by Escherichia coli and Potential as a Catalyst for Upgrading 5-Hydroxymethyl Furfural Into Liquid Fuel Precursors. *Frontiers in Microbiology*, 10, 1276. <https://doi.org/10.3389/fmicb.2019.01276>
- Gong, K., Du, F., Xia, Z., Durstock, M., & Dai, L. (2009). Nitrogen-Doped Carbon Nanotube Arrays with High Electrocatalytic Activity for Oxygen Reduction. *Science*, 323(5915), 760–764. <https://doi.org/10.1126/science.1168049>
- Gong, P., Wang, Z., Fan, Z., Hong, W., Yang, Z., Wang, J., & Yang, S. (2014). Synthesis of chemically controllable and electrically tunable graphene films by simultaneously fluorinating and reducing graphene oxide. *Carbon*, 72, 176–184. <https://doi.org/10.1016/j.carbon.2014.01.070>
- Gong, P., Wang, Z., Li, Z., Mi, Y., Sun, J., Niu, L., Wang, H., Wang, J., & Yang, S. (2013). Photochemical synthesis of fluorinated graphene via a simultaneous fluorination and reduction route. *RSC Advances*, 3(18), 6327–6330. <https://doi.org/10.1039/C3RA22029J>
- Gong, T., Qi, R., Liu, X., Li, H., & Zhang, Y. (2019). N, F-Codoped Microporous Carbon Nanofibers as Efficient Metal-Free Electrocatalysts for ORR. *Nano-Micro Letters*, 11(1), 1–11. <https://doi.org/10.1007/S40820-019-0240-X/FIGURES/6>
- Gottesfeld, S., Raistrick, I. D., & Srinivasan, S. (1987). Oxygen Reduction Kinetics on a Platinum RDE Coated with a Recast Nation Film. *J. Electrochem. Soc.*, 134(6), 1455–1462. <https://doi.org/https://doi.org/10.1149/1.2100689>
- Gregory Kleen, William Gibbons, & Julie Fornaciari. (2022). DOE Hydrogen Program Record: Heavy-Duty Fuel Cell System Cost – 2022. [https://www.hydrogen.energy.gov/pdfs/review22/fc339\\_weber\\_borup\\_2022\\_o.pdf](https://www.hydrogen.energy.gov/pdfs/review22/fc339_weber_borup_2022_o.pdf)
- Guo, D., Shibuya, R., Akiba, C., Saji, S., Kondo, T., & Nakamura, J. (2016). Active sites of nitrogen-doped carbon materials for oxygen reduction reaction clarified using model catalysts. *Science*, 351(6271), 361–365. <https://doi.org/10.1126/science.aad0832>

- Guo, F., Macdonald, T. J., Sobrido, A. J., Liu, L., Feng, J., & He, G. (2023). Recent Advances in Ultralow-Pt-Loading Electrocatalysts for the Efficient Hydrogen Evolution. *Advanced Science*, 10(21), 2301098. <https://doi.org/10.1002/adv.202301098>
- Guo, J., Zhang, J., Zhao, H., Fang, Y., Ming, K., Huang, H., Chen, J., & Wang, X. (2018). Fluorine-doped graphene with an outstanding electrocatalytic performance for efficient oxygen reduction reaction in alkaline solution. *Royal Society Open Science*, 5(10), 180925. <https://doi.org/10.1098/rsos.180925>
- Gupta, S., Tryk, D., Bae, I., Aldred, W., & Yeager, E. (1989). Heat-treated polyacrylonitrile-based catalysts for oxygen electroreduction. *Journal of Applied Electrochemistry*, 19(1), 19–27. <https://doi.org/10.1007/BF01039385/METRICS>
- Gutru, R., Turtayeva, Z., Xu, F., Maranzana, G., Thimmappa, R., Mamlouk, M., Desforges, A., & Vigolo, B. (2023). Recent progress in heteroatom doped carbon based electrocatalysts for oxygen reduction reaction in anion exchange membrane fuel cells. *International Journal of Hydrogen Energy*, 48(9), 3593–3631. <https://doi.org/10.1016/j.ijhydene.2022.10.177>
- Hansson, J., Nylander, A., Flygare, M., Svensson, K., Ye, L., Nilsson, T., Fu, Y., & Liu, J. (2020). Effects of high temperature treatment of carbon nanotube arrays on graphite: increased crystallinity, anchoring and inter-tube bonding. *Nanotechnology*, 31, 455708–455719. <https://doi.org/10.1088/1361-6528/ab9677>
- He, Y., & Wu, G. (2022). PGM-Free Oxygen-Reduction Catalyst Development for Proton-Exchange Membrane Fuel Cells: Challenges, Solutions, and Promises. *Accounts of Materials Research*, 3(2), 224–236. <https://doi.org/10.1021/accountsmr.1c00226>
- Herranz, J., Jaouen, F., Lefèvre, M., Kramm, U. I., Proietti, E., Dodelet, J.-P., Bogdanoff, P., Fiechter, S., Abs-Wurmbach, I., Bertrand, P., Arruda, T. M., & Mukerjee, S. (2011). Unveiling N-Protonation and Anion-Binding Effects on Fe/N/C Catalysts for O<sub>2</sub> Reduction in Proton-Exchange-Membrane Fuel Cells. *The Journal of Physical Chemistry C*, 115(32), 16087–16097. <https://doi.org/10.1021/jp2042526>
- Herranz, J., Lefèvre, M., Larouche, N., Stansfield, B., & Dodelet, J.-P. (2007). Step-by-Step Synthesis of Non-Noble Metal Electrocatalysts for O<sub>2</sub> Reduction under Proton Exchange Membrane Fuel Cell Conditions. *The Journal of Physical Chemistry C*, 111(51), 19033–19042. <https://doi.org/10.1021/jp0764438>
- Higgins, D., & Chen, Z. (2013). Recent Development of Non-precious Metal Catalysts. *Lecture Notes in Energy*, 9, 247–269. [https://doi.org/10.1007/978-1-4471-4911-8\\_9](https://doi.org/10.1007/978-1-4471-4911-8_9)
- Hiraike, Y., Saito, M., Niwa, H., Kobayashi, M., Harada, Y., Oshima, M., Kim, J., Nabae, Y., & Kakimoto, M. (2015). Active site formation mechanism of carbon-based oxygen reduction catalysts derived from a hyperbranched iron phthalocyanine polymer. *Nanoscale Research Letters*, 10(1), 179. <https://doi.org/10.1186/s11671-015-0881-8>
- Ho, K. I., Liao, J. H., Huang, C. H., Hsu, C. L., Zhang, W., Lu, A. Y., Li, L. J., Lai, C. S., & Su, C. Y. (2014). One-step formation of a single atomic-layer transistor by the selective fluorination of a graphene film. *Small*, 10(5), 989–997. <https://doi.org/10.1002/sml.201301366>
- Hu, X., Chen, S., Chen, L., Tian, Y., Yao, S., Lu, Z., Zhang, X., & Zhou, Z. (2022). What is the Real Origin of the Activity of Fe–N–C Electrocatalysts in the O<sub>2</sub> Reduction Reaction? Critical Roles of Coordinating Pyrrolic N and Axially Adsorbing Species. *Journal of the American Chemical Society*, 144(39), 18144–18152. <https://doi.org/10.1021/jacs.2c08743>
- Hummers, W. S., & Offeman, R. E. (1958). Preparation of Graphitic Oxide. *Journal of the American Chemical Society*, 80(6), 1339–1339. <https://doi.org/10.1021/ja01539a017>

- Hussain, S., Erikson, H., Kongi, N., Sarapuu, A., Solla-Gullón, J., Maia, G., Kannan, A. M., Alonso-Vante, N., & Tammeveski, K. (2020). Oxygen reduction reaction on nanostructured Pt-based electrocatalysts: A review. *International Journal of Hydrogen Energy*, 45(56), 31775–31797. <https://doi.org/10.1016/J.IJHYDENE.2020.08.215>
- Iijima, S. (1991). Helical microtubules of graphitic carbon. *Nature* 1991 354:6348, 354(6348), 56–58. <https://doi.org/10.1038/354056a0>
- Jahnke, H., Schönborn, M., & Zimmermann, G. (1976). Organic dyestuffs as catalysts for fuel cells. *Topics in current chemistry*, 61, 133–181. <https://doi.org/10.1007/BFB0046059/COVER>
- Jang, A. R., Lee, Y. W., Lee, S. S., Hong, J., Beak, S. H., Pak, S., Lee, J., Shin, H. S., Ahn, D., Hong, W. K., Cha, S., Sohn, J. I., & Park, I. K. (2018). Electrochemical and electrocatalytic reaction characteristics of boron-incorporated graphene via a simple spin-on dopant process. *Journal of Materials Chemistry A*, 6(17), 7351–7356. <https://doi.org/10.1039/C7TA09517A>
- Jannath, K. A., & Saputra, H. A. (2024). A Review on Recent Developments in Transition Metal and Heteroatom-Doped Carbon Catalysts for Oxygen Reduction Reaction. *Electrochemical Science Advances*, e202400033. <https://doi.org/10.1002/ELSA.202400033>
- Jaouen, F., Herranz, J., Lefèvre, M., Dodelet, J.-P., Kramm, U. I., Herrmann, I., Bogdanoff, P., Maruyama, J., Nagaoka, T., Garsuch, A., Dahn, J. R., Olson, T., Pylypenko, S., Atanassov, P., & Ustinov, E. A. (2009). Cross-Laboratory Experimental Study of Non-Noble-Metal Electrocatalysts for the Oxygen Reduction Reaction. *ACS Applied Materials & Interfaces*, 1(8), 1623–1639. <https://doi.org/10.1021/am900219g>
- Jaouen, F., Proietti, E., Lefèvre, M., Chenitz, R., Dodelet, J. P., Wu, G., Chung, H. T., Johnston, C. M., & Zelenay, P. (2010). Recent advances in non-precious metal catalysis for oxygen-reduction reaction in polymer electrolyte fuel cells. *Energy & Environmental Science*, 4(1), 114–130. <https://doi.org/10.1039/C0EE00011F>
- Jasinski, R. (1964). A New Fuel Cell Cathode Catalyst. *Nature* 1964 201:4925, 201(4925), 1212–1213. <https://doi.org/10.1038/2011212a0>
- Jennings, C. A., Aroca, R., Kovacs, G. J., & Hsiao, C. (1996). FT-Raman Spectroscopy of Thin Films of Titanyl Phthalocyanine and Vanadyl Phthalocyanine. *Journal of Raman Spectroscopy*, 27(12), 867–872. [https://doi.org/10.1002/\(SICI\)1097-4555\(199612\)27:12<867::AID-JRS43>3.0.CO;2-H](https://doi.org/10.1002/(SICI)1097-4555(199612)27:12<867::AID-JRS43>3.0.CO;2-H)
- Jeon, I. Y., Noh, H. J., & Baek, J. B. (2020). Nitrogen-Doped Carbon Nanomaterials: Synthesis, Characteristics and Applications. *Chemistry – An Asian Journal*, 15(15), 2282–2293. <https://doi.org/10.1002/ASIA.201901318>
- Ji, P., Gao, X., Du, X., Zheng, C., Luo, Z., & Cen, K. (2016). Relationship between the molecular structure of V2O5/TiO2 catalysts and the reactivity of SO2 oxidation. *Catalysis Science and Technology*, 6(4), 1187–1194. <https://doi.org/10.1039/c5cy00867k>
- Jia, Y., Zhang, L., Zhuang, L., Liu, H., Yan, X., Wang, X., Liu, J., Wang, J., Zheng, Y., Xiao, Z., Taran, E., Chen, J., Yang, D., Zhu, Z., Wang, S., Dai, L., & Yao, X. (2019). Identification of active sites for acidic oxygen reduction on carbon catalysts with and without nitrogen doping. *Nature Catalysis* 2019 2:8, 2(8), 688–695. <https://doi.org/10.1038/s41929-019-0297-4>



- Jiang, Z., Yu, J., Huang, T., & Sun, M. (2018). Recent Advance on Polyaniline or Polypyrrole-Derived Electrocatalysts for Oxygen Reduction Reaction. *Polymers*, 10(12), 1397. <https://doi.org/10.3390/polym10121397>
- Jo, G., & Shanmugam, S. (2012). Single-step synthetic approach for boron-doped carbons as a non-precious catalyst for oxygen reduction in alkaline medium. *Electrochemistry Communications*, 25(1), 101–104. <https://doi.org/10.1016/j.elecom.2012.09.025>
- Kakaei, K., & Balavandi, A. (2017). Hierarchically porous fluorine-doped graphene nanosheets as efficient metal-free electrocatalyst for oxygen reduction in gas diffusion electrode. *Journal of Colloid and Interface Science*, 490, 819–824. <https://doi.org/10.1016/J.JCIS.2016.12.011>
- Kasera, N., Kolar, P., & Hall, S. G. (2022). Nitrogen-doped biochars as adsorbents for mitigation of heavy metals and organics from water: a review. *Biochar* 2022 4:1, 4(1), 1–30. <https://doi.org/10.1007/S42773-022-00145-2>
- Kaur, P., Verma, G., & Sekhon, S. S. (2019). Biomass derived hierarchical porous carbon materials as oxygen reduction reaction electrocatalysts in fuel cells. *Progress in Materials Science*, 102, 1–71. <https://doi.org/10.1016/J.PMATSCI.2018.12.002>
- Kiani, M., Tian, X. Q., & Zhang, W. (2021). Single atom based electrocatalysts for oxygen reduction reaction in polymer electrolyte membrane fuel cell: Recent advances, challenges and future perspectives. *Journal of Physics and Chemistry of Solids*, 153, 109989. <https://doi.org/10.1016/j.jpcs.2021.109989>
- Kim, D. Y., Sugime, H., Hasegawa, K., Osawa, T., & Noda, S. (2011). Sub-millimeter-long carbon nanotubes repeatedly grown on and separated from ceramic beads in a single fluidized bed reactor. *Carbon*, 49(6), 1972–1979. <https://doi.org/10.1016/j.carbon.2011.01.022>
- Kim, J., Zhou, R., Murakoshi, K., & Yasuda, S. (2018). Advantage of semi-ionic bonding in fluorine-doped carbon materials for the oxygen evolution reaction in alkaline media. *RSC Advances*, 8(26), 14152–14156. <https://doi.org/10.1039/C8RA01636D>
- Klingele, M., Pham, C., Vuyyuru, K. R., Britton, B., Holdcroft, S., Fischer, A., & Thiele, S. (2017). Sulfur doped reduced graphene oxide as metal-free catalyst for the oxygen reduction reaction in anion and proton exchange fuel cells. *Electrochemistry Communications*, 77, 71–75. <https://doi.org/10.1016/J.ELECOM.2017.02.015>
- Kondo, T., Kodama, Y., Ikezoe, S., Yajima, K., Aikawa, T., & Yuasa, M. (2014). Porous boron-doped diamond electrodes fabricated via two-step thermal treatment. *Carbon*, 77, 783–789. <https://doi.org/10.1016/J.CARBON.2014.05.082>
- Kong, F., Cui, X., Huang, Y., Yao, H., Chen, Y., Tian, H., Meng, G., Chen, C., Chang, Z., & Shi, J. (2022). N-Doped Carbon Electrocatalyst: Marked ORR Activity in Acidic Media without the Contribution from Metal Sites? *Angewandte Chemie International Edition*, 61(15), e202116290. <https://doi.org/10.1002/anie.202116290>
- Kong, X., Zhu, Y., Lei, H., Wang, C., Zhao, Y., Huo, E., Lin, X., Zhang, Q., Qian, M., Mateo, W., Zou, R., Fang, Z., & Ruan, R. (2020). Synthesis of graphene-like carbon from biomass pyrolysis and its applications. *Chemical Engineering Journal*, 399, 125808. <https://doi.org/10.1016/J.CEJ.2020.125808>
- Kramm, U. I., Zana, A., Vosh, T., Fiechter, S., Arenz, M., & Schmeißer, D. (2016). On the structural composition and stability of Fe–N–C catalysts prepared by an intermediate acid leaching. *Journal of Solid State Electrochemistry*, 20(4), 969–981. <https://doi.org/10.1007/s10008-015-3060-z>

- Kruusenberg, I. (2013). *Electroreduction of oxygen on carbon nanomaterial-based catalysts*. University of Tartu Press. <https://www.digar.ee/arhiiv/nlib-digar:263173>
- Kruusenberg, I., Alexeyeva, N., & Tammeveski, K. (2009). The pH-dependence of oxygen reduction on multi-walled carbon nanotube modified glassy carbon electrodes. *Carbon*, 47(3), 651–658. <https://doi.org/10.1016/j.carbon.2008.10.032>
- Kruusenberg, I., Ramani, D., Ratso, S., Joost, U., Saar, R., Rauwel, P., Kannan, A. M., & Tammeveski, K. (2016). Cobalt–Nitrogen Co-doped Carbon Nanotube Cathode Catalyst for Alkaline Membrane Fuel Cells. *ChemElectroChem*, 3(9), 1455–1465. <https://doi.org/10.1002/celec.201600241>
- Kundu, S., Wang, Y., Xia, W., & Muhler, M. (2008). Thermal Stability and Reducibility of Oxygen-Containing Functional Groups on Multiwalled Carbon Nanotube Surfaces: A Quantitative High-Resolution XPS and TPD/TPR Study. *Journal of Physical Chemistry C*, 112(43), 16869–16878. <https://doi.org/10.1021/JP804413A>
- Ladouceur, M., Lalande, G., Guay, D., Dodelet, J. P., Dignard-Bailey, L., Trudeau, M. L., & Schulz, R. (1993). Pyrolyzed Cobalt Phthalocyanine as Electrocatalyst for Oxygen Reduction. *Journal of The Electrochemical Society*, 140(7), 1974–1981. <https://doi.org/10.1149/1.2220748/XML>
- Lalande, G., Côté, R., Guay, D., Dodelet, J. P., Weng, L. T., & Bertrand, P. (1997). Is nitrogen important in the formulation of Fe-based catalysts for oxygen reduction in solid polymer fuel cells? *Electrochimica Acta*, 42(9), 1379–1388. [https://doi.org/10.1016/S0013-4686\(96\)00361-1](https://doi.org/10.1016/S0013-4686(96)00361-1)
- Langley, L. A., Villanueva, D. E., & Fairbrother, D. H. (2006). Quantification of Surface Oxides on Carbonaceous Materials. *Chemistry of Materials*, 18(1), 169–178. <https://doi.org/10.1021/cm051462k>
- Lazar, P., Zbořil, R., Pumera, M., & Otyepka, M. (2014). Chemical nature of boron and nitrogen dopant atoms in graphene strongly influences its electronic properties. *Phys. Chem. Chem. Phys.*, 16(27), 14231–14235. <https://doi.org/10.1039/C4CP01638F>
- Lefèvre, M., Proietti, E., Jaouen, F., & Dodelet, J.-P. (2009). Iron-Based Catalysts with Improved Oxygen Reduction Activity in Polymer Electrolyte Fuel Cells. *Science*, 324(5923), 71–74. <https://doi.org/10.1126/science.1170051>
- Lehman, J. H., Terrones, M., Mansfield, E., Hurst, K. E., & Meunier, V. (2011). Evaluating the characteristics of multiwall carbon nanotubes. *Carbon*, 49(8), 2581–2602. <https://doi.org/10.1016/j.carbon.2011.03.028>
- Li, Jiang, Yin, D., & Qin, Y. (2023). Carbon materials: structures, properties, synthesis and applications. *Manufacturing Review*, 10, 13. <https://doi.org/10.1051/MFREVIEW/2023011>
- Li, Jiazhan, Chen, M., Cullen, D. A., Hwang, S., Wang, M., Li, B., Liu, K., Karakalos, S., Lucero, M., Zhang, H., Lei, C., Xu, H., Sterbinsky, G. E., Feng, Z., Su, D., More, K. L., Wang, G., Wang, Z., & Wu, G. (2018). Atomically dispersed manganese catalysts for oxygen reduction in proton-exchange membrane fuel cells. *Nature Catalysis*, 1(12), 935–945. <https://doi.org/10.1038/s41929-018-0164-8>
- Li, Jingkun, Jiao, L., Wegener, E., Richard, L. L., Liu, E., Zitolo, A., Sougrati, M. T., Mukerjee, S., Zhao, Z., Huang, Y., Yang, F., Zhong, S., Xu, H., Kropf, A. J., Jaouen, F., Myers, D. J., & Jia, Q. (2020). Evolution Pathway from Iron Compounds to Fe<sub>1</sub>(II)–N<sub>4</sub> Sites through Gas-Phase Iron during Pyrolysis. *Journal of the American Chemical Society*, 142(3), 1417–1423. <https://doi.org/10.1021/jacs.9b11197>



- Li, L., Ma, P., Hussain, S., Jia, L., Lin, D., Yin, X., Lin, Y., Cheng, Z., & Wang, L. (2019). FeS<sub>2</sub>/carbon hybrids on carbon cloth: a highly efficient and stable counter electrode for dye-sensitized solar cells. *Sustainable Energy & Fuels*, 3(7), 1749–1756. <https://doi.org/10.1039/C9SE00240E>
- Li, X., Liu, G., Zheng, H., Sun, K., Wan, L., Cao, J., Asif, S., Cao, Y., Si, W., Wang, F., & Bokhari, A. (2022). Recent Advances on Heteroatom-Doped Porous Carbon—Based Electrocatalysts for Oxygen Reduction Reaction. *Energies*, 16(1), 128. <https://doi.org/10.3390/en16010128>
- Li Zhu, A., Wang, H., Qu, W., Li, X., Jong, Z., & Li, H. (2010). Low temperature pyrolyzed cobalt tetramethoxy phenylporphyrin catalyst and its applications as an improved catalyst for metal air batteries. *Journal of Power Sources*, 195(17), 5587–5595. <https://doi.org/10.1016/J.JPOWSOUR.2010.03.015>
- Liang, Y., Li, Y., Wang, H., Zhou, J., Wang, J., Regier, T., & Dai, H. (2011). Co<sub>3</sub>O<sub>4</sub> nanocrystals on graphene as a synergistic catalyst for oxygen reduction reaction. *Nature Materials* 2011 10:10, 10(10), 780–786. <https://doi.org/10.1038/nmat3087>
- Liu, A., Li, W., Jin, H., Yu, X., Bu, Y., He, Y., Huang, H., Wang, S., & Wang, J. (2015). The enhanced electrocatalytic activity of graphene co-doped with chlorine and fluorine atoms. *Electrochimica Acta*, 177, 36–42. <https://doi.org/10.1016/J.ELECTACTA.2015.03.166>
- Liu, D., Tao, L., Yan, D., Zou, Y., & Wang, S. (2018). Recent Advances on Non-precious Metal Porous Carbon-based Electrocatalysts for Oxygen Reduction Reaction. *ChemElectroChem*, 5(14), 1775–1785. <https://doi.org/10.1002/celec.201800086>
- Liu, J., He, X., Guo, F., Liu, B., Sun, Z., Zhang, L., & Chang, H. (2022). Vanadium nitride nanoparticle decorated N-doped carbon nanotube/N-doped carbon nanosheet hybrids via a C<sub>3</sub>N<sub>4</sub> self-sacrificing method for electrochemical capacitors. *RSC Advances*, 12(24), 15354–15360. <https://doi.org/10.1039/D2RA02789E>
- Liu, L., & Corma, A. (2021). Identification of the active sites in supported subnanometric metal catalysts. *Nature Catalysis* 2021 4:6, 4(6), 453–456. <https://doi.org/10.1038/s41929-021-00632-y>
- Liu, S., Meyer, Q., Li, Y., Zhao, T., Su, Z., Ching, K., & Zhao, C. (2022). Fe–N–C/Fe nanoparticle composite catalysts for the oxygen reduction reaction in proton exchange membrane fuel cells. *Chemical Communications*, 58(14), 2323–2326. <https://doi.org/10.1039/D1CC07042H>
- Liu, Y., Fan, Y.-S., & Liu, Z.-M. (2019). Pyrolysis of iron phthalocyanine on activated carbon as highly efficient non-noble metal oxygen reduction catalyst in microbial fuel cells. *Chemical Engineering Journal*, 361, 416–427. <https://doi.org/10.1016/j.cej.2018.12.105>
- Liu, Y., Feng, Q., Xu, Q., Li, M., Tang, N., & Du, Y. (2013). Synthesis and photoluminescence of F and N co-doped reduced graphene oxide. *Carbon*, 61, 436–440. <https://doi.org/10.1016/J.CARBON.2013.05.027>
- Lu, H., & Kobayashi, N. (2016). Optically Active Porphyrin and Phthalocyanine Systems. *Chemical Reviews*, 116(10), 6184–6261. <https://doi.org/10.1021/acs.chemrev.5b00588>
- Luo, F., Roy, A., Silvioli, L., Cullen, D. A., Zitolo, A., Sougrati, M. T., Oguz, I. C., Mineva, T., Teschner, D., Wagner, S., Wen, J., Dionigi, F., Kramm, U. I., Rossmeisl, J., Jaouen, F., & Strasser, P. (2020). P-block single-metal-site tin/nitrogen-doped carbon fuel cell cathode catalyst for oxygen reduction reaction. *Nature Materials*, 19(11), 1215–1223. <https://doi.org/10.1038/s41563-020-0717-5>

- Ly, A., Asset, T., & Atanassov, P. (2020). Integrating nanostructured Pt-based electrocatalysts in proton exchange membrane fuel cells. *Journal of Power Sources*, 478, 228516. <https://doi.org/10.1016/J.JPOWSOUR.2020.228516>
- Ma, R., Lin, G., Zhou, Y., Liu, Q., Zhang, T., Shan, G., Yang, M., & Wang, J. (2019). A review of oxygen reduction mechanisms for metal-free carbon-based electrocatalysts. *npj Computational Materials*, 5(1), 78. <https://doi.org/10.1038/s41524-019-0210-3>
- Ma, Y., Lan, G., Fu, W., Lai, Y., Han, W., Tang, H., Liu, H., & Li, Y. (2020). Role of surface defects of carbon nanotubes on catalytic performance of barium promoted ruthenium catalyst for ammonia synthesis. *Journal of Energy Chemistry*, 41, 79–86. <https://doi.org/10.1016/j.jechem.2019.04.016>
- Madheswaran, D. K., Thangamuthu, M., Gnanasekaran, S., Gopi, S., Ayyasamy, T., & Pardeshi, S. S. (2023). Powering the Future: Progress and Hurdles in Developing Proton Exchange Membrane Fuel Cell Components to Achieve Department of Energy Goals—A Systematic Review. *Sustainability*, 15(22), 15923. <https://doi.org/10.3390/su152215923>
- Mamuru, S. A., & Ozoemena, K. I. (2010). Heterogeneous Electron Transfer and Oxygen Reduction Reaction at Nanostructured Iron(II) Phthalocyanine and Its MWCNTs Nanocomposites. *Electroanalysis*, 22(9), 985–994. <https://doi.org/10.1002/ELAN.200900438>
- Mannan, A., Hirano, Y., Quitain, A. T., Koinuma, M., & Kida, T. (2019). Graphene Oxide to B , N Co-doped Graphene through Tris-dimethylaminoborane Complex by Hydrothermal Implantation. *American Journal of Materials Science*, 9(1), 22–28. <https://doi.org/doi:10.5923/j.materials.20190901.04>
- Marshall-Roth, T., Libretto, N. J., Wrobel, A. T., Anderton, K. J., Pegis, M. L., Ricke, N. D., Voorhis, T. Van, Miller, J. T., & Surendranath, Y. (2020). A pyridinic Fe-N4 macrocycle models the active sites in Fe/N-doped carbon electrocatalysts. *Nature Communications*, 11(1), 1–14. <https://doi.org/10.1038/s41467-020-18969-6>
- Masheter, A. T., Xiao, L., Wildgoose, G. G., Crossley, A., Jones, J. H., & Compton, R. G. (2007). Voltammetric and X-ray photoelectron spectroscopic fingerprinting of carboxylic acid groups on the surface of carbon nanotubes via derivatisation with aryl nitro labels. *Journal of Materials Chemistry*, 17(33), 3515. <https://doi.org/10.1039/b705615j>
- Matter, P. H., Biddinger, E. J., & Ozkan, U. S. (2007). Non-precious metal oxygen reduction catalysts for PEM fuel cells. *Catalysis*, 338–366. <https://doi.org/10.1039/B602370N>
- Matter, P. H., Zhang, L., & Ozkan, U. S. (2006). The role of nanostructure in nitrogen-containing carbon catalysts for the oxygen reduction reaction. *Journal of Catalysis*, 239(1), 83–96. <https://doi.org/10.1016/j.jcat.2006.01.022>
- Mazzucato, M., Daniel, G., Perazzolo, V., Brandiele, R., Rizzi, G. A., Isse, A.A., Gennaro, A., & Durante, C. (2023). Mesoporosity and nitrogen doping: The leading effect in oxygen reduction reaction activity and selectivity at nitrogen-doped carbons prepared by using polyethylene oxide-block-polystyrene as a sacrificial template. *Electrochemical Science Advances*, 3(2), e2100203. <https://doi.org/10.1002/ELSA.202100203>
- Meng, H., Larouche, N., Lefvre, M., Jaouen, F., Stansfield, B., & Dodelet, J. P. (2010). Iron porphyrin-based cathode catalysts for polymer electrolyte membrane fuel cells: Effect of NH<sub>3</sub> and Ar mixtures as pyrolysis gases on catalytic activity and stability. *Electrochimica Acta*, 55(22), 6450–6461. <https://doi.org/10.1016/J.ELECTACTA.2010.06.039>

- Mineva, T., Matanovic, I., Atanassov, P., Sougrati, M.-T., Stievano, L., Clémancey, M., Kochem, A., Latour, J.-M., & Jaouen, F. (2019). Understanding Active Sites in Pyrolyzed Fe–N–C Catalysts for Fuel Cell Cathodes by Bridging Density Functional Theory Calculations and  $^{57}\text{Fe}$  Mössbauer Spectroscopy. *ACS Catalysis*, 9(10), 9359–9371. <https://doi.org/10.1021/acscatal.9b02586>
- Mjejri, I., Gaudon, M., Song, G., Labrugère, C., & Rougier, A. (2018). Crystallized  $\text{V}_2\text{O}_5$  as Oxidized Phase for Unexpected Multicolor Electrochromism in  $\text{V}_2\text{O}_3$  Thick Film. *ACS Applied Energy Materials*, 1(6), 2721–2729. <https://doi.org/10.1021/acsaem.8b00386>
- Mocchil, C., & Trasatti, S. (2003). Composite electrocatalysts for molecular  $\text{O}_2$  reduction in electrochemical power sources. *Journal of Molecular Catalysis A: Chemical*, 204–205, 713–720. [https://doi.org/10.1016/S1381-1169\(03\)00356-X](https://doi.org/10.1016/S1381-1169(03)00356-X)
- Monteverde Videla, A. H. A., Sebastián, D., Vasile, N. S., Osmieri, L., Aricò, A. S., Baglio, V., & Specchia, S. (2016). Performance analysis of Fe–N–C catalyst for DMFC cathodes: Effect of water saturation in the cathodic catalyst layer. *International Journal of Hydrogen Energy*, 41(47), 22605–22618. <https://doi.org/10.1016/J.IJHYDENE.2016.06.060>
- Müller-Hülstede, J., Uhlir, L. M., Schmies, H., Schonvogel, D., Meyer, Q., Nie, Y., Zhao, C., Vidakovic, J., & Wagner, P. (2023). Towards the Reduction of Pt Loading in High Temperature Proton Exchange Membrane Fuel Cells – Effect of Fe–N–C in Pt-Alloy Cathodes. *ChemSusChem*, 16(5), e202202046. <https://doi.org/10.1002/CSSC.202202046>
- Nabae, Y., Moriya, S., Matsubayashi, K., Lyth, S. M., Malon, M., Wu, L., Islam, N. M., Koshigoe, Y., Kuroki, S., Kakimoto, M., Miyata, S., & Ozaki, J. (2010). RETRACTED: The role of Fe species in the pyrolysis of Fe phthalocyanine and phenolic resin for preparation of carbon-based cathode catalysts. *Carbon*, 48(9), 2613–2624. <https://doi.org/10.1016/j.carbon.2010.03.066>
- Nagappan, S., Duraivel, M., Hira, S. A., Prabakar, K., Ha, C. S., Joo, S. H., Nam, K. M., & Park, K. H. (2022). Heteroatom-doped nanomaterials/core–shell nanostructure based electrocatalysts for the oxygen reduction reaction. *Journal of Materials Chemistry A*, 10(3), 987–1021. <https://doi.org/10.1039/D1TA09861F>
- Nail, J., Anderson, G., Ceasar, G., & Hansen, C. (2008). *The Evolution of the PEM Stationary Fuel Cell in the U. S. Innovation System*. [https://www.researchgate.net/publication/228544325\\_The\\_Evolution\\_of\\_the\\_PEM\\_Stationary\\_Fuel\\_Cell\\_in\\_the\\_US\\_Innovation\\_System](https://www.researchgate.net/publication/228544325_The_Evolution_of_the_PEM_Stationary_Fuel_Cell_in_the_US_Innovation_System)
- Nazir, H., Muthuswamy, N., Louis, C., Jose, S., Prakash, J., Buan, M. E. M., Flox, C., Chavan, S., Shi, X., Kauranen, P., Kallio, T., Maia, G., Tammeveski, K., Lymperopoulos, N., Carcadea, E., Veziroglu, E., Iranzo, A., & M. Kannan, A. (2020). Is the  $\text{H}_2$  economy realizable in the foreseeable future? Part III:  $\text{H}_2$  usage technologies, applications, and challenges and opportunities. *International Journal of Hydrogen Energy*, 45(53), 28217–28239. <https://doi.org/10.1016/J.IJHYDENE.2020.07.256>
- Ni, W., Xue, Y., Zang, X., Li, C., Wang, H., Yang, Z., & Yan, Y.-M. (2020). Fluorine Doped Cagelike Carbon Electrocatalyst: An Insight into the Structure-Enhanced  $\text{CO}$  Selectivity for  $\text{CO}_2$  Reduction at High Overpotential. *ACS Nano*, 14(2), 2014–2023. <https://doi.org/10.1021/acsnano.9b08528>

- NIST. (2021). *NIST Standard Reference Database, National Institute of Standards and Technology, Number 20, Gaithersburg MD, 20899*. NIST X-ray Photoelectron Spectroscopy Database. <https://doi.org/10.18434/T4T88K>
- Noori, M. T., Mukherjee, C. K., & Ghangrekar, M. M. (2017). Enhancing performance of microbial fuel cell by using graphene supported V<sub>2</sub>O<sub>5</sub>-nanorod catalytic cathode. *Electrochimica Acta*, 228, 513–521. <https://doi.org/10.1016/j.electacta.2017.01.016>
- Novoselov, K. S., Geim, A. K., Morozov, S. V., Jiang, D., Zhang, Y., Dubonos, S. V., Grigorieva, I. V., & Firsov, A. A. (2004). Electric Field Effect in Atomically Thin Carbon Films. *Science*, 306(5696), 666–669. <https://doi.org/10.1126/science.1102896>
- Nørskov, J. K., Rossmeisl, J., Logadottir, A., Lindqvist, L., Kitchin, J. R., Bligaard, T., & Jónsson, H. (2004). Origin of the Overpotential for Oxygen Reduction at a Fuel-Cell Cathode. *The Journal of Physical Chemistry B*, 108(46), 17886–17892. <https://doi.org/10.1021/jp047349j>
- Oh, H. S., & Kim, H. (2012). The role of transition metals in non-precious nitrogen-modified carbon-based electrocatalysts for oxygen reduction reaction. *Journal of Power Sources*, 212, 220–225. <https://doi.org/10.1016/j.jpowsour.2012.03.098>
- Okunola, A., Kowalewska, B., Bron, M., Kulesza, P. J., & Schuhmann, W. (2009). Electrocatalytic reduction of oxygen at electropolymerized films of metalloporphyrins deposited onto multi-walled carbon nanotubes. *Electrochimica Acta*, 54(7), 1954–1960. <https://doi.org/10.1016/J.ELECTACTA.2008.07.077>
- Ott, S., Du, F., Luna, M. L., Dao, T. A., Cuenya, B. R., Orfanidi, A., & Strasser, P. (2022). Understanding the Performance Increase of Catalysts Supported on N-Functionalized Carbon in PEMFC Catalyst Layers. *Journal of The Electrochemical Society*, 169(5), 054520. <https://doi.org/10.1149/1945-7111/AC6E4D>
- Pan, D., Ombaba, M., Zhou, Z.-Y., Liu, Y., Chen, S., & Lu, J. (2012). Direct Growth of Carbon Nanofibers to Generate a 3D Porous Platform on a Metal Contact to Enable an Oxygen Reduction Reaction. *ACS Nano*, 6(12), 10720–10726. <https://doi.org/10.1021/nn303910w>
- Panomsuban, G., Saito, N., & Ishizaki, T. (2015). Simple one-step synthesis of fluorine-doped carbon nanoparticles as potential alternative metal-free electrocatalysts for oxygen reduction reaction. *Journal of Materials Chemistry A*, 3(18), 9972–9981. <https://doi.org/10.1039/C5TA00244C>
- Parthiban, V., Bhuvaneshwari, B., Karthikeyan, J., Murugan, P., & Sahu, A. K. (2019). Fluorine-enriched mesoporous carbon as efficient oxygen reduction catalyst: understanding the defects in porous matrix and fuel cell applications. *Nanoscale Advances*, 1(12), 4926–4937. <https://doi.org/10.1039/C9NA00572B>
- Patowary, S., Chetry, R., Goswami, C., Chutia, B., & Bharali, P. (2022). Oxygen Reduction Reaction Catalysed by Supported Nanoparticles: Advancements and Challenges. *ChemCatChem*, 14(7), e202101472. <https://doi.org/10.1002/CCTC.202101472>
- Pavez, J., Páez, M., Ringuedé, A., Bedioui, F., & Zagal, J. H. (2005). Effect of film thickness on the electro-reduction of molecular oxygen on electropolymerized cobalt tetraaminophthalocyanine films. *Journal of Solid State Electrochemistry*, 9(1), 21–29. <https://doi.org/10.1007/S10008-004-0522-0/FIGURES/11>
- Pawbake, A. S., Mishra, K. K., Machuno, L. G. B., Gelamo, R. V., Ravindran, T. R., Rout, C. S., & Late, D. J. (2018). Temperature and pressure dependent Raman spectroscopy of plasma treated multilayer graphene nanosheets. *Diamond and Related Materials*, 84, 146–156. <https://doi.org/10.1016/J.DIAMOND.2018.03.021>

- Pederson, L. R. (1982). Two-dimensional chemical-state plot for lead using XPS. *Journal of Electron Spectroscopy and Related Phenomena*, 28(2), 203–209. [https://doi.org/10.1016/0368-2048\(82\)85043-3](https://doi.org/10.1016/0368-2048(82)85043-3)
- Peera, S. G., Menon, R. S., Das, S. K., Alfantazi, A., Karuppasamy, K., Liu, C., & Sahu, A. K. (2024). Oxygen reduction electrochemistry at F doped carbons: A review on the effect of highly polarized C-F bonding in catalysis and stability of fuel cell catalysts. *Coordination Chemistry Reviews*, 500, 215491. <https://doi.org/10.1016/J.CCR.2023.215491>
- Plug Power Inc. Financials - Annual Reports. (2021). <https://www.ir.plugpower.com/financials/annual-reports/default.aspx>
- Pollet, B. G., Kocha, S. S., & Staffell, I. (2019). Current status of automotive fuel cells for sustainable transport. *Current Opinion in Electrochemistry*, 16, 90–95. <https://doi.org/10.1016/J.COEEC.2019.04.021>
- Porstmann, S., Wannemacher, T., & Richter, T. (2019). Overcoming the Challenges for a Mass Manufacturing Machine for the Assembly of PEMFC Stacks. *Machines*, 7(4), 66. <https://doi.org/10.3390/machines7040066>
- Proietti, E., Jaouen, F., Lefèvre, M., Larouche, N., Tian, J., Herranz, J., & Dodelet, J.-P. (2011). Iron-based cathode catalyst with enhanced power density in polymer electrolyte membrane fuel cells. *Nature Communications*, 2(1), 416. <https://doi.org/10.1038/ncomms1427>
- Praats, R., Käärik, M., Kikas, A., Kisand, V., Aruväli, J., Paiste, P., Merisalu, M., Sarapuu, A., Leis, J., Sammelselg, V., Douglin, J. C., Dekel, D. R., & Tammeveski, K. (2021). Electroreduction of oxygen on cobalt phthalocyanine-modified carbide-derived carbon/carbon nanotube composite catalysts. *Journal of Solid State Electrochemistry*, 25(1), 57–71. <https://doi.org/10.1007/s10008-020-04543-z>
- Qasem, N. A. A., & Abdulrahman, G. A. Q. (2024). A Recent Comprehensive Review of Fuel Cells: History, Types, and Applications. *International Journal of Energy Research*, 2024(1), 7271748. <https://doi.org/10.1155/2024/7271748>
- Qian, L., Guo, F., Jia, X., Zhan, Y., Zhou, H., Jiang, X., & Tao, C. (2020). Recent development in the synthesis of agricultural and forestry biomass-derived porous carbons for supercapacitor applications: a review. *Ionics* 26:8, 26(8), 3705–3723. <https://doi.org/10.1007/S11581-020-03626-1>
- Quílez-Bermejo, J., Morallón, E., & Cazorla-Amorós, D. (2020). Metal-free heteroatom-doped carbon-based catalysts for ORR: A critical assessment about the role of heteroatoms. *Carbon*, 165, 434–454. <https://doi.org/10.1016/j.carbon.2020.04.068>
- Rabis, A., Rodriguez, P., & Schmidt, T. J. (2012). Electrocatalysis for Polymer Electrolyte Fuel Cells: Recent Achievements and Future Challenges. *ACS Catalysis*, 2(5), 864–890. <https://doi.org/10.1021/cs3000864>
- Ramasamy, P., Muruganatham, B., Rajasekaran, S., Babu, B. D., Ramkumar, R., Marthanda, A. V. A., & Mohan, S. (2024). A comprehensive review on different types of fuel cell and its applications. *Bulletin of Electrical Engineering and Informatics*, 13(2), 774–780. <https://doi.org/10.11591/EEI.V13I2.6348>
- Ramaswamy, N., & Mukerjee, S. (2011). Influence of Inner- and Outer-Sphere Electron Transfer Mechanisms during Electrocatalysis of Oxygen Reduction in Alkaline Media. *The Journal of Physical Chemistry C*, 115(36), 18015–18026. <https://doi.org/10.1021/jp204680p>

- Ramaswamy, N., & Mukerjee, S. (2012). Fundamental Mechanistic Understanding of Electrocatalysis of Oxygen Reduction on Pt and Non-Pt Surfaces: Acid versus Alkaline Media. *Advances in Physical Chemistry*, 2012, 1–17. <https://doi.org/10.1155/2012/491604>
- Ratso, S. (2020). *Electrocatalysis of oxygen reduction on non-precious metal catalysts*. University of Tartu Press. <http://hdl.handle.net/10062/70698>
- Ratso, S., Kruusenberg, I., Joost, U., Saar, R., & Tammeveski, K. (2016). Enhanced oxygen reduction reaction activity of nitrogen-doped graphene/multi-walled carbon nanotube catalysts in alkaline media. *International Journal of Hydrogen Energy*, 41(47), 22510–22519. <https://doi.org/10.1016/j.ijhydene.2016.02.021>
- Ratso, S., Kruusenberg, I., Sarapuu, A., Rauwel, P., Saar, R., Joost, U., Aruväli, J., Kanninen, P., Kallio, T., & Tammeveski, K. (2016). Enhanced oxygen reduction reaction activity of iron-containing nitrogen-doped carbon nanotubes for alkaline direct methanol fuel cell application. *Journal of Power Sources*, 332, 129–138. <https://doi.org/10.1016/j.jpowsour.2016.09.069>
- Raudsepp, R., Türk, K. K., Zarmehri, E., Joost, U., Rauwel, P., Saar, R., Mäeorg, U., Dyck, A., Bron, M., Chen, Z., Noda, S., Kruusenberg, I., & Tammeveski, K. (2024). Boron and Fluorine Co-Doped Graphene/Few-Walled Carbon Nanotube Composite as Highly Active Electrocatalyst for Oxygen Reduction Reaction. *ChemNanoMat*, 10(6), e202300546. <https://doi.org/10.1002/cnma.202300546>
- Rosas-Medellín, D., Rodríguez-Varela, F. J., & Escobar, B. (2022). Sulfur doped biocarbon obtained from Sargassum spp. for the oxygen reduction reaction. *International Journal of Hydrogen Energy*, 47(70), 30172–30177. <https://doi.org/10.1016/j.ijhydene.2022.05.166>
- Rukmani Krishnan, S., Verstraete, D., & Aguey-Zinsou, F. (2024). Performance of Non-Precious Metal Electrocatalysts in Proton-Exchange Membrane Fuel Cells: A Review. *ChemElectroChem*, 11(17). <https://doi.org/10.1002/celec.202400299>
- Sadhanala, H. K., & Nanda, K. K. (2016). Boron-doped carbon nanoparticles: Size-independent color tunability from red to blue and bioimaging applications. *Carbon*, 96, 166–173. <https://doi.org/10.1016/j.carbon.2015.08.096>
- Sajid, M. M., Shad, N. A., Javed, Y., Khan, S. B., Zhang, Z., Amin, N., & Zhai, H. (2020). Preparation and characterization of Vanadium pentoxide (V<sub>2</sub>O<sub>5</sub>) for photocatalytic degradation of monoazo and diazo dyes. *Surfaces and Interfaces*, 19, 100502. <https://doi.org/10.1016/J.SURFIN.2020.100502>
- Sakaushi, K., Lyalin, A., Tominaka, S., Taketsugu, T., & Uosaki, K. (2017). Two-Dimensional Corrugated Porous Carbon-, Nitrogen-Framework/Metal Heterojunction for Efficient Multielectron Transfer Processes with Controlled Kinetics. *ACS Nano*, 11(2), 1770–1779. <https://doi.org/10.1021/acs.nano.6b07711>
- Sankaran, M., & Viswanathan, B. (2007). Hydrogen storage in boron substituted carbon nanotubes. *Carbon*, 45(8), 1628–1635. <https://doi.org/10.1016/j.carbon.2007.04.011>
- Santoro, C., Arbizzani, C., Erable, B., & Ieropoulos, I. (2017). Microbial fuel cells: From fundamentals to applications. A review. *Journal of Power Sources*, 356, 225–244. <https://doi.org/10.1016/J.JPOWSOUR.2017.03.109>
- Schmidt, O., Hawkes, A., Gambhir, A., & Staffell, I. (2017). The future cost of electrical energy storage based on experience rates. *Nature Energy*, 2(8), 17110. <https://doi.org/10.1038/nenergy.2017.110>



- Schniepp, H. C., Li, J.-L., McAllister, M. J., Sai, H., Herrera-Alonso, M., Adamson, D. H., Prud'homme, R. K., Car, R., Saville, D. A., & Aksay, I. A. (2006). Functionalized Single Graphene Sheets Derived from Splitting Graphite Oxide. *The Journal of Physical Chemistry B*, 110(17), 8535–8539. <https://doi.org/10.1021/jp060936f>
- Sekhon, S. S., & Park, J. S. (2021). Biomass-derived N-doped porous carbon nanosheets for energy technologies. *Chemical Engineering Journal*, 425, 129017. <https://doi.org/10.1016/J.CEJ.2021.129017>
- Seredych, M., László, K., & Bandosz, T. J. (2015). Sulfur-Doped Carbon Aerogel as a Metal-Free Oxygen Reduction Catalyst. *ChemCatChem*, 7(18), 2924–2931. <https://doi.org/10.1002/CCTC.201500192>
- Serov, A., Artyushkova, K., Niangar, E., Wang, C., Dale, N., Jaouen, F., Sougrati, M. T., Jia, Q., Mukerjee, S., & Atanassov, P. (2015). Nano-structured non-platinum catalysts for automotive fuel cell application. *Nano Energy*, 16, 293–300. <https://doi.org/10.1016/J.NANOEN.2015.07.002>
- Sevilla, M., Sanchis, C., Valdés-Soh, T., Morallón, E., & Fuertes, A. B. (2007). Synthesis of graphitic carbon nanostructures from sawdust and their application as electrocatalyst supports. *Journal of Physical Chemistry C*, 111(27), 9749–9756. <https://doi.org/10.1021/jp072246x>
- Shakil, Md. R., El-Sawy, A. M., Tasnim, H., Meguerdichian, A. G., Jin, J., Dubrosky, J. P., & Suib, S. L. (2018). Single-Doped and Multidoped Transition-Metal (Mn, Fe, Co, and Ni) ZnO and Their Electrocatalytic Activities for Oxygen Reduction Reaction. *Inorganic Chemistry*, 57(16), 9977–9987. <https://doi.org/10.1021/acs.inorgchem.8b01153>
- Shao, M., Chang, Q., Dodelet, J.-P., & Chenitz, R. (2016). Recent Advances in Electrocatalysts for Oxygen Reduction Reaction. *Chemical Reviews*, 116(6), 3594–3657. <https://doi.org/10.1021/acs.chemrev.5b00462>
- Sheng, Z. H., Gao, H. L., Bao, W. J., Wang, F. Bin, & Xia, X. H. (2011). Synthesis of boron doped graphene for oxygen reduction reaction in fuel cells. *Journal of Materials Chemistry*, 22(2), 390–395. <https://doi.org/10.1039/C1JM14694G>
- Shui, J., Chen, C., Grabstanowicz, L., Zhao, D., & Liu, D.-J. (2015). Highly efficient nonprecious metal catalyst prepared with metal–organic framework in a continuous carbon nanofibrous network. *Proceedings of the National Academy of Sciences*, 112(34), 10629–10634. <https://doi.org/10.1073/pnas.1507159112>
- Shui, J., Wang, M., Du, F., & Dai, L. (2015). N-doped carbon nanomaterials are durable catalysts for oxygen reduction reaction in acidic fuel cells. *Science Advances*, 1(1). <https://doi.org/10.1126/sciadv.1400129>
- Sim, Y., Surendran, S., Cha, H., Choi, H., Je, M., Yoo, S., Chan Seok, D., Ho Jung, Y., Jeon, C., Jin Kim, D., Han, M.-K., Choi, H., Sim, U., & Moon, J. (2022). Fluorine-doped graphene oxide prepared by direct plasma treatment for supercapacitor application. *Chemical Engineering Journal*, 428, 132086. <https://doi.org/10.1016/j.cej.2021.132086>
- Simas, P. S., Antonin, V. S., Parreira, L. S., Hammer, P., Silva, F. L., Kronka, M. S., Valim, R. B., Lanza, M. R. V., & Santos, M. C. (2017). Carbon Modified with Vanadium Nanoparticles for Hydrogen Peroxide Electrogenation. *Electrocatalysis* 2017 8:4, 8(4), 311–320. <https://doi.org/10.1007/S12678-017-0366-X>
- Song, C., & Zhang, J. (2008). Electrocatalytic Oxygen Reduction Reaction. *PEM Fuel Cell Electrocatalysts and Catalyst Layers: Fundamentals and Applications*, 89–134. [https://doi.org/10.1007/978-1-84800-936-3\\_2](https://doi.org/10.1007/978-1-84800-936-3_2)

- Sorokin, A. B. (2013). Phthalocyanine Metal Complexes in Catalysis. *Chemical Reviews*, 113(10), 8152–8191. <https://doi.org/10.1021/cr4000072>
- Sreekanth, N., Nazrulla, M. A., Vineesh, T. V., Sailaja, K., & Phani, K. L. (2015). Metal-free boron-doped graphene for selective electroreduction of carbon dioxide to formic acid/formate. *Chemical Communications*, 51(89), 16061–16064. <https://doi.org/10.1039/C5CC06051F>
- Staffell, I., Scamman, D., Abad, A. V., Balcombe, P., Dodds, P. E., Ekins, P., Shah, N., & Ward, K. R. (2019). The role of hydrogen and fuel cells in the global energy system. *Energy Environ. Sci*, 12, 463. <https://doi.org/10.1039/c8ee01157e>
- Stein, T., & Ein-Eli, Y. (2020). Challenges and Perspectives of Metal-Based Proton Exchange Membrane's Bipolar Plates: Exploring Durability and Longevity. *Energy Technology*, 8(6), 2000007. <https://doi.org/10.1002/ENTE.202000007>
- Strickland, K., Miner, E., Jia, Q., Tylus, U., Ramaswamy, N., Liang, W., Sougrati, M. T., Jaouen, F., & Mukerjee, S. (2015). Highly active oxygen reduction non-platinum group metal electrocatalyst without direct metal–nitrogen coordination. *Nature Communications* 2015 6:1, 6(1), 1–8. <https://doi.org/10.1038/ncomms8343>
- Sun, L., Wang, L., Tian, C., Tan, T., Xie, Y., Shi, K., Li, M., & Fu, H. (2012). Nitrogen-doped graphene with high nitrogen level via a one-step hydrothermal reaction of graphene oxide with urea for superior capacitive energy storage. *RSC Advances*, 2(10), 4498–4506. <https://doi.org/10.1039/C2RA01367C>
- Sun, X., Song, P., Zhang, Y., Liu, C., Xu, W., & Xing, W. (2013). A Class of High Performance Metal-Free Oxygen Reduction Electrocatalysts based on Cheap Carbon Blacks. *Scientific Reports*, 3(1), 2505. <https://doi.org/10.1038/srep02505>
- Sun, X., Zhang, Y., Song, P., Pan, J., Zhuang, L., Xu, W., & Xing, W. (2013). Fluorine-Doped Carbon Blacks: Highly Efficient Metal-Free Electrocatalysts for Oxygen Reduction Reaction. *ACS Catalysis*, 3(8), 1726–1729. <https://doi.org/10.1021/cs400374k>
- Surnev, S., Ramsey, M. G., & Netzer, F. P. (2003). Vanadium oxide surface studies. *Progress in Surface Science*, 73(4–8), 117–165. <https://doi.org/10.1016/J.PROGSURF.2003.09.001>
- Sysoev, V. I., Bulavskiy, M. O., Pinakov, D. V., Chekhova, G. N., Asanov, I. P., Gevko, P. N., Bulusheva, L. G., & Okotrub, A. V. (2020). Chemiresistive Properties of Imprinted Fluorinated Graphene Films. *Materials*, 13(16), 3538. <https://doi.org/10.3390/ma13163538>
- Tammeveski, K., & Zagal, J. H. (2018). Electrocatalytic oxygen reduction on transition metal macrocyclic complexes for anion exchange membrane fuel cell application. *Current Opinion in Electrochemistry*, 9, 207–213. <https://doi.org/10.1016/j.coelec.2018.04.001>
- Tanaka, A. A., Fierro, C., Scherson, D., & Yeager, E. B. (1987). Electrocatalytic aspects of iron phthalocyanine and its .mu.-oxo derivatives dispersed on high surface area carbon. *The Journal of Physical Chemistry*, 91(14), 3799–3807. <https://doi.org/10.1021/j100298a016>
- Tang, C., Bando, Y., Huang, Y., Yue, S., Gu, C., Xu, F., & Golberg, D. (2005). Fluorination and Electrical Conductivity of BN Nanotubes. *Journal of the American Chemical Society*, 127(18), 6552–6553. <https://doi.org/10.1021/ja042388u>
- Tang, T., Ding, L., Jiang, Z., Hu, J.-S., & Wan, L.-J. (2020). Advanced transition metal/nitrogen/carbon-based electrocatalysts for fuel cell applications. *Science China Chemistry*, 63(11), 1517–1542. <https://doi.org/10.1007/s11426-020-9835-8>



- Tao, L., Qiao, M., Jin, R., Li, Y., Xiao, Z., Wang, Y., Zhang, N., Xie, C., He, Q., Jiang, D., Yu, G., Li, Y., & Wang, S. (2019). Bridging the Surface Charge and Catalytic Activity of a Defective Carbon Electrocatalyst. *Angewandte Chemie - International Edition*, 58(4), 1019–1024. <https://doi.org/10.1002/anie.201810207>
- Thompson, S. T., & Papageorgopoulos, D. (2019). Platinum group metal-free catalysts boost cost competitiveness of fuel cell vehicles. *Nature Catalysis*, 2(7), 558–561. <https://doi.org/10.1038/s41929-019-0291-x>
- Tian, L., Min, S., & Wang, F. (2019). Integrating noble-metal-free metallic vanadium carbide cocatalyst with CdS for efficient visible-light-driven photocatalytic H<sub>2</sub> evolution. *Applied Catalysis B: Environmental*, 259, 118029. <https://doi.org/10.1016/j.apcatb.2019.118029>
- Trusovas, R., Račiukaitis, G., Niaura, G., Barkauskas, J., Valušis, G., & Pauliukaite, R. (2016). Recent Advances in Laser Utilization in the Chemical Modification of Graphene Oxide and Its Applications. *Advanced Optical Materials*, 4(1), 37–65. <https://doi.org/10.1002/ADOM.201500469>
- Türk, Karl Kalev, Kruusenberg, I., Mondal, J., Rauwel, P., Kozlova, J., Matisen, L., Sammelselg, V., & Tammeveski, K. (2015). Oxygen electroreduction on MN4-macrocycle modified graphene/multi-walled carbon nanotube composites. *Journal of Electroanalytical Chemistry*, 756, 69–76. <https://doi.org/10.1016/j.jelechem.2015.08.014>
- Türk, K.K., Kruusenberg, I., Kibena-Pöldsepp, E., Bhowmick, G. D., Kook, M., Tammeveski, K., Matisen, L., Merisalu, M., Sammelselg, V., Ghangrekar, M. M., Mitra, A., & Banerjee, R. (2018). Novel multi walled carbon nanotube based nitrogen impregnated Co and Fe cathode catalysts for improved microbial fuel cell performance. *International Journal of Hydrogen Energy*, 43(51), 23027–23035. <https://doi.org/10.1016/j.ijhydene.2018.10.143>
- van Veen, J. A. R., & Colijn, H. A. (1981). Oxygen Reduction on Transition-Metal Porphyrins in Acid Electrolyte II. Stability. *Berichte der Bunsengesellschaft für physikalische Chemie*, 85(9), 700–704. <https://doi.org/10.1002/BBPC.19810850918>
- van Veen, J. A. R., van Baar, J. F., Kroese, C. J., Coolegem, J. G. F., de Wit, N., & Colijn, H. A. (1981). Oxygen Reduction on Transition-Metal Porphyrins in Acid Electrolyte I. Activity. *Berichte der Bunsengesellschaft für physikalische Chemie*, 85(9), 693–700. <https://doi.org/10.1002/BBPC.19810850917>
- Venkateswara Rao, C., & Ishikawa, Y. (2012). Activity, Selectivity, and Anion-Exchange Membrane Fuel Cell Performance of Virtually Metal-Free Nitrogen-Doped Carbon Nanotube Electrodes for Oxygen Reduction Reaction. *Journal of Physical Chemistry C*, 116(6), 4340–4346. <https://doi.org/10.1021/JP210840A>
- Vesborg, P. C. K., & Jaramillo, T. F. (2012). Addressing the terawatt challenge: scalability in the supply of chemical elements for renewable energy. *RSC Advances*, 2(21), 7933–7947. <https://doi.org/10.1039/C2RA20839C>
- Vijayakumar, P., Govindaraj, R., Santhosh, N., Pandian, M. S., Pandikumar, A., & Ramasamy, P. (2018). Investigation of suitable binder combination and electrochemical charge transfer dynamics of vanadium carbide nanoparticles-based counter electrode in Pt-free dye-sensitized solar cell. *Journal of Materials Science*, 53(6), 4444–4455. <https://doi.org/10.1007/s10853-017-1843-6>

- Vikkisk, M., Kruusenberg, I., Joost, U., Shulga, E., & Tammeveski, K. (2013). Electrocatalysis of oxygen reduction on nitrogen-containing multi-walled carbon nanotube modified glassy carbon electrodes. *Electrochimica Acta*, 87, 709–716. <https://doi.org/10.1016/J.ELECTACTA.2012.09.071>
- Vikkisk, M., Kruusenberg, I., Ratso, S., Joost, U., Shulga, E., Kink, I., Rauwel, P., & Tammeveski, K. (2015). Enhanced electrocatalytic activity of nitrogen-doped multi-walled carbon nanotubes towards the oxygen reduction reaction in alkaline media. *RSC Advances*, 5(73), 59495–59505. <https://doi.org/10.1039/C5RA08818F>
- Wang, B., Liu, B., & Dai, L. (2021). Non-N-Doped Carbons as Metal-Free Electrocatalysts. *Advanced Sustainable Systems*, 5(1), 2000134. <https://doi.org/10.1002/ADSU.202000134>
- Wang, Dan, Pan, X., Yang, P., Li, R., Xu, H., Li, Y., Meng, F., Zhang, J., & An, M. (2021). Transition Metal and Nitrogen Co-Doped Carbon-based Electrocatalysts for the Oxygen Reduction Reaction: From Active Site Insights to the Rational Design of Precursors and Structures. *ChemSusChem*, 14(1), 33–55. <https://doi.org/10.1002/CSSC.202002137>
- Wang, Dongliang, Hu, J., Wei, J., Liu, X., & Hou, H. (2023). Insights into Nitrogen-doped Carbon for Oxygen Reduction: The Role of Graphitic and Pyridinic Nitrogen Species. *ChemPhysChem*, 24(10), e202200734. <https://doi.org/10.1002/CPHC.202200734>
- Wang, H., Sun, J., Wang, J., Jiang, L., & Liu, H. (2021). Green synthesis of nitrogen and fluorine co-doped porous carbons from sustainable coconut shells as an advanced synergistic electrocatalyst for oxygen reduction. *Journal of Materials Research and Technology*, 13, 962–970. <https://doi.org/10.1016/J.JMRT.2021.05.048>
- Wang, J., Kim, J., Choi, S., Wang, H., & Lim, J. (2020). A Review of Carbon-Supported Nonprecious Metals as Energy-Related Electrocatalysts. *Small Methods*, 4(10), 2000621. <https://doi.org/10.1002/SMTD.202000621>
- Wang, W., Jia, Q., Mukerjee, S., & Chen, S. (2019). Recent Insights into the Oxygen-Reduction Electrocatalysis of Fe/N/C Materials. *ACS Catalysis*, 9(11), 10126–10141. <https://doi.org/10.1021/acscatal.9b02583>
- Wang, Xiaojuan, Zou, L., Fu, H., Xiong, Y., Tao, Z., Zheng, J., & Li, X. (2016). Noble Metal-Free Oxygen Reduction Reaction Catalysts Derived from Prussian Blue Nanocrystals Dispersed in Polyaniline. *ACS Applied Materials & Interfaces*, 8(13), 8436–8444. <https://doi.org/10.1021/acsami.5b12102>
- Wang, Xiqing, Du, P., Cheng, K., Hua, X., Xie, M., Li, Y., Zheng, Y., Wang, Y., Pi, C., & Zhang, S. (2025). Structural Regulation of Advanced Platinum-Based Core-Shell Catalysts for Fuel Cell Electrocatalysis. *Minerals* 2025, Vol. 15, Page 235, 15(3), 235. <https://doi.org/10.3390/MIN15030235>
- Wang, Y., Yuan, H., Martinez, A., Hong, P., Xu, H., & Bockmiller, F. R. (2021). Polymer electrolyte membrane fuel cell and hydrogen station networks for automobiles: Status, technology, and perspectives. *Advances in Applied Energy*, 2, 100011. <https://doi.org/10.1016/J.ADAPEN.2021.100011>
- Wei, K., Wang, X., & Ge, J. (2023). PGM-free carbon-based catalysts for the electrocatalytic oxygen reduction reaction: active sites and activity enhancement. *Energy Materials*, 3(6), 1–30. <https://doi.org/10.20517/energymater.2023.52>
- Wiesener, K. (1986). N4-chelates as electrocatalyst for cathodic oxygen reduction. *Electrochimica Acta*, 31(8), 1073–1078. [https://doi.org/10.1016/0013-4686\(86\)80022-6](https://doi.org/10.1016/0013-4686(86)80022-6)

- Woo, J., Lim, J. S., Kim, J. H., & Joo, S. H. (2021). Heteroatom-doped carbon-based oxygen reduction electrocatalysts with tailored four-electron and two-electron selectivity. *Chemical Communications*, 57(60), 7350–7361. <https://doi.org/10.1039/D1CC02667D>
- Wu, B., Meng, H., Morales, D. M., Zeng, F., Zhu, J., Wang, B., Risch, M., Xu, Z. J., & Petit, T. (2022). Nitrogen-Rich Carbonaceous Materials for Advanced Oxygen Electrocatalysis: Synthesis, Characterization, and Activity of Nitrogen Sites. *Advanced Functional Materials*, 32(31), 2204137. <https://doi.org/10.1002/ADFM.202204137>
- Wu, G., More, K. L., Johnston, C. M., & Zelenay, P. (2011). High-Performance Electrocatalysts for Oxygen Reduction Derived from Polyaniline, Iron, and Cobalt. *Science*, 332(6028), 443–447. <https://doi.org/10.1126/science.1200832>
- Wu, H., Zhang, Z., Qin, M., Wang, Q., Cao, Z., Yu, Y., Jia, B., & Qu, X. (2020). Solution combustion synthesis of crystalline V<sub>2</sub>O<sub>3</sub> and amorphous V<sub>2</sub>O<sub>3</sub>/C as anode for lithium-ion battery. *Journal of the American Ceramic Society*, 103(4), 2643–2652. <https://doi.org/10.1111/JACE.16962>
- Wu, J., Yang, Z., Li, X., Sun, Q., Jin, C., Strasser, P., & Yang, R. (2013). Phosphorus-doped porous carbons as efficient electrocatalysts for oxygen reduction. *Journal of Materials Chemistry A*, 1(34), 9889–9896. <https://doi.org/10.1039/C3TA11849E>
- Xia, W., Hunter, M. A., Wang, J., Zhu, G., Warren, S. J., Zhao, Y., Bando, Y., Searles, D. J., Yamauchi, Y., & Tang, J. (2020). Highly ordered macroporous dual-element-doped carbon from metal–organic frameworks for catalyzing oxygen reduction. *Chemical Science*, 11(35), 9584–9592. <https://doi.org/10.1039/D0SC02518F>
- Xiao, B., Boudou, J. P., & Thomas, K. M. (2005). Reactions of Nitrogen and Oxygen Surface Groups in Nanoporous Carbons under Inert and Reducing Atmospheres. *Langmuir*, 21(8), 3400–3409. <https://doi.org/10.1021/la0472495>
- Xing, G., Zhang, G., Wang, B., Tong, M., Tian, C., Wang, L., & Fu, H. (2023). Strengthening oxygen reduction activity based on the cooperation of pyridinic-N and graphitic-N for atomically dispersed Fe sites. *Journal of Materials Chemistry A*, 11(17), 9493–9503. <https://doi.org/10.1039/D3TA00899A>
- Xing, T., Zheng, Y., Li, L. H., Cowie, B. C. C., Gunzelmann, D., Qiao, S. Z., Huang, S., & Chen, Y. (2014). Observation of Active Sites for Oxygen Reduction Reaction on Nitrogen-Doped Multilayer Graphene. *ACS Nano*, 8(7), 6856–6862. <https://doi.org/10.1021/nn501506p>
- Xu, H., Zhang, S., & Zhang, H. (2024). Recent Progress in Atomically Dispersed Non-noble Metal Catalysts for Electrochemical Two-electron Oxygen Reduction Reaction. *ChemElectroChem*, 11(8), e202300630. <https://doi.org/10.1002/CELC.202300630>
- Xu, X., Yuan, T., Zhou, Y., Li, Y., Lu, J., Tian, X., Wang, D., & Wang, J. (2014). Facile synthesis of boron and nitrogen-doped graphene as efficient electrocatalyst for the oxygen reduction reaction in alkaline media. *International Journal of Hydrogen Energy*, 39(28), 16043–16052. <https://doi.org/10.1016/j.ijhydene.2013.12.079>
- Xu, Z., Li, H., Cao, G., Zhang, Q., Li, K., & Zhao, X. (2011). Electrochemical performance of carbon nanotube-supported cobalt phthalocyanine and its nitrogen-rich derivatives for oxygen reduction. *Journal of Molecular Catalysis A: Chemical*, 335(1–2), 89–96. <https://doi.org/10.1016/j.molcata.2010.11.018>
- Xu, Z., Li, H., Fu, M., Luo, H., Sun, H., Zhang, L., Li, K., Wei, B., Lu, J., & Zhao, X. (2012). Nitrogen-doped carbon nanotubes synthesized by pyrolysis of nitrogen-rich metal phthalocyanine derivatives for oxygen reduction. *Journal of Materials Chemistry*, 22(35), 18230–18236. <https://doi.org/10.1039/C2JM33568A>

- Xue, Y., Liu, Q., He, G., Xu, K., Jiang, L., Hu, X., & Hu, J. (2013). Excellent electrical conductivity of the exfoliated and fluorinated hexagonal boron nitride nanosheets. *Nanoscale Research Letters*, 8(1), 49. <https://doi.org/10.1186/1556-276X-8-49>
- Yamazaki, S. I., Yamada, Y., Ioroi, T., Fujiwara, N., Siroma, Z., Yasuda, K., & Miyazaki, Y. (2005). Estimation of specific interaction between several Co porphyrins and carbon black: its influence on the electrocatalytic O<sub>2</sub> reduction by the porphyrins. *Journal of Electroanalytical Chemistry*, 576(2), 253–259. <https://doi.org/10.1016/J.JELECHEM.2004.10.022>
- Yang, L., Jiang, S., Zhao, Y., Zhu, L., Chen, S., Wang, X., Wu, Q., Ma, J., Ma, Y., & Hu, Z. (2011). Boron-Doped Carbon Nanotubes as Metal-Free Electrocatalysts for the Oxygen Reduction Reaction. *Angewandte Chemie International Edition*, 50(31), 7132–7135. <https://doi.org/10.1002/anie.201101287>
- Yang, Shaoxuan, Yu, Y., Gao, X., Zhang, Z., & Wang, F. (2021). Recent advances in electrocatalysis with phthalocyanines. *Chemical Society Reviews*, 50(23), 12985–13011. <https://doi.org/10.1039/D0CS01605E>
- Yang, Shuxiu, Shu, Q., Fu, B., Liu, S., Zhang, Y., & Zhao, H. (2024). Synthesis of high-performance low-Pt (1 1 1)-loading catalysts for ORR by interaction between solution and nonthermal plasma. *Chemical Engineering Journal*, 488, 150905. <https://doi.org/10.1016/J.CEJ.2024.150905>
- Yang, Z., Yao, Z., Li, G., Fang, G., Nie, H., Liu, Z., Zhou, X., Chen, X., & Huang, S. (2012). Sulfur-Doped Graphene as an Efficient Metal-free Cathode Catalyst for Oxygen Reduction. *ACS Nano*, 6(1), 205–211. <https://doi.org/10.1021/nn203393d>
- Ye, C., Zhang, L., & Shen, Y. (2024). Activity Origin and Catalytic Mechanism of the M–N–C Catalysts for the Oxygen Reduction Reaction. *ACS Materials Letters*, 6(7), 2858–2887. <https://doi.org/10.1021/acsmaterialslett.4c00415>
- Yeager, E. (1984). Electrocatalysts for O<sub>2</sub> reduction. *Electrochimica Acta*, 29(11), 1527–1537. [https://doi.org/10.1016/0013-4686\(84\)85006-9](https://doi.org/10.1016/0013-4686(84)85006-9)
- Yeom, D.-Y., Jeon, W., Tu, N. D. K., Yeo, S. Y., Lee, S.-S., Sung, B. J., Chang, H., Lim, J. A., & Kim, H. (2015). High-concentration boron doping of graphene nanoplatelets by simple thermal annealing and their supercapacitive properties. *Scientific Reports*, 5(1), 9817. <https://doi.org/10.1038/srep09817>
- Yu, A., Liu, S., & Yang, Y. (2024). Recent advances in electrosynthesis of H<sub>2</sub>O<sub>2</sub> via two-electron oxygen reduction reaction. *Chemical Communications*, 60(40), 5232–5244. <https://doi.org/10.1039/D4CC01476F>
- Yu, D., Zhang, Q., & Dai, L. (2010). Highly Efficient Metal-Free Growth of Nitrogen-Doped Single-Walled Carbon Nanotubes on Plasma-Etched Substrates for Oxygen Reduction. *Journal of the American Chemical Society*, 132(43), 15127–15129. <https://doi.org/10.1021/ja105617z>
- Zagal, Jose H., & Bedioui, F. (2016). Electrochemistry of N<sub>4</sub> Macrocyclic Metal Complexes. I: Jose H. Zagal & F. Bedioui (Red.), *Electrochemistry of N<sub>4</sub> Macrocyclic Metal Complexes: Volume 1: Energy, Second Edition* (Bd. 1). Springer International Publishing. <https://doi.org/10.1007/978-3-319-31172-2>
- Zagal, José H., Bedioui, F., & Dodelet, J. P. (2006). N<sub>4</sub>-Macrocyclic Metal Complexes. I: José H. Zagal, F. Bedioui, & J.-P. Dodelet (Red.), *N<sub>4</sub>-Macrocyclic Metal Complexes*. Springer New York. <https://doi.org/10.1007/978-0-387-28430-9>

- Zagal, José H., Griveau, S., Ozoemena, K. I., Nyokong, T., & Bedioui, F. (2009). Carbon nanotubes, phthalocyanines and porphyrins: attractive hybrid materials for electrocatalysis and electroanalysis. *Journal of nanoscience and nanotechnology*, 9(4), 2201–2214. <https://doi.org/10.1166/JNN.2009.SE15>
- Zagal, José H., Griveau, S., Silva, J. F., Nyokong, T., & Bedioui, F. (2010). Metallophthalocyanine-based molecular materials as catalysts for electrochemical reactions. *Coordination Chemistry Reviews*, 254(23–24), 2755–2791. <https://doi.org/10.1016/J.CCR.2010.05.001>
- Zagal, José H., & Koper, M. T. M. (2016). Reactivity Descriptors for the Activity of Molecular MN<sub>4</sub> Catalysts for the Oxygen Reduction Reaction. *Angewandte Chemie International Edition*, 55(47), 14510–14521. <https://doi.org/10.1002/ANIE.201604311>
- Zaki, Z. I., El-Sadek, M. H., Ali, H. H., & Ahmed, H. (2020). Synthesis of Vanadium Carbide by Mechanical Activation Assisted Carbothermic Reduction. *Materials*, 13(19), 4408. <https://doi.org/10.3390/ma13194408>
- Zarmehri, E., Raudsepp, R., Danilson, M., Šutka, A., & Kruusenberg, I. (2023). Vanadium and carbon composite electrocatalyst for oxygen reduction reaction. *Materials Chemistry and Physics*, 307, 128162. <https://doi.org/10.1016/j.matchemphys.2023.128162>
- Zarmehri, E., Raudsepp, R., Šmits, K., Käämbre, T., Šutka, A., Yörük, C. R., Zacs, D., & Kruusenberg, I. (2023). Lead and Nitrogen Co-Doped Multi-Walled Carbon Nanotube Electrocatalyst for Oxygen Reduction Reaction. *Journal of The Electrochemical Society*, 170(11), 114505. <https://doi.org/10.1149/1945-7111/ad0072>
- Zarmehri, E., Sadeghi, M., & Mehrabani-Zeinabad, A. (2013). Construction of Composite Polymer Bipolar Plate for Pem Fuel Cell. *Iranica Journal of Energy & Environment*, 4(4), 357–360. <https://doi.org/10.5829/idosi.ijee.2013.04.04.07>
- Zeng, S., Wang, S., Zhuang, H., Lu, B., Li, C., Wang, Y., & Wang, G. (2022). Fluorine-doped carbon: A metal-free electrocatalyst for oxygen reduction to peroxide. *Electrochimica Acta*, 420, 140460. <https://doi.org/10.1016/j.electacta.2022.140460>
- Zhang, D., Ding, R., Shi, S., & He, Y. (2023). Efficient four-electron transfer platinum-based oxygen reduction catalysts: A mini review. *International Journal of Hydrogen Energy*, 48(78), 30391–30406. <https://doi.org/10.1016/J.IJHYDENE.2023.04.161>
- Zhang, H., Hwang, S., Wang, M., Feng, Z., Karakalos, S., Luo, L., Qiao, Z., Xie, X., Wang, C., Su, D., Shao, Y., & Wu, G. (2017). Single Atomic Iron Catalysts for Oxygen Reduction in Acidic Media: Particle Size Control and Thermal Activation. *Journal of the American Chemical Society*, 139(40), 14143–14149. <https://doi.org/10.1021/jacs.7b06514>
- Zhang, H. W., Chen, D. Z., Xianze, Y., & Yin, S. B. (2015). Anion-Exchange Membranes for Fuel Cells: Synthesis Strategies, Properties and Perspectives. *Fuel Cells*, 15(6), 761–780. <https://doi.org/10.1002/FUCE.201500039>
- Zhang, J., Zhang, J., He, F., Chen, Y., Zhu, J., Wang, D., Mu, S., & Yang, H. Y. (2021). Defect and Doping Co-Engineered Non-Metal Nanocarbon ORR Electrocatalyst. *Nano-Micro Letters*, 13(1), 65. <https://doi.org/10.1007/s40820-020-00579-y>
- Zhang, L., & Xia, Z. (2011). Mechanisms of Oxygen Reduction Reaction on Nitrogen-Doped Graphene for Fuel Cells. *The Journal of Physical Chemistry C*, 115(22), 11170–11176. <https://doi.org/10.1021/jp201991j>

- Zhang, S., Tang, S., Lei, J., Dong, H., & Ju, H. (2011). Functionalization of graphene nanoribbons with porphyrin for electrocatalysis and amperometric biosensing. *Journal of Electroanalytical Chemistry*, 656(1–2), 285–288. <https://doi.org/10.1016/J.JELECHEM.2010.10.005>
- Zhang, X., Huang, W., Wang, Y., Zhang, J., & Liu, X. (2023). Nitrogen and Carbon Co-Doped CoO<sub>x</sub> Nanostructures for Oxygen Reduction. *ACS Applied Nano Materials*, 6(7), 5527–5534. <https://doi.org/10.1021/acsanm.3c00019>
- Zhao, L., Miao, L., Liu, C., Li, C., Asaka, T., Kang, Y., Iwamoto, Y., Tanemura, S., Gu, H., & Su, H. (2014). Solution-Processed VO<sub>2</sub>-SiO<sub>2</sub> Composite Films with Simultaneously Enhanced Luminous Transmittance, Solar Modulation Ability and Anti-Oxidation property. *Scientific Reports* 2014 4:1, 4(1), 1–11. <https://doi.org/10.1038/srep07000>
- Zhao, Yu, Yang, L., Chen, S., Wang, X., Ma, Y., Wu, Q., Jiang, Y., Qian, W., & Hu, Z. (2013). Can Boron and Nitrogen Co-doping Improve Oxygen Reduction Reaction Activity of Carbon Nanotubes? *Journal of the American Chemical Society*, 135(4), 1201–1204. <https://doi.org/10.1021/ja310566z>
- Zhao, Yuan, Wang, Q., Hu, R., Liu, W., Zhang, X., Wang, W., Alonso-Vante, N., & Zhu, D. (2024). Oxygen reduction reaction performance of Fe-N-C catalyst with dual nitrogen source. *Frontiers in Energy*, 18(6), 841–849. <https://doi.org/10.1007/S11708-024-0956-2/METRICS>
- Zhi, L., Gorelik, T., Friedlein, R., Wu, J., Kolb, U., Salaneck, W. R., & Müllen, K. (2005). Solid-state pyrolyses of metal phthalocyanines: A simple approach towards nitrogen-doped CNTs and metal/carbon nanocables. *Small*, 1(8–9), 798–801. <https://doi.org/10.1002/smll.200500150>
- Zhou, N., Wang, N., Wu, Z., & Li, L. (2018). Probing Active Sites on Metal-Free, Nitrogen-Doped Carbons for Oxygen Electoreduction: A Review. *Catalysts*, 8(11), 509. <https://doi.org/10.3390/catal8110509>
- Zhou, X.-L., Zhang, H., Shao, L.-M., Lü, F., & He, P.-J. (2021). Preparation and Application of Hierarchical Porous Carbon Materials from Waste and Biomass: A Review. *Waste and Biomass Valorization*, 12(4), 1699–1724. <https://doi.org/10.1007/s12649-020-01109-y>
- Zhu, Y. P., Liu, Y., Liu, Y. P., Ren, T. Z., Chen, T., & Yuan, Z. Y. (2015). Direct Synthesis of Phosphorus-Doped Mesoporous Carbon Materials for Efficient Electrocatalytic Oxygen Reduction. *ChemCatChem*, 7(18), 2903–2909. <https://doi.org/10.1002/CCTC.201500148>
- Zine, Y., Benmouna, A., Becherif, M., & Hissel, D. (2024). Towards maximum efficiency of an open-cathode PEM fuel cell system: A comparative experimental demonstration. *International Journal of Hydrogen Energy*, 86, 72–85. <https://doi.org/10.1016/J.IJHYDENE.2024.08.318>
- Zion, N., Cullen, D. A., Zelenay, P., & Elbaz, L. (2020). Heat-Treated Aerogel as a Catalyst for the Oxygen Reduction Reaction. *Angewandte Chemie*, 132(6), 2504–2510. <https://doi.org/10.1002/ANGE.201913521>
- Zitolo, A., Goellner, V., Armel, V., Sougrati, M.-T., Mineva, T., Stievano, L., Fonda, E., & Jaouen, F. (2015). Identification of catalytic sites for oxygen reduction in iron- and nitrogen-doped graphene materials. *Nature Materials*, 14(9), 937–942. <https://doi.org/10.1038/nmat4367>

## Acknowledgments

First, I would like to express my deepest gratitude to my supervisor, Dr. Ivar Kruusenberg, and my co-supervisor, Dr. Ragle Raudsepp, for their invaluable guidance, support, and encouragement throughout my PhD journey. Your expertise and insight have been instrumental in shaping this research, and I am deeply grateful for your mentorship.

I am deeply grateful to my family, especially my wife, Maryam Kazemi, for her patience, love, and unwavering support during this challenging journey. To my children, Ava and Nila, thank you for being my constant source of joy and motivation. I would also like to dedicate this work to the memory of my beloved parents, whose love, sacrifices, and encouragement laid the foundation for all my achievements. Though they passed away some years ago, their values and guidance continue to inspire me every day.

I am also profoundly thankful to my colleagues at the National Institute of Chemical Physics and Biophysics (KBFI) Estonia for their collaborative spirit and enriching discussions. My sincere appreciation also goes to the professors, lab operators, and staff of the Faculty of Science at TalTech University for their invaluable teaching and assistance in helping me complete my PhD. A special thanks to Dr. Tim Patrik Fellingner, my supervisor at the Federal Institute of Materials Research and Testing (BAM) in Berlin, for his support and guidance during my mobility study in Germany.

I would like to extend my gratitude to the Estonian Research Council (projects PSG312, IUT19–28, TK–141), the ERA.Net RUS Plus funding mechanism (project HeDoCat), and the European Regional Development Fund (projects no. 2014–2020.4.01.16–0041 and 2014–2020.4.01.15–0005) for their financial support, which made this research possible.

A heartfelt thanks to the co-authors who contributed to the tests, analyses, and writing papers, especially Dr. Andris Šutka, Mati Danilson, Krišjānis Šmits, Dr. Tanel Käämbre, Can Rüstü Yörük, and Dzintars Zacs. Your efforts and support were invaluable. Finally, I am thankful to my friends and mentors, both within and outside the academic sphere, for their encouragement and inspiration over the years.

## **Abstract**

### **Development of Catalysts for Oxygen Electroreduction: A Doping Approach**

This thesis explores alternative carbon-based nanomaterials as potential catalysts for the oxygen reduction reaction (ORR), a key process in fuel cell and metal-air battery cathodes that traditionally rely on platinum-based catalysts due to slow reaction kinetics. The research focuses on non-precious metal catalysts, aiming to identify cost-effective and efficient alternatives to platinum. Two main catalyst categories were explored: non-noble metal–nitrogen-doped carbon catalysts and heteroatom-doped carbon nanomaterials. For metal–nitrogen doping, metal phthalocyanines (PbPc and VPc) were utilized.

The study evaluates the ORR performance of various catalysts in alkaline, neutral, and acidic media. Notably, PbPc and VPc-based materials exhibited performance that was close to commercial platinum catalysts, as well as BF-doped catalysts. Together, these findings underscore the significant potential of these catalyst materials for use in fuel cell and metal-air battery applications. Physical characterization methods, including SEM, TEM, XRD, N<sub>2</sub> adsorption analysis, Raman spectroscopy and XPS, were employed to confirm the successful doping of heteroatoms and the formation of metal nanoparticles within the catalysts. These analyses revealed the presence of pyrrolic-N, pyridinic-N, and graphitic-N, which are active towards ORR. In particular, the study dives into the electrocatalytic behavior of PbPc/MWCNT and VPc/MWCNT catalyst materials. The co-doping process, achieved through pyrolysis in a nitrogen atmosphere, was shown to enhance ORR activity in various media. The work demonstrates the potential of VPc and PbPc as co-doping agents for creating effective cathode catalysts for microbial, PEM, and AEM fuel cells. Additionally, the functionalization of nanocarbon materials with boron and fluorine was explored, utilizing a low-cost pyrolysis method to synthesize BF-rGO/FWCNT catalysts. These catalysts demonstrated significant electrocatalytic activity in both alkaline and acidic media, emphasis on the influence of fluorine, the most electronegative element, on the design of novel nanocarbon-based electrocatalysts. Overall, this thesis presents a comprehensive exploration of various non-noble metal catalysts as a promising alternative to platinum for the ORR, offering insights into the synthesis, characterization, and electrochemical performance of these materials.



## Lühikokkuvõte

### Katalüsaatormaterjalide arendamine hapniku redutseerumise tarvis: dopeerimispõhine lähenemine

Käesolevas väitekirjas uuritakse alternatiivseid süsinikupõhiseid katalüsaatormaterjale hapniku elektrokeemiliseks redutseerimiseks, mis on üheks olulisemaks protsessiks kütuseelementide ja metall-õhk akude katoodides. Hapniku redutseerumisreaktsiooni aeglase kineetika tõttu on seda traditsiooniliselt katalüüsitud plaatinapõhiste materjalidega. Antud uurimistöös keskendutakse mitteväärismetall- ja heteroatomitega modifitseeritud süsinikmaterjalidele, eesmärgiga leida odavaid ja tõhusaid alternatiive plaatinalle. Metall- ja lämmastikuga dopeeritud süsinikmaterjalide sünteesiks kasutati metallftalotsüaniini (PbPc ja VPc).

Uuringus hinnatakse erinevate katalüsaatorite mõju hapniku redutseerumisele leeliselistes, neutraalsetes ja happelistes keskkondades. Saadud tulemused demonstreerivad sünteesitud materjalide potentsiaali katalüüsima hapniku redutseerimist nii kütuseelementides kui ka metall-õhk patareides. Kinnitamaks katalüsaatormaterjalide edukat dopeerimist ja metalli nanoosakeste moodustumist, kasutati erinevaid füüsikalisi analüüsimeetodeid, sealhulgas SEM'i, TEM'i, XRD'd, N<sub>2</sub> adsorptsiooni analüüsi, Raman spektroskoopiat ja XPS'i. Analüüside tulemused näitasid pürroolse, püridiini ja grafiitse lämmastikvormi olemasolu, mis kõik mõjutavad hapniku redutseerumist. Eelkõige keskendutakse uuringus PbPc-MWCNT ja VPc-MWCNT komposiitide elektrokatalüütilisele käitumisele. Katalüsaatormaterjalide pürolüüsi lämmastiku atmosfääris ja saavutatud dopeerimine suurendas hapniku redutseerumise aktiivsust erinevates keskkondades. Tulemused näitavad VPc- ja PbPc-põhiste süsinikmaterjalide potentsiaali katalüüsima hapniku redutseerimist mikroobsete, prootoni- ja anioonivahetusmembraaniga kütuseelementide katoodidel. Lisaks uuriti süsiniknanomaterjalide modifitseerimist boori ja fluoriga. BF-rGO/FWCNT-katalüsaatorite sünteesimiseks kasutati samuti pürolüüsi lämmastiku keskkonnas. Need katalüsaatorid näitasid märkimisväärset elektrokatalüütilist aktiivsust nii leeliselises kui ka happelises keskkonnas, demonstreerides kõige elektronegatiivsema elemendi, fluori, mõju süsinikupõhiste elektrokatalüsaatorite disainil ja sünteesil. Kokkuvõttes uuritakse käesolevas väitekirjas mitmeid mitteväärismetallkatalüsaatoreid kui paljulubavaid alternatiive plaatina-põhiste materjalidele, pakkudes detailset ülevaadet nende materjalide sünteesist kui ka hapniku redutseerumise elektrokatalüütilisest käitumisest.

## Appendix 1

### Publication I

Zarmehri, E., Raudsepp, R., Šmits, K., Käämbre, T., Šutka, A., Yörük, C. R., Zacs, D., & Kruusenberg, I. (2023). Lead and Nitrogen Co-Doped Multi-Walled Carbon Nanotube Electrocatalyst for Oxygen Reduction Reaction. *Journal of The Electrochemical Society*, 170(11), 114505. <https://doi.org/10.1149/1945-7111/AD0072>





## Lead and Nitrogen Co-Doped Multi-Walled Carbon Nanotube Electrocatalyst for Oxygen Reduction Reaction

Ehsan Zarmehri,<sup>1</sup>  Ragle Raudsepp,<sup>1</sup> Krišjānis Šmits,<sup>2</sup> Tanel Käämbre,<sup>3</sup> Andris Šutka,<sup>4</sup> Can Rüstü Yörük,<sup>5</sup> Dzintars Zacs,<sup>6</sup> and Ivar Kruusenberg<sup>1,\*,</sup>

<sup>1</sup>National Institute of Chemical Physics and Biophysics, 12618 Tallinn, Estonia

<sup>2</sup>Institute of Solid-State Physics, University of Latvia, 1063 Riga, Latvia

<sup>3</sup>Institute of Physics, Department of Natural and Exact Sciences University of Tartu, 50411 Tartu, Estonia

<sup>4</sup>Faculty of Materials Science and Applied Chemistry, Riga Technical University, 1048 Riga, Latvia

<sup>5</sup>Department of Materials and Environmental Technology, Tallinn University of Technology, 19086 Tallinn, Estonia

<sup>6</sup>Institute of Food Safety, Animal Health and Environment, Riga 1076, Latvia

The electrocatalysis of oxygen reduction reaction (ORR) on lead and nitrogen co-doped multi-walled carbon nanotube (Pb/N/MWCNT) composite catalyst has been investigated in the neutral, acidic and alkaline media. The mixture of lead phthalocyanine (PbPc) and MWCNTs was pyrolysed in nitrogen atmosphere to achieve co-doping of lead and nitrogen. The successful co-doping as well as formation of Pb nanoparticles were confirmed with the use of various physical and surface characterisation methods such as scanning and transmission electron microscopy, Raman spectroscopy, X-ray photoelectron spectroscopy and X-ray diffraction analysis. This work brings forth the electrocatalytic effect of Pb and nitrogen co-doping of carbon by a detailed electrochemical analysis using rotating disk electrode (RDE) method. The Pb and nitrogen co-doped MWCNT material demonstrate a reasonable electrocatalytic ORR activity in acidic, neutral and alkaline media. The results indicate great potential of Pb to be employed in electrocatalyst design as co-doping agent to achieve superior cathode catalysts for microbial, proton and anion exchange membrane fuel cells.

© 2023 The Electrochemical Society ("ECS"). Published on behalf of ECS by IOP Publishing Limited. [DOI: [10.1149/1945-7111/ad0072](https://doi.org/10.1149/1945-7111/ad0072)]

Manuscript submitted January 2, 2023; revised manuscript received July 14, 2023. Published November 3, 2023.

Supplementary material for this article is available [online](#)

Fuel cells are among the most environmentally friendly energy technologies, which do not need recharging and can provide energy as long as fuel is provided on a continuous basis. Unfortunately, the high price and scarcity of the platinum, which is used for the hydrogen oxidation and oxygen reduction reaction (ORR) is a major limitation in the extensive commercialization of this technology.<sup>1</sup> Platinum is used because it is favouring the electrochemical O<sub>2</sub> reduction in the direct 4e<sup>-</sup> pathway. 4e<sup>-</sup> reduction to water is highly preferred, as the formation of peroxide via 2e<sup>-</sup> pathway is known to cause the corrosion of different fuel cell components.<sup>2</sup> Besides that, the low rate of the ORR, which is the key reaction of low-temperature fuel cells (LTFCs), causes a significant energy loss at the cathode in the form of over-potential. The slow reaction kinetics is one of the most problematic barriers in the development of LTFCs technology.<sup>3</sup> The limitations related to kinetics and consequently the usage of noble metals is the main reason why design and development of highly active and low-cost non-noble metal catalysts (NNMCs) have received wide attention.<sup>4</sup> Some of the NNMCs have the potential to replace Pt under the same condition, but until now most of them still suffer under low electrochemical activity towards the ORR as well as poor stability. Further studies are crucial in order to develop active and stable NNMCs that are superior or competitive to Pt.<sup>5,6</sup>

Among the NNMCs, nitrogen-doped carbon and in particular non-noble metal-nitrogen-carbon (M-N-C) materials have demonstrated outstanding catalytic activity that is comparable to Pt in LTFCs.<sup>7–11</sup> Transition metal macrocyclic complexes (MN<sub>4</sub>) have been extensively studied since the pioneering work by Jasinski with cobalt phthalocyanine.<sup>5,12,13</sup> From various macrocycle-based cathode catalysts, iron phthalocyanine (FePc) is reported as one of the most prominent catalyst precursors to synthesise NNMCs.<sup>12,14,15</sup> Baranton et al.<sup>16,17</sup> revealed that FePc/C catalyst showed better ORR activity in presence of methanol compared with Pt catalyst.

The main drawback of using transition metal macrocycle-modified carbon materials as a catalyst is the low electrochemical stability in acidic environment.<sup>18–20</sup> In order to improve the stability,

pyrolysis between 600 and 1000 °C in an inert gas environment is commonly used.<sup>21–24</sup> Phthalocyanine molecules undergo thermal decomposition during the heat treatment, leading to the formation of more stable and active ORR catalytic sites. MN<sub>x</sub> sites which are formed during thermal treatment at high temperature is one of the most active sites for the ORR.<sup>25–27</sup> Despite comprehensive studies, the best pyrolysis temperature remains a point of contention and seems to rather depend on respective precursors.<sup>28–30</sup>

Mainly Fe and Co-based phthalocyanines have been studied as doping agents for creating M-N-C catalysts. However, iron leaching due to the hydroxyl radicals degrades the membrane and promotes Fenton reactions.<sup>31,32</sup> On Co-based catalysts mostly two-electron reactions pathway dominants.<sup>33,34</sup> Pb-based catalysts could be used to improve ORR activity and in fuel cell systems. Morris et al.<sup>35</sup> showed that lead dioxide (PbO<sub>2</sub>) cathodes in microbial fuel cell (MFC) had a greater electrocatalytic activity than Pt/C cathodes. One of the main advantages of Pb is its relatively good long-term stability in sulfuric acid solutions.<sup>36,37</sup> It is known that in alkaline media Pt is less stable than in acidic media but there are numerous non-noble metal catalyst alternatives that work at high pH conditions.<sup>38,39</sup> This makes the usage of Pb as a catalyst if fuel cells very attractive since finding a stable alternative for a Pt in acidic media is a challenge. However, until now, Pb-based catalysts have been rather poorly investigated for the ORR. Usage of Pb as a potential fuel cell catalyst has also a practical value, every year a vast number of lead-acid batteries are produced, used, and recycled.<sup>38,39</sup> Industries shifting from traditional lead-acid batteries to Li-ion batteries will add value to the research related to finding an alternative usage to recycled Pb.<sup>40,41</sup>

The accompanying nitrogen doping into the carbon network taking place during the pyrolysis of the carbon supported phthalocyanines, also plays crucial role in achievement of active ORR catalysts.<sup>30,42–44</sup> It has been extensively reported that two types of nitrogen functional groups (pyridinic-N and graphitic-N) are mainly responsible for a direct 4e<sup>-</sup> ORR pathway.

In this work we used pyrolysis method to synthesise Pb and N co-doped carbon nanomaterials. The electrochemical activity and durability of the synthesised catalyst materials were tested in alkaline, neutral and acidic media using RDE setup. To the best of

\*E-mail: [ivar.kruusenberg@kbfi.ee](mailto:ivar.kruusenberg@kbfi.ee)

our knowledge this is the first published study on Pb and N co-doped carbon materials as a catalyst for LTFCs. Current research allows to observe the potential of Pb-based catalyst for microbial, proton and anion exchange membrane fuel cells.

## Experimental

**Materials and catalyst preparation.**—Lead (II) phthalocyanine (PbPc) (Sigma-Aldrich) was mixed with MWCNTs (Nanocyl Co. (Belgium)) in different PbPc-to-MWCNT ratios (1:3, 1:1, 3:1, 1:7) and suspended in 5 ml of ethanol followed by magnetic stirring and sonication for 2 h to achieve the adsorption of PbPc on the surface of MWCNT's. The catalyst suspension was poured in a quartz boat followed by drying at 70 °C for 20 min and heat-treatment at 600, 800, and 1000 °C for 2 h in a flowing nitrogen 99.999% (Linde) atmosphere. In addition, dihydrogen phthalocyanine (H<sub>2</sub>Pc) (Sigma-Aldrich) was mixed with MWCNT and pyrolysed at 800 °C for comparison with PbPc/MWCNT. Commercial Pt/C 20% (HiSPEC, JMFC, UK) was used as a benchmark. KOH and H<sub>2</sub>SO<sub>4</sub> (Sigma-Aldrich) were used for alkaline and acidic electrolyte preparation. NaCl (Lachner, Czech), Na<sub>2</sub>HPO<sub>4</sub>, KCl and KH<sub>2</sub>PO<sub>4</sub> (Sigma-Aldrich, U.K.) were used to prepare 0.1 M phosphor buffer solution at room temperature (23 ± 1 °C). All the solutions were made using MilliQ-water (Millipore, Inc).

**Physical characterization.**—The morphology of the PbPc/MWCNT catalyst was examined by scanning electron microscope (SEM) (LYRA3, Tescan) and transmission electron microscopy (TEM) (probe corrected Tecnai G2 F20 EFi) using a resolution of 2.4 Å in TEM mode and an acceleration voltage of 200 kV. X-ray diffraction (XRD) measurements were performed using a PANalytical apparatus, operating with Cu K $\alpha$  radiation ( $\lambda$  = 0.154 nm), 45 kV beam voltage and 40 mA beam current. Patterns were obtained in the range from 10° to 90° with 0.02° increments and the exposure time of 100 s, for the analysis High Score Plus software was used. NovaTouch 4LX Analyzer (Quantachrome) was used to record the N<sub>2</sub> adsorption/desorption isotherms of the catalyst samples at nitrogen's boiling temperature (77 K). Before the measurement, the samples were degassed for 20 h under vacuum at 200 °C and then backfilled with N<sub>2</sub>. Up to a nitrogen relative pressure of  $P/P_0$  = 0.2, the specific surface area ( $S_{\text{BET}}$ ) was determined using either the Brunauer–Emmett–Teller (BET) theory or the density functional theory (DFT). Near saturation pressure of N<sub>2</sub> ( $P/P_0$  = 0.98), the total volume of pores ( $V_{\text{tot}}$ ) was measured. Using the t-plot technique and deBoer statistical thickness, the microporosity ( $V$ ) was determined.  $dp = 2V_{\text{tot}}/S_{\text{BET}}$  was used to calculate the average diameter of pores ( $d_p$ ) for a slit-type pore shape. X-ray photoelectron spectroscopy (XPS) was used to analyse the surface composition of the pyrolysed PbPc/MWCNT samples. The XPS sample was prepared dissolving the PbPc/MWCNT catalyst in ethanol (4 mg ml<sup>-1</sup>) and applying it to a glassy carbon substrate (1.1 × 1.1 cm), after which the solvent was allowed to evaporated in the air. A Scintia Gammadata SES-100 hemispherical energy analyser (operated at 200 eV pass energy, with a ~0.9 eV overall spectral resolution) combined with a non-monochromated Mg K $\alpha$  X-ray source (h $\nu$  1253.6 eV, operated at 300 W source power) were used for the XPS measurements. To estimate the at% composition, the spectrometer transmission was checked against multiple spectral line intensities of sputter cleaned Au, Ag and Cu metals, and the photoionization cross sections. Most of the XPS data analysis was performed using the CasaXPS software, apart from the C 1s spectral fit, where the proper sp<sup>2</sup> carbon Doniach-Sunijic asymmetric peak was fitted using the SPANCF<sup>45,46</sup> macro package for IgorPro software. The Raman spectra were recorded in a Renishaw via Raman spectrometer using a green laser (max 20 mW) beam; objective x100, 514 nm, 100% laser power, 1 accumulation (extended), 150–4000 cm<sup>-1</sup>, exposure time 10 s. The substrates were a cleaned Si wafer plate. The  $I_D/I_G$  ratios were extracted by fitting the spectra with two Lorentzian.

**Electrode preparation and electrochemical characterisation of catalysts.**—A glassy carbon (GC) disk with a geometric surface area ( $A$ ) of 0.2 cm<sup>2</sup> was used as the substrate material for the rotating disk electrode (RDE) tests. GC disks (Sigma-Aldrich) were embedded in a Teflon holder, and the GC electrodes were meticulously polished with 1.0 and 0.3  $\mu$ m alumina powder to a mirror-like finish (Buehler). After the polishing process the GC disk electrodes were sonicated in isopropanol for 5 min and then in water for 5 min. The electrodes were modified with PbPc/MWCNT electrocatalysts utilizing aqueous suspensions (4 mg ml<sup>-1</sup>) containing ionomer to prepare a uniform catalyst layer on the GC surface. Ionomer was 0.25% Nafion perfluorinated resin solution (Aldrich, USA) for tests in acid and neutral media, and 0.15% FAA-3 OH<sup>-</sup> ionomer (FumaTech Germany) for alkaline media. The catalyst suspensions were sonicated for 1 h in the ultrasonication bath (keeping the temperature at <40 °C) and on a vortex mixer for 2 min. 5  $\mu$ l aliquot of the well-dispersed ink was loaded onto the polished, clean GC electrode, completely covering the GC. This was repeated 4 times to reach 20  $\mu$ l. The ink droplet was dried in the ambient atmosphere. Thus, for electrochemical testing, the electrocatalyst loading was 0.4 mg cm<sup>-2</sup>. For contrast, an industrial Pt/C catalyst with a 20 wt% Pt/C loading of 0.4 mg cm<sup>-2</sup> was used, resulting in a Pt loading of 80  $\mu$ g cm<sup>-2</sup>. The RDE setup of an OrigaTrod rotator with speed control device (OrigaLys, France) was used for electrochemical measurements, with the electrode rotation rate ( $\omega$ ) varied between 400 and 4400 rpm. The potential was applied with a Gamry potentiostat/galvanostat 1010E (Gamry Instruments, USA) at a scan rate of 10 mV s<sup>-1</sup> and step size 10 mV. A graphite rod served as the counter electrode, whereas a saturated calomel electrode (SCE) Hg/HgCl in 3 M KCl reference electrode (SI-Analytics B 3410 +, Germany) served as the reference electrode. All the potentials in this paper are expressed in terms of the reversible hydrogen electrode (RHE) except of stability curves. Three electrolytes 0.5 M H<sub>2</sub>SO<sub>4</sub> (pH 0.3), 0.1 M phosphoric buffer solution (pH 7.5) and 0.1 M KOH (pH 13) were used in the electrochemical experiments. The electrolyte solution was saturated with O<sub>2</sub> (99.999%, AGA) for current density and N<sub>2</sub> (99.999%) for background measurements. During the electrochemical testing, a steady flow of these gases was maintained over the solution. For comparison, H<sub>2</sub>Pc/MWCNT and 20% Pt/C catalysts were also tested in alkaline, neutral and acidic media, with the same catalyst ink preparation procedure as used for the PbPc/MWCNT.

## Results and Discussion

**Physical characterisation of PbPc/CNT catalysts.**—SEM and TEM were used to study the surface morphology of PbPc/MWCNT catalysis. The SEM images are shown in Figs. 1a–1c, and, despite the presence of certain agglomerates, large-scale agglomeration of the MWCNTs has been avoided. The catalyst is well dispersed on the electrode, allowing oxygen and solution diffuse through the annealed catalyst layer. During the pyrolysis, carbon structure is preserved in a good condition. The distribution of Pb nanoparticles on the catalyst pyrolysed at 1000 °C is better than on the materials which were pyrolysed at 800 °C and 600 °C. One can see more intense agglomeration of Pb particles in some parts of CNT clusters for the material heat treated at 800 °C (Fig. 1b), whereas less agglomerated particles and a low ratio of Pb to carbon is observed in sample annealed at 600 °C (Fig. 1a).

The TEM images of the PbPc/MWCNT (3:1) sample are presented in Figs. 1d–1f. As can be seen, the surface modification was accomplished without introducing major defects into the PbPc/MWCNT catalyst material. This is important to ensure that the Pb-N-doped carbon catalysts retain their expected properties. Also, no large amorphous carbon particles or other impurities can be observed from the TEM images. The catalyst synthesised at 600 °C shows some agglomeration of Pb particle that is visible in Fig. 1d. Energy-dispersive X-ray spectroscopy (EDX) images presented on Fig. 2 show that both nitrogen and Pb are well distributed on the surface of the carbon nanomaterial.



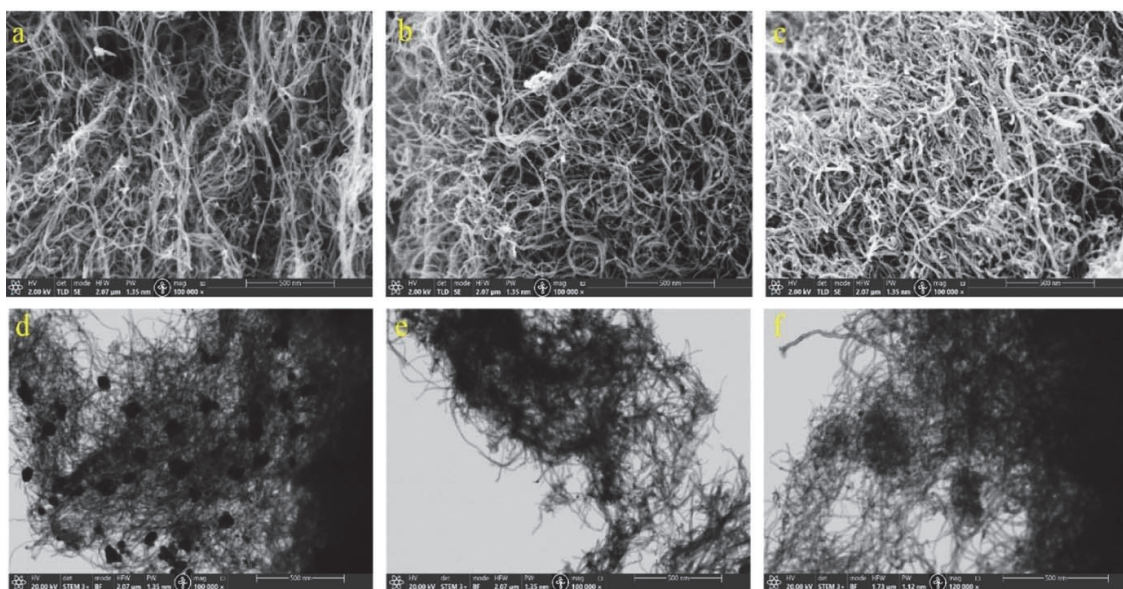


**Figure 1.** SEM images of PbPc/MWCNT (3:1) catalyst materials heat treated at 600 °C (a), 800 °C (b) and 1000 °C (c). TEM images of catalyst materials heat treated at 600 °C (d), 800 °C (e) and 1000 °C (f).

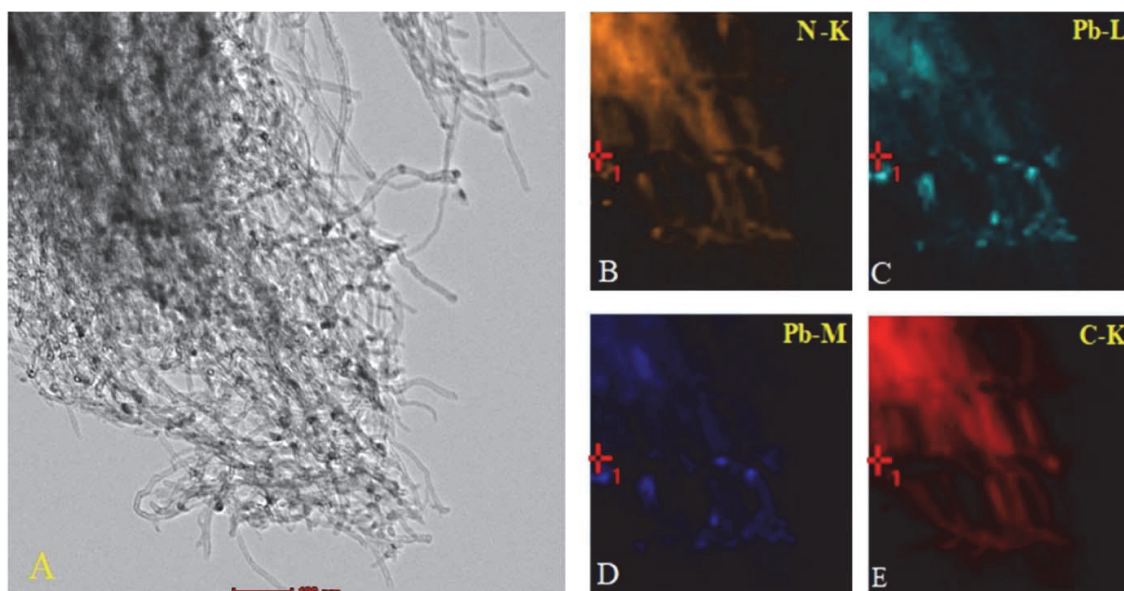


**Figure 2.** Distribution mapping via EDX of PbPc/MWCNT (3:1) 800 °C pyrolysed, Nitrogen (B), Lead (C), (D) and Carbon (D).

Raman spectra of PbPc/MWCNT (3:1) is presented in Fig. 3a. The D-band (Disordered) peaks around  $1350\text{ cm}^{-1}$  and the G-band (Graphitic) peaks in the range of  $1560\text{--}1600\text{ cm}^{-1}$  are the most prominent characteristics in the Raman spectrum of carbon materials. Considerable emphasis has been paid to the role of surface defects which play an important role in carbon catalyst performance. Through DFT calculations and physical characterisation, Tao et al. and Liu et al. showed that carbon atoms on the edge defect had a higher electron cloud density than ordinary carbon atoms.<sup>47,48</sup> The

D-band is a disorder induced characteristic that results from double resonance. The tangential vibrations of carbon atoms in graphite correspond to the G-peak at  $1580\text{ cm}^{-1}$ , while the peak at  $1345\text{ cm}^{-1}$  is associated with disordered amorphous carbon content. 2D-peak at  $2680\text{ cm}^{-1}$  is related to graphene and is sensitive to number of graphene layers, thus in this work associated to the average number of carbon layers in the MWCNT's.<sup>49</sup> The  $I_D/I_G$  ratio was found to be 1.26 for PbPc/MWCNT (3:1) @ 800 °C sample and it indicates that the amount of disordered carbon material is higher than ordered

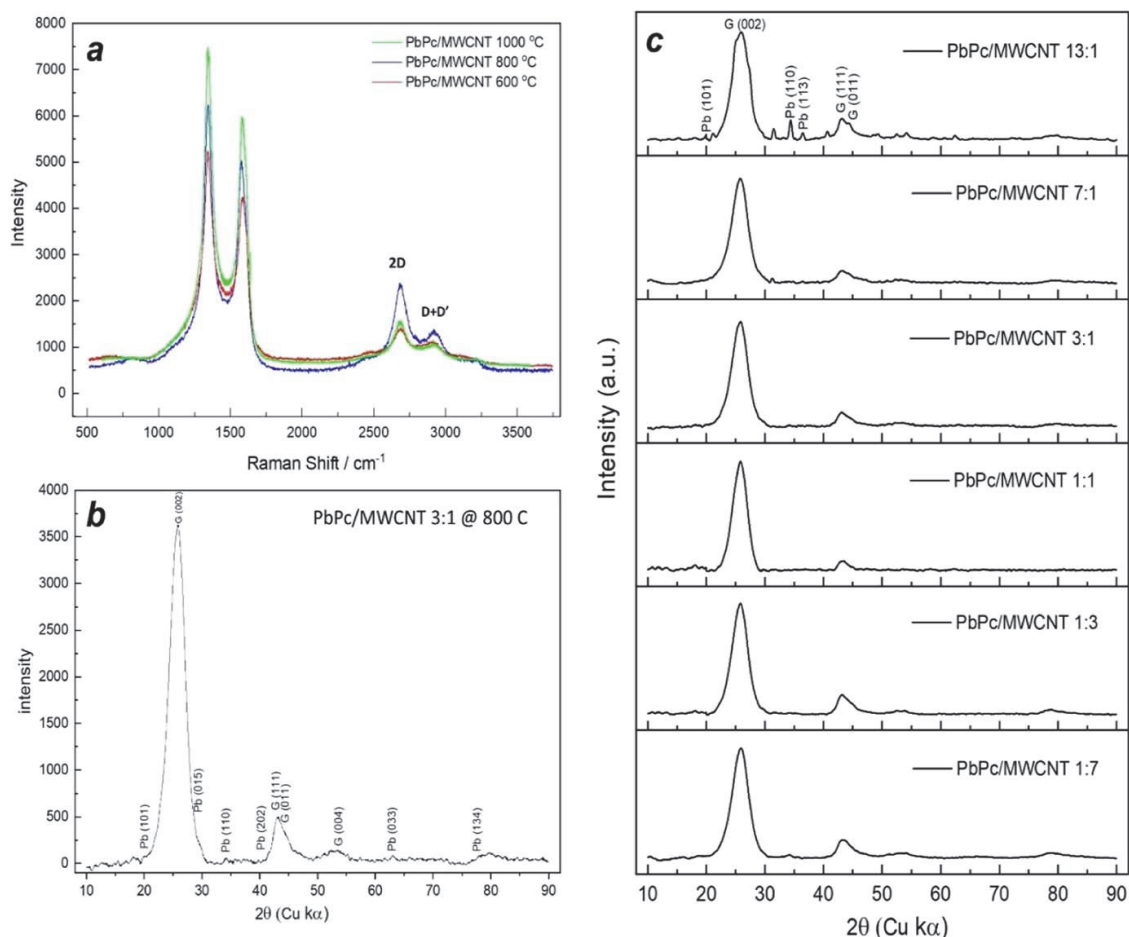


**Figure 3.** (a) Raman spectra of PbPc/MWCNT (3:1) catalyst, (b) XRD (Cu Kα) patterns for PbPc/MWCNT (3:1) catalyst, (c) XRD (Cu Kα) patterns for PbPc/MWCNT catalyst in several ratios of PbPc to MWCNT.

graphite in the compound. The  $I_D/I_G$  ratio for PbPc/MWCNT @ 1000 °C and PbPc/MWCNT @ 600 °C was found to be 1.14 and 1.23 respectively.

A XRD study was performed to explore the phase composition and crystallography of the catalyst materials (Fig. 3b). The XRD analysis revealed that the PbPc/MWCNT samples contain metallic phases. The diffraction patterns showed multiple peaks, which can be attributed to graphitic carbon and Pb (Fig. 3b). Pb characteristic reflections were set at 19.9°, 24.7°, 27.1°, 40.4°, 53.9°, 62.5° and 77.5° 2θ. The Miller indices were assigned to the closest matching peak locations of the lead phase (PDF card 98–005–4312 from the ICDD PDF-2 database). Graphitic carbon characteristic reflections were seen at 25.8°, 29.6°, 43.9°, 44.3°, 52.6° and 53.9° 2θ. The Miller indices were assigned to the closest matching peak locations of the lead phase (PDF card 98–018–5973 from the ICDD PDF-2 database). It can be concluded that Pb and nitrogen were ejected to the carbon material from the lead-phthalocyanine compound. In PbPc/MWCNT (7:1) and PbPc/MWCNT (13:1), excess Pb had no effect on increasing catalytic activity. XRD patterns also show some peaks of pure Pb that are evidence of unbonded Pb atoms in the compound (Fig. 3c).

Calculated BET specific surface areas, pore volumes, micropore volumes and average pore sizes are given in Table I. The PbPc/

MWCNT (3:1) 1000 °C has the highest surface area, the smallest average pore size and the largest pore volume of all of the catalysts, while PbPc/MWCNT (3:1) 600 °C has a lower surface area and pore volume than the other two catalysts. Pyrolysis of materials at different temperatures changes the final structure of the catalyst layer and also leads to a different pore structures.<sup>50–52</sup> The BET surface area of a catalyst pyrolysed at 800 °C is twice that of a catalyst prepared at 600 °C, and the surface area of a catalyst pyrolysed at 1000 °C is three times more than that of 600 °C.

The surface composition of catalyst material PbPc/MWCNT (3:1), pyrolysed at 800 °C, was investigated using XPS. The XPS survey spectra on Fig. 4a shows the presence of O, N, C and Pb elements. The elemental composition (at%) and the relative concentration (%) of nitrogen moieties were calculated from XPS peak intensities and are displayed in Table II and in Fig. 4 insets. The peaks in the high-resolution N1s spectrum in Fig. 4b can be assigned to: oxidized N (403.8 eV), graphitic N (401.1 eV), pyrrolic N (400.4 eV), metal-N (399.5 eV) and pyridinic N (398.1 eV) species.<sup>53</sup> A N atom that replaces the C atom in the hexagonal ring releases one p-electron to the aromatic π-system and thereby changing the electronic band structure and overall conductivity of the catalyst material. Pyrrolic N is found in a five-member ring, while pyridinic N is found in a six-member ring.<sup>54</sup> Under moderate

**Table I. Volume and surface properties of catalysts in various pyrolysis temperatures.**

Catalyst pyrolysis temperature	Multipoint BET (m <sup>2</sup> /g)	DFT method cumulative surface area (m <sup>2</sup> /g)	DFT method cumulative pore volume (cc/g)	Total pore volume (cc/g)	DFT method pore radius (nm)	Average pore size(nm)
600 °C	88.6984	91.5943	0.549765	0.883342	11.3846	19.9179
800 °C	169.733	146.414	0.814077	1.1832	11.3846	13.9419
1000 °C	246.115	206.478	1.08182	1.51912	11.3846	12.3448



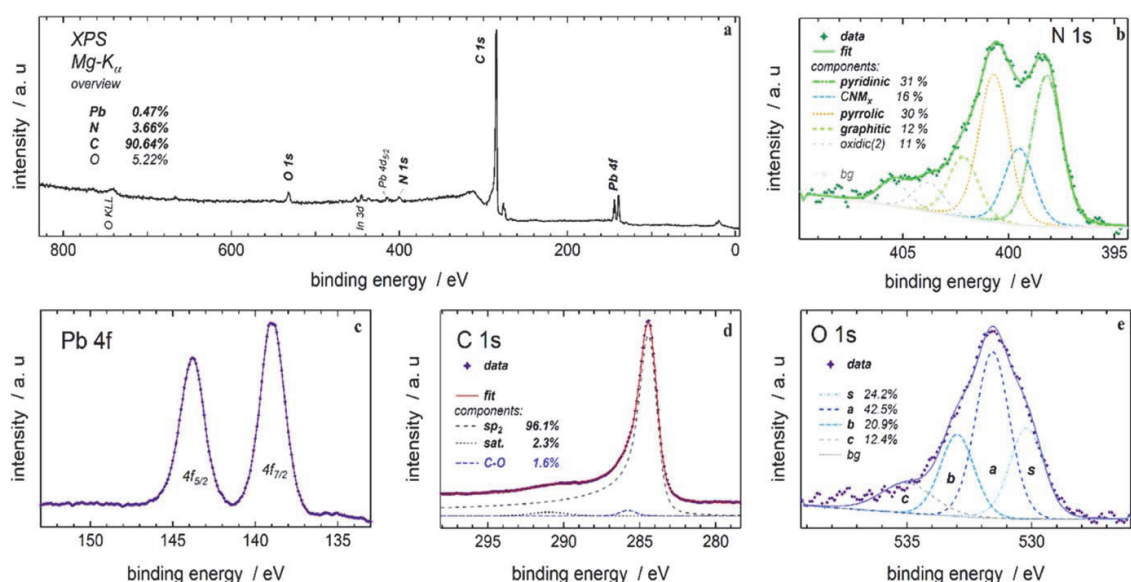
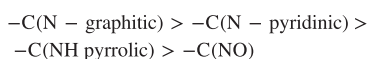


**Figure 4.** XPS spectra of PbPc/MWCNT (3:1) catalyst materials and high-resolution N1s (b), Pb4f (c), C1s (d) and O1s (e) spectra.

**Table II. Elemental composition of PbPc/MWCNT (3:1) @ 800 °C catalysts determined by XPS.**

Catalyst	C1s at%	N1s at%	O1s at%	Pb4f at%	
PbPc/MWCNT (3:1)	90.64	3.66	5.22	0.47	
Relative concentration (%) of N moieties in the catalysts	<b>Pyridinic</b>	<b>Pyrrolic</b>	<b>Graphitic</b>	<b>N-metal</b>	<b>N-Oxide</b>
PbPc/MWCNT (3:1)	30.88	30.27	12.37	15.57	10.90

pyrolysis conditions, nitrogen functional groups including pyridones, protonated pyridinic N, and pyridinic N oxides are converted to pyridinic N, whereas pyrrolic N is transformed to pyridinic N during the carbon matrix structural development.<sup>55–58</sup> Using higher pyrolysis temperatures nitrogen functional groups in a form of graphitic N are created in the graphene layer interior or in a form of pyridinic N at the edge of graphene layer.<sup>56</sup> The order of thermal stability of nitrogen functional groups is as follows:<sup>55</sup>



We note that the presence of metal-N<sub>x</sub> species is probable, with the component binding energy placing between the two relatively clearly distinguished peaks of pyridinic and pyrrolic N species.

Although the majority of oxygen groups on a carbon nanomaterial surface will be removed at higher pyrolysis temperatures, a clear O1s peak is still detected.<sup>59,60</sup> The O1s peak at 529.8 eV corresponds to binding energy between oxygen and Pb atom.<sup>61</sup> O1s peak at 531.5 eV belongs to doubly bonded oxygen in carbonyl group and 533.0 eV indicates the existence of carbon-oxygen single bond and is also assigned to adsorbed moisture and oxygen.<sup>62–64</sup> The O1s peak at the highest binding energy (535.1 eV) is attributed to hydroxyl group.<sup>62,64</sup> The C1s XPS spectrum demonstrates a relatively intact sp<sup>2</sup> hybridized bonding pattern, as based on literature, C1s peak at 284.7 ± 0.2 eV corresponds to C=C bonds.<sup>65</sup> C1s peak at 286 eV is associated to various carbon-oxygen moieties, e.g. carboxyl and quinone groups, which have been found on the surface of carbon nanotubes in numerous experiments.<sup>66–68</sup>

The Pb 4f spectrum is fitted with a single spin-orbit doublet with appropriate 4:3 intensity ratio corresponding to the electron count in

the 4f<sub>7/2</sub> and 4f<sub>5/2</sub> levels (Fig. 4c). The relatively narrow linewidth of 1.7 eV FWHM suggests the lead is included in the sample quite homogeneously.<sup>69</sup> The binding energy of the Pb 4f<sub>7/2</sub> peak at 138.9 eV is at least 2 eV too high for either PbO or PbO<sub>2</sub>.<sup>70</sup> However, some of the previous studies have shown the presence of Pb-N bond at binding energy at 139 eV.<sup>70,71</sup> XPS studies were also carried out with a catalyst material PbPc/MWCNT (3:1) synthesised at 600 °C and 1000 °C (Fig. S1). Raising the pyrolysis temperature decreases the relative percentage of metal-nitrogen species. In addition, ICP-MS studies were carried out with catalysts prepared at different temperature and the amount of impurities was negligible. ICP-MS results (Table S.I) showed that increasing the temperature decreases the amount of Pb content. Based on XPS and ICP-MS result we conclude that the metal in metal-nitrogen species is Pb.

#### Rotating disc electrode studies of oxygen reduction reaction.—

The electrochemical reduction of oxygen on PbPc/MWCNT catalyst was investigated using the RDE method. At first, the effect of three different PbPc to MWCNTs ratios to ORR performance was studied. The linear sweep voltammetry (LSV) comparative results in O<sub>2</sub>-saturated 0.1 M KOH, 0.1 M phosphoric buffer, and 0.5 M H<sub>2</sub>SO<sub>4</sub> solution at a 1600 rpm rotating speed are shown in Fig. S2. All the electrocatalysts displayed a strong reduction current, which is most likely attributed to the Pb and N co-doping of the MWCNTs and the formation of electrocatalytically active sites. It is clear from Figs. S2a–S2c that the catalyst material with a ratio of 75% PbPc to 25% MWCNTs (PbPc/MWCNT (3:1)) has the highest diffusion limited current density values (*j<sub>d</sub>*) in alkaline, neutral and acidic media. Highest onset potential was observed for the same catalyst in acidic media whereas in neutral and alkaline media the

onset potential was independent from the PbPc to MWCNT concentration. This can be associated to the agglomeration of the metal atoms into bigger particles, which was observed by TEM and SEM imaging, during high-temperature pyrolysis. This means that increasing the metal (PbPc) content in the initial catalyst precursor mixture will not contribute to a higher concentration of active sites. Agglomerated metal- and nitrogen-doped carbon catalysts show lower ORR performance compared with that of well dispersed M-N-C material.<sup>72,73</sup>

The effect of pyrolysis temperature on the lead and nitrogen co-doped material's electrocatalytic activity was also studied. While catalyst with the ratio of 75% PbPc/25% MWCNT heat treated at 800 °C showed the highest ORR activity, the pyrolysis at temperatures 600 °C and 1000 °C were also performed with the same ratio of lead phthalocyanine to carbon support. In Figs. S2d–S2f one can see that the catalyst material prepared by pyrolysis at 800 °C exhibits the best electrocatalytic activity for O<sub>2</sub> reduction in alkaline, neutral and acidic media. In addition, non-pyrolysed catalyst has been studied as well and as can be seen in Figs. S2d–S2f it shows the lowest ORR activity which clearly indicates a need for heat-treatment. Similar results have also been published by other research groups, e.g., Gupta et al. demonstrated that without annealing MN<sub>4</sub> macrocycles had only a minor impact on ORR activity in acidic media.<sup>74</sup> As can be seen in Table S.II, pyrolysis at 800 °C leads to the most positive  $E_{\text{onset}}$ ,  $E_{1/2}$  and highest limiting current density.

In previous works, it has been demonstrated that raising the pyrolysis temperature increases the amount of electrocatalytically active surface species and therefore the material prepared at 800 °C is more active than that prepared at 600 °C.<sup>75,76</sup> The reason for a lower concentration of active sites on the catalyst prepared at 600 °C may be due to the fact that the macrocyclic compound is only partially decomposed at lower pyrolysis temperature.<sup>77,78</sup> High pyrolysis temperature, 1000 °C and above, causes the carbon network to shrink partially and therefore the active surface area will be decreased.<sup>79,80</sup>

Figure 5 illustrates a set of ORR polarisation curves measured in alkaline, neutral and acidic media, respectively, at various electrode rotation rates ( $\omega$ ) with the most active being the PbPc/MWCNT (3:1) catalyst modified GC electrodes. The onset potentials for ORR are

approximately 0.93 V, 0.80 V and 0.76 V vs RHE in alkaline, neutral and acidic media respectively. For the PbPc/MWCNT (3:1) in neutral media (results presented in Fig. 5b) at higher negative potentials (around 0.0 V) and higher rotation rates a second reduction wave begins. This wave belongs to the 2e<sup>−</sup> pathway creating the H<sub>2</sub>O<sub>2</sub> intermediate which can either diffuse away or be captured by another active site and reduced to H<sub>2</sub>O in a subsequent 2e<sup>−</sup> step. This behaviour is common to the metal and heteroatom co-doped carbon materials in the neutral media and in agreement with previous reports.<sup>81,82</sup> The two-step reduction current plateau is also native to the carbon materials.<sup>83</sup> Multiple ORR pathways may occur on the Pb/N/C catalyst surfaces due to the simultaneous presence of various active sites with different structural patterns. However, at lower rotation rates no pre-wave is observed. This kind of electrocatalytic behaviour could be caused by new active sites resulting from the Pb and N co-doping. According to the research of Ge et al. doping of nitrogen into carbon structure induces more positive charge on neighbouring carbons by charge delocalization which in turn increases the activity of p-electrons and promotes the adsorption of O<sub>2</sub> molecule.<sup>84</sup> As already mentioned before, out of four nitrogen moieties, pyridinic and graphitic N show the highest catalytic activity towards the ORR. According to the XPS results PbPc/MWCNT (3:1) catalyst contains 3.66 at% nitrogen in which 30.88% is pyridinic N and 12.4% is graphitic N. 30.27% of the nitrogen species is pyrrolic, which is less stable than pyridinic and graphitic N and more tendentious to oxidation during the ORR process.<sup>85</sup> In addition, 15.57% of nitrogen is connected with metal (Pb) which is considered as an active site for ORR.<sup>86</sup> Pb atoms can act as an axial ligand and Pb-N doped carbon will catalyse the ORR via dual-site mechanism where oxygen will coordinate to the metal and to the N-atom of the Pb-N active center.<sup>87</sup> Since there is no published work regarding Pb and N co-doped carbon material for ORR purpose, we can suggest the contribution of Pb to enhanced ORR performance based on a work done by Luo et al.<sup>88</sup> They studied other p-block metal, tin (Sn), and nitrogen co-doped carbon nanomaterials to reduce the O<sub>2</sub> and found based on the DFT calculations that Sn centers strongly adsorb the O<sub>2</sub> even almost splitting it spontaneously.<sup>88</sup>

The Koutecky-Levich (K-L) equation was used to calculate the number of electrons transferred per O<sub>2</sub> molecule ( $n$ ).<sup>81</sup>

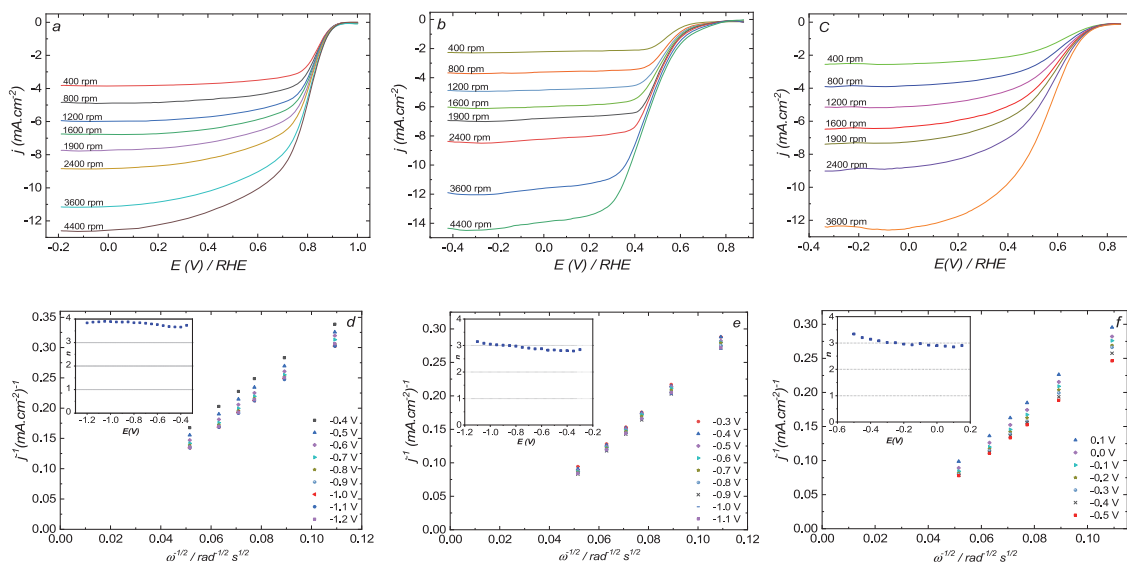


**Figure 5.** (a), (b), (c) LSV curves in various rotation speed for oxygen reduction on PbPc/MWCNT (3:1) catalyst in O<sub>2</sub>-saturated (a) 0.1 M KOH, (b) 0.1 M phosphoric buffer and (c) 0.5 M H<sub>2</sub>SO<sub>4</sub>,  $v = 10 \text{ mV} \cdot \text{s}^{-1}$ ,  $\omega = 400\text{--}4400 \text{ rpm}$ ; (d), (e), (f) Koutecky-Levich plots for ORR on PbPc/MWCNT (3:1) at various potentials per O<sub>2</sub> molecule in (d) 0.1 M KOH, (e) 0.1 M phosphoric buffer and (f) 0.5 M H<sub>2</sub>SO<sub>4</sub>.

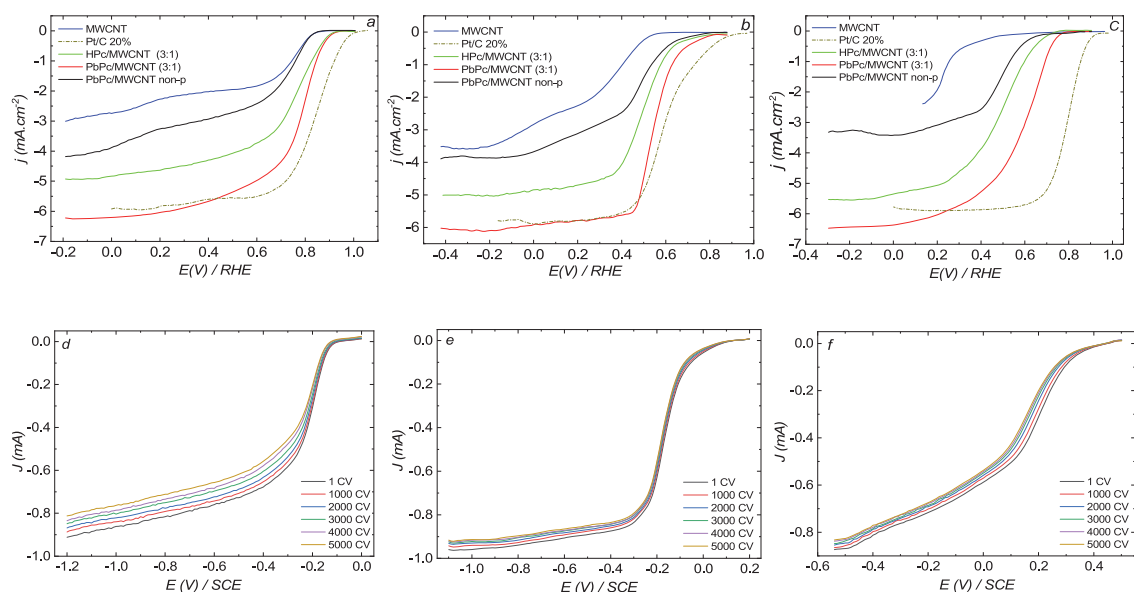


**Figure 6.** (a), (b), (c) Comparison of RDE results of oxygen reduction on MWCNT, non-pyrolysis material, HPC/MWCNT (3:1), PbPc/MWCNT (3:1) and Pt/C modified GC electrodes in O<sub>2</sub>-saturated (a) 0.1 M KOH, (b) 0.1 M phosphoric buffer and (c) 0.5 M H<sub>2</sub>SO<sub>4</sub>.  $v = 10 \text{ mV s}^{-1}$ ,  $\omega = 1600 \text{ rpm}$ ; (d), (e), (f) Stability of PbPc/MWCNT (3:1) coated GC electrodes in O<sub>2</sub>-saturated during 5000 cycles in (d) 0.1 M KOH, (e) 0.1 M phosphoric buffer and (f) 0.5 M H<sub>2</sub>SO<sub>4</sub>.  $v = 10 \text{ mV s}^{-1}$ ,  $\omega = 1600 \text{ rpm}$ .

$$\frac{1}{j} = \frac{1}{j_k} + \frac{1}{j_d} = -\frac{1}{nFkC_{O_2}^b} - \frac{1}{0.62nFD_{O_2}^{2/3}v^{-1/6}C_{O_2}^b\omega^{1/2}}$$

where *j* is the measured current density, *j<sub>d</sub>* and *j<sub>k</sub>* are the diffusion-limited currents density and kinetic current density, respectively, *A* is the geometric electrode area, *k* is the electrochemical rate constant for O<sub>2</sub> reduction,  $\omega$  is the rotation rate (rad s<sup>-1</sup>), *F* is the Faraday constant (96,485 C mol<sup>-1</sup>), *D<sub>O2</sub>* is the diffusion coefficient of oxygen ( $1.9 \times 10^{-5} \text{ cm}^2 \text{ s}^{-1}$  for alkaline and neutral media and  $1.8 \times 10^{-5} \text{ cm}^2 \text{ s}^{-1}$  for acid media), *C<sub>O2</sub><sup>b</sup>* is the concentration of oxygen in the bulk ( $1.2 \times 10^{-6} \text{ mol cm}^{-3}$  for alkaline and neutral media and  $1.132 \times 10^{-6} \text{ mol cm}^{-3}$  for acid media) and *v* is the kinematic viscosity of the solution ( $0.01 \text{ cm}^2 \text{ s}^{-1}$ ).<sup>81,89</sup> Figures 5d–5f presents the K-L plots obtained from the RDE data on oxygen reduction for the PbPc/MWCNT (3:1) catalyst in 0.1 M KOH, 0.1 M phosphoric buffer and 0.5 M H<sub>2</sub>SO<sub>4</sub> respectively. In alkaline media, the intercepts of the extrapolated K-L lines were close to zero, this illustrates that the mechanism of O<sub>2</sub> reduction is almost completely controlled by diffusion.<sup>81</sup> In acidic and neutral media, the non-zero intercepts of the extrapolated K-L lines indicating that the process of ORR is controlled by the mixed kinetic-diffusion. The insets of Figs. 5d–5f compare the *n* values calculated from the K-L equation at various potentials. The direct 4e<sup>-</sup> pathway is favoured for the fuel cells and thereby mainly platinum group metals are used for this purpose as they are well known to catalyse the 4e<sup>-</sup> ORR.<sup>2</sup> In alkaline media, for the N and Pb co-doped catalyst the *n* value was close to 4 over the entire potential range studied. This indicates the superiority of the PbPc/MWCNT catalysts and their great potential as cathode catalysts for the anion exchange membrane fuel cells. In neutral and acid media, the *n* was around 3 that shows the mixed 2e<sup>-</sup> + 2e<sup>-</sup> and 4e<sup>-</sup> electron transfer pathway. This is in agreement with previous studies, where the reduction of oxygen on phthalocyanine modified MWCNTs mostly follows a mixture of two and four electron pathway where the HO<sub>2</sub><sup>-</sup> at is formed at low potentials and is further reduced at more negative potentials.<sup>83,90–92</sup>

Figures 6a–6c shows a comparison of the ORR polarisation curves on various catalyst materials. The LSV curve of N and Pb co-doped catalysts is compared with the commercial carbon-supported Pt catalyst (20 wt% Pt/C 0.4 mg cm<sup>-2</sup>). Pt/C has almost 0.1 V more positive onset potential in alkaline media, 0.05 V in neutral media and 0.15 V more positive onset potential in acid media compared to the PbPc/MWCNT (3:1) catalyst. The LSV curves of MWCNT and H<sub>2</sub>Pc/MWCNT (3:1) have been added for comparison. *E<sub>onset</sub>* and *E<sub>1/2</sub>* for H<sub>2</sub>Pc/MWCNT are more negative in comparison to the PbPc/MWCNT (3:1) material, this clearly indicates that Pb atoms improve the catalyst performance. Table S.III, S.IV and S.V show a comparison of the RDE results obtained for PbPc/MWCNT catalysts in various ratios of PbPc to carbon (pyrolysed at 800 °C) and HPC/MWCNT and Pt/C in different media.

The best PbPc/MWCNT catalyst materials underwent stability testing during which LSV curves were cycled 5000 times, the results are presented in Figs. 6d–6f. PbPc/MWCNT (3:1) 800 °C revealed good stability in the ORR performance with a slight deviation in *E<sub>1/2</sub>* values and no shift in the onset potential in neutral and acidic media. The stability in alkaline media was lower as can be seen from the loss in *E<sub>1/2</sub>* values and diffusion current at *E* < -0.5 V. These results demonstrate well the superb stability of lead in sulfuric acid making it a promising non-noble metal dopant for fuel cell electrocatalyst preparation and utilization.

## Conclusions

In this work Pb and N co-doped carbon materials were synthesized using lead (II) phthalocyanine (PbPc) and MWCNTs as precursors. The structure of PbPc was decomposed during the pyrolysis and Pb and N atoms were doped into the carbon network which was proved by various physico-chemical characterisation methods. The electrochemical activity of the catalyst materials with different PbPc to MWCNTs ratio were studied in alkaline, neutral and acidic media using RDE setup. The ratio with the highest electrocatalytic activity was synthesized again using different pyrolysis temperature. Finally, the performance of the most promising catalyst was compared with commercial Pt/C 20% and with only N-doped MWCNTs. Although

the onset potential in all different media was more positive for Pt/C catalyst, the limiting current densities of the Pb and N co-doped catalyst were comparable with Pt/C. A catalyst synthesised without the Pb had a much lower electrocatalytic activity, proving the importance of Pb inclusion in the catalyst material. Koutecky-Levich analysis of the ORR results revealed that the value of  $n$  in alkaline media was near four in the major range of studied potentials showing that the catalyst favours the splitting of the O-O bond via  $4e^-$  reduction pathway. In neutral and acid media, the  $n$  was around 3 that shows the mixed  $2e^- + 2e^-$  and  $4e^-$  electron transfer pathway. The PbPc/MWCNT catalyst materials showed outstanding stability during the LSV cycling in neutral and acid media, in alkaline media the stability was lower. Based on these results, it can be concluded that PbPc/MWCNT materials have a great potential to be used as cathode catalysts in the LTFs. Battery technology is shifting away from old lead-acid batteries and lead from the recycled batteries can be used as a raw material to synthesise Pb-doped carbon materials to catalyse the electrochemical reactions in fuel cells.

### Acknowledgments

This research has been supported by the Estonian Research Council (PSG312, IUT19–28, TK–141), by ERA.Net RUS Plus funding mechanism (project HeDoCat) and the European Regional Development Fund (projects no: 2014–2020.4.01.16–0041 and 2014–2020.4.01.15–0005).

### Declaration of Competing Interest

The authors declare that they have no competing financial interests or personal relationships that could have influenced the work reported in this paper.

### ORCID

Ehsan Zarmehri  <https://orcid.org/0000-0002-3995-0228>  
Ivar Kruusenberg  <https://orcid.org/0000-0002-8199-9324>

### References

1. M. Shao, Q. Chang, J.-P. Dodelet, and R. Chenitz, *Chem. Rev.*, **116**, 3594 (2016).
2. H. Erikson, A. Sarapuu, and K. Tammeveski, *ChemElectroChem*, **6**, 73 (2019).
3. H. Rismani-Yazdi, S. M. Carver, A. D. Christy, and O. H. Tuovinen, *J. Power Sources*, **180**, 683 (2008).
4. M. Vikkisk, I. Kruusenberg, U. Joost, E. Shulga, and K. Tammeveski, *Electrochim. Acta*, **87**, 709 (2013).
5. N. A. Karim and S. K. Kamarudin, *Appl. Energy*, **103**, 212 (2013).
6. M. Kiani, J. Zhang, Y. Luo, C. Jiang, J. Fan, G. Wang, J. Chen, and R. Wang, *J. Energy Chem.*, **27**, 1124 (2018).
7. X. Zhang, J. Shi, P. Liang, J. Wei, X. Huang, C. Zhang, and B. E. Logan, *Bioresour. Technol.*, **142**, 109 (2013).
8. B. Erable, N. Duteanu, S. M. S. Kumar, Y. Feng, M. M. Ghangrekar, and K. Scott, *Electrochem. Commun.*, **11**, 1547 (2009).
9. Z. L. Whonchee Lee, H. N. Per, and W. A. Hamilton, *Biofouling*, **8**, 165 (1995).
10. Y. L. Yuan Lv, Z. C. Liu Yang, J. Y. Baojian Jing, Z. X. Xiankai Jiang, and J. Zou, *Chem. Eng. J.*, **342**, 228 (2018).
11. J. Zhang, M. Lv, D. Liu, L. Du, and Z. Liang, *Int. J. Hydrogen Energy*, **43**, 4311 (2018).
12. S. L. Gojković, S. Gupta, and R. Savinell, *Electrochim. Acta*, **45**, 889 (1999).
13. R. Jasinski, *Nature*, **201**, 1212 (1964), (<https://nature.com/articles/2011212a0>).
14. J. H. Zagal, I. Kruusenberg, K. Tammeveski, J. Recio, K. Muñoz, and R. Venegas, *Encyclopedia of Interfacial Chemistry* (Elsevier, Amsterdam) p. 812 (2018), (<https://linkinghub.elsevier.com/retrieve/pii/B9780124095472135723>).
15. S. L. Lj Gojković, S. Gupta, and R. F. Savinell, *J. Electroanal. Chem.*, **462**, 63 (1999).
16. S. Baranton, C. Coutanceau, E. Garnier, and J. M. Léger, *J. Electroanal. Chem.*, **590**, 100 (2006).
17. S. Baranton, C. Coutanceau, C. Roux, F. Hahn, and J. M. Léger, *J. Electroanal. Chem.*, **577**, 223 (2005).
18. J. Zagal, M. Páez, A. A. Tanaka, J. R. dos Santos, and C. A. Linkous, *J. Electroanal. Chem.*, **339**, 13 (1992).
19. J. H. Zagal and M. T. M. Koper, *Angew. Chemie Int. Ed.*, **55**, 14510 (2016).
20. A. A. Tanaka, C. Fierro, D. Scherson, and E. B. Yeager, *J. Phys. Chem.*, **91**, 3799 (1987).
21. G. Landale, G. Faubert, R. Côté, D. Guay, J. P. Dodelet, L. T. Weng, and P. Bertrand, *J. Power Sources*, **61**, 227 (1996).
22. J. H. Zagal, I. Ponce, D. Baez, R. Venegas, J. Pavez, M. Paez, and M. Gulpfi, *Electrochem. Solid-State Lett.*, **15**, B90 (2012).
23. J. H. Zagal, F. J. Recio, C. A. Gutierrez, C. Zuñiga, M. A. Páez, and C. A. Caro, *Electrochem. Commun.*, **41**, 24 (2014).
24. V. Bambagioni et al., *J. Power Sources*, **196**, 2519 (2011).
25. Á. García, T. Haynes, M. Retuerto, P. Ferrer, L. Pascual, M. A. Peña, M. A. Salam, M. Mokhtar, D. Gianolio, and S. Rojas, *Ind. Eng. Chem. Res.*, **60**, 18759 (2021).
26. J. H. Zagal, S. Specchia, and P. Atanassov, *Curr. Opin. Electrochem.*, **27**, 100683 (2021).
27. Y. Huang et al., *Mater. Today*, **47**, 53 (2021).
28. A. Morozan, S. Campidelli, A. Filoramo, B. Jousselmé, and S. Palacin, *Carbon N. Y.*, **49**, 4839 (2011).
29. L. Osmieri, A. H. A. M. Videla, M. Armandi, and S. Specchia, *Int. J. Hydrogen Energy*, **41**, 22570 (2016).
30. R. Praats et al., *Electrochim. Acta*, **299**, 999 (2019).
31. J. Chen, X. Yan, C. Fu, Y. Feng, C. Lin, X. Li, S. Shen, C. Ke, and J. Zhang, *ACS Appl. Mater. Interfaces*, **11**, 37779 (2019).
32. Q. Ma, H. Jin, J. Zhu, Z. Li, H. Xu, B. Liu, Z. Zhang, J. Ma, and S. Mu, *Adv. Sci.*, **8**, 2102209 (2021).
33. R. Zheng, Q. Meng, L. Zhang, J. Ge, C. Liu, W. Xing, and M. Xiao, *Chemistry*, **29**, e202203180 (2023).
34. A. Aljabour, H. Awada, L. Song, H. Sun, S. Offenthaler, F. Yari, M. Bechmann, M. C. Scharber, and W. Schöfberger, *Angew. Int. Chemie*, **62**, e202302208 (2023).
35. J. M. Morris, S. Jin, J. Wang, C. Zhu, and M. A. Urynowicz, *Electrochem. Commun.*, **9**, 1730 (2007).
36. A. Czerwinski, M. Żelazowska, M. Grdeń, K. Kuc, J. D. Milewski, A. Nowacki, G. Wójcik, and M. Kopczyk, *J. Power Sources*, **85**, 49 (2000).
37. P. Ruetschi, J. Sklarчук, and R. T. Angstadt, *Electrochim. Acta*, **8**, 333 (1963).
38. K. Huang, H. Liu, H. Dong, M. Lin, and J. Ruan, *Resour. Conserv. Recycl.*, **167**, 105385 (2021).
39. S. Dhundhara, Y. P. Verma, and A. Williams, *Energy Convers. Manag.*, **177**, 122 (2018).
40. M. Jacoby, *C&EN Glob. Entrep.*, **97**, 29 (2019).
41. F. A. V. Biggins, S. Homan, D. Roberts, and S. Brown, *Energy Reports*, **7**, 34 (2021).
42. M. Vikkisk, I. Kruusenberg, S. Ratso, U. Joost, E. Shulga, I. Kink, P. Rauwel, and K. Tammeveski, *RSC Adv.*, **5**, 59495 (2015).
43. I. Kruusenberg, L. Matisen, and K. Tammeveski, *J. Nanosci. Nanotechnol.*, **13**, 621 (2013).
44. N. Alexeyeva, E. Shulga, V. Kisand, I. Kink, and K. Tammeveski, *J. Electroanal. Chem.*, **648**, 169 (2010).
45. E. Kuk, G. Snell, J. D. Bozek, W. T. Cheng, and N. Berrah, *Phys. Rev. A*, **63**, 062702 (2001).
46. E. Kuk et al., *Phys. Rev. Lett.*, **95**, 133001 (2005).
47. L. Tao et al., *Angew. Chemie - Int.*, **58**, 1019 (2019).
48. D. Liu, L. Tao, D. Yan, Y. Zou, and S. Wang, *ChemElectroChem*, **5**, 1775 (2018).
49. J. H. Lehman, M. Terrones, E. Mansfield, K. E. Hurst, and V. Meunier, *Carbon N. Y.*, **49**, 2581 (2011).
50. K. Behler, S. Osswald, H. Ye, S. Dimovski, and Y. Gogotsi, *J. Nanoparticle Res.*, **8**, 615 (2006).
51. J. J. Contreras-Navarrete, F. G. Granados-Martínez, L. Domratheva-Lvova, N. Flores-Ramírez, M. R. Cisneros-Magaña, L. García-González, L. Zamora-Peredo, and M. L. Mondragón-Sánchez, *Superf. y Vacío*, **28**, 111 (2015).
52. J. Hansson, A. Nylander, M. Flygare, K. Svensson, L. Ye, T. Nilsson, Y. Fu, and J. Liu, *Nanotechnology*, **31**, 455708 (2020).
53. K. Artyushkova, *J. Vac. Sci. Technol. A*, **38**, 031002 (2020).
54. S. Ratso, I. Kruusenberg, U. Joost, R. Saar, and K. Tammeveski, *Int. J. Hydrogen Energy*, **41**, 22510 (2016).
55. B. Xiao, J. P. Boudjou, and K. M. Thomas, *Langmuir*, **21**, 3400 (2005).
56. J. R. Pels, F. Kapteijn, J. A. Moulijn, Q. Zhu, and K. M. Thomas, *Carbon N. Y.*, **33**, 1641 (1995).
57. Q. Zhu, S. L. Money, A. E. Russell, and K. M. Thomas, *Langmuir*, **13**, 2149 (1997).
58. J. M. Jones, Q. Zhu, and K. M. Thomas, *Carbon N. Y.*, **37**, 1123 (1999).
59. S. Chandra, S. Sahu, and P. Pramanik, *Mater. Sci. Eng. B*, **167**, 133 (2010).
60. S. Aliev, I. A. Badmaeva, and L. D. Pokrovsky, *J. Phys. D: Appl. Phys.*, **45**, 305202 (2012).
61. J. Gomez-Bolivar, I. P. Mikheenko, R. L. Orozco, S. Sharma, D. Banerjee, M. Walker, R. A. Hand, M. L. Merroun, and L. E. Macaskie, *Front. Microbiol.*, **10**, 1276 (2019).
62. A. Mannan, Y. Hirano, A. T. Qutain, M. Koinuma, and T. Kida, *Am. J. Mater. Sci.*, **9**, 22 (2019).
63. S. Kundu, Y. Wang, W. Xia, and M. Muhler, *J. Phys. Chem. C*, **112**, 16869 (2008).
64. A. M. Bakry, F. S. Awad, J. A. Bobb, and M. S. El-Shall, *Cite This ACS Omega*, **5**, 33100 (2020).
65. A. Ermoloeff, A. Chabli, F. Pierre, G. Rolland, D. Rouchon, C. Vannuffel, C. Vergnaud, J. Baylet, and M. N. Séméria, *Surf. Interface Anal.*, **31**, 185 (2001).
66. K.-K. Türk, I. Kruusenberg, J. Mondal, P. Rauwel, J. Kozlova, L. Matisen, V. Sammelsgel, and K. Tammeveski, *J. Electroanal. Chem.*, **756**, 69 (2015).
67. L. A. Langley, D. E. Villanueva, and D. H. Fairbrother, *Chem. Mater.*, **18**, 169 (2006).
68. A. T. Masheter, L. Xiao, G. G. Wildgoose, A. Crossley, J. H. Jones, and R. G. Compton, *J. Mater. Chem.*, **17**, 3515 (2007).
69. L. R. Pederson, *J. Electron Spectrosc. Relat. Phenomena*, **28**, 203 (1982).
70. NIST X-ray Photoelectron Spectroscopy, "X-ray Photoelectron Spectroscopy Database XPS, Version 4.1, NIST Standard Reference Database." *Database*, **20**, 20899 (2000).
71. S. Ai, Y. Huang, T. Xie, X. Zhang, and C. Huang, *Environ. Sci. Pollut. Res.*, **27**, 37927 (2020).



72. H. Zhang et al., *J. Am. Chem. Soc.*, **139**, 14143 (2017).
73. N. Zion, D. A. Cullen, P. Zelenay, and L. Elbaz, *Angew. Chemie*, **132**, 2504 (2020).
74. S. Gupta, D. Tryk, I. Bae, W. Aldred, and E. Yeager, *J. Appl. Electrochem.*, **19**, 19 (1989).
75. Y. Liu, Y.-S. Fan, and Z.-M. Liu, *Chem. Eng. J.*, **361**, 416 (2019).
76. G. Jo and S. Shanmugam, *Electrochem. Commun.*, **25**, 101 (2012).
77. J. Li et al., *J. Am. Chem. Soc.*, **142**, 1417 (2020).
78. Y. Hiraike, M. Saito, H. Niwa, M. Kobayashi, Y. Harada, M. Oshima, J. Kim, Y. Nabae, and M. -A. Kakimoto, *Nanoscale Res. Lett.*, **10**, 179 (2015).
79. Z. Zhou, A. Chen, A. Kong, X. Fan, X. Zhang, and Y. Shan, *J. Electrochem. Soc.*, **165**, H658 (2018).
80. Y. Xinxin Jin, J. Xie, A. F. Huang, J.-P. Lee, Dacquin, and K. Wilson, *Catal.* **2017**, 7, 201 (2017).
81. K. K. Türk et al., *Int. J. Hydrogen Energy*, **43**, 23027 (2018).
82. W. Wang, Q. Jia, S. Mukerjee, and S. Chen, *ACS Catal.*, **9**, 10126 (2019).
83. I. Kruusenberg, N. Alexeyeva, and K. Tammeveski, *Carbon N. Y.*, **47**, 651 (2009).
84. X. Ge, A. Sumboja, D. Wu, T. An, B. Li, F. W. T. Goh, T. S. A. Hor, Y. Zong, and Z. Liu, *ACS Catal.*, **5**, 4643 (2015).
85. T. Xing, Y. Zheng, L. H. Li, C. C. C. Bruce, D. Gunzelmann, S. Z. Qiao, S. Huang, and Y. Chen, *ACS Nano*, **8**, 6856 (2014).
86. A. A. Gewirth, J. A. Varnell, and A. M. DiAscro, *Chem. Rev.*, **118**, 2313 (2018).
87. J. H. Zagal, F. Bedioui, and J.-P. Dodelet, *N 4-Macrocyclic Metal Complexes* (Springer, New York Berlin) 1st ed. p. 41 (2006).
88. F. Luo et al., *Nat. Mater.*, **19**, 1215 (2020).
89. S. Gottesfeld, I. D. Raistrick, and S. Srinivasan, *J. Electrochem. Soc.*, **134**, 1455 (1987).
90. R. Praats et al., *J. Solid State Electrochem.*, **25**, 57 (2021).
91. S. Ratso, I. Kruusenberg, A. Sarapuu, P. Rauwel, R. Saar, U. Joost, J. Aruväli, P. Kanninen, T. Kallio, and K. Tammeveski, *J. Power Sources*, **332**, 129 (2016).
92. I. Kruusenberg, D. Ramani, S. Ratso, U. Joost, R. Saar, P. Rauwel, A. M. Kannan, and K. Tammeveski, *ChemElectroChem*, **3**, 1455 (2016).

## Appendix 2

### Publication II

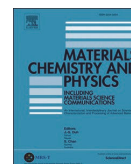
Zarmehri, E., Raudsepp, R., Danilson, M., Šutka, A., & Kruusenberg, I. (2023). Vanadium and carbon composite electrocatalyst for oxygen reduction reaction. *Materials Chemistry and Physics*, 307, 128162. <https://doi.org/10.1016/J.MATCHEMPHYS.2023.128162>





Contents lists available at ScienceDirect

## Materials Chemistry and Physics

journal homepage: [www.elsevier.com/locate/matchemphys](http://www.elsevier.com/locate/matchemphys)

# Vanadium and carbon composite electrocatalyst for oxygen reduction reaction

Ehsan Zarmehri<sup>a</sup>, Ragle Raudsepp<sup>a</sup>, Mati Danilson<sup>b</sup>, Andris Šutka<sup>c</sup>, Ivar Kruusenberg<sup>a,\*</sup><sup>a</sup> National Institute of Chemical Physics and Biophysics, Akadeemia Tee 23, 12618, Tallinn, Estonia<sup>b</sup> Department of Materials and Environmental Technology, Tallinn University of Technology, Ehitajate Tee 5, 19086, Tallinn, Estonia<sup>c</sup> Research Laboratory of Functional Materials Technologies, Faculty of Materials Science and Applied Chemistry, Riga Technical University, P. Valdena 3/7, 1048, Riga, Latvia

## HIGHLIGHTS

- One-step synthesis method was used to prepare V and N co-doped ORR catalysts.
- Vanadium incorporation significantly improved the ORR activity.
- V/N co-doped catalyst had outstanding stability in neutral and acidic media.
- V/N co-doped material showed remarkably better durability compared to 20% Pt/C.

## ARTICLE INFO

## Keywords:

Fuel cell  
ORR  
Carbon  
Vanadium  
Phthalocyanine

## ABSTRACT

Non-noble metal catalysts (NNMCs) are a promising alternative to platinum-based catalysts towards the large-scale commercial of hydrogen fuel cells and metal-air batteries. Improving the kinetics of oxygen reduction reaction (ORR) and reducing the price of catalysts for fuel cells and batteries has long time been of interest to researchers. NNMCs are a good choice for this purpose and have been studied extensively. The present study offers a low cost and straightforward method to fabricate inexpensive and durable ORR catalysts. By using vanadyl phthalocyanine, a promising carbon nanotube supported catalyst was synthesized, which shows competitive characteristics to platinum catalyst. Vanadium and nitrogen were co-doped on multiwall carbon nanotubes (MWCNTs) during a high temperature pyrolysis in argon atmosphere. Scanning and transmission electron microscopy, Raman spectroscopy, X-ray photoelectron spectroscopy and X-ray diffraction analysis were employed for physical characterization. V–N co-doped catalysts were electrochemically tested using the rotating disk electrode (RDE) setup in alkaline, neutral and acidic media.

## 1. Introduction

Fuel cell systems are regarded as one of the most environmentally friendly and efficient technologies for electric energy generation. However, such systems suffer from the scarcity and high cost of platinum that is generally applied for oxygen reduction reaction (ORR) and hydrogen oxidation reactions (HOR) [1]. It is estimated that approximately 50% of the whole fuel cell stack cost comes from noble-metal catalyst [2]. One of the reasons for the use of platinum is that it favors the O<sub>2</sub> reduction in the 4e<sup>−</sup> pathway. This O<sub>2</sub> reduction to H<sub>2</sub>O is greatly favorable since the production of peroxide using 2e<sup>−</sup> pathway can lead to the corrosion of various fuel cell components [3].

Thus, the sluggish kinetics of ORR and finding a replacement to expensive platinum catalyst are some of the main challenges to reduce the price and make the fuel cell technology more competitive. The low reaction rate contributes to a substantial loss of energy in the form of over potential at the cathode. Regarding the challenges mentioned above, many scientists have directed their attention to the development of suitable alternatives for platinum including non-noble metal catalysts (NNMCs) [4].

Among the NNMCs, single-atom catalysts (SACs) which includes well dispersed transition metal atoms in nitrogen-doped carbon [5–7], and transition metal macrocyclic complex (MN<sub>4</sub>) catalysts (e.g., phthalocyanines and porphyrins) are considered as one of the best alternatives to

\* Corresponding author.

E-mail address: [ivar.kruusenberg@kbfi.ee](mailto:ivar.kruusenberg@kbfi.ee) (I. Kruusenberg).<https://doi.org/10.1016/j.matchemphys.2023.128162>

Received 7 February 2023; Received in revised form 22 June 2023; Accepted 6 July 2023

Available online 10 July 2023

0254-0584/© 2023 Elsevier B.V. All rights reserved.



commercial Pt/C catalyst [8–10]. Using phthalocyanines and porphyrins leads to a metal and nitrogen co-doping and creation of metal-nitrogen (M–N) moieties which are considered as an active centre for ORR [11–19]. Iron phthalocyanine (FePc) is one of the most extensively used precursors for the synthesis of NNMCs [20].

Pyrolysis is one of the most effective and at the same time facile method for heteroatom doping. It is suggested that during the pyrolysis at high-temperatures, oxygen-containing groups are removed from the carbon nanomaterial surface and defects left in the framework act as active sites for doping [21,22]. For example, carboxylic groups start to decompose at temperatures of 350–750 °C and quinone as well as phenolic groups at 500–950 °C [23]. Although many studies have been carried out in this regard, finding the optimum pyrolysis temperature is still a challenge and fairly relies on the used precursors [24–27]. Tylus [28] and Zagal [29] perceived that using pyrolysis the structure of ligand across the active site improves, and thereby enhancing the electron-withdrawing properties. This improves the catalytic activity through shifting M(III)/(II) redox transition to much higher positive potentials relative to raw materials [30].

Mainly Co- and Fe-based phthalocyanines have been employed as dopants in order to synthesize M–N–C catalyst materials [31]. However, Fe–N–C catalyst is vulnerable against hydroxyl radicals which corrodes the catalyst and iron will be leached out [32]. Leached out iron degrades membrane and ionomer and is prone to Fenton reaction which further accelerates the degradation processes in fuel cells [33]. On Co–N–C catalyst two-electron reactions pathway is dominant and the catalyst is susceptible to oxidation and corrosion under certain operating conditions which leads to degradation of the catalyst structure and a loss of catalytic activity over time [34,35]. There are alternative phthalocyanines with central atoms other than Co and Fe, such as V, that may enhance the activity of the ORR catalyst and at the same time is not so prone to degradation.

Vanadium, which has been extensively investigated in battery research [36–38] and has proven its superb redox properties in redox flow batteries (VRFB), has in recent years also gained attention as a promising electrocatalyst candidate to facilitate ORR in fuel cells and metal-air batteries [39–42]. Elmouwahidi et al. [39] showed that a vanadium-based catalyst could have a comparable electrocatalytic activity to commercial Pt/C and Pd/C catalysts and that these composites provide a potential pathway for improving the activity of NNMCs. Another reason that makes the usage of vanadium attractive is that it is one of the most abundant element in earth crust and the second most abundant transition metal in sea water [43]. However, the synthesis of vanadium/carbon electrocatalyst contains several steps and is time consuming [40–42]. In this study we used simple and straightforward one-step synthesis method to prepare vanadium and carbon composite electrocatalysts for ORR. This makes the catalyst synthesis process more cost effective and the material attractive for practical use. The performance of vanadium-based catalyst was investigated in terms of electrocatalytic activity in acidic, alkaline and neutral media for proton-exchange membrane, anion-exchange membrane, and microbial fuel cell application.

## 2. Experimental

### 2.1. Materials and catalyst preparation

Vanadyl phthalocyanine (VPc) (Sigma-Aldrich) and MWCNTs (Nanocyl Co. Belgium) were mixed in different ratios (1:3, 1:1, 3:1) to synthesize vanadium and nitrogen co-doped carbon catalyst. The mixtures of VPc and MWCNTs were suspended in 5 ml of ethanol, followed by magnetic stirring and sonication for 2 h. Catalyst suspension was dried and pyrolyzed in a flowing argon atmosphere (99.999%) for 2 h at 600 °C, 800 °C, and 1000 °C. For comparison with VPc/MWCNT, dihydrogen phthalocyanine (H<sub>2</sub>Pc) (Sigma-Aldrich) was combined with MWCNT and pyrolyzed at 800 °C. Commercial Pt/C (20% Pt on carbon

black, from Alfa-Aesar, Germany) was utilized as a reference catalyst. To prepare a 0.1 M phosphor buffer solution (PBS), we utilized NaCl (Lachner, Czech Republic), Na<sub>2</sub>HPO<sub>4</sub>, KCl, and KH<sub>2</sub>PO<sub>4</sub> (Sigma-Aldrich, UK) (PBS). MilliQ-water (Millipore, Inc, 18.2 M cm) was used for all the solutions. KOH and H<sub>2</sub>SO<sub>4</sub> (Sigma-Aldrich) were used for alkaline and acidic electrolyte preparation.

### 2.2. Electrode preparation and electrochemical characterization of catalysts

For the rotating disk electrode (RDE) experiments, a glassy carbon (GC) disk with a geometric surface area (A) of 0.2 cm<sup>2</sup> was utilized as the substrate material. GC electrodes were carefully polished with 1.0 and 0.3 μm aluminum oxide powder (Buehler) to a mirror-like finish. The GC disk electrodes were sonicated in isopropanol and Milli-Q water for 5 min. To create a homogeneous catalyst layer on the GC surface, the electrodes were treated with VPc/MWCNT electrocatalysts using aqueous suspension (4 mg ml<sup>−1</sup>) containing ionomer. For acid and neutral media, 0.25% Nafion perfluorinated resin solution (Aldrich, USA) was used, while for alkaline media, 0.15% FAA-3 OH<sup>−</sup> ionomer (FumaTech Germany) was used. The catalyst suspensions were sonicated for 1 h in an ultrasonication bath (at < 30 °C) and then mixed for 2 min in a vortex mixer. The well-dispersed ink was then placed in a 5 μl aliquot onto the polished, clean GC electrode, fully covering the GC. This was repeated four times until the electrocatalyst loading of 0.4 mg cm<sup>−2</sup> was achieved. The RDE setup of a conventional five-neck three-electrode test cell, OrigaTrod rotator with speed control device (OrigaLys, France) and a potentiostat/galvanostat (Gamry Instruments1010E, USA) were used for electrochemical measurements. The electrode rotation rate (ω) was varied between 400 and 4400 rpm, scan rate was 10 mV s<sup>−1</sup> and step size 10 mV. A graphite rod was employed as the counter electrode, whereas a saturated calomel electrode (SCE) Hg/HgCl, 3 M KCl (SI-Analytics B 3410+, Germany) served as the reference electrode. All potentials in this article are given in terms of the reversible hydrogen electrode (RHE) and iR compensation value was applied. 0.5 M H<sub>2</sub>SO<sub>4</sub> (pH 0.3), 0.1 M PBS (pH 7.5) and 0.1 M KOH (pH 13) were used as electrolytes in the electrochemical experiments. The electrolyte solution was saturated with oxygen (99.999%, AGA) for current density and nitrogen (99.999%, AGA) for background measurements. During the electrochemical testing, a steady flow of these gases was maintained over the solution. Pt/C 20% and H<sub>2</sub>Pc/MWCNT catalysts were employed for the comparative purposes.

### 2.3. Physical characterization

The morphology of the VPc/MWCNT catalyst was examined by scanning electron microscopy (SEM) (Helios SUX from ThermoFisher) and transmission electron microscopy (TEM) (JEOL 2200 FS, Japan) using a resolution of 2.4 Å in TEM mode and 200 kV acceleration voltage. X-ray Diffraction (XRD) measurements were performed using a PANalytical apparatus, operating with Cu Kα radiation (λ = 0.154 nm) with 45 kV beam voltage and 40 mA beam current. Patterns were obtained in the range from 10° to 90° with 0.02° increments and the exposure time of 100 s. NovaTouch 4LX Analyzer (Quantachrome) was used to record the N<sub>2</sub> adsorption/desorption isotherms of the catalyst samples at nitrogen's boiling temperature (77 K). Before the measurements, the samples were degassed for 20 h under vacuum at 200 °C and then backfilled with N<sub>2</sub>. Up to a nitrogen relative pressure of P/P<sub>0</sub> = 0.2, the specific surface area (S<sub>BET</sub>) was determined using either the Brunauer-Emmett-Teller (BET) theory or the density functional theory (DFT). Near saturation pressure of N<sub>2</sub> (P/P<sub>0</sub> = 0.98), the total volume of pores (V<sub>tot</sub>) was measured. Using the t-plot technique and deBoer statistical thickness, the microporosity was determined. dp = 2V<sub>tot</sub>/S<sub>BET</sub> was used to calculate the average diameter of pores (d<sub>p</sub>) for a slit-type pore shape. X-ray photoelectron spectroscopy (XPS) (Axis Ultra DLD, Kratos Analytical) was used to analyze the surface chemistry of the

pyrolyzed VPc/MWCNT samples. Monochromatic Al K $\alpha$  X-ray source was used with source power of 105 W for survey scan and 225 W for characteristic energies to excite the photoelectrons. Pass energy of 160 eV was used for survey scan and pass energy of 20 eV for narrow core-level regions scans. The binding energy scale was corrected using C1 peak (284.6 eV) as a reference. Raman spectra of the as prepared catalyst material was collected with Raman spectrometer (Renishaw inVia) using a green laser beam (max 20 mW), x100 objective, 514 nm excitation wavelength, 100% laser power, 1 accumulation (extended), 150–4000 cm<sup>-1</sup> and exposure time of 30 s. The  $I_D/I_G$  ratios were extracted by fitting the spectra with two Lorentzian.

### 3. Results and discussion

#### 3.1. Physical characterization of VPc/CNT catalysts

The morphology and structure of the VPc/MWCNT (1:3) 800 °C catalyst was investigated with SEM and TEM (Fig. 1). From the SEM image (Fig. 1a) it can be observed that the catalyst material is evenly distributed all over the electrode surface and no larger agglomeration can be seen. In addition, SEM results evidence that the structure of carbon nanotube is remained in a good condition after the pyrolysis. HR-TEM analysis (Fig. 1b and c) demonstrates vanadium placement in a carbon nanotubes structure. Bright areas in a dark-field HR-TEM image (Fig. 1c) belong to a metallic element, in this case vanadium as no other metals were detected with XPS and XRD measurements which will be covered in the following sections of this manuscript.

Raman spectra of VPc/MWCNT is represented in Fig. 2. For the carbon-based materials, the most important peaks of Raman spectrum are observed around 1350 cm<sup>-1</sup> (D-band) and 1560–1600 cm<sup>-1</sup> (G-band). The D-band is a disorder induced characteristic that results from double resonance. The tangential vibrations of carbon atoms in graphite correspond to the G-band. The 2D-peak observed at 2680 cm<sup>-1</sup> corresponds to graphene-like carbon structure, which intensity is related to the average numbers of carbon layers in MWCNTs [44]. Many scientists have associated the effect of surface defects with the catalytic performance of carbon materials. Liu et al. and Tao et al. used the physical characterization and density functional theory (DFT) and indicated that the density of electron cloud for carbon atoms on the edge of defect is greater than that of the sp<sup>2</sup>-hybridized carbon atoms [45,46]. The ratio of  $I_D/I_G$  is obtained to be 1.14 for the VPc/MWCNT (1:3) pyrolyzed at 800 °C, indicating that the quantity of disordered carbon is the highest in comparison to the other catalysts. There are four extra peaks in VPc/MWCNT @ 600 °C at 1105 cm<sup>-1</sup>, 1210 cm<sup>-1</sup>, 1430 cm<sup>-1</sup> and 1455 cm<sup>-1</sup> that are related to the H–C bend and isoindole stretch [47] that is related to VPc. It shows that VPc structure has not been completely destroyed and there is still some non-decomposed VPc left after pyrolysis.

XRD analysis is conducted to investigate the phase composition together with the crystallography of the catalyst sample Fig. 3. The

peaks at 26.5° and 44.5° are related to graphitic carbon (ICDD 96-901-1578). V<sub>2</sub>O<sub>3</sub> and V<sub>2</sub>O<sub>5</sub> vanadium species were detected with XRD. The reference pattern of V<sub>2</sub>O<sub>3</sub> shows the characteristic peaks at 24.7°, 26.2°, 35.8°, 36.1°, 41.0°, 42.3°, 54.0° and 62.7° (JCPDS 41-1426) and (ICDD 98-000-6286) [48–51]. The highest intensity peak of V<sub>2</sub>O<sub>3</sub> at 26.2° overlaps with a broad graphite carbon. The peak at 42.3° overlaps with graphitic C, C–N and metallic V peaks. Peak at 36.0° corresponds to two V<sub>2</sub>O<sub>3</sub> reference peaks at 35.8° and 36.1°. Characteristic diffraction peaks for V<sub>2</sub>O<sub>5</sub> are at 20.4°, 26.3°, 32.5°, 34.4°, 41.5°, 42.3° and 51.5° (ICDD 98-009-4904). Similarly with V<sub>2</sub>O<sub>3</sub>, the highest intensity peaks of V<sub>2</sub>O<sub>5</sub> at 26.3° overlaps with graphitic carbon peak. The presence of V<sub>2</sub>O<sub>3</sub> and V<sub>2</sub>O<sub>5</sub> species were also confirmed with XPS which will be covered in the next section. In addition, with XRD and XPS, the only elements that were detected are C, N, V, O and since C and N do not have any characteristic peaks around 36° and 54° then it is another evidence that these peaks belong to vanadium compound. XRD spectra shows three peaks for metallic vanadium at 42.6°, 61.8° and 78.0° (ICDD 96-151-2550) and (ICSD 426983) for materials with 50 and 75% of VPc in the catalyst mixture and two peaks (at 42.6° and 78.0°) for catalyst with 25% of VPc. Three characteristic peaks of C<sub>3</sub>N<sub>4</sub> are located at 27.4°, 44.0° and 46.2° (PDF 98-24-8326) and (JCPDS 87-1526) but are difficult to identify due to an overlay of strong graphitic peaks. Based on XRD results it is rather ambitious to confirm or refute the presence of V and N. In order to validate the presence of vanadium and nitrogen after the doping we performed XPS measurements which will be covered in the following section.

The chemical composition of catalyst surface was evaluated through XPS. In Fig. 4 the XPS analysis of VPc/MWCNT (1:3) sample prepared at 800 °C is shown. Four peaks attributed to the C1s, O1s, N1s and V2p can be observed in the survey spectrum, revealing that nitrogen and vanadium doping occurred during the pyrolysis of VPc with MWCNT. According to the N1s XPS spectrum Fig. 4, four different kinds of nitrogen species are clearly observed over the surface of carbon nanomaterial. The observed peaks are deconvoluted to pyrrolic-N (400.0 eV), N-oxide (401.9 eV), pyridinic-N (398.6 eV), and graphitic-N (401.1 eV). The distribution of elemental components along with the relative amount of various nitrogen species is listed in Table 1. It is known that pyridinic-N and graphitic-N act as active centers for ORR in MN<sub>4</sub> doped carbon materials [52].

Graphitic-N atoms are linked to three adjacent C atoms in the hexagonal ring of graphene basal plane. Pyridinic-N found in six member carbon ring and pyrrolic-N in five member carbon ring, correspondingly transfer one and two p electrons to the aromatic  $\pi$ -system [44,52]. When the pyrolysis temperature is moderate (800 °C), the N functional groups involving pyridinic-N oxides, pyridones, and protonated pyridinic-N can be converted to pyridinic-N [53]. At higher temperatures, the graphitic-N and pyridinic-N are created at interior graphene layers and edges of graphene layer, respectively. The thermal stability of nitrogen functional groups is in the following order [53]:

–C(graphitic-N) > –C(pyridinic-N) > –C(pyrrolic-N) > –C(oxidized N).

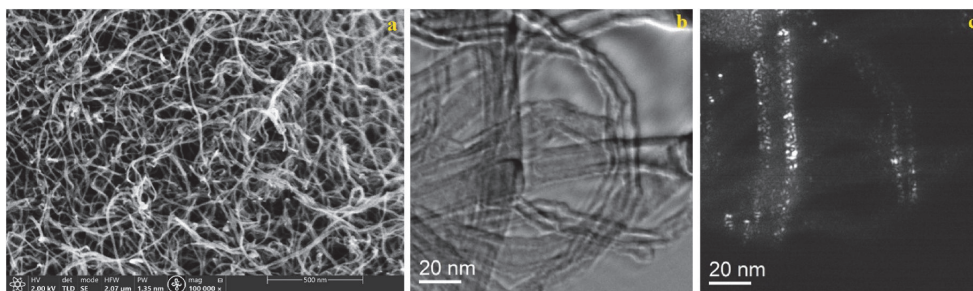


Fig. 1. SEM (a) and HR-TEM (b, c) images of VPc/MWCNT (1:3) catalyst materials heat treated at 800 °C.

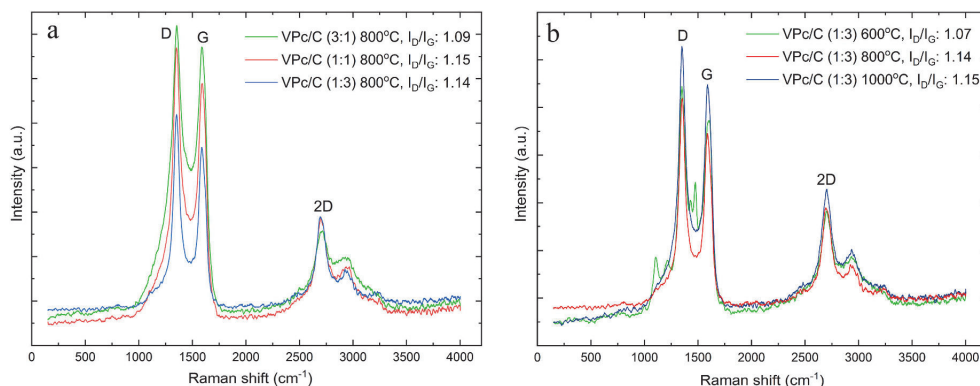


Fig. 2. Raman spectra of VPC/MWCNT @ 800 °C catalyst with different VPC to CNT ratio (a) and VPC/MWCNT (1:3) synthesized using different pyrolysis temperature (b).

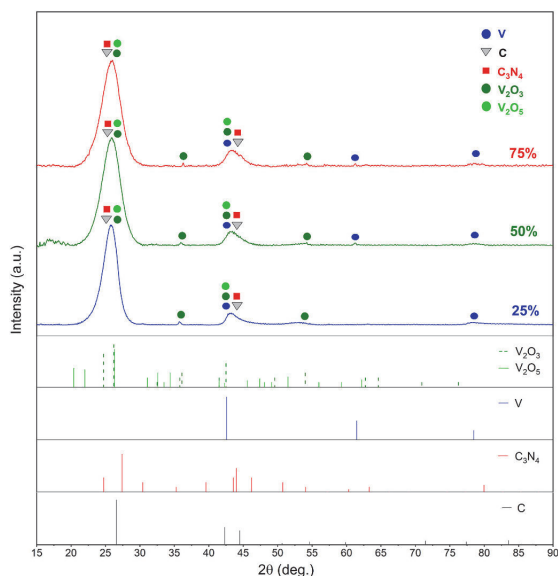


Fig. 3. XRD spectra of VPC/MWCNT @ 800 °C for different VPC to MWCNT ratios with corresponding reference patterns.

Since the binding energies between different oxygen groups are very close to each other, it is rather challenging to determine the exact type of oxygen groups remained on the surface. Based on the literature, the O1s peaks at 530.3 and 531.7 eV and correspond to V–O and C=O respectively [54–56]. The peaks at 533.3 (O1s) and 286.0 eV (C1s) are related to different C–O functional groups over the surface of MWCNT, involving quinone and carboxyl groups that are observed on the carbon nanotube surfaces in several earlier studies [57–59]. The V2p peaks at 517.2 and 524.4 eV corresponds to  $V^{5+}$  component in V–O bond [60, 61]. There are no visible peaks for the presence of V–C and V–N bonding and therefore we can conclude that V exists only in oxidized form. Transition metal oxides can be bonded to carbon network via oxygen ligands as suggested by Liang et al. [62].

BET surface area measurement, micropore volumes, pore volumes and average pore sizes for samples synthesized at different temperatures, are listed in Table 2. BET analysis revealed that VPC/MWCNT

catalyst heat treated at 1000 °C has the lowest average pore size, greatest surface area, and highest pore volume, whereas for the VPC/MWCNT 600 °C, the lowest pore volume and surface area is obtained. The pyrolysis of samples at various temperatures results in different catalyst structure and consequently various structures of pores [63–65]. Based on these results, the BET surface area of sample is decreasing in the following order: VPC/MWCNT 1000 °C > 800 °C > 600 °C.

This can be explained by the vanadium content at different temperatures (Table S1). The sample pyrolyzed at 600 °C has the highest at % of vanadium and the sample heat treated at 1000 °C has the lowest vanadium content. It has been shown that transition metals promote graphitization [66,67] which in turn decreases the surface area by decreasing the number of defects, therefore the material with highest V content (VPC/MWCNT (1:3) 600 °C) has the lowest surface area and the sample with lowest V content (VPC/MWCNT (1:3) 1000 °C) has the highest surface area.

### 3.2. Rotating disc electrode studies of oxygen reduction reaction

Electrochemical reduction of oxygen on VPC/MWCNT was studied with the RDE technique. Firstly, the effect of different VPC/MWCNTs ratios were studied. The linear sweep voltammetry (LSV) results measured in  $O_2$ -saturated 0.5 M  $H_2SO_4$ , 0.1 M PBS, and 0.1 M KOH solution at the rotating rate of 1600 rpm are presented in Figs. S2a–c. A strong reduction current can be seen for all synthesized electrocatalysts, which is most likely due to the creation of electrocatalytic active sites by nitrogen and vanadium co-doping. The material with the lowest VPC to MWCNT ratio (1:3) has the most positive onset potential in alkaline and acid media. In the neutral electrolyte, the onset is similar for the VPC/MWCNT (1:3) and (1:1).

The impact of pyrolysis temperature over the electrocatalytic activity of nitrogen and vanadium co-doped catalyst was also investigated. Results are presented in Figs. S2d–f, in all three media the highest activity is obtained at the pyrolysis temperature of 800 °C. The non-pyrolyzed catalyst showed the lowest activity in all three pH levels, proving that heat treatment of VPC is necessary. It was showed by Gupta et al. [68] that  $Mn_4$  can exert only a negligible impact over the ORR activity in acidic medium without annealing, which is confirmed by the results represented in Figs. S2d–f. According to Table 3, the most positive  $E_{onset}$  and  $E_{1/2}$  along with the largest limiting current density is related to the pyrolysis temperature of 800 °C.

In earlier studies it has been revealed that higher doping temperature can increase the electrocatalytic active species over the surface, and thus the catalyst prepared at 800 °C gives a higher activity than 600 °C [69, 70]. This is because the macrocyclic compound cannot be decomposed



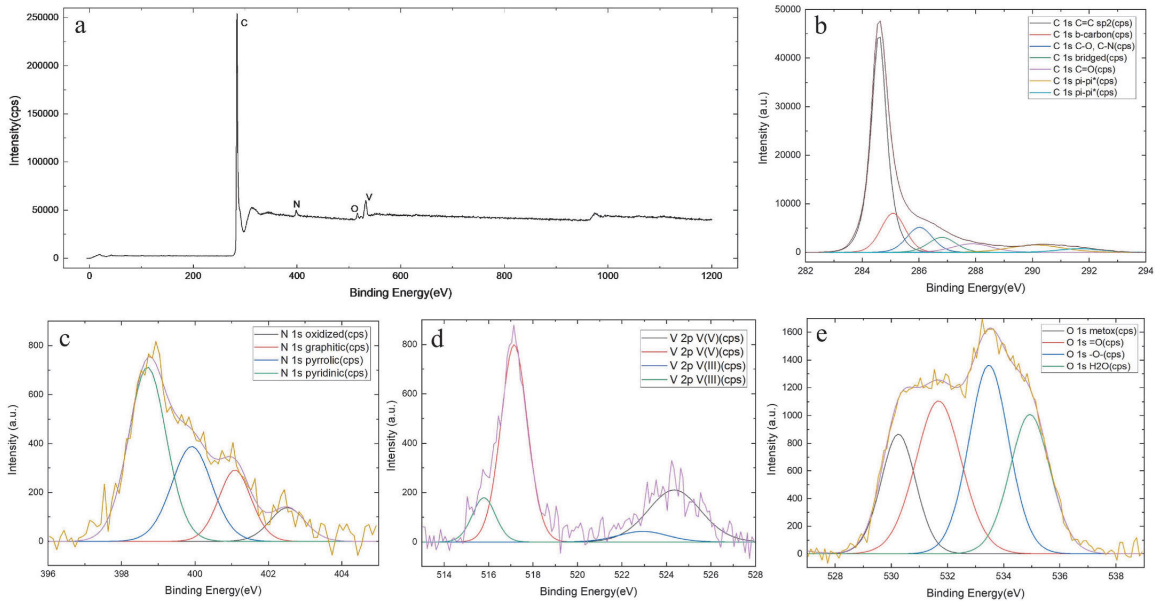


Fig. 4. XPS survey spectra of VPC/MWCNT (1:3) catalyst material (a) and high-resolution C1s (b) N1s (c), V2p (d), and O1s (e) spectra.

**Table 1**  
Elemental composition of VPC/MWCNT (atomic concentration percent) catalysts determined by XPS.

Catalyst	C1s at. %	N1s at. %	O1s at. %	V2p at. %
VPC/MWCNT (1:3) 800 °C	95.89	1.65	1.43	1.03
VPC/MWCNT (1:1) 800 °C	93.45	1.89	3.01	1.65
VPC/MWCNT (3:1) 800 °C	92.57	1.83	2.65	2.95
Relative concentration (%) of N moieties in the catalysts				
	Pyridinic at. %	Pyrrolic at. %	Graphitic at. %	N-Oxide at. %
VPC/MWCNT (1:3) 800 °C	45.4	38.8	9.7	6.1
VPC/MWCNT (1:1) 800 °C	47.6	27.5	16.4	8.4
VPC/MWCNT (3:1) 800 °C	44.2	8.8	42.6	4.4

**Table 2**  
Volume and surface properties of catalysts in various pyrolysis temperature.

Catalyst pyrolysis temperature	Multipoint BET (m <sup>2</sup> /g)	DFT method cumulative surface area (m <sup>2</sup> /g)	DFT method cumulative pore volume (cc/g)	DFT method pore radius (nm)	Average pore size (nm)
600 °C	136.81	112.87	0.2074	2.042	6.918
800 °C	153.76	143.01	0.2331	2.038	5.812
1000 °C	180.40	194.45	0.2812	2.038	5.344

completely at low temperatures (e.g., 600 °C), and thus the active sites are not formed over the catalyst surface [71]. It should be noted that the pyrolysis conditions should not exceed a certain temperature as it can lead to elimination of active sites, and thereby lowering the onset potential and current densities. Zhi et al. showed that pyrolysis of cobalt phthalocyanine at 1000 °C decreased the N/C ratio almost double compared with pyrolysis at 800 °C [72].

The ORR polarization curves are depicted Fig. 5a–c for alkaline, neutral and acidic media at different electrode rotation rates ( $\omega$ ) using

**Table 3**  
ORR results obtained for catalysts of VPC/MWCNT (1:3) in various pyrolysis temperatures and various electrolytes.

Electrolyte	Pyrolysis Temperature	$E_{onset}$ (V)	$E_{1/2}$ (V)	$j_d$ (mA cm <sup>-2</sup> )	$n$
Alkaline KOH 0.1 M	600 °C	0.89	0.72	−4.8	3.6
	800 °C	0.93	0.80	−5.0	3.9
	1000 °C	0.91	0.76	−5.2	3.7
Neutral PBS 0.1 M	600 °C	0.61	0.45	−4.1	2.7
	800 °C	0.76	0.50	−5.2	2.9
	1000 °C	0.71	0.46	−4.9	2.8
Acid H <sub>2</sub> SO <sub>4</sub> 0.5 M	600 °C	0.56	0.35	−3.8	2.9
	800 °C	0.70	0.52	−4.9	3.0
	1000 °C	0.64	0.46	−3.9	3.0

the catalyst material with highest activity, i.e., VPC/MWCNT (1:3) @ 800 °C. For the alkaline, neutral and acidic media, the onset potential is respectively 0.93 V, 0.80 V and 0.76 V vs RHE. In the neutral and acidic media, at lower rotation rate and more negative potentials, a 2nd reduction wave is observable, which indicates that subsequently O<sub>2</sub> is reduced to H<sub>2</sub>O<sub>2</sub> intermediate through the 2e<sup>−</sup> pathway followed by decomposition or further reduction to H<sub>2</sub>O by another subsequent 2e<sup>−</sup> pathway, which is expected to happen for heteroatom and metal co-doped carbon materials in a neutral medium according to previous similar studies [73,74]. In addition, it has been noted that the two-step reduction is inherent to carbon-based materials [75].

The Koutecky-Levich (K-L) equation is applied to measure the number of electrons ( $n$ ) which is transferred per oxygen molecule [73]:

$$\frac{1}{j} = \frac{1}{j_k} + \frac{1}{j_d} = -\frac{1}{nFk^b} - \frac{1}{0.62nFD^{2/3}\nu^{-1/6}c_O^b\omega^{1/2}}$$

In which,  $j$ ,  $j_d$  and  $j_k$  denote for the measured current density, diffusion-limited current density and kinetic current density, correspondingly.  $A$ ,  $K$ , and  $\omega$  are the geometric electrode area, electrochemical rate constant for O<sub>2</sub> reduction, and rotation rate respectively,  $F$  is Faraday constant (96,485C mol<sup>−1</sup>),  $D_{O_2}$  is oxygen diffusion coefficient (1.9 × 10<sup>−5</sup> cm<sup>2</sup> s<sup>−1</sup>

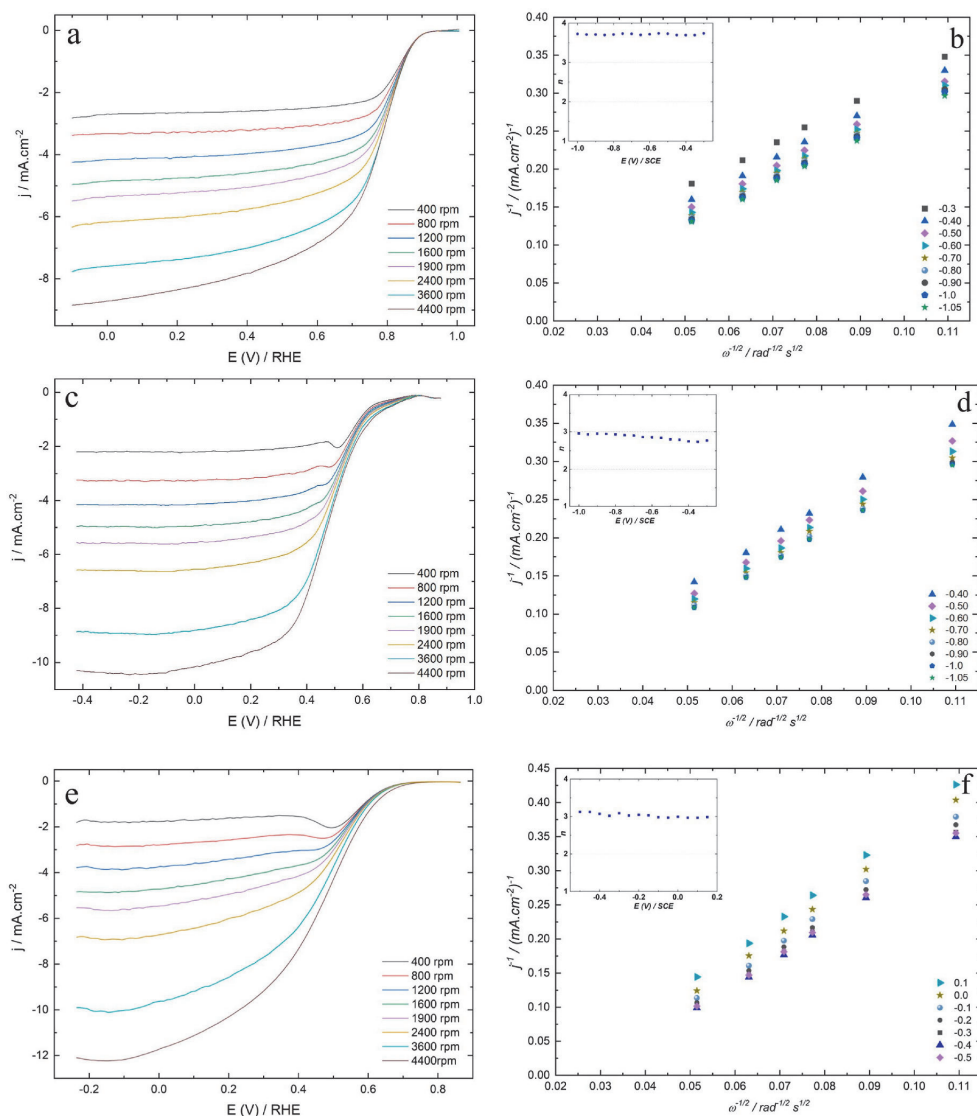


**Fig. 5.** RDE polarization curves for the ORR on VpC/MWCNT (1:3) @ 800 °C catalyst in O<sub>2</sub>-saturated 0.1 M KOH (a), 0.1 M PBS (c) and 0.5 M H<sub>2</sub>SO<sub>4</sub> (e),  $v = 10 \text{ mV s}^{-1}$ ,  $\omega = 400\text{--}4400 \text{ rpm}$ ; Koutecky-Levich plots for ORR on VpC/MWCNT (1:3) modified GC electrodes in O<sub>2</sub> molecule in 0.1 M KOH (b), 0.1 M PBS (d) and 0.5 M H<sub>2</sub>SO<sub>4</sub> (f). Inset shows the potential dependence of  $n$ .

for alkaline and neutral media and  $1.8 \times 10^{-5} \text{ cm}^2 \text{ s}^{-1}$  for acid medium),  $C_{\text{O}_2}^b$  is the oxygen concentration in the bulk ( $1.132 \times 10^{-6} \text{ mol cm}^{-3}$  for alkaline and neutral media and  $1.2 \times 10^{-6} \text{ mol cm}^{-3}$  in acidic media) and  $v$  is the kinematic viscosity of the solution ( $0.01 \text{ cm}^2 \text{ s}^{-1}$ ) [73,76]. Fig. 5d–f shows the K-L plots derived from the RDE analysis on ORR for the samples of VpC/MWCNT (1:3) @ 800 °C in alkaline, neutral and acidic media. For the alkaline medium, it is observed that the extrapolated K-L lines intercept near zero, indicating that the ORR mechanism is fairly controlled by the diffusion [73]. However, for the neutral and acidic media, the non-zero intercepts reveal that the ORR is dominantly controlled by the mixed kinetic diffusion. It is observed that in alkaline environment, the achieved  $n$  value is around four within the whole potential range studied. This demonstrates the great potential of

VpC/MWCNTs as cathode catalysts, specifically for the anion-exchange membrane fuel cells. In acidic and neutral environments, however, the  $n$  value is obtained to be about 3, which is an indicator of simultaneous  $4e^-$  and  $2e^- + 2e^-$  transfer pathways [75,77].

Multiple ORR pathways can happen on the surface of V/N/C catalyst because of simultaneous existence of different active sites with various structures. Ge et al. [78] stated that doping of nitrogen to carbon structure generates more positive charge on neighboring carbons to counteract the strong electronic affinity of the nitrogen atom. At the Fermi level, the conjugation effect of nitrogen lone-pair electrons increases bulk electrical conductivity and density of states [74]. The charge delocalization is thought to modify the adsorption behavior of carbon material towards O<sub>2</sub> molecules, effectively weakening the O–O

bond and facilitating oxygen electroreduction [79,80]. Lower separation energy of the O–O bond can be explained by electron transfer from nitrogen to the conjugated orbital of carbon, which increases the chance of electron donation to the oxygen orbital [81]. The nature and quantity of nitrogen on the catalyst, and thus the forming of catalytically active centers, has been found to be influenced by the metal center chosen [82, 83]. XPS results in this work revealed that the vanadium is in oxidation state of +5.  $V_2O_5$  possesses spaces between its connections which promotes oxygen adsorption on its surface [84,85]. The conduction electrons of the  $V_2O_5$  are adsorbed by the exposed  $O_2$  molecule leading to enhanced ORR [86,87]. Based on the RDE analysis, it can be concluded that the enhancement of catalytic activity with respect to limiting current values and onset potential is mainly owing to the presence of ORR active vanadium oxide and nitrogen surface groups.

To the best of our knowledge, there is no published work about V–N co-doped carbon materials for ORR. Our hypothesis about possible ORR mechanism on this catalyst material is based on other transition metal and nitrogen co-doped carbon materials, as well as vanadium oxide modified catalyst materials.

Fig. 6a–c represents the comparative LSV curves of five different types of catalyst. Commercial Pt/C, pure MWCNTs, N-doped MWCNT ( $H_2Pc/MWCNT$ ) and N/V co-doped MWCNT ( $VPc/MWCNT$ ) with and without pyrolysis are compared. The novel catalyst ( $VPc/MWCNT$  1:3) gives 0.04, 0.07, and 0.20 V more negative onset potential ( $E_{onset}$ ) in alkaline, neutral and acidic environments, in comparison to commercial Pt/C catalyst. Since the difference in  $E_{onset}$  between Pt/C and N/V co-doped catalyst is lower in alkaline media, compared to other two mediums, it can be concluded that V-doped catalyst performs better in alkaline medium. This result was also confirmed by comparison of  $n$  values. Compared with  $VPc/MWCNT$  (1:3),  $E_{onset}$  of  $H_2Pc/MWCNT$  is 20, 50 and 20 mV more negative in alkaline, neutral and acidic media respectively. Also,  $E_{1/2}$  is 60, 40 and 30 mV more negative when using  $H_2Pc/MWCNT$  in alkaline, neutral and acidic media respectively, which addresses the role of V atoms in performance improvement of the catalyst. It should be noted that since the material doped with vanadium and nitrogen is more active than the catalyst doped with only nitrogen, it proves that vanadium oxide is not only mixed within carbon nanotubes but is also bonded to carbon material and thereby enhancing the electrocatalytic activity. Table S2.1, S2.2 and S2.3 show a comparison of the RDE results obtained for  $VPc/MWCNT$  catalysts in various ratios of VPc to carbon that was pyrolyzed at 800 °C and  $H_2Pc/MWCNT$  and Pt/C in different media.

In order to measure the stability of prepared catalysts, the best sample of  $VPc/MWCNT$  was cycled 1000 times in alkaline, neutral and acid media. The LSV curves (Fig. 7) prove that the V–N/MWCNT catalyst gives superior stability with a little deviation in  $E_{1/2}$  for the acidic environment, and minor decrease in both  $E_{1/2}$  and limiting current density values for the alkaline environment. The fact that ORR polarization curves show very small losses in current density values, with no

shift in the onset potential, demonstrates that these materials have superior stability in both neutral and acidic environments.

Since the durability of the catalyst material is one of the major concerns in fuel cell technology, long-term chronoamperometric tests were performed with the  $VPc/MWCNT$  composite materials. The test was performed at a constant potential of 0.4 V vs SCE in 0.1 M KOH solution saturated with oxygen. As shown in Fig. 8, a high relative current of 87% for  $VPc/MWCNT$  is preserved after 20 h test. Chronoamperometry was repeated for 0.1 M PBS and 0.5 M  $H_2SO_4$  solutions. Relative current in these media is decreased to 92% from the initial current value, whereas the relative current of Pt/C catalyst decreases to 77% at a constant potential of 0.4 V vs RHE in the 0.5 M  $H_2SO_4$  solutions and reach to 82% in the alkaline medium and 79% in the neutral medium. These results strongly suggest that the  $VPc/MWCNT$  catalyst has much better electrochemical stability than the Pt/C catalyst.

#### 4. Conclusion

For the first time, nitrogen and vanadium co-doped carbon nanomaterials were prepared using a facile and cost effective one-step synthesis method. Vanadyl phthalocyanine (VPC) was used as a vanadium and nitrogen precursor and MWCNTs as a carbon support. The electrocatalytic activity of the prepared catalysts was studied in alkaline, basic and acidic media using the RDE setup. The catalyst, which was synthesized using VPC to MWCNT ratio of 1:3 had the most positive  $E_{onset}$  in alkaline and acidic media and highest diffusion-limited current values in neutral and acidic electrolytes. This catalyst was heat treated using three different temperatures from 600 to 1000 °C and the best ORR performance was obtained with the material synthesized at 800 °C. Compared to only N-doped MWCNT ( $H_2Pc/MWCNT$ ), V–N co-doped catalyst had higher diffusion-limited current values in all three electrolyte solutions, more positive  $E_{onset}$  in basic and alkaline media and the same  $E_{onset}$  in alkaline media. These results indicate clearly that vanadium doping increases the performance of ORR catalyst. Compared with the commercial Pt/C 20%, the  $E_{onset}$  of the  $VPc/MWCNT$  (1:3) @ 800 °C was 20, 50 and 20 mV more negative in alkaline, basic and acidic media accordingly, however, V–N co-doped catalyst material showed superior stability. In acidic electrolyte, after 20 h, relative current decreased to 92% from the initial current value, whereas the commercial Pt/C 20% performed with 77% of the initial current value. By taking into account the electrocatalytic activity, stability and economical synthesis method used in this work, it can be concluded that V–N co-doped materials have a great potential for being used as a cathode catalyst in the LTFs.

#### Description of authors contribution to the published work

Ehsan Zarmehri – synthesized the catalyst materials, performed RDE tests and physical characteristic studies (BET, XRD, Raman), formal analysis, wrote the initial draft. Ragle Raudsepp – critical review of the

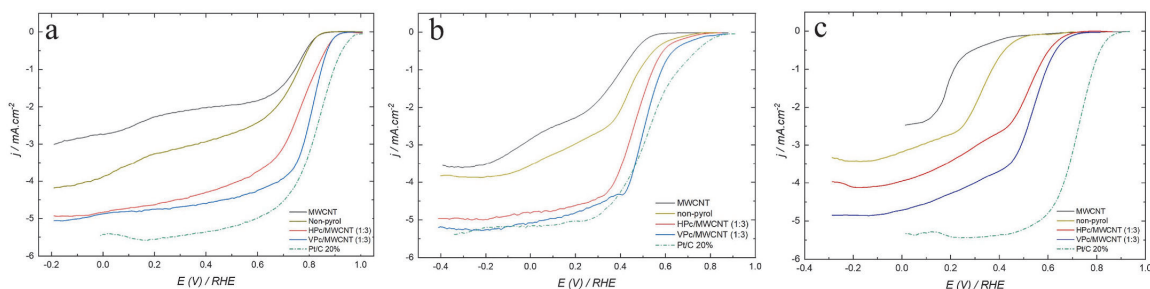


Fig. 6. Comparison of RDE results of oxygen reduction on MWCNT, non-pyrolysis material,  $H_2Pc/MWCNT$  (1:3),  $VPc/MWCNT$  (1:3) and Pt/C modified GC electrodes in  $O_2$ -saturated 0.1 M KOH (a), 0.1 M PBS (b) and 0.5 M  $H_2SO_4$  (c),  $v = 10 \text{ mV s}^{-1}$ ,  $\omega = 1600 \text{ rpm}$ .

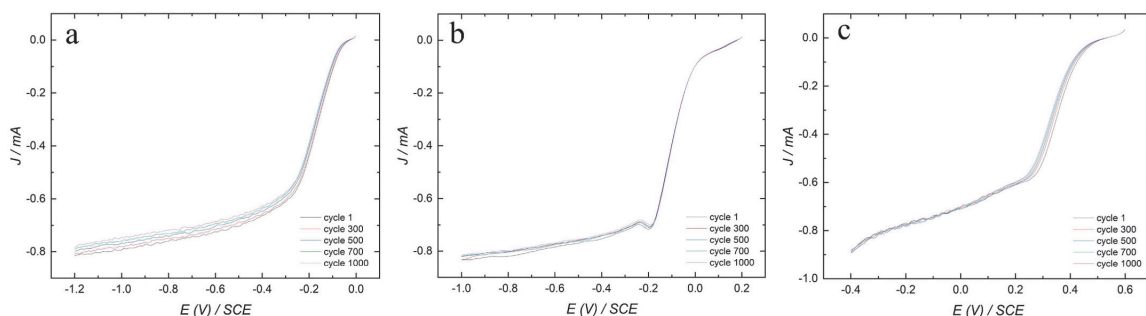


Fig. 7. Stability of VPC/MWCNT (1:3) in O<sub>2</sub>-saturated during 1000 cycles in 0.1 M KOH (a), 0.1 M PBS (b), and 0.5 M H<sub>2</sub>SO<sub>4</sub> (c),  $v = 10 \text{ mV s}^{-1}$ ,  $\omega = 1600 \text{ rpm}$ .

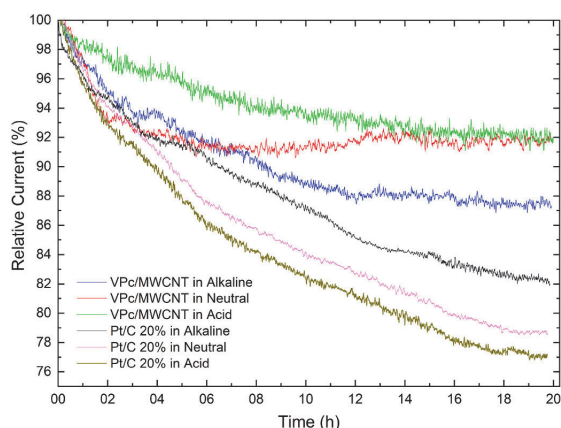


Fig. 8. Chronoamperometric responses for the ORR on VPC/MWCNT and Pt/C catalysts in O<sub>2</sub> saturated 0.1 M KOH, 0.1 M PBS and 0.5 M H<sub>2</sub>SO<sub>4</sub> solution for 20 h at 0.4 V vs RHE. Rotation speed: 200 rpm.

first draft, editing, writing the initial draft, formal analysis. **Mati Danilson** – performed XPS measurements, formal analysis. **Andris Sutka** – performed SEM measurements, formal analysis. **Ivar Kruusenberg** – helped to plan the research, supervising the laboratory work, manuscript writing. Critical review of the first draft.

#### Declaration of competing interest

The authors declare that they have no known competing financial interests or personal relationships that could have appeared to influence the work reported in this paper.

#### Data availability

Data will be made available on request.

#### Acknowledgements

This research has been supported by the Estonian Research Council (PSG312, IUT19-28, TK-141), by ERA.Net RUS plus funding mechanism (project HeDoCat) and the European Regional Development Fund (projects no: 2014-2020.4.01.16-0041 and 2014-2020.4.01.15-0005). The authors also acknowledge the high-resolution transmission electron microscopy facility at the federal institute of materials research and testing (BAM) and Dr. Julian Rosalie for acquiring HR-TEM images.

#### Appendix A. Supplementary data

Supplementary data to this article can be found online at <https://doi.org/10.1016/j.matchemphys.2023.128162>.

#### References

- [1] M. Shao, Q. Chang, J.P. Dodelet, R. Chenitz, Recent advances in electrocatalysts for oxygen reduction reaction, *Chem. Rev.* 116 (2016) 3594–3657, <https://doi.org/10.1021/acs.chemrev.5b00462>.
- [2] Y. Nie, L. Li, Z. Wei, Recent advancements in Pt and Pt-free catalysts for oxygen reduction reaction, *Chem. Soc. Rev.* 44 (2015) 2168–2201, <https://doi.org/10.1039/c4cs00484a>.
- [3] H. Erikson, A. Sarapu, K. Tammeveski, Oxygen reduction reaction on silver catalysts in alkaline media: a minireview, *Chemelectrochem* 6 (2019) 73–86, <https://doi.org/10.1002/celc.201800913>.
- [4] M. Vikkisk, I. Kruusenberg, U. Joost, E. Shulga, K. Tammeveski, Electrocatalysis of oxygen reduction on nitrogen-containing multi-walled carbon nanotube modified glassy carbon electrodes, *Electrochim. Acta* 87 (2013) 709–716, <https://doi.org/10.1016/j.electacta.2012.09.071>.
- [5] P. Rao, D. Wu, T.-J. Wang, J. Li, P. Deng, Q. Chen, Y. Shen, Y. Chen, X. Tian, Single atomic cobalt electrocatalyst for efficient oxygen reduction reaction, *eScience* 2 (2022) 399–404, <https://doi.org/10.1016/j.escl.2022.05.004>.
- [6] P. Rao, D. Wu, J. Luo, J. Li, P. Deng, Y. Shen, X. Tian, A plasma bombing strategy to synthesize high-loading single-atom catalysts for oxygen reduction reaction, *Cell Reports Phys. Sci.* 3 (2022), 100880, <https://doi.org/10.1016/j.xcrp.2022.100880>.
- [7] P. Rao, Y. Deng, W. Fan, J. Luo, P. Deng, J. Li, Y. Shen, X. Tian, Movable type printing method to synthesize high-entropy single-atom catalysts, *Nat. Commun.* 13 (2022) 1–9, <https://doi.org/10.1038/s41467-022-32850-8>, 2022.
- [8] I. Kruusenberg, L. Matisen, K. Tammeveski, Oxygen electroreduction on multi-walled carbon nanotube supported metal phthalocyanines and porphyrins in alkaline media, *J. Nanosci. Nanotechnol.* 13 (2013) 621–627, <https://doi.org/10.1166/jnn.2013.6918>.
- [9] I. Kruusenberg, L. Matisen, K. Tammeveski, Oxygen electroreduction on multi-walled carbon nanotube supported metal phthalocyanines and porphyrins in alkaline media, *J. Nanosci. Nanotechnol.* 13 (2013) 621–627, <https://doi.org/10.1166/jnn.2013.6918>.
- [10] I. Kruusenberg, J. Mondal, L. Matisen, V. Sammelsg, K. Tammeveski, Oxygen reduction on graphene-supported MN4 macrocycles in alkaline media, *Electrochim. Commun.* 33 (2013) 18–22, <https://doi.org/10.1016/j.elecom.2013.04.005>.
- [11] X. Huang, T. Shen, T. Zhang, H. Qiu, X. Gu, Z. Ali, Y. Hou, Efficient oxygen reduction catalysts of porous carbon nanostructures decorated with transition metal species, *Adv. Energy Mater.* 10 (2020), 1900375, <https://doi.org/10.1002/aenm.201900375>.
- [12] L. Tong, Y.-C. Wang, M.-X. Chen, Z.-Q. Chen, Q.-Q. Yan, C.-L. Yang, Z.-Y. Zhou, S.-Q. Chu, X. Feng, H.-W. Liang, Hierarchically porous carbons as supports for fuel cell electrocatalysts with atomically dispersed Fe-N x moieties, *Chem. Sci.* 10 (2019) 8236–8240, <https://doi.org/10.1039/C9SC01154D>.
- [13] A. Zitolo, V. Goellner, V. Arnel, M.T. Sougrati, T. Mineva, L. Stievano, E. Fonda, F. Jaouen, Identification of catalytic sites for oxygen reduction in iron- and nitrogen-doped graphene materials, *Nat. Mater.* 14 (2015) 937–942, <https://doi.org/10.1038/nmat4367>.
- [14] J. Li, S. Ghoshal, W. Liang, M.T. Sougrati, F. Jaouen, B. Halevi, S. McKinney, G. McCool, C. Ma, X. Yuan, Z.F. Ma, S. Mukerjee, Q. Jia, Structural and mechanistic basis for the high activity of Fe-N-C catalysts toward oxygen reduction, *Energy Environ. Sci.* 9 (2016) 2418–2432, <https://doi.org/10.1039/C6EE01160H>.
- [15] J. Li, M. Chen, D.A. Cullen, S. Hwang, M. Wang, B. Li, K. Liu, S. Karakalos, M. Lucero, H. Zhang, C. Lei, H. Xu, G.E. Sterbinsky, Z. Feng, D. Su, K.L. More, G. Wang, Z. Wang, G. Wu, Atomically dispersed manganese catalysts for oxygen reduction in proton-exchange membrane fuel cells, *Nat. Catal.* 112 (1) (2018) 935–945, <https://doi.org/10.1038/s41929-018-0164-8>, 2018.



- [16] F. Li, G.F. Han, H.J. Noh, S.J. Kim, Y. Lu, H.Y. Jeong, Z. Fu, J.B. Baek, Boosting oxygen reduction catalysis with abundant copper single atom active sites, *Energy Environ. Sci.* 11 (2018) 2263–2269, <https://doi.org/10.1039/C8EE01169A>.
- [17] A. Han, W. Chen, S. Zhang, M. Zhang, Y. Han, J. Zhang, S. Ji, L. Zheng, Y. Wang, L. Gu, C. Chen, Q. Peng, D. Wang, Y. Li, A polymer encapsulation strategy to synthesize porous nitrogen-doped carbon-nanosphere-supported metal isolated-single-atomic-site catalysts, *Adv. Mater.* 30 (2018), 1706508, <https://doi.org/10.1002/ADMA.201706508>.
- [18] J. Li, S. Chen, N. Yang, M. Deng, S. Ibraheem, J. Deng, J. Li, L. Li, Z. Wei, Ultrahigh-loading zinc single-atom catalyst for highly efficient oxygen reduction in both acidic and alkaline media, *Angew. Chemie Int. Ed.* 58 (2019) 7035–7039, <https://doi.org/10.1002/ANIE.201902109>.
- [19] E. Luo, H. Zhang, X. Wang, L. Gao, L. Gong, T. Zhao, Z. Jin, J. Ge, Z. Jiang, C. Liu, W. Xing, Single-atom Cr–N4 sites designed for durable oxygen reduction catalysis in acid media, *Angew. Chemie Int. Ed.* 58 (2019) 12469–12475, <https://doi.org/10.1002/ANIE.201906289>.
- [20] T. Marshall-Roth, N.J. Libretto, A.T. Wrobel, K.J. Anderton, M.L. Pegis, N.D. Rickes, T. Van Voorhis, J.T. Miller, Y. Surendranath, A pyridinic Fe–N4 macrocycle mediates the active sites in Fe/N-doped carbon electrocatalysts, *Nat. Commun.* 11 (2020) 1–14, <https://doi.org/10.1038/s41467-020-18969-6>.
- [21] Z.-H. Sheng, H.-L. Gao, W.-J. Bao, F.-B. Wang, X.-H. Xia, Synthesis of boron doped graphene for oxygen reduction reaction in fuel cells, *J. Mater. Chem.* 22 (2012) 390–395, <https://doi.org/10.1039/C1JM14694G>.
- [22] X. Bo, M. Li, C. Han, L. Guo, The influence of boron dopant on the electrochemical properties of graphene as an electrode material and a support for Pt catalysts, *Electrochim. Acta* 114 (2013) 582–589, <https://doi.org/10.1016/j.electacta.2013.10.088>.
- [23] R.C. Bansal, M. Goyal, *Activated Carbon Adsorption*, first ed., CRC Press, 2005 <https://doi.org/10.1680/bwse.63341.147>.
- [24] A. Morozan, S. Campidelli, A. Filoramo, B. Jousselm, S. Palacin, Catalytic activity of cobalt and iron phthalocyanines or porphyrins supported on different carbon nanotubes towards oxygen reduction reaction, *Carbon N. Y.* 49 (2011) 4839–4847, <https://doi.org/10.1016/j.carbon.2011.07.004>.
- [25] L. Osmieri, A.H.A. Monteverde Videla, M. Armandi, S. Specchia, Influence of different transition metals on the properties of Me–N–C (Me = Fe, Co, Cu, Zn) catalysts synthesized using SBA-15 as tubular nano-silica reactor for oxygen reduction reaction, *Int. J. Hydrogen Energy* 41 (2016) 22570–22588, <https://doi.org/10.1016/j.ijhydene.2016.05.223>.
- [26] L. Osmieri, Transition metal–nitrogen–carbon (M–N–C) catalysts for oxygen reduction reaction. Insights on synthesis and performance in polymer electrolyte fuel cells, *ChemEngineering* 3 (2019) 16, <https://doi.org/10.3390/chemengineering3010016>.
- [27] R. Praats, I. Krusenbergh, M. Käärrik, U. Joost, J. Aruväli, P. Paiste, R. Saar, P. Rauwel, M. Kook, J. Leis, J.H. Zagal, K. Tammeveski, Electroreduction of oxygen in alkaline solution on iron phthalocyanine modified carbide-derived carbons, *Electrochim. Acta* 299 (2019) 999–1010, <https://doi.org/10.1016/j.electacta.2019.01.062>.
- [28] U. Tylus, Q. Jia, K. Strickland, N. Ramaswamy, A. Serov, P. Atanassov, S. Mukerjee, Elucidating oxygen reduction active sites in pyrolyzed metal–nitrogen coordinated non-precious-metal electrocatalyst systems, *J. Phys. Chem. C* 118 (2014) 8999–9008, <https://doi.org/10.1021/jp500781v>.
- [29] J.H. Zagal, I. Ponce, D. Baez, R. Venegas, J. Pavez, M. Paez, M. Gulppi, A possible interpretation for the high catalytic activity of heat-treated non-precious metal nx/C catalysts for O2 reduction in terms of their formal potentials, *Electrochem. Solid State Lett.* 15 (2012), <https://doi.org/10.1149/2.032206esl>, B90–B92.
- [30] J.H. Zagal, S. Griveau, J.F. Silva, T. Nyokong, F. Bedioui, Metallophthalocyanine-based molecular materials as catalysts for electrochemical reactions, *Coord. Chem. Rev.* 254 (2010) 2755–2791, <https://doi.org/10.1016/j.ccr.2010.05.001>.
- [31] W. Orellana, Metal-phthalocyanine functionalized carbon nanotubes as catalyst for the oxygen reduction reaction: a theoretical study, *Chem. Phys. Lett.* 541 (2012) 81–84, <https://doi.org/10.1016/j.cplett.2012.05.048>.
- [32] J. Chen, X. Yan, C. Fu, Y. Feng, C. Lin, X. Li, S. Shen, C. Ke, J. Zhang, Insight into the rapid degradation behavior of nonprecious metal Fe–N–C electrocatalyst-based proton exchange membrane fuel cells, *ACS Appl. Mater. Interfaces* 11 (2019) 37779–37786, <https://doi.org/10.1021/ACSAMI.9B13474>.
- [33] Q. Ma, H. Jin, J. Zhu, Z. Li, H. Xu, B. Liu, Z. Zhang, J. Ma, S. Mu, Stabilizing Fe–N–C catalysts as model for oxygen reduction reaction, *Adv. Sci.* 8 (2021), 2102209, <https://doi.org/10.1002/ADVS.202102209>.
- [34] Q. Ma, H. Jin, J. Zhu, Z. Li, H. Xu, B. Liu, Z. Zhang, J. Ma, S. Mu, Stabilizing Fe–N–C catalysts as model for oxygen reduction reaction, *Adv. Sci.* 8 (2021), 2102209, <https://doi.org/10.1002/ADVS.202102209>.
- [35] A. Morozan, S. Campidelli, A. Filoramo, B. Jousselm, S. Palacin, Catalytic activity of cobalt and iron phthalocyanines or porphyrins supported on different carbon nanotubes towards oxygen reduction reaction, *Carbon N. Y.* 49 (2011) 4839–4847, <https://doi.org/10.1016/j.carbon.2011.07.004>.
- [36] Z. Abidin, K.R. Khalilpour, Single and polystorage technologies for renewable-based hybrid energy systems, *Polygeneration with Polystorage Chem. Energy Hubs.* (2019) 77–131, <https://doi.org/10.1016/B978-0-12-813306-4.00004-5>.
- [37] H. Huang, Y. Ouyang, D. Wu, F. Wang, S. Wang, X. Meng, W. Yuan, P. Guo, L. Y. Zhang, Holey PdPb nanosheet array: an advanced catalyst for methanol electrooxidation, *Int. J. Hydrogen Energy* 46 (2021) 2236–2243, <https://doi.org/10.1016/j.ijhydene.2020.10.093>.
- [38] Y. Guo, J. Huang, J.K. Feng, Research progress in preparation of electrolyte for all-vanadium redox flow battery, *J. Ind. Eng. Chem.* 118 (2023) 33–43, <https://doi.org/10.1016/J.JIEC.2022.11.037>.
- [39] A. Elmouhahidi, E. Bailón-García, A.F. Pérez-Cadenas, J. Castelo-Quibén, F. Carrasco-Marín, Carbon-vanadium composites as non-precious catalysts for electro-reduction of oxygen, *Carbon N. Y.* 144 (2019) 289–300, <https://doi.org/10.1016/j.carbon.2018.12.038>.
- [40] R. Mehek, N. Iqbal, T. Noor, Z.A. Ghazi, M. Umair, Metal organic framework derived vanadium oxide supported nanoporous carbon structure as bifunctional electrocatalyst for metal air batteries, *SSRN Electron. J.* (2022), <https://doi.org/10.2139/ssrn.4232998>.
- [41] H. Zhang, S. Wu, D. Deng, H. Wang, S. Xun, F. Chen, J. Zhang, L. Xu, The nitrogen-doped carbon supported ultra-small vanadium nitride nanoparticles as a highly efficient oxygen reduction electrocatalyst for the rechargeable Zn–air battery, *Inorg. Chem. Commun.* 137 (2022), 109230, <https://doi.org/10.1016/j.inoche.2022.109230>.
- [42] L. Cheng, H. Huang, Z. Lin, Y. Yang, Q. Yuan, L. Hu, C. Wang, Q. Chen, N. O multi-coordinated vanadium single atom with enhanced oxygen reduction activity, *J. Colloid Interface Sci.* 594 (2021) 466–473, <https://doi.org/10.1016/j.jcis.2021.03.074>.
- [43] D. Rehder, Vanadium. Its role for humans, *Met. Ions Life Sci.* 13 (2013) 139–169, [https://doi.org/10.1007/978-94-007-7500-8\\_5](https://doi.org/10.1007/978-94-007-7500-8_5).
- [44] J.H. Lehman, M. Terrones, E. Mansfield, K.E. Hurst, V. Meunier, Evaluating the characteristics of multiwall carbon nanotubes, *Carbon N. Y.* 49 (2011) 2581–2602, <https://doi.org/10.1016/j.carbon.2011.03.028>.
- [45] L. Tao, M. Qiao, R. Jin, Y. Li, Z. Xiao, Y. Wang, N. Zhang, C. Xie, Q. He, D. Jiang, G. Yu, Y. Li, S. Wang, Bridging the surface charge and catalytic activity of a defective carbon electrocatalyst, *Angew. Chemie - Int. Ed.* 58 (2019) 1019–1024, <https://doi.org/10.1002/anie.201810207>.
- [46] D. Liu, L. Tao, D. Yan, Y. Zou, S. Wang, Recent advances on non-precious metal porous carbon-based electrocatalysts for oxygen reduction reaction, *ChemElectrochem* 5 (2018) 1775–1785, <https://doi.org/10.1002/celec.201800086>.
- [47] C.A. Jennings, R. Aroca, G.J. Kovacs, C. Hsiao, FT-Raman spectroscopy of thin films of titanyl phthalocyanine and vanadyl phthalocyanine, *J. Raman Spectrosc.* 27 (1996) 867–872, [https://doi.org/10.1002/\(SICI\)1097-4555\(199612\)27:12<867::AID-JRS43>3.0.CO;2-H](https://doi.org/10.1002/(SICI)1097-4555(199612)27:12<867::AID-JRS43>3.0.CO;2-H).
- [48] I. Mjejri, M. Gaudon, G. Song, C. Labrugère, A. Rougier, Crystallized V2O5 as oxidized phase for unexpected multi-color electrochromism in V2O3 thick film, *ACS Appl. Energy Mater.* 1 (2018) 2721–2729, <https://doi.org/10.1021/ACS.AEM.8B00386>.
- [49] Z.I. Zaki, M.H. El-Sadek, H.H. Ali, H. Ahmed, Synthesis of vanadium carbide by mechanical activation assisted carbothermic reduction, *Materials* 13 (2020) 1–11, <https://doi.org/10.3390/ma13194408>.
- [50] L. Zhao, L. Miao, C. Liu, C. Li, T. Asaka, Y. Kang, Y. Iwamoto, S. Tanemura, H. Gu, H. Su, Solution-processed V2O2–SiO2 composite films with simultaneously enhanced luminous transmittance, solar modulation ability and anti-oxidation property, *Sci. Reports* 41 (4) (2014) 1–11, <https://doi.org/10.1038/srep07000>, 2014.
- [51] Y. Bai, P. Jin, S. Ji, H. Luo, Y. Gao, Preparation and characterization of V2O3 micro-crystals via a one-step hydrothermal process, *Ceram. Int.* 39 (2013) 7803–7808, <https://doi.org/10.1016/j.ceramint.2013.03.040>.
- [52] S. Ratso, I. Krusenbergh, U. Joost, R. Saar, K. Tammeveski, Enhanced oxygen reduction reaction activity of nitrogen-doped graphene/multi-walled carbon nanotube catalysts in alkaline media, *Int. J. Hydrogen Energy* 41 (2016) 22510–22519, <https://doi.org/10.1016/j.ijhydene.2016.02.021>.
- [53] B. Xiao, J.P. Boudou, K.M. Thomas, Reactions of nitrogen and oxygen surface groups in nanoporous carbons under inert and reducing atmospheres, *Am. Chem. Soc.* 21 (2005) 3400–3409, <https://doi.org/10.1021/la0472495>.
- [54] V. Bondarenko, Z. Martunas, S. Kaciulis, L. Pandolfi, Sol-gel synthesis and XPS characterization of sodium–vanadium oxide bronze thin films, *J. Electron Spectrosc. Relat. Phenomena* 131–132 (2003) 99–103, [https://doi.org/10.1016/S0368-2048\(03\)00110-5](https://doi.org/10.1016/S0368-2048(03)00110-5).
- [55] H. Wu, Z. Zhang, M. Qin, Q. Wang, Z. Cao, Y. Yu, B. Jia, X. Qu, Solution combustion synthesis of crystalline V2O3 and amorphous V2O3/C as anode for lithium-ion battery, *J. Am. Ceram. Soc.* 103 (2020) 2643–2652, <https://doi.org/10.1111/JACE.16962>.
- [56] L. Li, P. Ma, S. Hussain, L. Jia, D. Lin, X. Yin, Y. Lin, Z. Cheng, L. Wang, FeS2/carbon hybrids on carbon cloth: a highly efficient and stable counter electrode for dye-sensitized solar cells, *Sustain. Energy Fuels* 3 (2019) 1749–1756, <https://doi.org/10.1039/C9SE00240E>.
- [57] K.-K. Türk, I. Krusenbergh, J. Mondal, P. Rauwel, J. Kozlova, L. Matisen, V. Sammelsg, K. Tammeveski, Oxygen electroreduction on MN4-macrocycle modified graphene/multi-walled carbon nanotube composites, *J. Electroanal. Chem.* 756 (2015) 69–76, <https://doi.org/10.1016/j.jelechem.2015.08.014>.
- [58] L. Tian, S. Min, F. Wang, Integrating noble-metal-free metallic vanadium carbide cocatalyst with CdS for efficient visible-light-driven photocatalytic H2 evolution, *Appl. Catal. B Environ.* 259 (2019), 118029, <https://doi.org/10.1016/j.apcatb.2019.118029>.
- [59] P. Vijayakumar, R. Govindaraj, N. Santhosh, M.S. Pandian, A. Pandikumar, P. Ramasamy, Investigation of suitable binder combination and electrochemical charge transfer dynamics of vanadium carbide nanoparticles-based counter electrode in Pt-free dye-sensitized solar cell, *J. Mater. Sci.* 53 (2018) 4444–4455, <https://doi.org/10.1007/s10853-017-1843-6>.
- [60] P.S. Simas, V.S. Antonin, L.S. Parreira, P. Hammer, F.L. Silva, M.S. Kronka, R. B. Valim, M.R.V. Lanza, M.C. Santos, Carbon modified with vanadium nanoparticles for hydrogen peroxide electrogeneration, *Electrochim. Acta* 84 (8) (2017) 311–320, <https://doi.org/10.1007/S12678-017-0366-X>, 2017.
- [61] Jinghua Liu, He Xiong, Fei Guo, Baosheng Liu, Zijun Sun, Li Zhang, Haixin Chang, Vanadium nitride nanoparticle decorated N-doped carbon nanotube/N-doped



- carbon nanosheet hybrids via a C 3 N 4 self-sacrificing method for electrochemical capacitors, *RSC Adv.* 12 (2022) 15354–15360, <https://doi.org/10.1039/D2RA02789E>.
- [62] Y. Liang, Y. Li, H. Wang, J. Zhou, J. Wang, T. Regier, H. Dai, Co<sub>3</sub>O<sub>4</sub> nanocrystals on graphene as a synergistic catalyst for oxygen reduction reaction, *Nat. Mater.* 10 (2011) 780–786, <https://doi.org/10.1038/nmat3087>, 2011 1010.
- [63] K. Behler, S. Osswald, H. Ye, S. Dimovski, Y. Gogotsi, Effect of thermal treatment on the structure of multi-walled carbon nanotubes, *J. Nanoparticle Res.* 8 (2006) 615–625, <https://doi.org/10.1007/s11051-006-9113-6>.
- [64] J.J. Contreras-Navarrete, F.G. Granados-Martínez, L. Domratheva-Lvova, N. Flores-Ramírez, M.R. Cisneros-Magaña, L. García-González, L. Zamora-Peredo, M.L. Mondragón-Sánchez, MWCNTs oxidation by thermal treatment with air conditions, *Superf. y Vacío*. 28 (2015) 111–114.
- [65] J. Hansson, A. Nylander, M. Flygare, K. Svensson, L. Ye, T. Nilsson, Y. Fu, J. Liu, Effects of high temperature treatment of carbon nanotube arrays on graphite: increased crystallinity, anchoring and inter-tube bonding, *Nanotechnology* 31 (2020) 455708–455719, <https://doi.org/10.1088/1361-6528/ab9677>.
- [66] S.J. Goldie, S. Jiang, K.S. Coleman, Cobalt nanoparticle catalysed graphitization and the effect of metal precursor decomposition temperature, *Mater. Adv.* 2 (2021) 3353–3361, <https://doi.org/10.1039/D1MA00125F>.
- [67] M. Sevilla, C. Sanchis, T. Valdés-Soh, E. Morallón, A.B. Fuertes, Synthesis of graphitic carbon nanostructures from sawdust and their application as electrocatalyst supports, *J. Phys. Chem. C* 111 (2007) 9749–9756, <https://doi.org/10.1021/jp072246x>.
- [68] S. Gupta, D. Tryk, I. Bae, W. Aldred, E. Yeager, Heat-treated polyacrylonitrile-based catalysts for oxygen electroreduction, *J. Appl. Electrochem.* 19 (1989) 19–27, <https://doi.org/10.1007/BF01039385>.
- [69] Y. Liu, Y.-S. Fan, Z.-M. Liu, Pyrolysis of iron phthalocyanine on activated carbon as highly efficient non-noble metal oxygen reduction catalyst in microbial fuel cells, *Chem. Eng. J.* 361 (2019) 416–427, <https://doi.org/10.1016/j.cej.2018.12.105>.
- [70] G. Jo, S. Shanmugam, Single-step synthetic approach for boron-doped carbons as a non-precious catalyst for oxygen reduction in alkaline medium, *Electrochem. Commun.* 25 (2012) 101–104, <https://doi.org/10.1016/j.elecom.2012.09.025>.
- [71] J. Li, L. Jiao, E. Wegener, L.L. Richard, E. Liu, A. Zitolo, M.T. Sougrati, S. Mukerjee, Z. Zhao, Y. Huang, F. Yang, S. Zhong, H. Xu, A.J. Kropf, F. Jaouen, D.J. Myers, Q. Jia, Evolution pathway from iron compounds to Fe 1 (II)–N 4 sites through gas-phase iron during pyrolysis, *J. Am. Chem. Soc.* 142 (2020) 1417–1423, <https://doi.org/10.1021/jacs.9b11197>.
- [72] L. Zhi, T. Gorelik, R. Friedlein, J. Wu, U. Kolb, W.R. Salaneck, K. Müllen, Solid-state pyrolyses of metal phthalocyanines: a simple approach towards nitrogen-doped CNTs and metal/carbon nanocables, *Small* 1 (2005) 798–801, <https://doi.org/10.1002/smll.200500150>.
- [73] K.K. Türk, I. Kruusenberg, E. Kibena-Pöldsepp, G.D. Bhowmick, M. Kook, K. Tammeveski, L. Matisen, M. Merisalu, V. Sammelselg, M.M. Ghangrekar, A. Mitra, R. Banerjee, Novel multi walled carbon nanotube based nitrogen impregnated Co and Fe cathode catalysts for improved microbial fuel cell performance, *Int. J. Hydrogen Energy* 43 (2018) 23027–23035, <https://doi.org/10.1016/j.ijhydene.2018.10.143>.
- [74] W. Wang, Q. Jia, S. Mukerjee, S. Chen, Recent insights into the oxygen-reduction electrocatalysis of Fe/N/C materials, *ACS Catal.* 9 (2019) 10126–10141, <https://doi.org/10.1021/acscatal.9b02583>.
- [75] I. Kruusenberg, N. Alexeyeva, K. Tammeveski, The pH-dependence of oxygen reduction on multi-walled carbon nanotube modified glassy carbon electrodes, *Carbon* N. Y. 47 (2009) 651–658, <https://doi.org/10.1016/j.carbon.2008.10.032>.
- [76] S. Gottesfeld, I.D. Raistrick, S. Srinivasan, Oxygen reduction kinetics on a platinum RDE coated with a recast nation film, *J. Electrochem. Soc.* 134 (1987) 1455–1462, <https://doi.org/10.1149/1.2100689>.
- [77] E.E. Switzer, T.S. Olson, A.K. Datye, P. Atanasov, M.R. Hibbs, C. Fujimoto, C. J. Cornelius, Novel KOH-free anion-exchange membrane fuel cell: performance comparison of alternative anion-exchange ionomers in catalyst ink, *Electrochim. Acta* 55 (2010) 3404–3408, <https://doi.org/10.1016/j.electacta.2009.12.073>.
- [78] X. Ge, A. Sumboja, D. Wu, T. An, B. Li, F.W.T. Goh, T.S.A. Hor, Y. Zong, Z. Liu, Oxygen reduction in alkaline media: from mechanisms to recent advances of catalysts, *ACS Catal.* 5 (2015) 4643–4667, <https://doi.org/10.1021/acscatal.5b00524>.
- [79] P.H. Matter, L. Zhang, U.S. Ozkan, The role of nanostructure in nitrogen-containing carbon catalysts for the oxygen reduction reaction, *J. Catal.* 239 (2006) 83–96, <https://doi.org/10.1016/j.jcat.2006.01.022>.
- [80] G. Lalande, G. Faubert, R. Côté, D. Guay, J.P. Dodelet, L.T. Weng, P. Bertrand, Catalytic activity and stability of heat-treated iron phthalocyanines for the electroreduction of oxygen in polymer electrolyte fuel cells, *J. Power Sources* 61 (1996) 227–237, [https://doi.org/10.1016/S0378-7753\(96\)02356-7](https://doi.org/10.1016/S0378-7753(96)02356-7).
- [81] Q. Liu, H. Zhang, H. Zhong, S. Zhang, S. Chen, N-doped graphene/carbon composite as non-precious metal electrocatalyst for oxygen reduction reaction, *Electrochim. Acta* 81 (2012) 313–320, <https://doi.org/10.1016/j.electacta.2012.07.022>.
- [82] H.S. Oh, H. Kim, The role of transition metals in non-precious nitrogen-modified carbon-based electrocatalysts for oxygen reduction reaction, *J. Power Sources* 212 (2012) 220–225, <https://doi.org/10.1016/j.jpowsour.2012.03.098>.
- [83] G. Wu, C.M. Johnston, N.H. Mack, K. Artyushkova, M. Ferrandon, M. Nelson, J. S. Lezama-Pacheco, S.D. Conradson, K.L. More, D.J. Myers, P. Zelenay, Synthesis–structure–performance correlation for polyaniline–Me–C non-precious metal cathode catalysts for oxygen reduction in fuel cells, *J. Mater. Chem.* 21 (2011), 11392, <https://doi.org/10.1039/c0jm03613g>.
- [84] S. Surnev, M.G. Ramsey, F.P. Netzer, Vanadium oxide surface studies, *Prog. Surf. Sci.* 73 (2003) 117–165, <https://doi.org/10.1016/J.PROGSURF.2003.09.001>.
- [85] M.M. Sajid, N.A. Shad, Y. Javed, S.B. Khan, Z. Zhang, N. Amin, H. Zhai, Preparation and characterization of Vanadium pentoxide (V<sub>2</sub>O<sub>5</sub>) for photocatalytic degradation of monoazo and diazo dyes, *Surface. Interfac.* 19 (2020), 100502, <https://doi.org/10.1016/J.SURFINT.2020.100502>.
- [86] M.T. Noori, C.K. Mukherjee, M.M. Ghangrekar, Enhancing performance of microbial fuel cell by using graphene supported V<sub>2</sub>O<sub>5</sub>-nanorod catalytic cathode, *Electrochim. Acta* 228 (2017) 513–521, <https://doi.org/10.1016/J.ELECTACTA.2017.01.016>.
- [87] P. Ji, X. Gao, X. Du, C. Zheng, Z. Luo, K. Cen, Relationship between the molecular structure of V<sub>2</sub>O<sub>5</sub>/TiO<sub>2</sub> catalysts and the reactivity of SO<sub>2</sub> oxidation, *Catal. Sci. Technol.* 6 (2016) 1187–1194, <https://doi.org/10.1039/C5CY00867K>.

## Appendix 3

### Publication III

Raudsepp, R., Türk, K. K., **Zarmehri, E.**, Joost, U., Rauwel, P., Saar, R., Mäeorg, U., Dyck, A., Bron, M., Chen, Z., Noda, S., Kruusenberg, I., & Tammeveski, K. (2024). Boron and Fluorine Co-Doped Graphene/Few-Walled Carbon Nanotube Composite as Highly Active Electrocatalyst for Oxygen Reduction Reaction. *ChemNanoMat*, 10(6), e202300546. <https://doi.org/10.1002/CNMA.202300546>



# Boron and Fluorine Co-Doped Graphene/Few-Walled Carbon Nanotube Composite as Highly Active Electrocatalyst for Oxygen Reduction Reaction

Ragle Raudsepp,<sup>[a]</sup> Karl-Kalev Türk,<sup>[a]</sup> Ehsan Zarmehri,<sup>[b]</sup> Urmas Joost,<sup>[c]</sup> Protima Rauwel,<sup>[c]</sup> Rando Saar,<sup>[c]</sup> Uno Mäeorg,<sup>[a]</sup> Alexander Dyck,<sup>[d]</sup> Michael Bron,<sup>[e]</sup> Zhongming Chen,<sup>[ff]</sup> Suguru Noda,<sup>[f]</sup> Ivar Kruusenberg,<sup>\*,[a]</sup> and Kaido Tammeveski<sup>[a]</sup>

Functionalization of nanocarbon materials with heteroatoms is of paramount interest as doping of carbon with electron withdrawing groups results in change of electrochemical properties of the potential catalyst. Adding fluorine, as the most electronegative element into the doping process next to boron is expected to have significant effect on the design of novel nanocarbon-based electrocatalysts. In this paper boron and fluorine co-doped reduced graphene oxide/few-walled carbon nanotube (BF-rGO/FWCNT) catalysts are synthesized *via* simple and low-cost direct pyrolysis method using boron trifluoride diethyl etherate (BTDE). Composition analysis confirmed that

boron and fluorine have been grafted onto the carbon support. Rotating disk electrode (RDE) measurements revealed that BF-rGO/FWCNT has remarkable electrocatalytic activity toward the oxygen reduction reaction (ORR) both in alkaline and acid media. The onset potential of the best BF-rGO/FWCNT catalyst was 50 mV more positive in alkaline and 600 mV more positive in acidic media compared with un-doped rGO/FWCNT. The half-wave potential was 100 mV more positive in alkaline media and 700 mV more positive in acidic media in comparison with un-doped rGO/FWCNT.

## Introduction

The advancement of catalysts with high performance, stability, and efficiency for oxygen reduction reaction (ORR), hydrogen evolution reaction (HER), and oxygen evolution reaction (OER) is the fundamental basis for renewable energy technologies, such

as fuel cells and water electrolysis. In fuel cells the ORR plays an extremely important role in the development and commercialization of fuel cell technologies as well as next generation metal-air batteries.<sup>[1–3]</sup> Although fuel cells and metal-air batteries have been investigated intensively there are still obstacles that need to be overcome in order to envisage commercialization of these technologies.<sup>[1]</sup> The main drawback is related to the electrochemical reduction of oxygen attributed to the slow kinetics of breaking the strong O=O bond. An active electrocatalyst is needed in order to speed up the ORR process by lowering the activation energy of the reaction.<sup>[4]</sup> Up to now mainly Pt-based catalysts have been preferred but considering many disadvantages of platinum i.e. high cost, poor durability and sensitivity towards fuel impurities, much effort has now been devoted to the exploration of materials which have a similar electrocatalytic activity to that of platinum along with the potential to overcome the above-mentioned drawbacks.<sup>[5–8]</sup> Non-precious metal catalysts containing transition metal atoms have attracted interest as promising ORR electrocatalysts, in particular for anion exchange membrane fuel cells.<sup>[9–12]</sup> Metal macrocyclic complexes like phthalocyanines, porphyrins and chalcogenides containing Co and Fe atoms have been considered as one of the best non-noble metal ORR catalysts.<sup>[13–19]</sup> Among the other non-platinum catalysts heteroatom doping of nanocarbons has been found to be an easy and effective way to improve the ORR and OER kinetics.<sup>[20–25]</sup> In fact, doped carbon materials are attractive due to their low cost, good tolerance to fuel impurities, long-term stability and good electrocatalytic activity towards the ORR.<sup>[22,26]</sup> Mostly N, P, S and B doping have been investigated owing to their reasonable atomic size in order to enter the carbon network.<sup>[26–32]</sup> Fluorine-doped carbon

[a] Dr. R. Raudsepp, K.-K. Türk, Prof. U. Mäeorg, Dr. I. Kruusenberg, Prof. K. Tammeveski  
Institute of Chemistry  
University of Tartu  
Ravila 14a, 50411 Tartu, Estonia  
E-mail: ivar.kruusenberg@ut.ee


[b] E. Zarmehri  
National Institute of Chemical Physics and Biophysics  
Akadeemia tee 23, 12618, Tallinn, Estonia

[c] Dr. U. Joost, Prof. P. Rauwel, Dr. R. Saar  
Institute of Physics  
University of Tartu  
W. Ostwald Str. 1, 50411 Tartu, Estonia

[d] Dr. A. Dyck  
DLR-Institut für Vernetzte Energiesysteme e.sa V.  
Urban and Residential Technologies  
Carl-von Ossietzky-Str. 15, 26129 Oldenburg, Germany

[e] Prof. M. Bron  
Martin-Luther-Universität Halle-Wittenberg, Naturwissenschaftliche Fakultät II,  
Institut für Chemie  
von-Danckelmann-Platz 4, 06120 Halle (Saale), Germany

[f] Dr. Z. Chen, Prof. S. Noda  
Department of Applied Chemistry  
Waseda University  
3-4-1 Okubo, Shinjuku-ku, Tokyo 169-8555, Japan

 Supporting information for this article is available on the WWW under <https://doi.org/10.1002/cnma.202300546>

materials have lately attracted much attention mostly because of the high electronegativity of this element.<sup>[33–36]</sup> High electronegativity is also one of the main reasons why fluorine has been widely used as co-dopant along with N, B and S.<sup>[37–41]</sup> Previous works have shown that introducing other atoms with different electronegativities than the host atomic network breaks the electroneutrality of the material and creates favorable adsorption sites for O<sub>2</sub>.<sup>[23,42–44]</sup> The latter, which is slightly negatively charged while approaching the carbon network, favors adsorption on the positively charged sites of carbon connected to electronegative heteroatoms.<sup>[45,46]</sup> The most examined heteroatom-doped materials are nitrogen-doped nanocarbons like mesoporous carbons, single- and multi-walled carbon nanotubes and graphene.<sup>[26,47–49]</sup> While the doping of carbon materials with nitrogen has been well explored, materials doped with boron and fluorine on the other hand are still rather poorly studied.

There are three main methods to introduce boron atoms into the carbon network: (1) chemical vapor deposition using carbon and boron sources and a catalyst, (2) thermal annealing of carbon material in the presence of a boron precursor and (3) a two-step thermal treatment method.<sup>[50–53]</sup> Another alternative method is single-step pyrolysis, which is a facile approach for doping boron into the carbon network.<sup>[54–56]</sup> Similarly to boron atoms, fluorine can be introduced into the carbon structure. Among the aforementioned methods, plasma treatment and direct chemical synthesis have also been used for fluorine doping.<sup>[33–35,57]</sup>

It is suggested that during the pyrolysis at high-temperatures, oxygen-containing groups are removed from the carbon nanomaterial surface and defects left in the framework act as active sites for boron or fluorine doping.<sup>[52,54,58]</sup> For example carboxylic groups start to decompose at temperatures of 350–750 °C and quinone as well as phenolic groups at 500–950 °C.<sup>[59,60]</sup> Schniepp et al. examined the C/O ratio after heat-treatment of graphene oxide (GO) and found that at temperatures below 500 °C the C/O ratio was 7 and at temperatures above 750 °C the C/O ratio was higher than 13.<sup>[61]</sup>

Lazar et al. showed that depending on the chemical nature of doping, boron can be added substitutionally or additionally into the carbon network.<sup>[62]</sup> After substitutional doping boron will be bonded to carbon the sp<sup>2</sup> network by replacement of carbon atoms within the network.<sup>[52]</sup> On additional boron doping, sp<sup>3</sup> carbon atoms will be introduced into the sp<sup>2</sup> carbon network while BH<sub>2</sub> species are added on the surface and at the edges of the carbon material.<sup>[62]</sup> Most common bonding configurations of boron incorporated into carbon network are BCO<sub>2</sub>, BC<sub>2</sub>O, BC<sub>3</sub> and B<sub>4</sub>C.<sup>[63–65]</sup> According to earlier study by Jo and Shanmugam, the amount of B–C bonding plays a key role in the ORR process. They demonstrated that the catalysts which contained higher amounts of B<sub>3</sub>C, B<sub>4</sub>C and BC<sub>3</sub> species were more active towards the ORR.<sup>[55]</sup> This indicates that higher B/C ratio could be favorable to enhance the ORR kinetics, which was also reinforced by Cheng and co-workers.<sup>[51]</sup>

Fundamental studies have shown that positively charged boron induces chemisorption of O<sub>2</sub>. In fact, the electrons that are transferred to O<sub>2</sub> weaken the O–O bond leading to ORR.

These electrons come from adjacent carbon atoms with boron acting as a bridge.<sup>[66]</sup> Fazio et al. demonstrated that associative ORR is preferred to dissociative ORR on B-doped carbon materials.<sup>[30]</sup> Meaning that after the adsorption of O<sub>2</sub> end-on dioxygen species are formed, which will be directly reduced to hydroperoxo species without going through an energetically expensive side-on intermediates as it is in the dissociative mechanism.<sup>[30]</sup>

Compared to the B-doping of carbon materials, F-doping is rather poorly studied. This implies that the mechanism of the ORR on doped material and the exact role of fluorine in such materials is not yet clear. Up to now fluorine has been mainly associated with the increase of electrical conductivity of the catalyst material.<sup>[67]</sup> As F is a highly electronegative element and has excessive valence electrons in contrast with nitrogen and boron, doping fluorine into carbon materials should consistently lead to a semiconducting behavior on F-doping in low amounts and to formation of conductor behavior at high content.<sup>[68,69]</sup> It has also been reported that fluorine could effectively remove and replace oxygen functional groups of GO along with simultaneous F-doping on the basal plane and edges of graphene.<sup>[35,70,71]</sup> Therefore F-doping can be also considered as simultaneous method for GO reduction.<sup>[35,70,72]</sup>

Boron and fluorine dual-doped carbon nanomaterials prepared by single-step solution plasma process has been studied by Chokradjaroen, et al..<sup>[41]</sup> They found that the BF dual doped catalyst had the highest ORR activity compared with non-doped and only boron-doped carbon materials. However, the dual-doped catalyst material also drove ORR via two-electron pathway.

In this work, a simple and low-cost method was developed to produce boron and fluorine co-doped carbon nanomaterials. Graphene oxide was mixed with acid-treated few-walled carbon nanotubes (FWCNT) and boron trifluoride diethyl etherate was used as a boron and fluorine source. The GO/FWCNT composite and boron trifluoride diethyl etherate were mixed in four different ratios and the mixtures were pyrolyzed at different temperatures. The electrocatalytic activity towards the ORR was studied both in alkaline and acid media using the rotating disk electrode method. Electrochemical characterizations indicate that the synthesized boron- and fluorine co-doped nanocarbon catalyst possesses excellent electrocatalytic activity for ORR as compared to un-doped carbon nanomaterial. The surface morphology, composition and chemical nature of the co-doped catalysts were investigated with different physical methods and the results of surface characterization were correlated with the electrochemical results.

## Results and Discussion

### Surface Characterization

Scanning electron microscopy was used to examine the GC electrode surface modified with boron and fluorine co-doped carbon nanomaterial. Figure 1 presents a SEM image of a BF-doped reduced graphene oxide/few-walled carbon nanotube



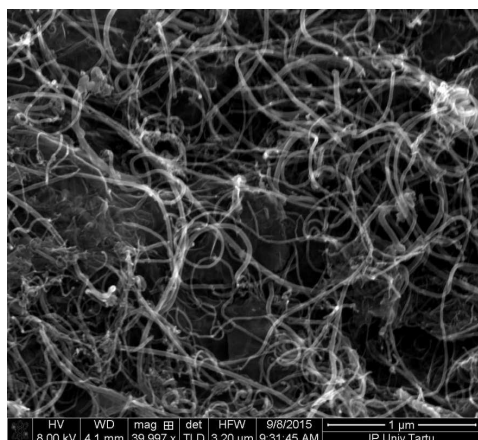


**Figure 1.** SEM image of boron and fluorine co-doped rGO/FWCNT composite material.

(rGO/FWCNT) catalyst material. In the figure BF-doped rGO/FWCNT material is evenly distributed all over the electrode surface.

TEM investigations of the B and F co-doped catalyst provided morphological information on the material. The co-doped reduced graphene oxide in Figure 2a appears to be in the form of nano-platelets ranging from 50–200 nm in diameter. These nano-platelets are homogeneously distributed over the FWCNT. The TEM image of the catalyst in Figure 2b gives an overview of the catalyst material and further demonstrates that not all the nanotubes interact with the graphene platelets and are graphene free. In the same image we start observing larger platelets of graphene along with few-layered graphene. One

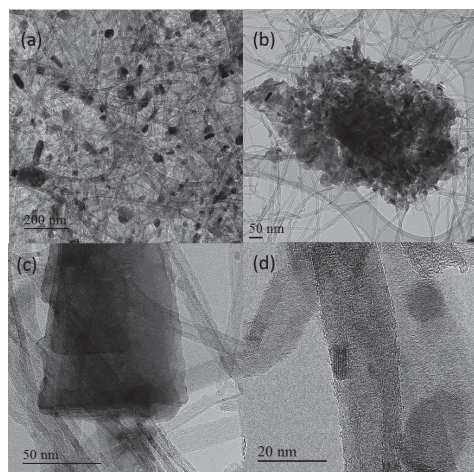


**Figure 2.** TEM image of boron and fluorine co-doped rGO/FWCNT composite material. (a) and (b) overview of the catalyst. (c) larger flakes of rGO. (d) FWCNT used in the study.

such larger platelet is observed in Figure 2c. This platelet is made up of a few layers of graphene and has many nanotubes in its vicinity, which act as spacers and tend to suppress possible graphitization of the layers.<sup>[73]</sup> In Figure 2d a high magnification image of the FWCNT used in the study is shown. Here we observe that the FWCNTs have between 5–10 walls that are well defined and devoid of any amorphous carbon. Smaller spherical graphene platelets are visible with sizes as small as 10 nm. These graphene platelets are known to harbor large quantities of surface defects which could be a result of doping.

The degree of graphitization and defect sites in the catalyst material were investigated with Raman spectroscopy. Figure 3 illustrates that before B and F co-doping the composite material exhibits an intense D and G peak at  $1310\text{ cm}^{-1}$  and  $1584\text{ cm}^{-1}$ , respectively. After the boron and fluorine-doping D and G peak appear at  $1303\text{ cm}^{-1}$  and  $1586\text{ cm}^{-1}$ , respectively. It is known that G band is caused because of scattering of  $E_{2g}$  phonons by  $sp^2$  hybridized carbon atoms and D band arises because of resonance Raman spectra caused by distortions in  $sp^2$  carbon system. An intense D band indicates that many defects have been created into the carbon network during the acid treatment and doping.

By calculating the D/G ratio it is possible to obtain information about the extent of defects in studied material. The ratio between D and G band intensities ( $I_D/I_G$ ) is 1.69 for undoped carbon material and 1.76 for BF-doped carbon material. Since the higher ratio indicates higher amount of surface defects it can be said that boron and fluorine doping leads to an increase of surface imperfections. This is confirmed by Kakaie and Balavandi who found that  $I_D/I_G$  ratio is significantly increasing after incorporation of fluorine into graphene structure, suggesting that disordered and defective carbon surface is largely caused by the fluorine doping.<sup>[74]</sup> Similar effect is reported for the N and F co-doping of carbon, which induces defect sites and destroys the graphene carbon skeleton and thereby increases the degree of distortion.<sup>[75]</sup> Another visible change in the Raman spectra is that the D peak gradually widens which indicated that the  $sp^2$  hybridization is

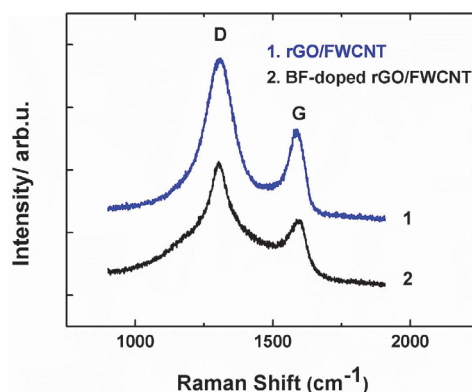


**Figure 3.** Raman spectra of rGO/FWCNT and BF co-doped rGO/FWCNT.

disrupted after B and F doping. These Raman spectroscopy results are also in good agreement with previous results reported by Gong et al.<sup>[76]</sup>

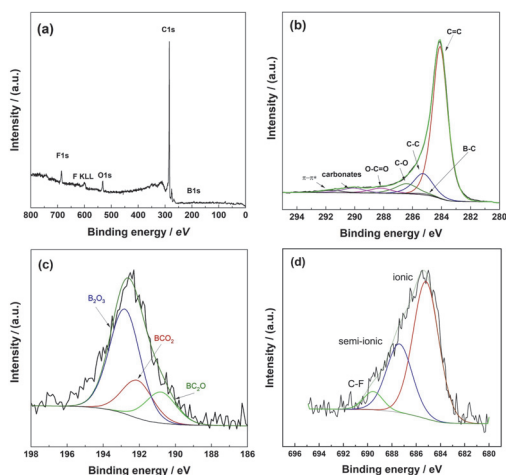
The surface chemical composition of the B and F co-doped composite material was studied by XPS. The XPS data shows the presence of boron, carbon, oxygen and fluorine with atomic percentages of 1.7%, 92%, 6% and 0.6%, respectively. As seen from Figure 4a, a distinguishable B1s peak appeared at 192.5 eV, C1s peak at 284 eV, O1s peak at 534.5 eV and F1s peak at 685.5 eV. The C1s peak in Figure 4b, was deconvoluted into five separate peaks, C=C peak at 284 eV, B–C peak at 285 eV, C–C peak at 285.5 eV, C–O at 286.5 eV and O–C=O at 288.2 eV. The XPS peak for C–F<sub>3</sub> should appear at around 291.8 eV, but because of the low amount of fluorine in the sample, which is close to the detection limit of the instrument, it is rather difficult to separate current peak from the C1s peak. Gong et al. have found that the fluorine doping level is extremely sensitive to high temperature treatment. The percentage of carbon-incorporated fluorine increases slowly during the heat-treatment until 700 °C and then starts decreasing with a dramatic drop at 800 °C.<sup>[76]</sup> This could occur because of the decomposition of fluorine-containing species at higher temperatures.<sup>[76,77]</sup>

High resolution B1s XPS spectrum presented in Figure 4c, showed three distinguishable peaks for different boron species, B<sub>2</sub>O<sub>3</sub>, BCO<sub>2</sub> and BC<sub>2</sub>O at 193, 192.2 and 190.8 eV, respectively. The proportion of different boron species is 60% of B<sub>2</sub>O<sub>3</sub>, 22% of BCO<sub>2</sub> and 18% of BC<sub>2</sub>O. The current B1s XPS peak with binding energy of 192.5 eV is positively shifted compared with that of pure boron (187.0 eV).<sup>[78,79]</sup> This indicates that some of the boron was incorporated into the carbon material by replacing C atoms in the sp<sup>2</sup> carbon network. From the inspection of the high resolution F1s XPS peak (Figure 4d), it appears that F1s peak can be deconvoluted into three peaks whereas it is rather hard to identify the exact nature and

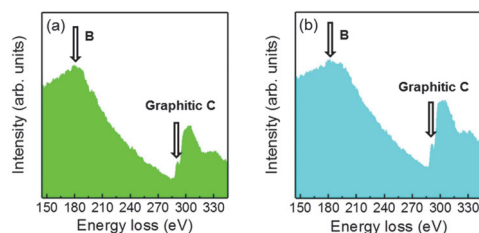
localization of the different forms of fluorine bonding. We could expect that BF co-doping can introduce a weaker peak of covalent C–F bonding at higher binding energy values and a more intense peak of semi-ionic and ionic C–F bonds which play the main role in improvement of charge transfer properties of the catalyst material.<sup>[33,77,80]</sup> It is also clear that fluorine is well doped into the carbon structure as it has been demonstrated in the previous scientific works that the F in the ionic and semi-ionic CF bonds is different from free F ions in the solution.<sup>[77]</sup> Fu et al. have proposed that the higher ratio of ionic C–F bond can also contribute to the higher ORR activity of the heteroatom-doped carbon catalysts.<sup>[81]</sup> Reportedly, the ionic and semi-ionic fluorine bonds tightly with carbon and makes the catalyst also less vulnerable to corrosion effects.<sup>[81]</sup> Parthiban et al. found that excellent ORR activity is primarily governed by the formation on semi-ionic C–F bonds.<sup>[80]</sup>

Figure 5 shows the electron energy loss spectroscopy (EELS) analysis of the randomly selected two areas of the BF-doped carbon sample. EELS is a powerful technique to study the chemical composition and bonding configuration of the catalyst materials, especially as the electrocatalytic activity of these dopants strongly depends on their position and atomic configuration.<sup>[82]</sup> Typical EELS spectra of B-doped carbon has two distinct absorption features at around 188 and 292 eV, corresponding to the expected B and C absorption K-edges respectively.<sup>[83]</sup> A K-edge is an excitation of a 1 s core electron, and the excitations to the 2p unoccupied states causes the fine structure within the edge.<sup>[83]</sup> At the same time the  $\pi$  bonding of 2p electrons or their existence in the sp<sup>2</sup> hybridization will express in the feature known as a  $\pi^*$  peak, which appears close to the onset of K-edge peak in the EELS spectrum.<sup>[84,85]</sup> Intensive  $\pi^*$  peak would mean that vast number of B atoms are located within flat graphene structure.<sup>[86]</sup> The spectra a and b in Figure 5 do not exhibit a strong  $\pi^*$  feature and has thereby most probably also some amorphous B in presence.<sup>[87]</sup> However, the features of the 1 s  $\rightarrow$   $\pi^*$  and 1 s  $\rightarrow$   $\sigma^*$  transitions, which are characteristic of the graphite sp<sup>2</sup> bonding configuration of the two elements, are still well-defined on the spectra and is thereby confirming the substitutional incorporation of B into the carbon matrix.<sup>[84]</sup>

As the spectra for the boron are so wide, then we can expect not only K-edge and  $\pi^*$  and  $\sigma^*$  transition related carbon incorporated B to be in presence, but a wide range of different types of boron. It is most likely that the BF-doped carbon



**Figure 4.** (a) XPS wide-scan spectrum of BF-doped carbon material. Core-level XPS spectra in (b) C1s, (c) B1s and (d) F1s regions.



**Figure 5.** EELS spectra of BF-rGO/FWCNT obtained from two randomly selected sample areas (a) and (b).

catalyst contains also boron oxide and the slight decrease in energy of the  $\pi^*$  peak compared with the boron oxide reference suggests that the bonding environment differs from the typical  $B_2O_3$ . Part of the boron is most probably oxidized on exposure to air after synthesis.<sup>[84]</sup>

Another phenomenon that can be seen from Figure 5a and b is that B K-edge peak is shifted to the negative direction and has much lower intensity peaks at higher energetic values suggesting that boron is in  $sp^2$ -hybridised electron system, rather than a physical mixture of different forms of B. All of that confirms that the boron K-edge and boron overall is coordination sensitive meaning that there are different local coordination of the probed boron atoms in both areas.<sup>[88]</sup> Unfortunately, it was not possible to detect any fluorine with EELS as the percentage of fluorine in the sample was under the detection limit. Thereby the energy-dispersive X-ray spectroscopy (EDS) was used for the fluorine detection. It is clear from the EDS images in Figure 6 that the fluorine is well doped to the surface of rGO/FWCNT. From the EDS and EELS results we conclude that the bright particles are the amorphous carbon particles attached to it. Due to high number of defects including abundant edge defects which are known as anchor sites for doping, amorphous carbon is more heavily doped compared with long-range ordered carbon. No impurities were detected in the samples.

### Oxygen Reduction in Alkaline and Acidic Media

Rotating disk electrode method (RDE) was used to study the electrocatalytic activity of BF-doped rGO/FWCNT material towards the ORR. GC electrodes modified with BF co-doped carbon composite catalysts were used as working electrode and measurements were carried out in  $O_2$ -saturated 0.1 M KOH and 0.5 M  $H_2SO_4$  electrolyte solutions. In the first part, the ORR activity as a function of mass ratio of carbon composite to BF source was investigated. Figures 7a and 7b show the RDE results in alkaline and acid media, respectively, for all four different mass ratios of BF source to rGO/FWCNT pyrolyzed at 800 °C. These ORR polarization curves were compared with those of unmodified rGO/FWCNT material bare GC and commercial 40% Pt/C catalyst.

One can see from Figure 7a that 1BFC, 2BFC and 3BFC show the same onset potential for ORR in alkaline media, which is approximately 0.87 V vs. RHE and is slightly more positive than that of 4BFC indicating that at some point increasing the boron

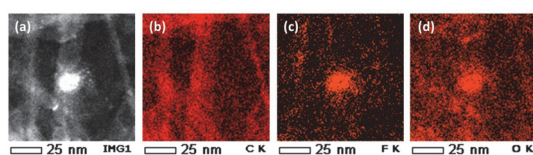


**Figure 6.** (a) Higher magnification STEM of the area used for elemental EDS mapping. (b–d) EDS elemental distribution of C, F, and O, respectively.

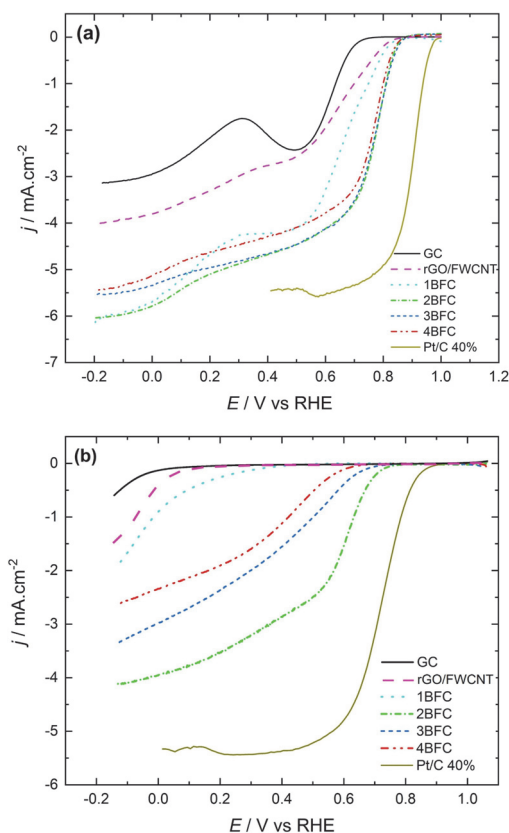


**Figure 7.** RDE voltammetry curves for oxygen reduction on GC electrodes modified with undoped rGO/FWCNT and BF-doped carbon composite materials in  $O_2$ -saturated (a) 0.1 M KOH and (b) 0.5 M  $H_2SO_4$ ,  $v = 10 \text{ mV s}^{-1}$ ,  $\omega = 1900 \text{ rpm}$ . Curve GC corresponds to unmodified glassy carbon.

and fluorine doping level will start to decrease the electrocatalytic activity towards the ORR. Similar behavior is also observed in Figure 7b for acidic media, however, the effect of dopant concentration is even more pronounced and the superiority of the 2BFC catalyst over the others is clearly evident. Although some of the previous works show that the ORR electrocatalytic activity of the catalyst material increases with increasing boron content, it should be mentioned that there is no literature about the application of boron trifluoride diethyl etherate (BTDE) as a boron or fluorine source for heteroatom doping of carbon nanomaterials.<sup>[51,52]</sup> It has been shown previously that at some point it will be rather difficult to increase the boron content in the carbon network just by increasing the amount of the boron source.<sup>[51]</sup> Moreover, defects and oxygen-containing functional groups on carbon surface play an important role in the electrocatalytic activity. Another reason for enhanced ORR kinetics on BF-doped carbon is that by introducing boron into the material, the oxygen content also increases as boron atoms enhance oxygen adsorption.<sup>[51]</sup> It has been proposed that positively charged boron atoms on the



carbon surface facilitate oxygen chemisorption which then act as a bridge transferring electrons from the adjacent carbon atoms to oxygen and thereby weakening the O–O bond.<sup>[66]</sup> On the other hand, the fluorine-doping of rGO and FWCNTs will lead to the formation of effective doped p-type semiconductor at low fluorine concentration and behave as a conductor at higher coverage of fluorine in carbon composite material.<sup>[76,87]</sup> The electrical conductivity of catalyst material will be improved as fluorine is a highly electronegative element and has excess valence electrons compared to boron or some other heteroatoms.<sup>[76,87]</sup> Another reason for the improved ORR activity of BF-doped rGO/FWCNT could be that the incorporation of fluorine atoms into the carbon structure will cause the formation of some specific structural defects where the electrocatalytically active sites could be positioned.<sup>[33]</sup> This supposition is also in good agreement with Raman spectroscopy results presented above.

Various studies have revealed that co-doping of graphene sheets with two or more different heteroatoms is more effective to modify the chemical surface composition of graphene and coordinate the interaction between the different atoms.<sup>[57,88]</sup> Hence, the improved electrocatalytic activity is also expected when graphene oxide and FWCNTs are doped with hydrophobic fluorine and boron, which facilitates the hydrophilic properties of carbon by chemisorption of oxygen. With co-doping the electronic hybrid structure of the carbon material will be manipulated *via* covalent bonds with the local  $\pi$ -orbital system of graphitic carbon, along with the generation of new bond interaction.<sup>[89]</sup>

It can also be seen that in alkaline media the ORR polarization curves of the heat-treated mixture of rGO and acid-treated FWCNTs have approximately 100 mV more positive onset potential compared with unmodified GC. After the boron and fluorine co-doping the onset potential for ORR is shifted to the positive direction. The half-wave potential value is shifted approximately 200 mV more positive compared to bare GC and also the reduction current values show a noticeable increase. The electrocatalytic effect is even more visible in acid media, where the onset potential of the 2BFC electrocatalyst is shifted positive for 600 mV as compared to the heat-treated rGO/FWCNTs and close to 700 mV compared to bare GC (see Figure 7b). On the basis of these RDE results it can be stated that the incorporation of boron and fluorine atoms into the carbon matrix of rGO and FWCNTs remarkably changes the electrocatalytic properties of the catalyst material. Nevertheless, compared with commercial 40% Pt/C catalyst, the  $E_{\text{onset}}$  of 2BFC is 130 mV less positive in alkaline and 140 mV less positive in acidic environment.  $E_{1/2}$  of Pt/C 40% is 160 mV more positive in both alkaline and acidic media compared with 2BFC.

The influence of pyrolysis temperature on the electrocatalytic activity of the boron and fluorine co-doped material was also investigated. While at 800 °C 2BFC showed the highest ORR activity, the pyrolysis at temperatures 600 °C and 1000 °C were performed with the same ratio of boron and fluorine source to carbon material. In Figures 8a and 8b one can see that the catalyst material prepared by pyrolysis at 800 °C shows the best electrocatalytic activity for O<sub>2</sub> reduction both in

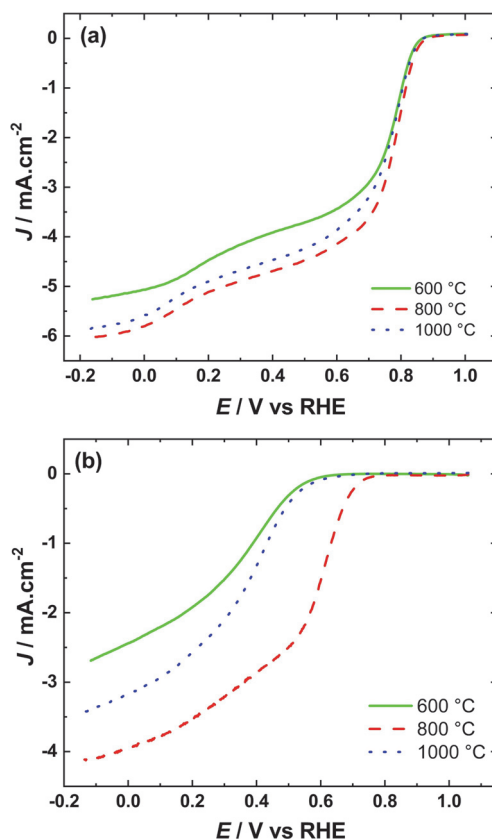


**Figure 8.** RDE voltammetry curves for oxygen reduction on a 2BFC/GC electrode in O<sub>2</sub>-saturated (a) 0.1 M KOH and (b) 0.5 M H<sub>2</sub>SO<sub>4</sub>.  $\nu = 10 \text{ mV s}^{-1}$ ,  $\omega = 1900 \text{ rpm}$ . 2BFC material was prepared by pyrolysis at temperatures of 600, 800 and 1000 °C.

alkaline and acid media respectively, while having most positive onset potential and also largest reduction current values. In previous works, it has been demonstrated that raising the temperature of the doping process increases the amount of electrocatalytically active surface species and therefore the material prepared at 800 °C is more active than that prepared at 600 °C.<sup>[55,90]</sup> Some of the previous reports have demonstrated that increasing the temperature of pyrolysis higher than 800 °C is more effective for heteroatom doping.<sup>[91,92]</sup> Nevertheless, in our case, raising temperature from 800 to 1000 °C for BF co-doping using BTDE, did not enhance the material's electrocatalytic activity for ORR. Therefore using BTDE for B and F co-doping may be considered as more cost-effective than using boron sources which show close by electrocatalytic ORR activity after doping at higher temperatures.<sup>[66]</sup>

Durability and methanol tolerance tests with the most active catalyst (2BFC) synthesized at 800 °C were performed in both alkaline and acidic media and the results were compared with commercial 40% Pt/C catalyst. During the durability tests (see Figure S1) 2BFC material has lost around 30% of the initial

current value after 60 000 seconds in both media it seems to have reached a plateau whereas the 40% Pt/C has lost around 35% of the initial current value after 60 000 seconds and the decrease in the current seems to continue. Compared with the commercial Pt/C the 2BFC material has significantly better methanol tolerance in both alkaline and acidic media (see Figure S2). In alkaline media the 2BFC lost around 12% of the initial current value and 40% Pt/C around 27%. In acid media the 2BFC lost 15% of the initial current value after 900 seconds from the methanol insertion whereas the commercial catalyst lost almost 40% of the current value.

Figures 9a and 9b illustrate a set of ORR polarization curves measured at different electrode rotation rates with the most active 2BFC catalyst modified GC electrode both in alkaline and acid media, respectively. The onset potential for ORR is approximately 0.86 V vs RHE in alkaline medium and 0.73 V vs RHE in acidic medium and at lower rotation rates the reduction current plateaus are formed indicating that the ORR process is almost entirely under the diffusion control.

All the same, this kind of electrocatalytic behavior could also be caused by new active sites resulting from boron and

fluorine co-doping where fluorine tends to cause the surface defects, while boron contributes to attracting oxygen species.<sup>[33,66]</sup> It has been found in many previous studies that doping of fluorine into carbon structure induces more positive charge on neighboring carbon atoms and thereby increases the activity of p-electrons. This in turn enhances the interaction between the catalyst sites and O<sub>2</sub> molecules and increases the electrocatalytic activity for ORR.<sup>[80,91,93]</sup> According to the RDE results we can conclude that the simultaneous incorporation of boron and fluorine atoms into the graphitic structures of graphene and FWCNTs can lead to the improvement of electrocatalytic ORR activity in terms of the onset potential and limiting current values.

In order to predict the number of electrons transferred per O<sub>2</sub> molecule (*n*) Koutecky-Levich (K–L) equation was used for calculations.<sup>[94]</sup>

$$\frac{1}{I} = \frac{1}{I_k} + \frac{1}{I_D} = -\frac{1}{nFAkC_{O_2}^b} - \frac{1}{0.62nFAD_{O_2}^{2/3}\nu^{-1/6}C_{O_2}^b\omega^{1/2}}$$

where *I* is the measured ORR current, *I<sub>k</sub>* and *I<sub>D</sub>* are the kinetic and diffusion-limited currents, respectively, *k* is the rate constant for oxygen reduction, *A* is the geometric electrode area, *F* is the Faraday constant (96,485 C mol<sup>−1</sup>), *D<sub>O<sub>2</sub></sub>* is the diffusion coefficient of oxygen (1.9×10<sup>−5</sup> cm<sup>2</sup> s<sup>−1</sup>),<sup>[95]</sup> *C<sub>O<sub>2</sub></sub><sup>b</sup>* is the concentration of the oxygen in the bulk (1.2×10<sup>−6</sup> mol cm<sup>−3</sup>),<sup>[95]</sup> *ν* is the kinematic viscosity of the electrolyte (0.01 cm<sup>2</sup> s<sup>−1</sup>)<sup>[96]</sup> and *ω* is the rotation rate (rad s<sup>−1</sup>). These O<sub>2</sub> solubility and diffusion coefficient values are given for 0.1 M KOH. For 0.5 M H<sub>2</sub>SO<sub>4</sub> solution the respective values are: *D<sub>O<sub>2</sub></sub>* = 1.8×10<sup>−5</sup> cm<sup>2</sup> s<sup>−1</sup> and *C<sub>O<sub>2</sub></sub><sup>b</sup>* = 1.13×10<sup>−6</sup> mol cm<sup>−3</sup>.<sup>[97]</sup> From the K–L plots shown in Figures 10a and 10b it can be seen that the intercepts of the extrapolated K–L lines are close to zero, which indicates that the ORR process is mostly under the diffusion control. The insets of Figures 10a and 10b compare the *n* values calculated from the K–L equation at various potentials. It should be noted that since higher rotation speeds (3100 and 4600 rpm) do not show a proper plateau, they were excluded from the K–L analysis. Based on K–L equation, *n* value in alkaline media is close to four, however, based on RRDE measurements the *n* value in alkaline was around three and the production of peroxide species increased from 40% to 60% when moving towards more negative potentials (see Figure S3a). RRDE measurements show that contradictory to K–L analysis results, the reaction takes place not via four electron but two-step two electron pathway on 2BFC nanocarbon catalyst. In the previous work done by Chokradjaroen, et al., they found that mostly two electron pathway takes place on a boron and fluorine co-doped material in alkaline media.<sup>[41]</sup> This can be explained by the ratio of different fluorine species in the catalyst material. In this work fluorine is mostly in ionic form as in study conducted by Chokradjaroen, et al. fluorine is mostly in semi-ionic form.<sup>[41]</sup> Although both forms are shown to enhance ORR activity, the ionic F results in higher electrical conductivity and therefore has a higher impact on the electronic structure of carbon network.<sup>[39]</sup> In acidic media at lower overpotentials (*E* > 0.36 V) the *n* value is close to two and the reduction of O<sub>2</sub> produces

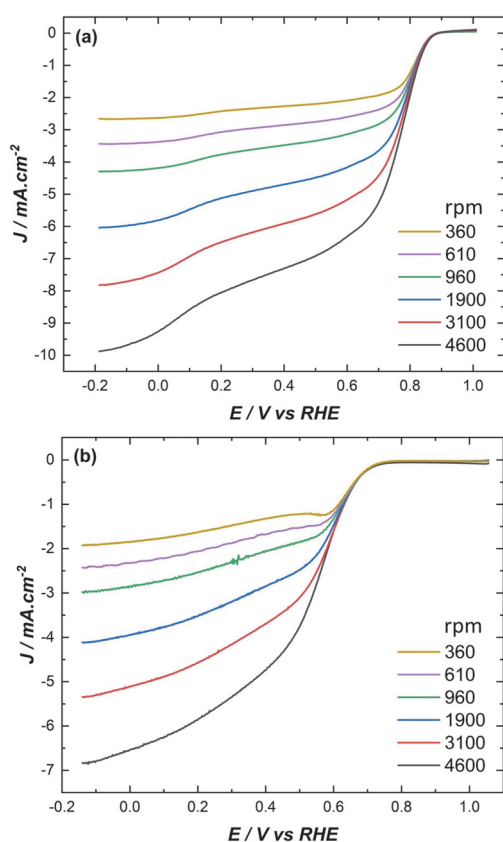


**Figure 9.** RDE voltammetry curves for oxygen reduction on a 2BFC/GC electrode in O<sub>2</sub>-saturated (a) 0.1 M KOH and (b) 0.5 M H<sub>2</sub>SO<sub>4</sub> at different rotation rates. *ν* = 10 mV s<sup>−1</sup>.

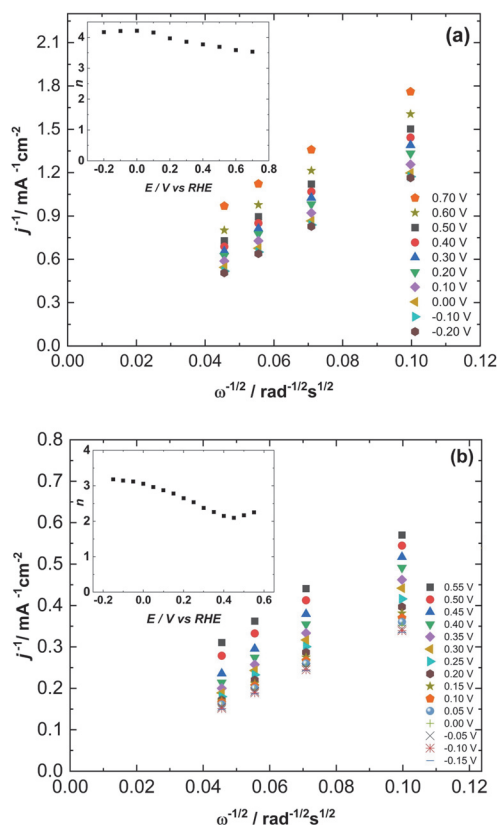


**Figure 10.** Koutecky-Levich plots for oxygen reduction on a 2BFC/GC electrode in (a) 0.1 M KOH and (b) 0.5 M H<sub>2</sub>SO<sub>4</sub>. Inset shows the potential dependence of the number of electrons transferred per O<sub>2</sub> molecule ( $n$ ). Data derived from Figure 9.

peroxide, which is the final product in this case. At more negative potentials the value of  $n$  gradually increased up to three, which indicates that some of the peroxide formed reduces further in this potential range. Based on RRDE measurements,  $n$  is three in all potential range and 40% of peroxide is produced (See Figure S3b). It should be mentioned that the K–L analysis of the undoped rGO/FWCNT material showed the  $n$  value of 2–2.5 in both alkaline and acid media. This demonstrates that although both doped and undoped catalysts form peroxide during ORR the B and F co-doped material is better catalyst in further reduction of peroxide.

Based on the XPS, EELS, EDS and RDE results presented above, it is clear that boron and fluorine are playing key roles in the electrocatalytic activity of these B and F co-doped reduced rGO/FWCNT catalysts and the electrochemical oxygen reduction reaction behavior is greatly enhanced due to a synergetic effect between doped B and F atoms. The RDE results clearly demonstrate that B and F co-doping can effectively improve the electrocatalytic ORR activity in both alkaline and acidic media.

## Conclusions

In summary, electrocatalytically active boron and fluorine co-doped nanocarbon catalyst materials were successfully synthesized and tested for oxygen reduction reaction (ORR). BF-doping was achieved by using few-walled carbon nanotubes (FWCNTs) and graphene oxide (GO) mixture as a carbon support and boron trifluoride diethyl etherate (BTDE) as a boron and fluorine source. Morphological analysis reveals that graphene also exists as nanoplatelets with sizes as small as 10 nm. Combining the XPS, EELS, EDS and RDE results reveal that the incorporation of boron and fluorine leads to the formation of electrocatalytically active boron and fluorine containing sites. The highest ORR activity was shown by the catalyst material prepared by heat-treatment of GO/FWCNT and BTDE with the mass ratio of 1:5 at 800 °C. It is important to note that boron and fluorine co-doping of GO/CNT composites have not been reported as ORR electrocatalysts before and BTDE has not been used as source for boron and fluorine co-doping in previous research. The synthesized boron and fluorine co-doped catalyst were electrochemically characterized with RDE in both alkaline and acidic media. The most active co-doped catalyst demonstrated a notable 50 mV increase in onset potential in alkaline conditions and a remarkable 600 mV increase in acidic conditions compared to the undoped catalyst. Additionally, the half-wave potential was 100 mV more positive in alkaline media and 700 mV more positive in acidic media when compared to the undoped carbon material. The results revealed that these materials possess a promising electrocatalytic activity towards O<sub>2</sub> reduction, and therefore have great potential in ion exchange membrane fuel cells and metal-air batteries.

## Experimental

### Preparation of BF-doped Carbon Nanomaterials

Over 99.6 wt%-pure few-walled carbon nanotubes (FWCNT), synthesized by fluidized-bed chemical vapor deposition, purchased from Noda Lab (Japan) were used<sup>[98,99]</sup> and graphene oxide (GO) was synthesized from graphite powder (Graphite Trading Company) by a modified Hummers method.<sup>[100,101]</sup> Boron trifluoride diethyl etherate (BTDE) (Sigma Aldrich) was used as boron and fluorine source in the doping process. Firstly, the FWCNTs were oxidized at room temperature in a mixture of 1:1 H<sub>2</sub>SO<sub>4</sub> and HNO<sub>3</sub> solution in order to introduce oxygen-containing groups on the carbon nanotube surface, which in turn introduces reactive sites for further modification of FWCNTs.

B and F co-doped carbon nanomaterials were synthesized by a single-step pyrolysis method. FWCNTs and GO with a ratio of 1:1 were mixed with a BTDE. Four different mass ratios were used (FWCNT, GO/boron, fluorine source = 1:2.5, 1:5, 1:10 and 1:20) and the prepared catalysts are designated as 1BFC, 2BFC, 3BFC and 4BFC, respectively. All the mixtures were sonicated for 1 hour and then dried in a vacuum oven. The materials were pyrolyzed in nitrogen atmosphere at 800 °C for 2 hours and then cooled down to room temperature. For comparison purposes also pyrolysis at temperatures of 600 °C and 1000 °C was carried out.

## Physical Characterization of BF-Doped Catalyst Materials

X-ray photoelectron spectroscopy (XPS) was used to analyze the surface composition of BF-doped carbon materials. The catalyst material was suspended in ethanol and deposited on a glassy carbon (GC) plate (1.1×1.1 cm) after which the plate was dried in a vacuum oven at 70 °C. An electron energy analyzer (SCIENTA SES100) and a non-monochromatic twin anode X-ray tube (XR3E2) with characteristic energies of 1253.6 eV (Mg  $K_{\alpha 1,2}$ , FWHM 0.68 eV) and 1486.6 eV (Al  $K_{\alpha 1,2}$ , FWHM 0.83 eV) were used for XPS studies. Pressure in the analysis chamber was below  $10^{-9}$  Torr. To collect the survey spectra the energy range from 800 to 0 eV, pass energy 200 eV and step size 0.5 eV was applied. For obtaining high resolution XPS spectra at certain regions a pass energy of 200 eV with step of 0.1 eV was applied.

To investigate the surface morphology of catalysts a scanning electron microscope (SEM) Helios NanoLab 600 (FEI) was used operating at 8 kV. The catalyst materials were suspended in ethanol and pipetted onto the GC plate. Many different areas of the sample were examined to gain the most representative characteristics of the same. For studying material morphology at the nanometer scale, transmission electron microscope (TEM) probe corrected FEI Titan G2 80–200 was used. At 200 keV the point-to-point resolution in TEM and STEM modes are around 2.4 Å and 0.9 Å. Samples for TEM imaging were prepared by mixing the catalyst powders in ethanol followed by sonication for uniform dispersion. A drop of the solution was then placed on a lacey carbon grid and was allowed to dry in air. F and B-doped GO-FWCNT samples were analyzed also with electron energy loss spectroscopy (EELS) and energy-dispersive X-ray spectroscopy (EDS) using JEM-ARM200F (atomic resolution microscope) (JEOL, Japan).

Raman spectrometer (Renishaw inVia) was also used to characterize the catalyst materials. For these measurements, an excitation  $Ar^{+}$  laser with wavelength of 514 nm was employed.

## Electrode Preparation and Electrochemical Measurements

The electrochemical measurements were performed with a standard three-electrode system using the rotating disk electrode (RDE) method. Pt foil was used as a counter electrode and a saturated calomel electrode (SCE) as reference electrode. All the potentials are represented against RHE. In order to avoid any migration of Pt nanoparticles into the electrolyte solution the Pt foil was placed in a separate quartz cuvette with a filter. This counter electrode has been validated and the results have been compared with a graphite rod electrode. A modified glassy carbon (GC) disk (GC-20SS, Tokai Carbon) with a geometric area of 0.2 cm<sup>2</sup> was used as a working electrode. A GC disk was pressed into a Teflon holder and polished to a mirror finish using alumina slurry (Buehler) with a grain size of 1 µm. After polishing the electrodes were sonicated in Milli-Q water (Millipore, Inc.) and isopropanol both for 5 min. The BF-doped carbon material was suspended in isopropanol (4 mg ml<sup>-1</sup>) containing 0.25% Tokuyama ionomer AS-4 (Tokuyama Corporation, Japan) or 0.5% Nafion solution (Sigma-Aldrich) for the alkaline and acidic media respectively. 20 µL of the prepared catalyst suspension was dropped onto the GC surface and then dried at 70 °C for 30 min. RDE measurements were carried out in 0.1 M KOH (Merck) and in 0.5 M H<sub>2</sub>SO<sub>4</sub> (Sigma-Aldrich) solution using electrode rotation rates ( $\omega$ ) from 360 to 4600 rpm which were varied employing an EDI101 rotator (Radiometer) and speed control unit CTV101. The potential was applied with an Autolab potentiostat PGSTAT30 (Eco Chemie B.V., The Netherlands) and the experiments were controlled using the General Purpose Electrochemical System (GPES) software. The activity of the prepared catalysts was evaluated by cyclic voltammetry (CV) and linear sweep voltammetry

(LSV) with a scan rate of 100 mV s<sup>-1</sup> and 10 mV s<sup>-1</sup>, respectively. The chronoamperometry method was employed for long time stability (60000 s) and methanol tolerance tests (1200 s). The counter electrode was graphite rod and reference electrode SCE. For acidic electrolyte the applied potential was 0.0 V vs RHE and for alkaline electrolyte was 0.5 V vs RHE. For methanol tolerance measurement, methanol was added at 300 s, so that the overall methanol concentration in the cell was 3.0 M.

For the rotating ring-disk electrode (RRDE) measurements an AFMT28T fixed-disk tip of GC disc/Pt ring (Pine Research) was used. The geometric area of the GC disc was 0.164 cm<sup>2</sup>. The electrochemical experiments were conducted on PGSTAT30 Autolab potentiostat/galvanostat (Eco Chemie B.V., The Netherlands) controlled with General Purpose Electrochemical System (GPES) software. For the RRDE measurements, an AFMSRX rotator together with a MSRX speed controller (Pine Research, USA) were employed. For the detection of hydroperoxide anion (HO<sub>2</sub><sup>-</sup>) formation during the RRDE measurements in 0.1 M KOH solution, the Pt ring electrode was kept at a constant potential of 0.55 V vs SCE. The ring electrode was electrochemically cleaned before each measurement by applying at least five potential cycles from -0.95 to 0.65 V vs SCE at 100 mV s<sup>-1</sup>. For the detection of hydrogen peroxide (H<sub>2</sub>O<sub>2</sub>) formation during the RRDE measurements in 0.5 M H<sub>2</sub>SO<sub>4</sub> solution, the Pt ring electrode was kept at a constant potential of 1.2 V vs SCE. The ring electrode was electrochemically cleaned before each measurement by applying at least five potential cycles from -0.2 to 1.4 V vs SCE at 100 mV s<sup>-1</sup>.

## Acknowledgements

This research was financially supported by institutional research funding (IUT20-16 and IUT20-17) of the Estonian Ministry of Education and Research and by the Estonian Research Council (Grant No. 9323). This work was also financed by the EU through the European Regional Development Fund (TK141 “Advanced materials and high-technology devices for energy recuperation systems”). The funding for the research stay at the DLR Institute of Networked Energy Systems e.V. (Germany) from the Bundesministerium für Bildung und Forschung in the framework of the project NETonia is greatly appreciated. Authors would like to thank Estonian Road Map infrastructure’s NAMUR project. The authors thank Ms. Michiko Edo at Waseda University for her support in the STEM-EELS analysis. Suguru Noda thanks JSPS for support through Kakenhi grant JP16H06368.

## Conflict of Interests

The authors declare no conflict of interest.

## Data Availability Statement

The data that support the findings of this study are available from the corresponding author upon reasonable request.



**Keywords:** ORR • heteroatom doping • graphene • carbon nanotubes • fuel cell

- [1] M. Liu, X. Xiao, Q. Li, L. Luo, M. Ding, B. Zhang, Y. Li, J. Zou, B. Jiang, *J. Colloid Interface Sci.* **2022**, 607, 791–815.
- [2] M. Li, X. Bi, R. Wang, Y. Li, G. Jiang, L. Li, C. Zhong, Z. Chen, J. Lu, *Matter* **2020**, 2, 32–49.
- [3] A. Radwan, H. Jin, D. He, S. Mu, *Nano-Micro Lett.* **2021**, 13, 132.
- [4] W. Xing, G. Yin, J. Zhang, *Rotating Electrode Methods and Oxygen Reduction Electrocatalysts*, Elsevier B.V., **2014**.
- [5] R. Ma, G. Lin, Y. Zhou, Q. Liu, T. Zhang, G. Shan, M. Yang, *Npj Comput. Mater.* **2019**, 5, 1–15.
- [6] H. Li, A. Xie, Y. Tang, H. Yang, Q. Huang, P. Wan, W. Yang, *Energy Technol.* **2021**, 9, 2100301.
- [7] P. Chandran, A. Ghosh, S. Ramaprabhu, *Sci. Rep.* **2018**, 8, 3591.
- [8] Y. He, G. Wu, *Acc. Mater. Res.* **2022**, 3, 224–236.
- [9] Md. M. Hossen, Md. S. Hasan, Md. R. I. Sardar, J. bin Haider, Mottakin, K. Tammeveski, P. Atanassov, *Appl. Catal. B* **2022**, 325, 121733.
- [10] A. Sarapuu, E. Kibena-Pöldsepp, M. Borghei, K. Tammeveski, *J. Mater. Chem. A* **2018**, 6, 776–804.
- [11] X. Bai, J. Guan, *Chin. J. Catal.* **2022**, 43, 2057–2090.
- [12] X. Bai, J. Guan, *Small Structures* **2023**, 4, 2200354.
- [13] T. Marshall-Roth, N. J. Libretto, A. T. Wrobel, K. J. Anderton, M. L. Pegis, N. D. Ricke, T. V. Voorhis, J. T. Miller, Y. Surendranath, *Nat. Commun.* **2020**, 11, 5283.
- [14] Z. Tian, Y. Wang, Y. Li, G. Yao, Q. Zhang, L. Chen, *iScience* **2022**, 25, 104557.
- [15] S. Chen, Z. Xu, J. Li, J. Yang, X. Shen, Z. Zhang, H. Li, W. Li, Z. Li, *Nanotechnology* **2022**, 33, 182001.
- [16] A. Kumar, Y. Zhang, W. Liu, X. Sun, *Coord. Chem. Rev.* **2020**, 402, 213047.
- [17] M. Song, Y. Song, W. Sha, B. Xu, J. Guo, Y. Wu, *Catalysts* **2020**, 10, 141.
- [18] Y.-H. Wang, B. Mondal, S. S. Stahl, *ACS Catal.* **2020**, 10, 12031–12039.
- [19] T. Tang, Y. Wang, J. Han, Q. Zhang, X. Bai, X. Niu, Z. Wang, J. Guan, *Chin. J. Catal.* **2023**, 46, 48–55.
- [20] M. Vikkisk, I. Kruusenberg, S. Ratso, U. Joost, E. Shulga, I. Kink, P. Rauwel, K. Tammeveski, *RSC Adv.* **2015**, 5, 59495–59505.
- [21] J. Chattopadhyay, T. S. Pathak, D. Pak, *Molecules* **2022**, 27, 670.
- [22] J. Woo, J. S. Lim, J. H. Kim, S. H. Joo, *Chem. Commun.* **2021**, 57, 7350–7361.
- [23] R. Gutru, Z. Turtayeva, F. Xu, G. Maranzana, R. Thimmappa, M. Mamlouk, A. Desforges, B. Vigolo, *Int. J. Hydrogen Energy* **2022**, DOI 10.1016/j.ijhydene.2022.10.177.
- [24] J. Han, J. Guan, *Nano Res.* **2023**, 16, 1913–1966.
- [25] T. Tang, S. Li, J. Sun, Z. Wang, J. Guan, *Nano Res.* **2022**, 15, 8714–8750.
- [26] F. Kong, X. Cui, Y. Huang, H. Yao, Y. Chen, H. Tian, G. Meng, C. Chen, Z. Chang, J. Shi, *Angew. Chem. Int. Ed.* **2022**, 61, e202116290.
- [27] E. Montiel Macías, A. M. Valenzuela-Muñiz, G. Alonso-Núñez, M. H. Fariás Sánchez, R. Gauvin, Y. Verde Gómez, *Diamond Relat. Mater.* **2020**, 103, 107671.
- [28] D. Rosas-Medellín, F. J. Rodríguez-Varela, B. Escobar, *Int. J. Hydrogen Energy* **2022**, 47, 30172–30177.
- [29] A. Ghosh, S. Ramaprabhu, *ECS Meet. Abstr.* **2017**, MA2017-02, 1497.
- [30] G. Fazio, L. Ferrighi, C. Di Valentin, *J. Catal.* **2014**, 318, 203–210.
- [31] M. Wang, Y. Li, J. Fang, C. J. Villa, Y. Xu, S. Hao, J. Li, Y. Liu, C. Wolverton, X. Chen, V. P. Dravid, Y. Lai, *Adv. Energy Mater.* **2020**, 10, 1902736.
- [32] J. Wu, R. Yang, W. Yan, *Int. J. Hydrogen Energy* **2019**, 44, 12941–12951.
- [33] G. Panomsuwan, N. Saito, T. Ishizaki, *J. Mater. Chem. A* **2015**, 3, 9972–9981.
- [34] S. Zeng, S. Wang, H. Zhuang, B. Lu, C. Li, Y. Wang, G. Wang, *Electrochim. Acta* **2022**, 420, 140460.
- [35] Y. Sim, S. Surendran, H. Cha, H. Choi, M. Je, S. Yoo, D. Chan Seok, Y. Ho Jung, C. Jeon, D. Jin Kim, M.-K. Han, H. Choi, U. Sim, J. Moon, *Chem. Eng. J.* **2022**, 428, 132086.
- [36] J. Guo, J. Zhang, H. Zhao, Y. Fang, K. Ming, H. Huang, J. Chen, X. Wang, *R. Soc. Open Sci.* **2018**, 5, 180925.
- [37] S. Akula, A. K. Sahu, *ACS Appl. Mater. Interfaces* **2020**, 12, 11438–11449.
- [38] X. Bai, Q. Wang, G. Xu, Y. Ning, K. Huang, F. He, Z. Wu, J. Zhang, *Chem. Eur. J.* **2017**, 23, 16862–16870.
- [39] T. Gong, R. Qi, X. Liu, H. Li, Y. Zhang, *Nano-Micro Lett.* **2019**, 11, 9.
- [40] Y. Lv, L. Yang, D. Cao, *ChemElectroChem* **2019**, 6, 741–747.
- [41] C. Chokradjaroen, S. Kato, K. Fujiwara, H. Watanabe, T. Ishii, T. Ishizaki, *Sustain. Energy Fuels* **2020**, 4, 4570–4580.
- [42] Y. Zhao, L. Yang, S. Chen, X. Wang, Y. Ma, Q. Wu, Y. Jiang, W. Qian, Z. Hu, *J. Am. Chem. Soc.* **2013**, 135, 1201–1204.
- [43] N. An, M. Zhao, X. Zheng, Q. Wang, X. Huang, B. Sun, Y. Shen, J. Wang, B. Chen, R. Liu, *J. Hazard. Mater.* **2022**, 424, 127444.
- [44] Z. Qu, F. Sun, J. Gao, G. Zhao, *J. Colloid Interface Sci.* **2022**, 613, 47–56.
- [45] D.-W. Wang, D. Su, *Energy Environ. Sci.* **2014**, 7, 576–591.
- [46] W. Xia, M. A. Hunter, J. Wang, G. Zhu, S. J. Warren, Y. Zhao, Y. Bando, D. J. Searles, Y. Yamauchi, J. Tang, *Chem. Sci.* **2020**, 11, 9584–9592.
- [47] J. Quilez-Bermejo, E. Morallón, D. Cazorla-Amorós, *Carbon* **2022**, 189, 548–560.
- [48] W. Al-Hajri, Y. De Luna, N. Bensalah, *Energy Technol.* **2022**, 10, 2200498.
- [49] J. Wu, Z. Pan, Y. Zhang, B. Wang, H. Peng, *J. Mater. Chem. A* **2018**, 6, 12932–12944.
- [50] T. Kondo, Y. Kodama, S. Ikezoe, K. Yajima, T. Aikawa, M. Yuasa, *Carbon* **2014**, 77, 783–789.
- [51] Y. Cheng, Y. Tian, X. Fan, J. Liu, C. Yan, *Electrochim. Acta* **2014**, 143, 291–296.
- [52] X. Bo, M. Li, C. Han, L. Guo, *Electrochim. Acta* **2013**, 114, 582–589.
- [53] Y. Xia, X. Zhao, C. Xia, Z.-Y. Wu, P. Zhu, J. Y. (Timothy) Kim, X. Bai, G. Gao, Y. Hu, J. Zhong, Y. Liu, H. Wang, *Nat. Commun.* **2021**, 12, 4225.
- [54] Z.-H. Sheng, H.-L. Gao, W.-J. Bao, F.-B. Wang, X.-H. Xia, *J. Mater. Chem.* **2011**, 22, 390–395.
- [55] G. Jo, S. Shanmugam, *Electrochem. Commun.* **2012**, 25, 101.
- [56] Z. Lei, H. Chen, M. Yang, D. Yang, H. Li, *Appl. Surf. Sci.* **2017**, 426, 294–300.
- [57] A. Liu, W. Li, H. Jin, X. Yu, Y. Bu, Y. He, H. Huang, S. Wang, J. Wang, *Electrochim. Acta* **2015**, 177, 36–42.
- [58] D.-Y. Yeom, W. Jeon, N. D. K. Tu, S. Y. Yeo, S.-S. Lee, B. J. Sung, H. Chang, J. A. Lim, H. Kim, *Sci. Rep.* **2015**, 5, 9817.
- [59] R. C. Bansal, M. Goyal, in *Carbon Adsorpt.*, CRC Press, **2005**.
- [60] V. Bernal, L. Giraldo, J. C. Moreno-Piraján, *J. Carbon research* **2018**, 4, 62.
- [61] H. C. Schniepp, J.-L. Li, M. J. McAllister, H. Sai, M. Herrera-Alonso, D. H. Adamson, R. K. Prud'homme, R. Car, D. A. Saville, I. A. Aksay, *J. Phys. Chem. B* **2006**, 110, 8535–8539.
- [62] P. Lazar, R. Zboril, M. Pumera, M. Otyepka, *Phys. Chem. Chem. Phys.* **2014**, 16, 14231–14235.
- [63] W. Cheng, X. Liu, N. Li, J. Han, S. Li, S. Yu, *RSC Adv.* **2018**, 8, 11222–11229.
- [64] H. K. Sadhanala, K. K. Nanda, *Carbon* **2016**, 96, 166–173.
- [65] N. Sreekanth, M. Azeezulla Nazrulla, T. Veetil Vineesh, K. Sailaja, K. Lakshminarasimha Phani, *Chem. Commun.* **2015**, 51, 16061–16064.
- [66] L. Yang, S. Jiang, Y. Zhao, L. Zhu, S. Chen, X. Wang, Q. Wu, J. Ma, Y. Ma, Z. Hu, *Angew. Chem. Int. Ed.* **2011**, 50, 7132–7135.
- [67] W. Ni, Y. Xue, X. Zang, C. Li, H. Wang, Z. Yang, Y.-M. Yan, *ACS Nano* **2020**, 14, 2014–2023.
- [68] Y. Xue, Q. Liu, G. He, K. Xu, L. Jiang, X. Hu, J. Hu, *Nanoscale Res. Lett.* **2013**, 8, 49.
- [69] C. Tang, Y. Bando, Y. Huang, S. Yue, C. Gu, F. Xu, D. Golberg, *J. Am. Chem. Soc.* **2005**, 127, 6552–6553.
- [70] X. Cheng, J. Long, R. Wu, L. Huang, L. Tan, L. Chen, Y. Chen, *ACS Omega* **2017**, 2, 2010–2016.
- [71] V. I. Sysoev, M. O. Bulavskiy, D. V. Pinakov, G. N. Chekhova, I. P. Asanov, P. N. Gevko, L. G. Bulusheva, A. V. Okotrub, *Materials* **2020**, 13, 3538.
- [72] S.-H. Kim, C.-H. Lee, J.-M. Yun, Y.-J. Noh, S.-S. Kim, S. Lee, S. M. Jo, H.-I. Joh, S.-I. Na, *Nanoscale* **2014**, 6, 7183–7187.
- [73] K.-K. Türk, I. Kruusenberg, J. Mondal, P. Rauwel, J. Kozlova, L. Matisen, V. Sammelselg, K. Tammeveski, *J. Electroanal. Chem.* **2015**, 756, 69–76.
- [74] K. Kakaei, A. Balavandi, *J. Colloid Interface Sci.* **2017**, 490, 819–824.
- [75] H. Wang, J. Sun, J. Wang, L. Jiang, H. Liu, *J. Mater. Res. Technol.* **2021**, 13, 962–970.
- [76] P. Gong, Z. Wang, Z. Fan, W. Hong, Z. Yang, J. Wang, S. Yang, *Carbon* **2014**, 72, 176–184.
- [77] J. Kim, R. Zhou, K. Murakoshi, S. Yasuda, *RSC Adv.* **2018**, 8, 14152–14156.
- [78] S. Murugesan, B. Viswanathan, *Carbon* **2007**, 45, 1628–1635.
- [79] A. V. Naumkin, A. Kraut-Vass, S. W. Gaarenstroom, C. J. Powell, *NIST X-Ray Photoelectron Spectroscopy Database, NIST Stand. Ref. Database 20, Version 4.1*. **2012**, DOI 10.18434/T4T88K.
- [80] V. Parthiban, B. Bhuvaneshwari, J. Karthikeyan, P. Murugan, A. K. Sahu, *Nanoscale Adv.* **2019**, 1, 4926–4937.
- [81] S. Fu, C. Zhu, J. Song, M. Engelhard, B. Xiao, D. Du, Y. Lin, *Chem. Weinh. Bergstr. Ger.* **2017**, 23, DOI 10.1002/chem.201701969.
- [82] W.-H. Chiang, C.-Y. Hsieh, S.-C. Lo, Y.-C. Chang, T. Kawai, Y. Nonoguchi, *Carbon* **2016**, 109, 49–56.

- [83] W.-Q. Han, J. Cumings, A. Zettl, *Appl. Phys. Lett.* **2001**, *78*, 2769–2771.
- [84] R. J. Nicholls, Z. Aslam, M. C. Sarahan, A. Koós, J. R. Yates, P. D. Nellist, N. Grobert, *ACS Nano* **2012**, *6*, 7800–7805.
- [85] J. Lu, S.-P. Gao, J. Yuan, *Ultramicroscopy* **2012**, *112*, 61–68.
- [86] R. Arenal, F. de la Peña, O. Stéphan, M. Walls, M. Tencé, A. Loiseau, C. Colliex, *Ultramicroscopy* **2008**, *109*, 32–38.
- [87] K.-I. Ho, J.-H. Liao, C.-H. Huang, C.-L. Hsu, W. Zhang, A.-Y. Lu, L.-J. Li, C.-S. Lai, C.-Y. Su, *Small* **2014**, *10*, 989–997.
- [88] Y. Liu, Q. Feng, Q. Xu, M. Li, N. Tang, Y. Du, *Carbon* **2013**, *61*, 436–440.
- [89] P. Gong, Z. Wang, Z. Li, Y. Mi, J. Sun, L. Niu, H. Wang, J. Wang, S. Yang, *RSC Adv.* **2013**, *3*, 6327–6330.
- [90] X. Xu, T. Yuan, Y. Zhou, Y. Li, J. Lu, X. Tian, D. Wang, J. Wang, *Int. J. Hydrogen Energy* **2014**, *39*, 16043–16052.
- [91] X. Sun, P. Song, Y. Zhang, C. Liu, W. Xu, W. Xing, *Sci. Rep.* **2013**, *3*, 2505.
- [92] C. V. Rao, Y. Ishikawa, *J. Phys. Chem. C* **2012**, *116*(6), 4340–4346.
- [93] X. Sun, Y. Zhang, P. Song, J. Pan, L. Zhuang, W. Xu, W. Xing, *ACS Catal.* **2013**, *3*, 1726–1729.
- [94] A. J. Bard, L. R. Faulkner, *Electrochemical Methods: Fundamentals and Applications, 2nd Edition*, John Wiley & Sons, Incorporated, **2000**.
- [95] R. E. Davis, G. L. Horvath, C. W. Tobias, *Electrochim. Acta* **1967**, *12*, 287–297.
- [96] J. M. Tanko, *J. Am. Chem. Soc.* **2005**, *127*, 4542–4542.
- [97] S. Gottesfeld, I. D. Raistrick, S. Srinivasan, *J. Electrochem. Soc.* **1987**, *134*, 1455.
- [98] Z. Chen, D. Y. Kim, K. Hasegawa, T. Osawa, S. Noda, *Carbon* **2014**, *80*, 339–350.
- [99] D. Y. Kim, H. Sugime, K. Hasegawa, T. Osawa, S. Noda, *Carbon* **2011**, *49*, 1972–1979.
- [100] W. S. Hummers, R. E. Offeman, *J. Am. Chem. Soc.* **1958**, *80*, 1339–1339.
- [101] L. Sun, L. Wang, C. Tian, T. Tan, Y. Xie, K. Shi, M. Li, H. Fu, *RSC Adv.* **2012**, *2*, 4498–4506.

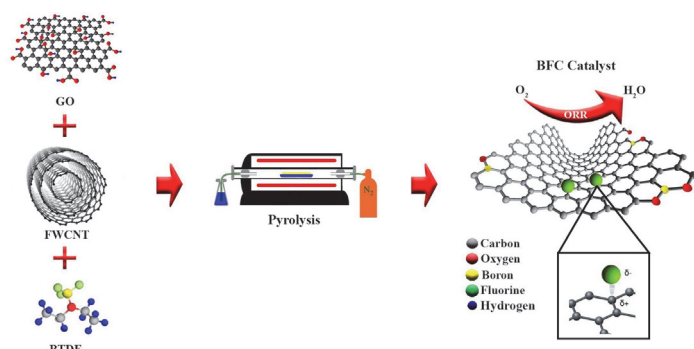
Manuscript received: November 14, 2023

Revised manuscript received: March 13, 2024

Accepted manuscript online: March 21, 2024

Version of record online: ■■■

## RESEARCH ARTICLE



Boron and fluorine co-doped carbon catalyst was synthesized via simple and low-cost direct pyrolysis method. Various physical characterization methods revealed the incorporation of boron and fluorine into the carbon

matrix. Rotating disc electrode method showed the enhanced electrocatalytic activity of the co-doped catalyst compared with the undoped material.

Dr. R. Raudsepp, K.-K. Türk, E. Zarmehri,  
Dr. U. Joost, Prof. P. Rauwel, Dr. R. Saar,  
Prof. U. Mäeorg, Dr. A. Dyck, Prof. M.  
Bron, Dr. Z. Chen, Prof. S. Noda, Dr. I.  
Kruusenberg\*, Prof. K. Tammeveski

1 – 12

**Boron and Fluorine Co-Doped  
Graphene/Few-Walled Carbon  
Nanotube Composite as Highly  
Active Electrocatalyst for Oxygen  
Reduction Reaction**



# Curriculum vitae

## Personal data

Name: Ehsan Zarmehri  
Date of birth: 04.04.1985  
Place of birth: Mashhad, Iran  
Citizenship: Iranian

## Contact data

E-mail: [ehzarm@taltech.ee](mailto:ehzarm@taltech.ee)  
Web: <https://www.linkedin.com/in/ehsan-zarmehri>

## Education

2018–2025 Tallinn University of Technology, Ph.D. in electrochemistry  
2008–2011 Isfahan University of Technology, M.Sc. in Chemical engineering  
2004–2008 Mazandaran University, B.Sc. in Chemical engineering  
2000–2004 Razi High school, physic-mathematic

## Language competence

English Fluent  
German B1  
Persian Native

## Professional employment

10.2024–ongoing Product manager alkaline electrolyser, ThyssenKrupp Nucera, Dortmund, Germany  
12.2022–09.2024 Fuel cell and electrolyser developer, Fuel cell & Hydrogen research center, Duisburg, Germany  
02.2022–11.2022 Guest researcher, Federal Institute of Materials Research and Testing (BAM), Berlin, Germany

## Scientific work

### Publications

1. Zarmehri, E., Raudsepp, R., Šmits, K., Käämbre, T., Šutka, A., Yörük, C. R., Zacs, D., & Kruusenberg, I. (2023). Lead and Nitrogen Co-Doped Multi-Walled Carbon Nanotube Electrocatalyst for Oxygen Reduction Reaction. *Journal of The Electrochemical Society*, 170(11), 114505. <https://doi.org/10.1149/1945-7111/AD0072>
2. Zarmehri, E., Raudsepp, R., Danilson, M., Šutka, A., & Kruusenberg, I. (2023). Vanadium and carbon composite electrocatalyst for oxygen reduction reaction. *Materials Chemistry and Physics*, 307, 128162. <https://doi.org/10.1016/J.MATCHEMPHYS.2023.128162>
3. Raudsepp, R., Türk, K. K., Zarmehri, E., Joost, U., Rauwel, P., Saar, R., Mäeorg, U., Dyck, A., Bron, M., Chen, Z., Noda, S., Kruusenberg, I., & Tammeveski, K. (2024). Boron and Fluorine Co-Doped Graphene/Few-Walled Carbon Nanotube Composite as Highly Active Electrocatalyst for Oxygen Reduction Reaction. *ChemNanoMat*, 10(6), e202300546. <https://doi.org/10.1002/CNMA.202300546>



### **Conference and workshop**

1. School of Catalysis, 24-26 May 2022, Charles University, Prague, Czech Republic. <https://school.katalyza.cz>
2. Concepts in heterogeneous catalysis and applications to energy conversion, September – December 2021, Denmark University of Technology, Denmark. <http://www.dtu.dk>
3. E. Zarmehri et al., Vanadium and nitrogen co-doped multi-walled carbon nanotube, electrocatalyst for oxygen reduction reaction”, GSFMT Scientific conference 2021, Tartu, Estonia.
4. Fuel cell tutorial workshop, 8th European Low Temperature Fuel Cells, Electrolysers & H<sub>2</sub> Processing Forum, 29<sup>th</sup> June – 1<sup>st</sup> July 2021, Lucerne, Switzerland. <http://www.efcf.com>
5. European summer school on Fuel cell, Electrolyzer and Battery, (LT-FC) 4 – 11 September 2020. Athene, Greece. <https://www.jess-summerschool.eu>

## Elulookirjeldus

### Isikuandmed

Nimi: Ehsan Zarmehri  
Sünniaeg: 04.04.1985  
Sünnikoht: Mashhad, Iraan  
Kodakondsus: Iraani

### Kontaktandmed

E-mail: [ehzarm@taltech.ee](mailto:ehzarm@taltech.ee)  
Veeb: <https://www.linkedin.com/in/ehsan-zarmehri>

### Hariduskäik

2018–2025 Tallinna Tehnikaülikool, Ph.D. elektrokeemias  
2008–2011 Isfahani Tehnikaülikool, M.Sc. keemiatehnoloogias  
2004–2008 Mazandarani Ülikool, B.Sc. keemiatehnoloogias  
2000–2004 Razi keskkool, füüsika-matemaatika suund

### Keelteoskus

Inglise keel C1  
Saksa keel B1  
Pärsia keel emakeel

### Töökogemus

10.2024– ... leeliselektrolüüserite tootejuht, ThyssenKrupp Nucera, Dortmund, Saksamaa  
12.2022–09.2024 kütuseelementide ja elektrolüüserite arendaja, Kütuseelementide ja Vesiniku Uurimise Keskus (Fuel cell & Hydrogen research center), Duisburg, Saksamaa  
02.2022–11.2022 külalisteadur, Föderaalne Materjalide Uurimise ja Testimise Instituut (Federal Institute of Materials Research and Testing (BAM)), Berliin, Saksamaa  
12.2018–11.2022 nooremteadur, Keemilise ja Bioloogilise Füüsika Instituut, Tallinn, Eesti

### Teadustöö

#### Publikatsioonid

1. Zarmehri, E., Raudsepp, R., Šmits, K., Käämbre, T., Šutka, A., Yörük, C. R., Zacs, D., & Kruusenberg, I. (2023). Lead and Nitrogen Co-Doped Multi-Walled Carbon Nanotube Electrocatalyst for Oxygen Reduction Reaction. *Journal of The Electrochemical Society*, 170(11), 114505. <https://doi.org/10.1149/1945-7111/AD0072>
2. Zarmehri, E., Raudsepp, R., Danilson, M., Šutka, A., & Kruusenberg, I. (2023). Vanadium and carbon composite electrocatalyst for oxygen reduction reaction. *Materials Chemistry and Physics*, 307, 128162. <https://doi.org/10.1016/J.MATCHEMPHYS.2023.128162>
3. Raudsepp, R., Türk, K. K., Zarmehri, E., Joost, U., Rauwel, P., Saar, R., Mäeorg, U., Dyck, A., Bron, M., Chen, Z., Noda, S., Kruusenberg, I., & Tammeveski, K. (2024). Boron and Fluorine Co-Doped Graphene/Few-Walled Carbon Nanotube Composite as Highly Active Electrocatalyst for Oxygen Reduction Reaction. *ChemNanoMat*, 10(6), e202300546. <https://doi.org/10.1002/CNMA.202300546>

### **Konverentsid ja töötoad**

1. School of Catalysis, 24-26 May 2022, Charles University, Prague, Czech Republic. <https://school.katalyza.cz>
2. Concepts in heterogeneous catalysis and applications to energy conversion, September – December 2021, Denmark University of Technology, Denmark. <http://www.dtu.dk>
3. E. Zarmehri et al., Vanadium and nitrogen co-doped multi-walled carbon nanotube, electrocatalyst for oxygen reduction reaction”, GSFMT Scientific conference 2021, Tartu, Estonia.
4. Fuel cell tutorial workshop, 8th European Low Temperature Fuel Cells, Electrolysers & H<sub>2</sub> Processing Forum, 29<sup>th</sup> June – 1<sup>st</sup> July 2021, Lucerne, Switzerland. <http://www.efcf.com>
5. European summer school on Fuel cell, Electrolyzer and Battery, (LT-FC) 4 – 11 September 2020. Athene, Greece. <https://www.jess-summerschool.eu>

ISSN 2585-6901 (PDF)  
ISBN 978-9916-80-380-6 (PDF)